

https://dspace.org/

Development of Lanthanide metal complxes as contrast agents for magnetic resonance imaging (MRI).

Sannasy, Desigan

2013-02-14
http://hdl.handle.net/10539/12424

Downloaded from a DSpace repository. https://dspace.org/

Development of Lanthanide Metal Complexes as Contrast Agents for Magnetic Resonance Imaging (MRI).

-Desigan Sannasy-

In Partial Fulfillment of the Requirements for the
degree of
Doctor of Philosophy

University of the Witwatersrand
Johannesburg, South Africa
2012

(Defended September 17, 2010)

Declaration

I declare that this is my own unaided work. It is being submitted for the Degree of Doctor of Philosophy at the University of the Witwatersrand, Johannesburg. It has not been submitted before any degree or examination at any other university.



D. Sannasy

31 March 2012

Preface

The topics covered in this thesis encompass different scientific fields: supramolecular/ coordination chemistry, biological physics, and medical diagnostics, under the common theme of magnetic interactions in matter. The work performed presents a comprehensive analysis of the chemistry of some lanthanide(III) complexes of novel ligands that are of interest as magnetic resonance imaging (MRI) agents, and from the florescence point of view. The first chapter introduces the topic of metal complex coordination chemistry, specifically lanthanide-based polyaminocarboxylate macrocycles, with emphasis on the underlying principles leading to landmark discoveries. The historical background, coordination chemistry and underlying principles for both lanthanides and macrocycles are explained in detail. The second part of the introduction presents the basic principles of MRI and how it can be improved using MRI contrast agents (MRI-CAs). It also explains the historical significance of the MRI protocol and the role of ligand architecture towards improving on current contrast agents. In the second chapter a detailed account of the strategy taken towards the synthesis of target lanthanide complexes will be explored, along with full characterization of all precursors, intermediates and final target complexes using NMR, ESI-MS, FTIR and in some cases X-ray crystallography. Furthermore, the solution chemistry of the complexes will be described and investigated using UV-vis spectroscopy, luminescence spectroscopy and cyclic voltammetry (CV). Using these techniques it was then possible to ascertain the pK_as, the number of hydration waters (q) and electrochemical behavior of these complexes across the pH range 2 to 12. However, the main aim of this work was to investigate the effect of suitable buffers by observing their photophysical behavior and how they affect the coordination chemistry with the complexes synthesized. In the third chapter the results of the above-mentioned synthetic goals, solid state chemistry and solution behavior are analyzed and expounded upon with three specific sections the first being solid state chemistry, then spectroscopic analyses (luminescence and UV-vis) followed by electrochemistry. The analyses and discussion appear separately. Finally, in the fourth chapter the findings are discussed and tied up with the hypothesis followed by concluding remarks for each investigation and some future work suggestions.

Abstract

This work describes work related to the search for new and improved MRI contrast agents. It is a focused study that describes the synthesis and characterization of three novel macrocyclic ligands, two of which incorporates a pendant *β*-amino alcohol (cyclohexyl) arm for complexation with Eu^{3+} and Gd^{3+}. The target products were synthesized successfully in quantitatively high yields and confirmed using general analytical characterization techniques including NMR, ESI-MS, FTIR and in some cases X-ray crystallography.

Crystal structures of two of the *N*-substituted cyclen based ligands, namely molecules **2** and **3** are reported. They both formed in the monoclinic crystal system and found to be in the $P_{21/c}$ and $P_{21/n}$ space group, respectively. Although **2** crystallized as a free base, **3** formed a complex with sodium with iodide as a counter ion. In addition, three lanthanide crystal structures are reported and each adopts a distorted capped square anitiprismatic geometry. Molecule **2** formed crystals with both Eu^{3+} and Gd^{3+} to give molecule **5** and **6**, respectively. They both formed in the triclinic and orthorhombic crystal system and found to be in the P_{-1} and Pcca space group, respectively. Efforts to grow lanthanide crystals with **7** failed, however its Eu^{3+} complex was satisfactorily synthesized. For comparative purposes molecule **9** was synthesized and the crystal structure is reported.

In an effort to elucidate the solution structure of these new Eu^{3+} complexes in the absence and presence of KHP, their interaction with the metal center and ligand were studied further using luminescence and UV-visible analyses to determine pK_as spectroscopically. Comparing the pK_a for the hydrolysis of water in **5** and **9** in MCB with KHP, it was observed that the pK_a for **5** is larger. This increase is attributed to the compression induced by the cyclohexyl moiety which consequently causes an overall decrease in bond distance between the metal center and amidic oxygen donors as shown in the solid-state data. Furthermore, the hydrophobic nature of the cyclohexyl side arm which replaces one of the acetamide arms in **9** also contributes to the overall decrease in pK_a observed. Comparing the pK_a for the hydrolysis of water in **5** and **7** in MCB excluding KHP, again it was observed that the pK_a for **5** is larger. The coordinated water in **5**

appears to be more acidic than for **7**, possibly due to the weaker inductive effect of **7** which possess arms that are of a sp_3 nature and impossible to deprotonate.

In addition, the number of coordinated water molecules (*q)* to the metal center were determined using luminescent lifetime measurements and corrected for the estimation according to structural functionalities innate to the complexes in this study. In solution, the *q* values obtained agreed well with the proposition that the phthalate moiety coordinates with the central Eu^{3+} ion in a unidentate fashion and maintains a nine coordination number. The *q* values also agree with luminescent spectroscopic data which shows two valid spectroscopic pK_as; the deprotonation of the phthalate carboxylate and the deprotonation of the water molecule coordinated to the metal center. The mean pK_a values were found to be pK_1 = 4.67 ± 0.06 and pK_2 = 8.69 ± 0.12, respectively. The *q* values obtained for **5** in MCB with KHP from pH 4.710 and 9.484 ranged from 1.77 to 0.70 using Equation 3.1 and from 1.79 to 0.72 using Equation 3.2, respectively. It is proposed that the due to the coordination of the phthalate moiety the hydroxyl group of the cyclohexyl moiety no longer coordinates itself to the metal center. The *q* values obtained for **5** in water from pH 4.375 and 8.645 ranged from 0.94 to 0.55 using Equation 3.1 and from 0.95 to 0.56 using Equation 3.2, respectively. The slight increase in the *q* value is attributed to the hydrogen bonding the cyclohexyl group is involved in with water molecules in the second coordination sphere which is very close to 0.5.

Finally, the electrochemical behavior of complex **5** and **9** across the pH range were investigated using CV. Only a single electrochemically active species exists for both complexes. The results for **5** show that the metal is encapsulated between pH 3 to 10 ($E_{1/2}$ = -0.83 V), however above pH 11 the complex is demetalated ($E_{1/2}$ = -1.02 V). The results for **9** show that the metal is encapsulated between pH 3 to 10 ($E_{1/2}$ = -0.83 V), however below pH 11 the complex shows a decrease in overall current ($E_{1/2}$ = -0.90 V). This result shows that complex **9** is more resistant to oxidation as compared to complex **5**, meaning that having four acetamide arms at higher pH is better than having three. This difference can also be related to the role and tautomeric effect of the amidic arms in stabilizing the complex. In addition, the standard rate constant was determined for electron transfer and is close to 1.0 for both complexes investigated, which means the reductions in both complexes are not diffusion controlled but the electrochemically active

species are adsorbed on the electrode surface. The above electrochemical results show that the metal remains encapsulated for most of the pH range and only becomes toxic free metal above pH 11. This vast pH range of complex intactness is a favorable attribute if it were to be considered in its application as a potential MRI agent.

Key words: MRI, europium(III), gadolinium(III), polyazamacrocycles, luminescence, cyclic voltammetry, MRI contrast agent.

This work is dedicated to God and my loving Family:

My Parents: Dhanpaul Jason and Rani Sannasy

My son: Ethan Joshua Sannasy

My Brother: Poovendran Sannasy

My Grandparents: Ma and Nine Daddy, Umma and Shinah

My Uncle: Visanathan Sannasy (Vis Mama)

My Aunts: Naguratham Nair (Aka) and Jenny Chetty

The person that initially believed in when I first came to Wits: Mrs Joyce Smith

The Govender Family and Herelall Family

My mentors and life coaches: Prof and Doc

Thanks to all of you for the love and support throughout the years. I cannot thank you enough.

Acknowledgements

The knowledge imparted throughout the course of this degree has indelibly become a part of who I am. That is itself a worthy achievement but the successful completion of my project would not have been possible without the selfless efforts of those who supported me on this journey. I have found this rare opportunity to evince a word of thanks to all those who have played a key role in my self-development. My heartfelt thanks to Prof. Helder Marques and Prof. Alvaro de Sousa, Bioinorganic Research Group, School of Chemistry, University of the Witwatersrand, for providing their foresight and optimal resources allocation that helped me in the successful completion of my thesis project. I wish to express my deepest reverence to them for their suggestions, valuable guidance and providing me the facilities during the course of the investigation. I extend an appreciative thank you to my mentor Dr. Fanie Otto from Sasol Ltd for his mentorship and patience.

I owe a sincere thanks to my esteemed colleagues who helped in the general characterisation of my products namely, Dr. Richard Mampa, NMR Spectroscopy; Dr. Andrew Dinsmore and Mrs. M. Ferreira, Mass Spectroscopy; Dr. Manuel Fernandes, X-ray crystallographic data acquisition; Mr Tapoa Dzara, Glassblowing; and Dr. Karen Billing, Cyclic Voltammetry experimental setup, for their sincere guidance, co-operation, constant encouragement, patience and the standard of results obtained is true testament to that. I express my cordial gratitude to the Bioinorganic Group and especially my friends, Kamen Padayachee, Sadhna Mathura, Dr. Chris Ealand, Dr. Mabel Conyanis, Caitlin Zipp, Dr. Chris Perry, Dr. Winston Nxumalo, Dr. Sandra Reisinger, Dr. Susan Chemaly, Dr Andreas Lemmerrer, Warren Thompson, Lee Madeley and Desiree Govender (UKZN) for their help, belief in me and timely suggestions when it most mattered.

I would like to thank the University of the Witwatersrand, the National Research Foundation (NRF) and Sasol Ltd for the much needed financial support. Finally, most of all, I thank my family members for their unconditional love, reassurance and invaluable support to complete my thesis project. I also thank all those who I could not find a separate name for but have helped directly and indirectly.

Table of Contents

Declaration 1

Preface 2

Abstract 3

Acknowledgements 7

Chapter One Introduction 27

1.1 Solid state and Supramolecular Chemistry of Polyazamacrocycles and their Lanthanide Complexes 27

1.1.1 General Background to Supramolecular Chemistry 27

1.1.2 Introduction to Polyazamacrocycles 29

1.1.3 Coordination Chemistry of Polyazamacrocycles 31

1.1.4 Selectivity of Cation Complexation 33

1.2 Lanthanides 34

1.2.1 Historical Background and Relevance 34

1.2.2 Coordination Chemistry of Lanthanides 39

1.2.3 Donor Group Orientation and Chelate Ring Size Effects 41

1.2.4 Introduction to Stereochemistry of Lanthanide Complexes 42

1.3 Metal Complex Coordination meets Medical Imaging 46

1.3.1 Introduction 46

1.3.2 Suitable Imaging Characteristics of Lanthanides and their Applications in Medicine **47**

1.4 Magnetic Resonance Imaging **51**

1.4.1 Applications of MRI **51**

1.4.2 Historical Background **52**

1.4.3 Principles of MRI **53**

1.4.4 The biological parameters T_1 and T_2 in MRI **56**

1.4.5 Factors related to Image Quality **59**

1.4.6 Luminescence Lifetime Studies in the Rapid-Exchange Limit **60**

1.4.7 Biomedical Considerations Toward the Development of MRI-CAs **63**

1.4.8 Biological Buffers **72**

1.5 Scope and Objectives of the Research Project **75**

Chapter Two Experimental **80**

2.1 Materials and Methods **80**

2.1.1 General Materials **80**

2.1.2 Distillation of Solvents **82**

2.1.2.1 Acetonitrile **82**

2.1.2.2 Ethanol **82**

2.1.3 General Analytical Characterisation Techniques **82**

2.1.3.1 Nuclear Magnetic Resonance Spectroscopy (NMR) **82**

2.1.3.2 Electrospray Ionization-Mass Spectroscopy (ESI-MS) **83**

2.1.3.3 Fourier Transform Infrared Spectroscopy (FTIR) **83**

2.1.3.4 Melting Point Determination **83**

2.1.3.5 Solid State Chemistry of Polyazamacrocycles and their Complexes with Lanthanides **84**

2.1.3.5.1 Crystal Growth Techniques Employed **84**

2.1.3.5.2 Solving Crystal Structures **85**

2.2 Synthetic Aspects and Strategies of Designing Lanthanide Complexes under Standard Laboratory Conditions **86**

2.2.1 Synthesis of Precursor: Preparation of *N*-methyl-chloroacetamide **88**

2.2.2 Preparation of *Di*-methyl-chloroacetamide **89**

2.2.2.1 Synthesis of *β*-amino alcohol Intermediate: 1-(2-Hydoxycyclohexyl)-1,4,7,10-tetraazacyclodecane (**1**) **90**

2.2.3 Synthesis of *N*-substituted Cyclen based Ligands **91**

2.2.3.1 Preparation of 1,4,7-tris[N-methylcarbomylmethyl]-10-2(hydroxycyclohexyl)-1,4,7,10-tetraazacyclododecane (**2**) **91**

2.2.3.2 Preparation of 1,4,7-tris[*N,N*-dimethylcarbamylmethyl]-10-(2-hydroxycyclohexyl)-1,4,7,10-tetraazacyclododecane (**3**) **93**

2.2.3.3 Preparation of 1,4,7,10-Tetrakis(methylcarbamylmethyl)-1,4,7,10-tetraazacyclodecane (**4**) **94**

2.2.4 Synthesis of Eu^{3+} and Gd^{3+} Macrocyclic Complexes **95**

2.2.4.1 Metal Complexation of 1,4,7-tris[*N*-methylcarbamylmethyl]-10-(2-hydroxycyclohexyl)-1,4,7,10-tetraazacyclododecane with Europium (**5**) **95**

2.2.4.2 Metal Complexation of 1,4,7-tris[*N,N*-dimethylcarbamylmethyl]-10-(2-hydroxycyclohexyl)-1,4,7,10-tetraazacyclododecane with Europium (**7**)..... **96**

2.2.4.3 Metal Complexation of 1,4,7,10-Tetrakis(methylcarbamylmethyl)-1,4,7,10-tetraazacyclodecane with Europium (**9**)..... **98**

2.2.4.4 Metal Complexation 1,4,7-tris[*N*-methylcarbamylmethyl]-10-(2-hydroxycyclohexyl)-1,4,7,10-tetraazacyclododecane with Gadolinium (**6**) **99**

2.2.4.5 Metal Complexation of 1-(2-hydroxycyclohexyl)-4,7,10-tris-(*N'-N'*-dimethylacetamide)–1,4,7,10-tetra-azacyclodecane with Gadolinium (**8**) **100**

2.3 Solution Chemistry of Complexes with Lanthanides **101**

2.3.1 General Apparatus and Materials..... **101**

2.3.1.1 pH Measurements and Calibration of pH meter **101**

2.3.1.2 Preparation of Standard Solutions **101**

2.3.2 Luminescence Studies and UV-visible Studies: Determination of Spectroscopic pK_as of Europium Complexes in Multicomponent Buffer Solutions (MCB) **102**

2.3.2.1 Preparation of Europium Complexes in Multicomponent Buffer (MCB) with Potassium Hydrogen Phthalate (KHP)..... **103**

2.3.2.1.1 Europium-1,4,7-tris[*N*-methylcarbamylmethyl]-10-(2-hydroxycyclohexyl)-1,4,7,10-tetraazacyclododecane (**5**)..... **103**

2.3.2.1.2 Europium-1,4,7,10-Tetrakis(methylcarbamylmethyl)-1,4,7,10-tetraazacyclodecane (**9**) **104**

2.3.2.2 Preparation of Europium Complexes in MCB excluding KHP **104**

2.3.2.2.1 Preparation of Europium-1,4,7-tris[*N*-methylcarbamylmethyl]-10-(2-hydroxycyclohexyl)-1,4,7,10-tetraazacyclododecane (**5**)..... **104**

2.3.2.2.2 Preparation of Europium-1,4,7-tris[*N'*-*N'*-dimethylcarbamylmethyl]-10-(2-hydroxycyclohexyl)-1,4,7,10-tetraazacyclododecane (**7**)..... **104**

2.3.2.2.3 Preparation of Europium-1,4,7-tris[*N*-methylcarbamylmethyl]-10-(2-hydroxycyclohexyl)-1,4,7,10-tetraazacyclododecane Complex (**5**) in Water **105**

2.3.3 Luminescent Lifetime Measurements on Europium-1,4,7-tris[*N*-methyl-carbamylmethyl]-10-(2-hydroxycyclohexyl)-1,4,7,10-tetraazacyclododecane (**5**): Determination of *q* **105**

2.3.3.1.1 Preparation of Europium-1,4,7-tris[*N*-methylcarbamylmethyl]-10-(2-hydroxycyclohexyl)-1,4,7,10-tetraazacyclododecane (**5**) Solutions in Water (H_2O). **106**

2.3.3.1.2 Europium-1,4,7-tris[*N*-methylcarbamylmethyl]-10-(2-hydroxycyclohexyl)-1,4,7,10-tetraazacyclododecane (**5**) in MCB with KHP in Water..... **106**

2.3.3.1.3 Europium-1,4,7-tris[*N*-methylcarbamylmethyl]-10-(2-hydroxycyclohexyl)-1,4,7,10-tetraazacyclododecane (**5**) in Water..... **106**

2.3.3.2 Preparation of Europium-1,4,7-tris[*N*-methylcarbamylmethyl]-10-(2-hydroxycyclohexyl)-1,4,7,10-tetraazacyclododecane (**5**) Solutions in Deuterated Water (D_2O) **106**

2.3.3.2.1 Europium-1,4,7-tris[*N*-methylcarbamylmethyl]-10-(2-hydroxycyclohexyl)-1,4,7,10-tetraazacyclododecane (**5**) in Multi-component Buffer with KHP **106**

2.3.3.2.2 Europium-1,4,7-tris[*N*-methylcarbamylmethyl]-10-(2-hydroxycyclohexyl)-1,4,7,10-tetraazacyclododecane (**5**) in Deuterated Water **107**

2.3.4 Using Cyclic Voltammetry to Observe Solution Behavior of Europium Complexes. **108**

2.3.4.1 Preparation of Multi-component Buffer with Europium Complexes **108**

2.3.4.1.1 Europium-1,4,7-tris[*N*-methylcarbamylmethyl]-10-(2-hydroxycyclohexyl)-1,4,7,10-tetraazacyclododecane (**5**) **108**

2.3.4.1.2 Europium-1,4,7,10-Tetrakis(methylcarbamylmethyl)-1,4,7,10-tetraazacyclodecane (**9**) **109**

Chapter Three Results and Discussion **110**

3.1 Synthetic Comments and Discussion **110**

3.1.1 Synthesis of Precursors **110**

3.1.2 Synthesis of *β*-amino alcohol Intermediate: 1-(2-Hydoxycyclohexyl)-1,4,7,10-tetraazacyclodecane (**1**) **111**

3.1.3 Synthesis of *N*-substituted Cyclen based Ligands **112**

3.1.4 Lanthanide Complexation of Target Ligands **113**

3.2.1 Crystal Analysis Polyazamacrocyclic Ligands.....**114**

3.2.1.1 Crystal Structure of 1,4,7-tris[*N*-methylcarbamylmethyl]-10-(2-hydroxy-cyclohexyl)-1,4,7,10-tetraazacyclododecane or (**2**):..... **114**

3.2.2.2 Crystal Structure of Na-1,4,7-tris[*N,N*-dimethylcarbamylmethyl]-10-(2-hydroxy-cyclohexyl)-1,4,7,10-tetraazacyclododecane or (**3**):..... **116**

3.2.2 Polyazamacrocyclic Lanthanide Complexes **119**

3.2.2.1 Crystal Structure of Europium-1,4,7-tris[*N*-methylcarbamylmethyl]-10-(2-hydroxycyclohexyl)-1,4,7,10-tetraazacyclododecane or (**5**): **119**

3.2.2.2 Crystal Structure of Europium-1,4,7,10-Tetrakis(methylcarbamylmethyl)-1,4,7,10-tetraazacyclodecane or (**9**): **123**

3.2.2.3 Crystal Structure of Gadolinium-1,4,7-tris[*N*-methylcarbamylmethyl]-10-(2-hydroxycyclohexyl)-1,4,7,10-tetraazacyclododecane or (**6**): **128**

3.3 Solution Chemistry of Europium Complexes..... **134**

3.3.1 Luminescence Studies and UV-vis Studies of Europium Complexes: Determination of Spectroscopic pK_as **134**

3.3.1.1 Europium-11,4,7-tris[*N*-methylcarbamylmethyl]-10-(2-hydroxycyclohexyl)-1,4,7,10-tetraazacyclododecane (**5**) in MCB with KHP **135**

3.3.1.2 Europium-1,4,7,10-Tetrakis-(methylcarbamylmethyl)-1,4,7,10-tetraazacyclodecane Complex (**9**) in MCB with KHP.....**141**

3.3.1.3 Europium-1,4,7-tris[*N*-methylcarbamylmethyl]-10-(2-hydroxycyclohexyl)-1,4,7,10-tetraazacyclododecane (**5**) in MCB without KHP **146**

3.3.1.4 Europium-1,4,7-tris[*N,N*-dimethylcarbamylmethyl]-10-(2-hydroxycyclohexyl)-1,4,7,10-tetraazacyclododecane (**7**) in MCB without KHP **149**

3.3.1.5 Europium-1,4,7-tris[*N*-methylcarbamylmethyl]-10-(2-hydroxycyclohexyl)-1,4,7,10-tetraazacyclododecane (**5**) in Water **153**

3.3.2 Lifetime Studies- Determination of *q* for Europium-1,4,7-tris[*N*-methylcarbamyl-methyl]-10-(2-hydroxycyclohexyl)-1,4,7,10-tetraazacyclododecane (**5**) **157**

3.3.2.1 Europium-1,4,7-tris[*N*-methylcarbomylmethyl]-10-2(hydroxycyclohexyl)-1,4,7,10-tetraazacyclododecane (**5**) in MCB with KHP **160**

3.3.2.2 Europium-1,4,7-tris[*N*-methylcarbomylmethyl]-10-2(hydroxycyclohexyl)-1,4,7,10-tetraazacyclododecane (**5**) in Water **162**

3.4 Cyclic Voltammetry of Eu-complexes across pH Range **164**

3.5 Discussion ..... **.170**

Chapter Four Conclusions and Future work **184**

4.1 Concluding Remarks……..……**184**

4.2 Futurework……..……..**187**

References **188**

Appendices **205**

A - NMR **205**

A1: *N*-Me-chloroacetamide – ^{1}H **205**

A2: *N*-Me-chloroacetamide - ^{13}C **206**

A3: *N*-Me-chloroacetamide – C-H correlation **207**

A4: *Di*-Me-chloroacetamide – ^{1}H **208**

A5: *Di*-Me-chloroacetamide – ^{13}C **209**

A6: 1-(2-Hydroxycyclohexyl)-1,4,7,10-tetraazacyclodecane (**1**) – ^{1}H **210**

A7: 1-(2-Hydroxycyclohexyl)-1,4,7,10-tetraazacyclodecane (**1**) – ^{13}C **211**

A8: 1-(2-Hydroxycyclohexyl)-1,4,7,10-tetraazacyclodecane (**1**) – COSY **212**

A9: 1-(2-Hydroxycyclohexyl)-1,4,7,10-tetraazacyclodecane (**1**) – C-H correlation **213**

A10: 1,4,7-tris[*N*-methylcarbamylmethyl]-10-(2-hydroxycyclohexyl)-1,4,7,10-tetraazacyclododecane (**2**) -^{1}H **214**

A11: 1,4,7-tris[*N*-methylcarbamylmethyl]-10-(2-hydroxycyclohexyl)-1,4,7,10-tetraazacyclododecane (**2**) ^{13}C **215**

A12: 1,4,7-tris[*N*-methylcarbamylmethyl]-10-(2-hydroxycyclohexyl)-1,4,7,10-tetraazacyclododecane (**2**)– C-H correlation **216**

A13: 1,4,7-tris[*N*-methylcarbamylmethyl]-10-(2-hydroxycyclohexyl)-1,4,7,10-tetraazacyclododecane (**2**) – COSY **217**

A14: 1,4,7-tris[*N*,*N*-dimethylcarbamylmethyl]-10-(2-hydroxycyclohexyl)-1,4,7,10-teraazacyclododecan (**3**) – ^{1}H **218**

A15: 1,4,7-tris[*N*,*N*-dimethylcarbamylmethyl]-10-(2-hydroxycyclohexyl)-1,4,7,10-teraazacyclododecan (**3**) – C-H correlation **219**

A16: 1,4,7,10-Tetrakis(methylcarbamylmethyl)-1,4,7,10-tetraazacyclodecane (4) – ^{1}H **220**

A17: 1,4,7,10-Tetrakis(methylcarbamylmethyl)-1,4,7,10-tetraazacyclodecane (4) – ^{13}C.....**221**

A18: Eu-1,4,7-tris[*N*-methylcarbamylmethyl]-10-(2-hydroxycyclohexyl)-1,4,7,10-tetraazacyclododecane (**5**) – ^{1}H **222**

A19: Eu-1,4,7-tris[N-methylcarbamylmethyl]-10-(2-hydroxycyclohexyl)-1,4,7,10-tetraazacyclododecane (**5**) – COSY **223**

A20: Eu-1-1,4,7-tris[N-methylcarbamylmethyl]-10-(2-hydroxycyclohexyl)-1,4,7,10-..... **224**

tetraazacyclododecane (**5**) – 3D COSY **224**

A21: Eu-1,4,7-tris[*N,N*-dimethylcarbamylmethyl]-10-(2-hydroxycyclohexyl)-1,4,7,10-tetraazacyclododecane (**7**) – ^{1}H **225**

A22: Eu-1,4,7,10-Tetrakis(methylcarbamylmethyl)-1,4,7,10-tetraazacyclodecane (**9**) – 1H ... **226**

B – ESI-MS..... **227**

B1: 1-(2-Hydoxycyclohexyl)-1,4,7,10-tetraazacyclodecane (**1**) **227**

B2: 1,4,7-tris[*N*-methylcarbamylmethyl]-10-(2-hydroxycyclohexyl)-1,4,7,10-tetraazacyclododecane (**2**)..... **228**

B3: 1,4,7-tris[*N,N*-dimethylcarbamylmethyl]-10-(2-hydroxycyclohexyl)-1,4,7,10-tetraazacyclododecane (**3**)..... **229**

B4: 1,4,7,10-Tetrakis(methylcarbamylmethyl)-1,4,7,10-tetraazacyclodecane (**4**) **230**

B5: Eu-1,4,7-tris[*N*-methylcarbamylmethyl]-10-(2-hydroxycyclohexyl)-1,4,7,10-..... **231**

tetraazacyclododecane (**5**)..... **231**

B6: Eu-1,4,7-tris[*N*,*N*-dimethylcarbamylmethyl]-10-(2-hydroxycyclohexyl)-1,4,7,10-tetraazacyclododecane (**7**)..... **232**

B7: Eu-1,4,7,10-Tetrakis(methylcarbamylmethyl)-1,4,7,10-tetraazacyclodecane (**9**) **233**

C - FTIR..... **236**

C1: *N*-Me-chloroacetamide..... **236**

C2: *Di*-Me-chloroacetamide **237**

C3: 1-(2-Hydoxycyclohexyl)-1,4,7,10-tetraazacyclodecane (**1**) **238**

C4: 1,4,7-tris[*N*-methylcarbamylmethyl]-10-(2-hydroxycyclohexyl)-1,4,7,10-tetraazacyclododecane (**2**)..... **239**

C5: 1,4,7,10-Tetrakis(methylcarbamylmethyl)-1,4,7,10-tetraazacyclodecane (**4**) **240**

C6: Eu-1,4,7-tris[*N*-methylcarbamylmethyl]-10-(2-hydroxycyclohexyl)-1,4,7,10-tetraazacyclododecane (**5**)..... **241**

C7: Eu-1,4,7,10-Tetrakis(methylcarbamylmethyl)-1,4,7,10-tetraazacyclodecane (**9**) **242**

D: Some Important Calculations and Electrode Standardization **243**

E: Spectroscopic Data..... **248**

F: Lifetime Measurements..... **295**

G: Crystallographic Data - Data Disc

H: Cyclic Voltammetry Data - Data Disc

List of Figures and Tables

Figure 1.1: 3D image of Cyclen. 29
Figure 1.2: Different types of polyazamacrocycles. 29
Figure 1.3: Different permutations of pendant arms from small to large metal centers. 33
Figure 1.4: Showing lanthanides on the Periodic Table. 34
Figure 1.5: Energy levels involved in fluorescence and phosphorescence in lanthanides. 36
Figure 1.6: Energy level transitions from $^5D_0 \rightarrow {}^7F_J$ characteristic for J = 0, 1, 2, 3 and 4. 37
Figure 1.7: Schematic representation of the "antenna effect" involving distinct absorbing (species) and emitting (metal ion) components. 37
Figure: 1.8: LnDOTA−complexes exist as a mixture of stereoisomeric complexes, related as two enantiomeric pairs. These stereoisomers interconvert by ring inversion or arm rotation. Sequential ring inversion and arm rotation interconverts enantiomers. ... 44
Figure 1.9: Targeted enantiopure derivatives of LnDOTA. 45
Figure 1.10: The structure of Arsphenamine has been proposed to be akin to the azobenzene (A), but mass spectral studies published in 2005 suggest that it is actually a mixture of the trimer B and the pentamer C. 46
Figure 1.11: Researchers continue to search for cancer treatments that effectively destroy tumor cells while protecting surrounding healthy tissue and the body. One intriguing approach involves photoactivated drugs: an inactive precursor would be administered, then the diseased tissue could be irradiated to convert the drug into its cytotoxic form locally. 46
Figure 1.12: The different kinds of radiation emitted, when a lanthanide is excited. 48
Figure 1.13: Simplified energy diagram showing the lowest lanthanide excited states and the estimated triplet state of some lanthanides. 49
Figure 1.14: MRI scan of human abdomen, spine, head, entire body, head and articular cartilage. 49
Figure 1.15: (A) Procession of protons in an external magnetic field.
(B) Proton spin energy in a magnetic field.
(C) Change in proton spin energy with increasing RF energy at the LF). 55
Figure 1.16: MRI images of the brain. T_1-weighted (left) and T_2-weighted (right) 58

Figure 1.17: (A) Transverse fast acquisition breast MRI images at same level without contrast (upper) and with contrast (lower). The anomalies, emphasized by the green circles, show how the abnormality in the lower breast image on the right is "highlighted" by the contrast (Gadolinium DTPA).
(B) MRI scans of breast without (upper) and with (lower) contrast agent (Magnevist). 58
Figure 1.18: Vibrational quenching of Eu^{3+} emissive state by water. An offset has been applied so that the lowest vibrational level of OH/OD is shown at the same energy as the highest level of the ground-state manifold of the Eu^{3+}. 60
Figure 1.19: Illustration of the different parameters that require optimisation for maximum relaxivity of gadolinium contrast agents 65
Figure 1.20: Commercial aminocarboxylate-based MRI contrast agents (Bayer Schering Parma AG). 67
Figure 1.21: The DTPA ligand and two of its derivatives prepared for water exchange rate studies. 68
Figure 1.22: The DOTA ligand and derivatives prepared to increase water exchange rates 69
Figure 1.23: Examples of dinuclear, q=2 DTPA-based Gd^{3+} complexes proposed as improved high-relaxivity MRI contrast agents. 70
Figure 1.24: Target Ligands. 76
Figure 1.25: Strategic paths taken toward target molecules. 76
Figure 2.1: General reaction set up for all synthetic reactions in this work. 86
Figure 2.3: Generalized reaction conditions toward respective target molecules. 87
Figure 2.4: Preparation of *N*-methyl-chloroacetamide. 88
Figure 2.5: Reaction showing preparation of Di-methyl-chloroacetamide. 89
Figure 2.6: Preparation of 1-(2-Hydoxycyclohexyl)-1,4,7,10-tetraazacyclodecane (**1**). 90
Figure 2.7: Preparation of 1,4,7-tris[*N*-methylcarbamylmethyl]-10-(2-hydroxycyclohexyl)-1,4,7,10-teraazacyclododecan (**2**). 91
Figure 2.8: Reaction scheme showing preparation of 1,4,7-tris[*N,N*-dimethylcarbamylmethyl]-10-(2-hydroxycyclohexyl)-1,4,7,10-tetraazacyclododecane (**3**). 93
Figure 2.9: Preparation of 1,4,7,10-Tetrakis(methylcarbamylmethyl)-1,4,7,10-tetra-azacyclodecane (**4**). 94

Figure 2.10: Preparation of Europium-1,4,7-tris[*N*-methylcarbamylmethyl]-10-(2-hydroxycyclohexyl)-1,4,7,10-tetraazacyclododecane (**5**). 95
Figure 2.11: Reaction scheme showing preparation of Europium-1,4,7-tris[*N,N*-dimethylcarbamylmethyl]-10-(2-hydroxycyclohexyl)-1,4,7,10-tetraazacyclododecane (**7**). 96
Figure 2.12: Reaction scheme showing preparation of Europium-1,4,7,10-Tetrakis-(methylcarbamylmethyl)-1,4,7,10-tetraazacyclodecane (**9**). 98
Figure 2.13: Reaction scheme showing preparation of Gadolinium-1,4,7-tris[*N*-methylcarbamylmethyl]-10-(2-hydroxycyclohexyl)-1,4,7,10-tetraazacyclododecane (**6**). 99
Figure 2.14: Reaction scheme showing preparation of Gadolinium-11,4,7-tris[*N,N*-dimethylcarbamylmethyl]-10-(2-hydroxycyclohexyl)-1,4,7,10-tetraazacyclododecane (**8**). 100
Figure 3.1: Mechanism of Reaction Toward Target Precursors. 110
Figure 3.2: Mechanism of Reaction Toward Target Intermediate. 111
Figure 3.3: Mechanism of Reaction Toward Target Ligands. 113
Figure 3.4: Conformation of **2** - Ortep illustration. 114
Figure 3.5: Packing of **2** in the unit cell along the a axis- Ortep illustration. 115
Figure 3.6: Conformation of **3** - Ortep illustration: Hydrogen atoms removed for clarity. 116
Figure 3.7: Packing of **3** in unit cell along b axis - Ortep illustration. 117
Figure 3.8: Conformation of **5** - Ortep illustration: Hydrogen atoms removed for clarity. 119
Figure 3.9: Packing of **5** in unit cell along b axis - Ortep illustration. 121
Figure 3.10: Shows the capped square anitiprismatic geometry of **5**. 121
Figure 3.11: Interconversion of stereoisomers for the (*R,S*)-**5** isomer. 122
Figure 3.12: Conformation of **9** - Ortep illustration. 123
Figure 3.13: Packing of **9** in unit cell along b axis - Ortep illustration. 124
Figure 3.14: Capped square anitiprismatic geometry of **9**. 125
Figure 3.15: General interconversion of stereoisomers in lanthanide complexes of cyclen based macrocylic ligands. 126
Figure 3.16: Conformation of **6** - Ortep illustration: Hydrogen atoms removed for clarity. 128
Figure 3.17: Packing of **6** in unit cell along a axis - Ortep illustration. 129

Figure 3.18: Capped square anitiprismatic geometry of **6**. 130
Figure 3.19: Interconversion of stereoisomers for the (*S*,*R*)-**5** isomer..... 131
Figure 3.20: Diagram explaining lanthanide excitation and electronic states when associated with an antenna. 134
Figure 3.21: Variation of intensity for emission spectrum of **5** in MCB with KHP upon titration with NaOH. 135
Figure 3.22: Non-linear least square fits for **5** in MCB with KHP corresponding to J = 0, 1, 2, 3 and 4. 138
Figure 3.23: Variation in absorbance of **5** in MCB with KHP upon titration with NaOH. 139
Figure 3.24: Non-linear least square fit for **5** in MCB with KHP corresponding monitoring at λ = 270 nm across pH range..... 139
Figure 3.25: Proposed protonation equilibrium for **5** in MCB with KHP upon titration with NaOH. 140
Figure 3.26: Variation of intensity for emission spectrum of **9** in MCB with KHP upon titration with NaOH. 141
Figure 3.27: Non-linear least square fits for **9** in MCB with KHP corresponding to J = 0, 1, 2, 3 and 4. 143
Figure 3.28: Variation in absorbance of **9** in MCB with KHP upon titration with NaOH. 144
Figure 3.29: Non-linear least square fit for **9** in MCB with KHP corresponding to monitoring at λ = 280 nm across pH range..... 144
Figure 3.30: Proposed protonation equilibrium for **9** in MCB with KHP upon titration with NaOH. 145
Figure 3.31: Variation of intensity for emission spectrum of **5** in MCB excluding KHP upon titration with NaOH. 146
Figure 3.32: Non-linear least square fits for variation of emission band intensity as a function of pH for 5 in MCB excluding KHP corresponding to J = 0, 1, 2, 3 and 4..... 147
Figure 3.33: Variation in absorbance of **5** in MCB excluding KHP upon titration with NaOH.
Figure 3.34: Non-linear least square fit for variation of absorbance band intensity as a function of pH for **5** in MCB excluding KHP corresponding to monitoring at λ = 308 nm. 148

Figure 3.35: Proposed protonation equilibrium for complex **5** in MCB excluding KHP upon titration with NaOH. 149
Figure 3.36: Variation of intensity for emission spectrum of **7** in MCB excluding KHP upon titration with NaOH. 149
Figure 3.37: Non-linear least square fits for **7** in MCB excluding KHP corresponding to J = 0, 1, 2, 3 and 4. 151
Figure 3.38: Variation in absorbance of complex **7** in MCB excluding KHP upon titration with NaOH. 152
Figure 3.39: Scatter of the absorbance (λ = 263 nm) observed for **7** in MCB excluding KHP across pH range from 2 to 12. 152
Figure 3.40: Proposed protonation equilibrium for **7** in MCB excluding KHP upon titration with NaOH. 153
Figure 3.41: Variation of intensity for emission spectrum of **5** in water upon titration with NaOH. 153
Figure 3.42: Non-linear least square fits for complex **5** in water corresponding to J = 0, 1, 2, 3 and 4. 155
Figure 3.43: Variation in absorbance of **5** in water upon titration with NaOH. 156
Figure 3.44: Non-linear least square fit for **5** in water corresponding monitoring at λ = 313 nm across pH range. 156
Figure 3.45: Proposed protonation equilibrium for **5** in water upon titration with NaOH……..152
Figure 3.46: Eu^{3+} $^7F_0 \rightarrow {}^5D_0$ excitation and emission spectra of complex **5** containing 1 mM KHP in MCB at 25 ºC……...…155
Figure 3.47: Change in *q* value for **5** across the pH range 4.710 to 9.484…….……156
Figure 3.48: Change in *q* value for **5** across the pH range 4.375 to 8.645……..158
Figure 3.49: Cyclic voltammograms of **5** (top) and **9** (bottom) at pH 6.294 and pH 6.212, when scanned from (100-1000mV). 164
Figure 3.50: Peak Separation in **5** (red) and **9** (blue) at pH 6.294 and 6.212, respectively..... 165
Figure 3.51: Showing $E_{1/2}$ (top) and Peak separation (bottom) versus pH for **5** (red) and **9** (blue)..... 166

Figure 3.52: Change in potential observed of selected pH points in **5** (top) and **9** (bottom) at constant current versus Ag/AgCl. 167
Figure 3.53: Plots obtained using Nicholson Method to determine whether electrochemical reaction is diffusion controlled for **5** and **9**. 169
Figure 3.54: Target molecules in the study. 172
Figure 3.55: Metal compression induced by cyclohexyl causes an increase in pK_a value of water molecule attached to Europium metal center. 177
Figure 3.56: Inductive effects can cause a decrease in pK_a value of water molecule attached to lanthanide metal center. 178
Figure 3.57: The proposed coordination environment of **5** in the presence of KHP. 180
Figure 3.58: The proposed coordination environment of **5** in water remains unchanged. 181

Tables

Table 1.1: Examples of T_1 and T_2 values of different tissues in the brain. 57
Table 1.2: Common Buffers Used in Experiments. 74
Table 2.1: Materials used in this study. 80
Table 3.1: Crystal Data, Collection and Structure Refinement Parameters for Ligands. 118
Table 3.2: Summary of selected bond distances in **5**. 120
Table 3.3: Summary of selected bond distances in **9**. 125
Table 3.4: Summary of selected bond distances in **6**. 129
Table 3.5: Crystal Data, Collection and Structure Refinement Parameters for Complex..... 134
Table 3.6: Eu^{3+} Excited State Lifetimes of **5** in MCB with KHP. 160
Table 3.7: q values determined at 580 nm for **5** in MCB with KHP. 161
Table 3.8: Eu^{3+} Excited State Lifetimes of **5** in water. 162
Table 3.9: *q* values determined at 580 nm for **5** in water. 162
Table 3.10: Summary of Spectroscopic pK_a Determination. 175

Abbreviations and Symbols

A	UV-Vis absorbance
Arb.	Arbitrary
B_0	Magnetic field vector
B_1	RF generated field
Boc	Tert-butyloxycarbonyl
CAPS	3-[Cylohexylamino]-1-propanesulfonic acid
CHES	3-[N-Cylohexylamino]-ethansulfonic acid
CR	Commercial reagent
CV	Cyclic Voltammetry
Cyclen	1,4,7,10-Tetraazacyclododecane
DMF	Dimethylformamide
DO3A	1,4,7-Tris(acetic acid)-1,4,7,10-tetraazacyclododecane
DOTA	1,4,7,10-Tetraazacyclododecane-1,4,7,10-tetraacetic acid
DPP	di-Phosporus pentoxide
DTMA	1,4,7,10-Tetrakis(methylcarbamylmethyl)-1,4,7,10-tetraazacyclododecane
DTPA	Diethylenetriaminepentaacetic acid
DTPA-BMA	{bis-[2 (Carboxymethylmethylcarba-moylmethylamino) ethyl]amino}acetic acid
DTTA	Diethylenetriamine-N,N,N'',N''-tetraacetate
ESI-MS	Electrospray ionization-mass spectrometry
I	ionic strength
I	Integrated area under the fluorescence emission peak
J	Coupling constant
k_{D_2O}	Rate of luminescence decay in D_2O
k_{ex}	Water exchange rate
k_{H_2O}	Rate of luminescence decay in H_2O
KHP	Potassium Hydrogen Phthalate

LF	Lamor frequency
LFSE	Ligand field stabilization energy
LMCT	Ligand to metal charge transfer
M	Net magnetization vector
m/z	Mass to charge ratio
M^+	Molecular ion
MCB	Multicomponent buffer
MDM	Magnetic dipole moment
MES	4-morpholineethanesulfonic acid monohydrate
MOPS	3-[N-Mopholino]-propanessulfonic acid
MRI	Magnetic resonance imaging
MRI-CAs	Magnetic resonance imaging contrast agents
q	The number of bound water molecules per paramagnetic ion
R_1	Longitudinal relaxivity
R_2	Transverse relaxivity
RF	Radio frequency
SPIO	Super Paramagnetic iron oxide
T_1	Longitudinal relaxation time
T_{1e}	Electronic longitudinal relaxation time
T_2	Transverse relaxation time
T_{2e}	Electronic transverse relaxation time
Tosyl	*p*-Toluene sulfonyl
Tris	Tris-(hydroxymethyl)-aminomethane
δ	Chemical shift
λ_{ex}	Fluorescence excitation wavelength
λ_{max}	Maximum wavelength
τ_D	Difussion Coefficient
τ_M	Residence lifetime
τ_R	Reorientational correlation time
Nd-YAG	Yttrium aluminum garnet

Chapter One Introduction

1.1 Solid state and Supramolecular Chemistry of Polyazamacrocycles and their Lanthanide Complexes

1.1.1 General Background to Supramolecular Chemistry

In the past decade supramolecular chemistry has been transformed by the revolution in small molecule crystallography and much of the interest in this area lies in the manipulation, understanding and construction of new architectures and topologies. Supramolecular chemistry has been defined by one of its leading proponents, Jean-Marie Lehn, who won the Nobel Prize for his work in the area in 1987, as the 'chemistry of molecular assemblies and of intermolecular bonds'.[1] If we regard supramolecular chemistry in its simplest sense as involving some kind of (non-covalent) binding or complexation event, we must immediately define what is doing the binding. In this context we generally consider a molecule (a 'host') binding another molecule (a 'guest') to produce a 'host-guest' complex or supermolecule. Commonly the host is a large molecule or aggregate such as an enzyme or synthetic cyclic compound possessing a sizeable, central hole or cavity. The guest may be a monoatomic cation, a simple inorganic anion, an ion pair or a more sophisticated molecule such as a hormone, pheromone or neurotransmitter. More formally, the host is defined as the molecular entity possessing convergent binding sites (e.g. Lewis basic donors, hydrogen bond donors etc.). The guest possesses divergent binding sites (e.g. spherical, Lewis acidic metal cation or hydrogen bond acceptor halide anion). In turn a binding site is defined as a region of the host or guest capable of taking part in a non-covalent interaction.[1] Ligand design is currently of great importance in coordination chemistry. The word ligand is derived from the Latin verb ligare meaning "to bind". In a coordination complex, the central atom (the metal) is coordinated to one or more molecules or ions (ligands). The atom in the ligand that is directly bound to the central atom or ion is called the donor atom.

Supramolecular chemistry, as it is now defined, is a young discipline dating back to the late 1960s and early 70s. However, its concepts and roots may be traced back almost to the beginnings of modern chemistry itself. Much of supramolecular chemistry has sprung from

developments of macrocyclic ligands for metal cations. The design of new macrocylic ligands continues to be an expanding area with exploration of ring size and investigation into various combinations of donor set. New macrocycles with larger compartments are being designed that may allow use in nanoscale chemistry as devices.[2] Many new wheel clusters have been discovered that incorporate several types of transition metal ions[3] as well as some examples with lanthanides.[4] Ligand design has also played a major role in producing unexpected architectures[5,6] and functional cages that can facilitate photochemical reactions in a confined space.[7]

The encapsulation of metal ions with a cavity or superstructure offers many possibilities for control of reactivity and the development of host guest chemistry. Recently there has been a resurgence of interest in the coordination chemistry of lanthanide complexes in aqueous solution. Interest in this work may be related to an enhanced appreciation of the rich functionality of the ground and excited states of lanthanide complexes. The high-spin paramagnetism and long electronic relaxation time of Gd^{3+} has made it pre-eminent among contrast agents for magnetic resonance imaging (MRI).[8,9] Related complexes of Dy and Tm with much shorter electronic relaxation times are effective NMR shift reagents.[10] The controlled modulation of Lewis acidity across the series is allowing the development of complexes exhibiting phosphatase activity, while the redox activity of cerium, samarium, and europium may be expected to allow the development of further selective oxidants and reductants.[4] The first section of the thesis focuses on the development in design, synthesis, and self-assembly of lanthanide-based architectures together with macrocyclic ligands designed to aid the construction of new MRI contrast agents.

However, much of the current research into the chemistry of lanthanide complexes is carried out in the solution states. It is the properties of these complexes in aqueous solution that are of great interest in their application in science and medicine. Furthermore, potentially important interactions between the complex and its environment in solution and specifically the interaction with solvent water molecules may be probed through the study of the solid-state structure where the exact information about conformation, bond distances and bond angles can be obtained. Of specific interest is the geometric 'makeup' of nine-coordinate lanthanide complexes where there

is at least one ligating water molecule present. With respect to MRI contrast agents, those in which the number of bound water molecules is one (q = 1) is of particular interest.

1.1.2 Introduction to Polyazamacrocycles

Cyclen (1,4,7,10-tetraazacyclododecane), shown in Figure 1.1 is a representative of macrocyclic polyamines shown in Figure 1.2. Many of its derivatives accommodate metal cations with 0.7 or 0.8 Å ionic radii in their 12-membered rings, but few examples were reported to effectively encapsulate larger metal ions like transition metals or lanthanides. Although the cyclen ring is too small to include alkali and alkaline earth metal ions, the ring often adopts a well defined "square" conformation and its arm-functionalization with mixed pendant donors can offer the topology suitable for effective encapsulation of the larger lanthanide metal ions like gadolinium.[11-13] It has been used extensively in metal complexation[14-16] and as a synthetic precursor to related pendant-armed[17-21] and bridged polydentate ligands,[20-23] some of which have biomedical applications.[22-25] The decrease in cost and ease of synthesis of cyclen has generated substantial interest in this area of research.[24]

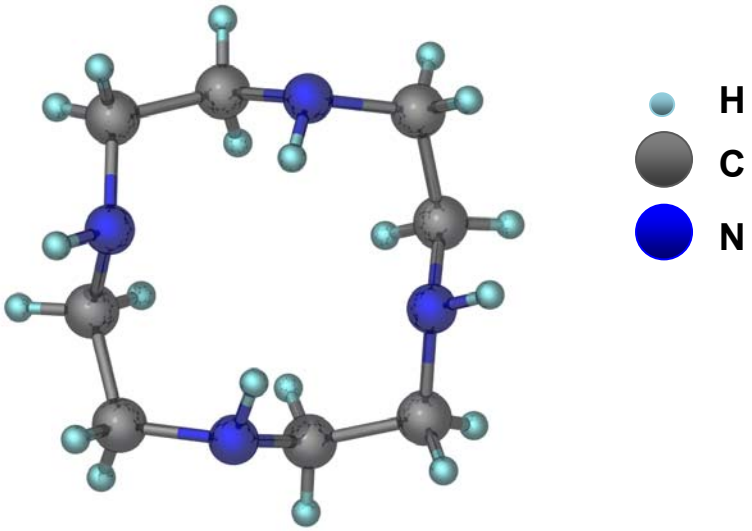


Figure 1.1: 3D image of Cyclen.[26]

The coordination chemistry of macrocyclic ligands is well documented and specifically the synthetic, kinetic and structural aspects[27,28] of polyazamacrocyclic complexes have received considerable attention.[29-35] Polyaminocarboxylates featuring cycloalkyl pendant groups directly

grafted onto cyclen feature interesting properties such as higher rigidity and better kinetic inertness. The relationship of electronic properties and reactivity of these synthetic macrocyclic complexes to those of naturally occurring macrocycles, such as porphyrins[36] and corrins, continues to promote great interest in their design and preparation. They mimic important biological ligands developed by nature, for example the porphyrin prosthetic group of many metalloproteins. These types of ligands impart thermodynamic and kinetic stabilities to their metal complexes uncommon or non-existent with ligands of acyclic origin that dramatically accentuates the advantages of macrocyclic ligands.

A successful design strategy for the development of effective metal ion complexes is to preorganize the host molecule to obtain a single conformation that is optimal for metal encapsulation; in other words the sites for binding must be optimally positioned to structurally complement the metal ion.[37-39] The more preorganised a ligand is the more closely are the ligand donor atoms arranged as required for coordination to the metal ion. However examples of the deliberate design of highly efficient preorganized hosts remain limited.[40] By introducing the cyclohexyl ring as a pendant amino alcohol donor it is envisaged to bring about an increase of metal compression due to steric intermolecular interaction provided by the ligand backbone. This increased compression consequently leads to faster water exchange of the metal-bound water molecule.

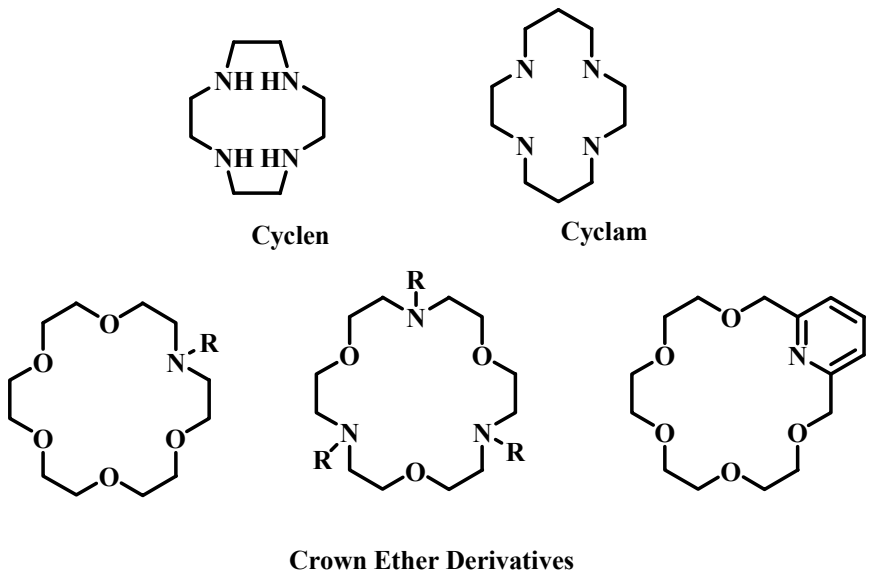


Figure 1.2: Different types of polyazamacrocycles.

1.1.3 Coordination Chemistry of Polyazamacrocycles

The characteristics present in macrocycles, like the ones shown in Figure 1.2, leading to their stable metal complexes can be grouped together under the term "molecular organization".[1] The two major areas of molecular organization, as related to coordination chemistry, are complementarity and constraint factors.[1] To design the ultimately stable metal-ligand complex, both of these factors should be maximized. Complementarity is the sum of size, geometry and electronics matching between the metal ion and the ligand and is conceptually the simpler of these two to understand and to manipulate. For a given metal ion, selection of the electronic properties, number, geometrical arrangement and bond distance of donor atoms to maximize complex stability, either using predictive theory or by iterative experimentation or a combination of the two, results in the best pairing from the range of possibilities. Much of the theory and experimentation necessary to make an advantageous selection is well established and constitutes the vast database of coordination chemistry knowledge. Complementarity of metal ion and ligand geometries can often be predicted on the basis Ligand Field Stabilization Energy (LFSE). This value is the extra stabilization over a corresponding spherical field that is attributable to the partial population of the d-orbitals. Certain metal ions, corresponding to specific numbers of d electrons, gain considerable energetic stabilization in a specific ligand field geometry. Since there are a finite number of metal ions, donor types, geometries and useful ligand sizes, it is apparent that for a given metal ion, the complementarity of a ligand can be maximized. However, maximizing complementarity is only the first step in maximizing metal-ligand complex stability. It is only through the exploitation of the constraint factors that metal-ligand binding can be increased further.

Constraint is concerned with the number and flexibility of the connections between those donor atoms. Complementarity is a necessary, but not sufficient condition for maximum stability of a complex. Complementarity may be described as a "first-order" factor for complex stability; it is a requirement of stable complexes, but can only be improved to a finite level, because the number of donor types, geometries, and sizes is finite.[1]

Constraint, on the other hand, might be described as a "second-order" factor and is concerned with factors of seemingly infinite variability.[1] These parameters can be manipulated to produce large jumps in complex stability, compared to ligand systems that lack them, if care is taken to maintain the difficultly achieved complementarity relationships.[1] The components of constraint are topology, meaning the interconnectedness of ligand donor atoms, and rigidity, how fixed in space those donor atoms are with respect to each other. Among the two, topology is the most well studied, and described in the chelate, macrocyclic, and cryptate effects.[1] Rigidity, although intimately involved in the three effects just mentioned, has been less well treated both theoretically and experimentally.[1] In this study the role of hydroxycycloalkyl substitution on cyclen and the feasibility to perform such *N*-alkylations is examined in detail.

Selective *N*-alkylation of cyclen (1,4,7,10-tetraazacyclododecane) is an important step in the preparation of functionalized nitrogenous macrocycles. To date, several synthetic routes have been reported for the selective mono *N*-alkylation of such frameworks. However, these usually involve multi-step syntheses, which often require the temporary protection of several of the amines in the cyclic framework prior to their selective alkylation. There are many examples of such synthetic strategies that involve the use of common protecting groups such as tert-butyloxycarbonyl (Boc),[41-44] *p*-toluene-sulfonyl (tosyl)[45-47] or the formyl[48-52] group in the 1, 4 and 7 positions of cyclen, followed by the alkylation of the remaining amino moiety and then deprotection. An alternative method often employed is the introduction of bulky substituents on three of the nitrogens of the macrocycle. Glyoxal[53,54] or transition metal carbonyls[55] such as $Mo(CO)_6$, are the most commonly used for this kind of protection. However, boron or phosphorus derivatives have also been used for this purpose.[56,57] Again, a final deprotection step is necessary to provide the desired mono *N*-alkylated product. Direct alkylation of cyclen has been much more rarely observed.

Wong and co-workers recently reported the preparation of various mono *N*-alkylated derivatives of such macrocycles.[59] However, both bis and tris substitutions were often observed, which led to the need for purification by column chromatography, which is a real drawback in macrocyclic chemistry[60] as we have actually experienced. Furthermore, the cyclen, used in excess as the

starting material, was not recovered. Generally, the purification methods utilized were tedious and challenging, except in a few rare cases.

Considering how few direct *N*-alkylations exist in known literature and the fact that the formation of bis and tris-*N*-alkylated adducts cannot be avoided,[60] apart from using excess cyclen,[61,62] strategies based on the use of temporary nitrogen protection groups [63, 64-66] avoid the formation of mixtures due to over-alkylation and consequently avoid purification by column chromatography. Hence, there exists a need for an improved strategy for the introduction of cyclic *β*-amino alcohol groups into such macrocycles in both high yields and in a versatile manner.

1.1.4 Selectivity of Cation Complexation

The thermodynamic selectivity of a given host for a particular cation represents the ratio between the host's affinity for a given metal (e.g. Gd^{3+}) and the other guest cations. Strong but selective binding is the basis of molecular recognition. Thus a successful host exhibits a strong affinity for one particular guest and much lower affinity for other cations. Designing a synthetic host that will be highly selective for a given cation is a very complicated task because the selectivity is governed by an enormous number of factors,[67] some of the most important of which are listed below:

- size complementarity between cation and host cavity;
- electronic complementarity between cation and the host binding sites;
- solvent (polarity, hydrogen bonding and coordination ability);
- electronic charge;
- degree of host preorganization;
- enthalpic and entropic contributions to cation-host interactions;
- cation and host free energies of solvation;
- nature of the counter-anion and its interactions with solvent and the cation;
- cation binding kinetics; and
- chelate ring size and donor group orientation.

Figure 1.3 illustrates the change in orientation of the pendant arms as the size of the metal center is varied.

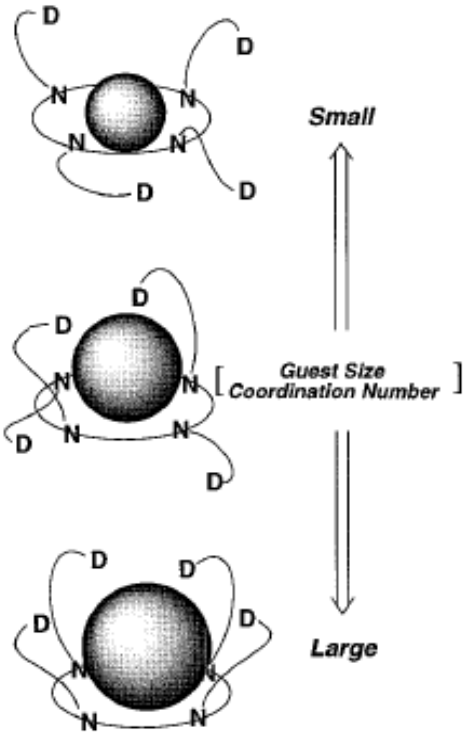


Figure 1.3: Different permutations of pendant arms from small to large metal centers.[68]

1.2 Lanthanides

1.2.1 Historical Background and Relevance

The lanthanides comprise the fifteen elements of the top row in the 'f-block' of the Periodic Table and have the electronic configuration [Xe] $6s^2 4f^n$, but with exceptions for La, Ce, Gd and Lu which have a $5d^1 4f^{n-1}$ configuration where *n* varies from 0 to 14. Their relative atomic positions on the periodic table is shown in Figure 1.4. Also known as 'rare earth elements' due to the etymology of the term 'lanthanide' (derived from the Greek *lanthanein*, meaning 'to lie hidden') and the uncommon oxides from which they were first isolated, lanthanides are in actual fact neither 'rare' nor 'earths', an old term used to describe certain metal oxides such as lime and magnesia.[69] Even the rarest lanthanides, thulium and lutetium are nearly 200 times more

abundant than gold.[70] Yet, the name 'rare earths' has persisted, perhaps due to the enigmatic nature of these unusual metals, and their ability to 'hide' behind each other in minerals. Indeed, the similar chemical properties of lanthanides make their separation quite difficult, even today.

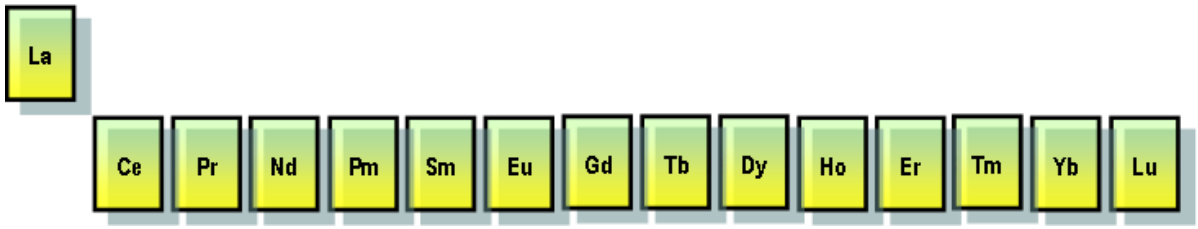


Figure 1.4: Showing lanthanides on the Periodic Table.

Lanthanides have found uses in a wide variety of industries and materials, such as catalysts, glasses, ceramics, permanent magnets, optics and electronics.[71,72] Solid phosphors containing europium, cerium and terbium are major contributors to commercial markets in fluorescent lighting and color displays. Various lanthanide ions can be used in lasers, with neodymium as the most famous in yttrium aluminum garnet (Nd-YAG). The green, blue and red luminescent bands in Euro banknotes are attributed to europium complexes.[73] Certain lanthanides (Eu, La, Lu, Nd, Pr, Sm, Th, Tm and Yb) are used as tracers in wine chemistry to discriminate wines according to geographical region.[74] The ratio of europium, which is almost entirely (~ 97%) formed in stars, to other rare earth elements in meteorites has helped decipher much of the history of processes in our solar system, such as the early development of the feldspar-rich lunar crust.[75] In aqueous solution, lanthanides are most stable in the 3+ oxidation state, leading to high coherent behavior and hence making them difficult to separate and purify. The preference for the trivalent oxidation state is due in part to the energy of the 4f electrons being below those of the 5d and 6s electrons (except in the cases of La and Ce). When forming ions, electrons from the 6s and 5d orbitals are lost first, so that all Ln^{3+} ions have [Xe] $4f^n$ electronic configurations. This, coupled to the high enthalpies of hydration for trivalent lanthanides, results in the stability of the 3+ oxidation state. In reducing conditions, europium, samarium and ytterbium can be stable in the divalent form; cerium has also been known to adopt a +4 oxidation state. Lanthanide ions possess relatively high charge densities and have a strong electrostatic nature in

their bonding, as the ions are polarizing and can be classified as hard Lewis acids. The 4f orbitals in Ln^{3+} ions are well shielded by the 5s and 6p orbitals, and therefore do not participate directly in bonding. Therefore, π-bonding is not possible, and no Ln=O or Ln≡N multiple bonds are known for lanthanide complexes.

The importance of the luminescence of lanthanide ions is related to its peculiar characteristics, for example long lifetime and line-like emission bands in the visible, which make these ions unique among the species that are known to luminesce. Because of these characteristics, lanthanide ions are widely used as luminescent species in non-molecular solids. In solution, application of complexes of lanthanide ions with conventional ligands is hindered by their kinetic lability. Luminescence can be classified into two types based on the origin of the emission of the excited molecules: fluorescence and phosphorescence. Fluorescence is the emission from an excited singlet state, while phosphorescence is the emission from an excited triplet state. In phosphorescence, some energy may be dissipated through the intersystem crossing which arises when the electron in the singlet state relaxes to a triplet state instead of directly to the ground state. Figure 1.5 illustrates the different energy levels involved in fluorescence and phosphorescence in lanthanides. Phosphorescent bands have a longer wavelength and a much longer luminescence lifetime than the fluorescent bands.

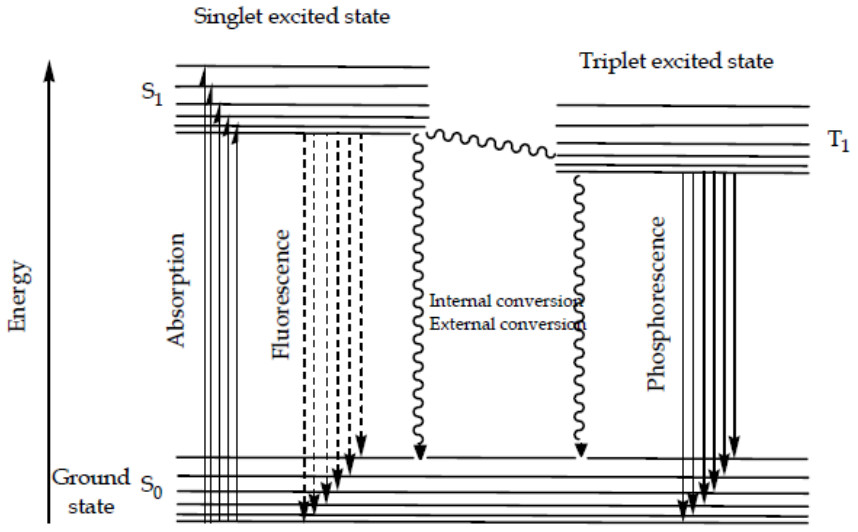


Figure 1.5: Energy levels involved in fluorescence and phosphorescence in lanthanides.[76]

In Eu^{3+} the transitions are $5D_0 \rightarrow 7F_J$ where the most common are those of J = 0, 1, 2, 3 and 4, shown in Figure 1.6, which corresponds to λ_{em} = 580 nm, 592 nm, 616 nm, 653 nm, 685 nm and 700 nm, respectively. With J = 4 having two bands at 685 nm and 700 nm.

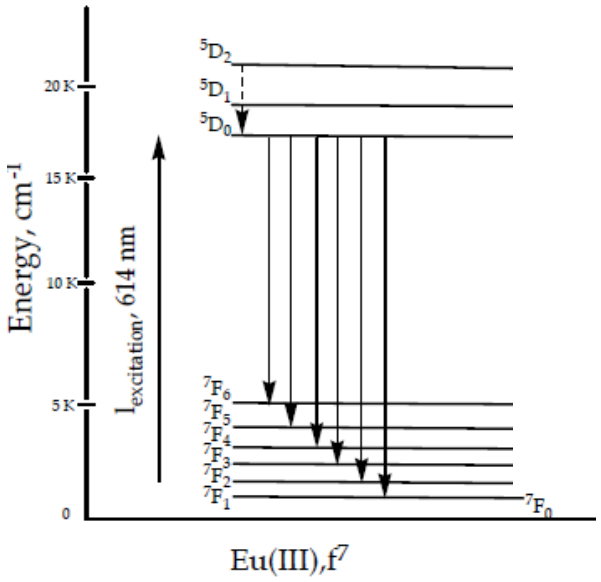


Figure 1.6: Energy level transitions from $5D_0 \rightarrow 7F_J$ characteristic for J = 0, 1, 2, 3 and 4.[76]

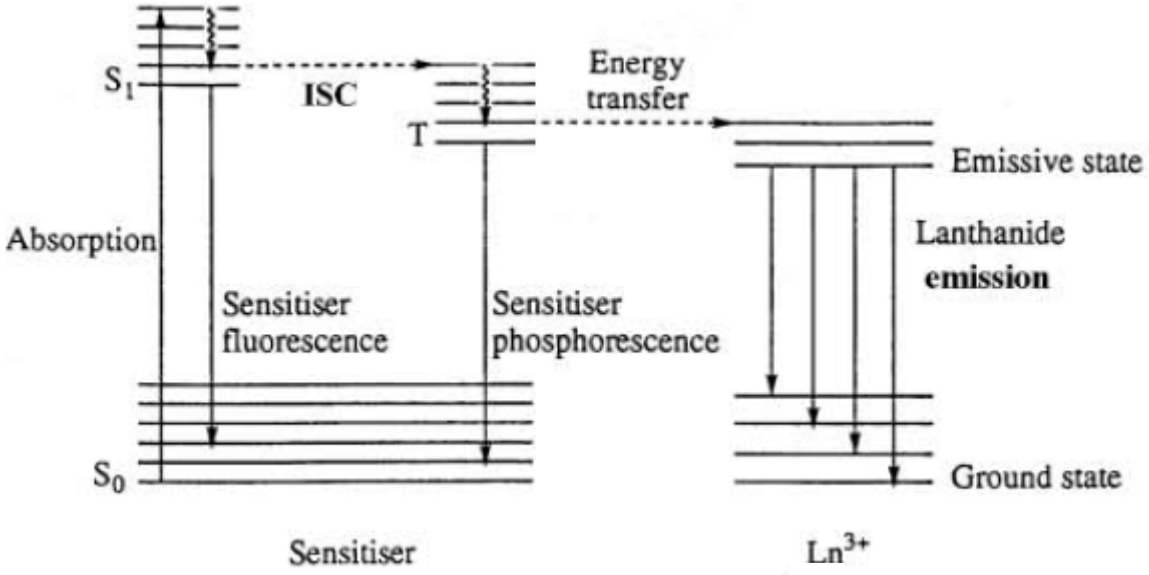


Figure 1.7: Schematic representation of the "antenna effect" involving distinct absorbing (species) and emitting (metal ion) components.[77]

The recognition of ions and molecules is of great interest in supramolecular photochemistry.[78] Effective excitation can be performed *via* a light-harvesting antenna incorporated into the ligand backbone and is capable of transferring the excitation energy to the metal center. Figure 1.7 shows a schematic representation of the "antenna effect" involving distinct absorbing (species) and emitting (metal ion) components. This is well established and europium and terbium have been sensitized with, among others, benzyloxyquinoline,[79] acridone derivatives,[80] phenanthridine,[81] pyridines[82] and dansyl groups.[83,84] Sensitization of Nd^{3+}, $Yb^{3+}$and Er^{3+} is possible with fluorescein,[85,86] pyrene,[87] Pd-porphyrins,[88] eosin,[89] Tb^{3+}-complexes,[90] rhenium^{2+} and ruthenium^{2+} bipyridyl moieties,[91,92] and quinoline.[93] However, efforts to control the degree and extent of sensitization by the antenna are more limited. Attention has focused mainly on the visible-emitting europium and terbium complexes,[94,95,96] which have found applications in fields as diverse as pH-sensing,[97] DNA-,[98] oxygen-,[99] organophosphate-[100] and Cu^{+1}- detection.

The need to devise structural and lanthanide probe complexes for biomolecules in particular has received much attention recently.[101] These lanthanide probes can be classified into two categories, the first involves systems that are effectively coordinatively saturated in aqueous media, involving octa- or nonadentate ligands that form kinetically stable 1:1 complexes as mentioned earlier.[9,102,103] The interaction with a given biomolecule or ion is likely to be determined primarily by the nature of the ligand, defining complex size, geometry, hydrophilicity, and relative disposition of hydrogen-bond donors and acceptors. The second category relates to complexes of heptadentate ligands that are typically diaqua systems of overall stability with respect to lanthanide ion dissociation.[104] Here stepwise displacement of the bound water molecules leads to monoaqua and then $q = 0$ species, the latter being particularly favored with chelating oxyanions.

1.2.2 Coordination Chemistry of Lanthanides

Coordination to trivalent lanthanides tends to be ionic in character, which leads to a strong preference for negatively charged or neutral donor groups possessing large ground state dipole moments. Therefore, combinations of amines and carboxylic acid groups are often used in lanthanide complexation.[105,106] This ionic character of binding also means lanthanide complexes tend to undergo facile exchange of the ligands.[74] Coordination geometries in lanthanides are determined by ligand steric factors as opposed to orbital overlap or crystal field effects.[107,108] In aqueous solution, donor groups containing neutral oxygen or nitrogen atoms generally bind when present in multidentate ligands (podands, crown ethers, cryptates, etc.).[109-112] Relatively few complexes of unidentate nitrogen donors exist, reinforcing the oxophilic tendency of lanthanide binding. This preference for oxygen donors also makes lanthanides quite lithophilic, and explains their occurrence in silicates as opposed to metallic or sulphidic minerals.[113]

The coordination number of $[Ln(H_2O)_n]^{3+}$ is normally 9 for the early lanthanides (La-Eu) and 8 for those later in the series (Dy-Lu), with the intermediate metals (Sm-Dy) exhibiting a mixture of species. However, the coordination number can be dictated by the steric bulk of the coordinating ligands, and species with coordination numbers as low as 2 and as high as 12 are known.[75,105] As the 4f electrons of the lanthanides are well shielded from the environment, the spectroscopic and magnetic properties of these ions (e.g., electronic spectra and crystal field splittings) are largely independant of environment (solvent, coordinated ligands, etc.).[114] The number of configurations for n electrons rapidly increases with the number of unpaired electrons, with the lowest energy term for each ion consistent with the predictions of Hund's first and second rules.[115,116] Since all configurations have different energies, the lanthanides tend to exhibit rich and complex energy level structure.[117] Due to spin-orbit coupling, the excited states of the lanthanides are well separated from the ground state manifold. Thus, the excited states are thermally inaccessible and ideal for electronic transitions. With the exceptions of the $4f^0$, $4f^1$, $4f^{13}$ and $4f^{14}$ species (La^{3+}, Ce^{3+}, Yb^{3+} and Lu^{3+}, respectively), all lanthanide ions absorb electromagnetic radiation, primarily in the visible region, which is manifested in f-electrons from the partially filled 4f subshell being excited from the ground state to an excited state. These f–f transitions can be excited by both magnetic dipole and electric dipole radiation. Magnetic dipole

transitions are Laporte allowed, while electric dipole transitions are Laporte forbidden.[103,118] Electric dipole transitions are much weaker in lanthanides ($\varepsilon \sim 0.1$ mol^{-1} dm^3 cm^{-1}) than in the transition metals, meaning magnetic dipole transitions can often be seen.[113,111] Electronic transitions must involve promotion of an electron without a change in its spin (S = 0) and with a variation of either the total angular momentum and the total angular quantum number of one unit at most (L = ±1,0; J = ±1,0). Though absorption of radiation can in theory promote the lanthanide ion to any energetically accessible state, emission normally occurs only from the lowest lying spectroscopic level of the first excited term due to rapid internal conversion.[119] In cases of low symmetry or vibronic coupling, the f–f transitions can gain intensity through f- and d-state mixing with higher electronic states of opposite parity. Broad $4f^n \rightarrow 4f^{n-1}\ 5d^1$ transitions can also be seen in the infrared region for some lanthanides. The electronic configuration of lanthanides is split due to a variety of interactions. The initial configuration is split into spectroscopic terms by electronic repulsion, with separations on the order of 10^4 cm^{-1}.[120]

These terms can be further split into spectroscopic levels, or J states, due to spin-orbit coupling effects. The energy differences between split J states lies in the range of 10^3 cm^{-1}.[121] These levels, in turn, can be split again into what are termed Stark sublevels due to ligand field effects from the coordination sphere around the lanthanide; Stark sublevel splitting is on the order of 10^2 cm^{-1}.[122] This results in the overall emission peak position remaining largely unchanged as the f-electrons remain shielded, but the emission profile of a lanthanide (defined as the relative intensity and degree of splitting of emission peaks) can vary greatly depending on modulation of these influences.[123,124] The number of Stark sublevels depends on the site symmetry of the lanthanide ion, and these can be thermally populated at room temperature, yielding more complex emission spectra. Filling of the inner 4f electron shell across the lanthanide series results in a diminution of the ionic radius by as much as 15% from lanthanum to lutetium, referred to as the lanthanide contraction.[125] Though atomic radius contraction is not unique across a series (i.e., the actinides and the first two rows of the d-block), the fact that all lanthanides primarily adopt the trivalent oxidation state means that this particular row of elements exhibits a traceable change in properties in a way that is not observed elsewhere in the periodic table. Lanthanides behave similarly in reactions as long as the number of 4f electrons is

conserved.[126] Thus, lanthanide substitution can be used as a tool to tune the ionic radius in a lanthanide complex without changing its chemistry, to better understand how the size of the metal cation affects various properties especially geometry.

1.2.3 Donor Group Orientation and Chelate Ring Size Effects

A key criterion for a complementary host for metal cations is that the host geometry should allow the metal to bond to all the donor atoms or groups of the ligand at the optimal metal-ligand distance. Moreover in metal-donor atom bonds that have some degree of covalency there must be the correct alignment of ligand orbitals (e.g. lone pair orbitals) and the metal orbitals in order to achieve optimum bond strength. Similarly, in ionic metal-ligand bonds the orientation of the ligand dipoles with respect to the metal ion must be in such a way as to result in optimum electrostatic interaction. For sp^3 hybridised amine nitrogen donors the strongest interaction with metals occurs when M-N-X angle has a value of 109.5 ° and the M-N-C-X torsion angle has a value of ± 60 or 180 °. This corresponds to the M-N axis being coincident with the orientation of the amine lone pair. Any deviation from this angle weakens the M-N interaction, thus a 10 ° compression of the M-N-C angle weakens the bond interaction by 2.9 $kJ.mol^{-1}$.

When multiple donor groups are included within a ligand framework then the constraints of the ligand backbone can result in an inability of all the donor groups to simultaneously form optimal interactions with the metal center. We can represent the donor group orientations as lines drawn along the vectors of optimal metal ion approach. In a perfectly preorganised ligand these vectors will overlap at a single point at the optimal M-L bond length. The more widely the vectors diverge from the situation the less preorganised the ligand will be.[1]

1.2.4 Introduction to Stereochemistry of Lanthanide Complexes

It is well established that macrocyclic complexes show high thermodynamic stability, conformational rigidity, and kinetic inertia. For example Ln-1,4,7,10-tetraaza-1,4,7,10-tetrakis-(carboxymethyl)-cyclododecane (DOTA) complexes are the result of a very good match between sizes of Ln^{3+} ions and the preformed cavity of the DOTA ligand.[127] From the reported X-ray solid-state structures of Ln^{3+}(DOTA) complexes (Ln) Eu,[128] Gd,[129,130] Lu[131]), it is known that the ligand provides eight coordination sites (four nitrogens and four oxygens) arranged in a square-antiprismatic geometry around the lanthanide ion. A ninth coordination site, at a capping position above the plane of the four oxygens, is occupied by one water molecule. In solution this water molecule is exchanging rapidly with the bulk solvent, and, in the case of Gd(DOTA), it results in an overall, remarkable increase in the relaxation rate of the solvent water protons. These two properties have been of primary importance in promoting the use of Gd(DOTA) as a contrast agent for magnetic resonance imaging applications.[132] The square-antiprismatic geometry of Ln(DOTA) complexes implies the occurrence of two helicities (one belonging to the cycle and one associated with the layout of the acetate arms) which may give rise to two enantiomeric pairs of diastereoisomers.[133]

Two isomers were observed in solution in the ^{1}H- and ^{13}C-NMR spectra of all Ln(DOTA) complexes in slow exchange at room temperature. Their structures were determined from the analysis of the dipolar shifts in the 1H-NMR spectrum of Yb(DOTA).[134] Because of their relative concentrations in the Yb(DOTA) solutions, the relative intensities of the corresponding resonances in the ^{1}H-NMR spectrum, these isomers were called M (major) and m (minor).[135] The structure found for the M isomer closely resembles those observed in the X-ray diffraction studies of Eu,[128] Gd,[129] Y,[130] and Lu(DOTA)[130] complexes, displaying a regular antiprismatic geometry of the DOTA ligand around the lanthanide ion. Conversely, a less regular coordination geometry has been found for the m isomer, whose structure may be envisaged as an inverted antiprism, strongly distorted toward a regular prism.[136] Thus, on going from the M to the m structure the O_4 square rotates around the symmetry axis, changing both the sign and the magnitude of the antiprism tilt angle. This m-type structure may be recognized in several X-ray

solid-state structures of other macrocyclic complexes such as La(DOTAM) where (DOTAM) = *1,4,7,10-tetrakis(2-carbamoylethyl)-1,4,7,10-tetraazacyclododecane)*,[137] Eu(THP) where (THP) = *1,4,7,10-tetrakis(2-hydroxypropyl)-1,4,7,10-tetraazacyclododecane)*,[138] Y(DOTPBz$_4$) where (DOTPBz$_4$) = *1,4,7,10-tetraazacyclododecane tetrakis(methylenebenzylphosphinic acid)*,[139] and Gd(DO3MA) where (DO3MA) = *(1R,4R,7R)-R,R,R-trimethyl-1,4,7,10-tetraazacyclododecane-1,4,7-triacetic acid)*.[140] An analogous structure made up of eight nitrogens has been reported for the sodium salt of a pyrazole functionalized tetraazamacrocycle Mn^{2+} complex.[141,142]

In 1999, Aime and co-workers[143] performed a study where the stereochemical properties of these complexes lanthanide DOTA complexes were investigated using variable temperature, -pressure, and -ionic strength ^{1}H NMR of different trivalent cations (Sc, Y, La, Ce, Lu). They reported that a two-isomer equilibrium cannot explain the newly observed apparent reversal of the isomer ratio at the end of the series. As both conformers may lose their inner sphere water molecule, a coordination equilibrium may be superimposed on this conformational equilibrium, as shown by large positive reaction volumes for the isomerization of [Ln(DOTA)(H_2O)x]$^-$ (Ln) Yb, Lu; x) 1, 0). The isomerization of [Nd(DOTA)(H_2O)]$^-$ and [Eu(DOTA)(H_2O)]$^-$ is purely conformational, as shown by near-zero reaction volumes. The measured isomerization enthalpies and entropies agree with this model. The shift of the isomerization equilibria by a variety of non-coordinative salts depends on the ligand conformation rather than the presence or absence of the inner sphere water molecule. This results from weak ion binding and water solvent stabilization of one ligand conformation, rather than the decrease of the activity of the bulk water in the solution, as shown by UV-vis measurements of the coordination number sensitive transition $5F_0$ to $7D_0$ of Eu^{3+} as a function of ionic strength. Fluoride ions replace a water molecule in the inner coordination sphere, preferentially for one of the conformational isomers, as proven by ^{19}F-NMR shifts and the appearance of a third set of resonances corresponding to [Eu(DOTA)F]$^{-2}$ in the ^{1}H-NMR spectrum of [Eu(DOTA)(H_2O)]$^-$.

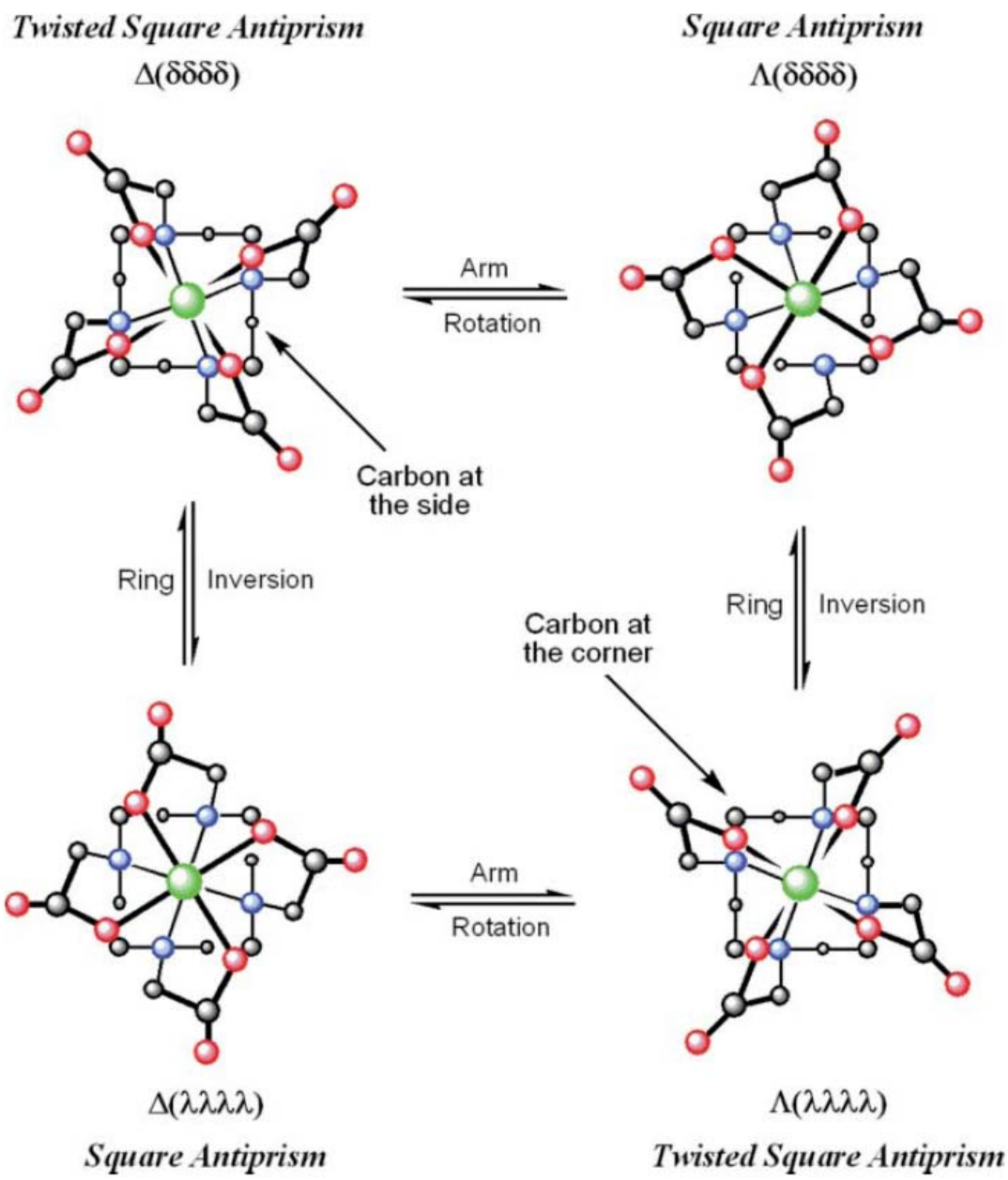


Figure: 1.8: LnDOTA− complexes exist as a mixture of stereoisomeric complexes, related as two enantiomeric pairs. These stereoisomers interconvert by ring inversion or arm rotation. Sequential ring inversion and arm rotation interconverts enantiomers.[144]

In 2003, Sherry and coworkers explored the coordination geometry of Gd(DOTA). Their approach was controlling water exchange by influencing the coordination geometry of the complex derivative by selective substitution.[144] LnDOTA− complexes exist as a mixture of two

coordination isomers:[134,145] a capped square anitiprismatic geometry (*SAP*) that exhibits slower water exchange and a capped twisted square antiprismatic geometry (*TSAP*) that exhibits faster water exchange.[144,146–150] These two coordination isomers interchange by one of two processes: ring inversion or arm rotation as illustrated in Figure 1.8.[144] However, it has been shown that by appropriate substitution of the pendant arms, arm rotation can be halted.[146,151–153] Likewise, appropriate substitution of the macrocyclic ring will halt ring inversion.[154] Their study combined these two effects to halt all intramolecular exchange in this type of complex.[144] Each coordination isomer is defined by the relative conformation of the macrocyclic ring (δδδδ or λλλλ) and the pendant arm orientation (Δ or Λ), and each of these is in turn defined by the configuration at the chiral carbon. One may therefore obtain either coordination isomer by careful selection of the chirality at each chiral center in the complex. Two stereoisomeric complexes of the ligand NO_2BnDOTMA, *S-RRRR*-**1** and *S-SSSS*-**1**, were previously shown to adopt a *SAP* and *TSAP* coordination geometry, respectively as shown in Figure 1.9. They were also found to exhibit significantly different water residence lifetimes, τ_M = 120 ns (*S-RRRR*-**1**) and τ_M = 15 ns *(S-SSSS*-**1**), the latter value falling within the optimal range for use in high relaxivity or targeted contrast agents at 20 MHz.[155,156]

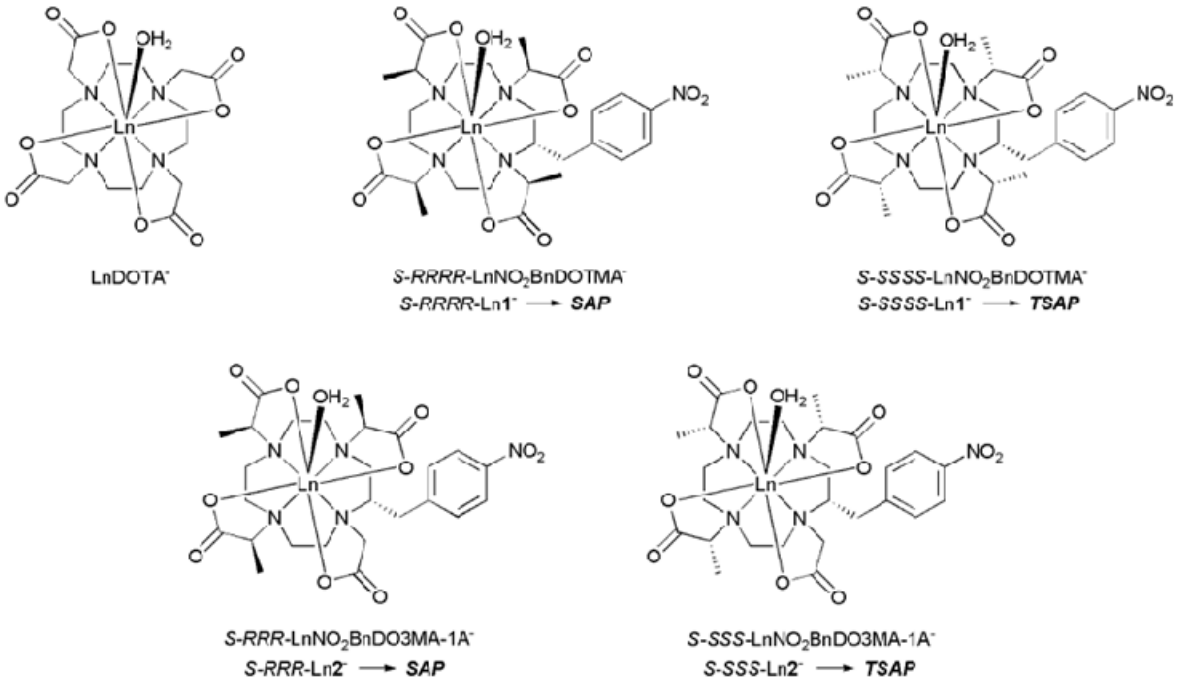


Figure 1.9: Targeted enantiopure derivatives of LnDOTA.

1.3 Metal Complex Coordination meets Medical Imaging

1.3.1 Introduction

The use of metal complexes in therapy and diagnostic imaging occurs in several protocols. Throughout history, both ancient and modern, metals and metal compounds have been used in medicine to treat a variety of medical conditions. In the last century, metal complexes were used to treat diseases ranging from syphilis (organoarsenic compounds)[157] illustrated in Figure 1.10, arthritis (gold compounds)[158] and to cancer (platinum anti-tumor drugs)[159] shown in Figure 1.11. The use of metal complexes as diagnostic agents is a relatively new area of medical research, and has flourished during the last 50 years.

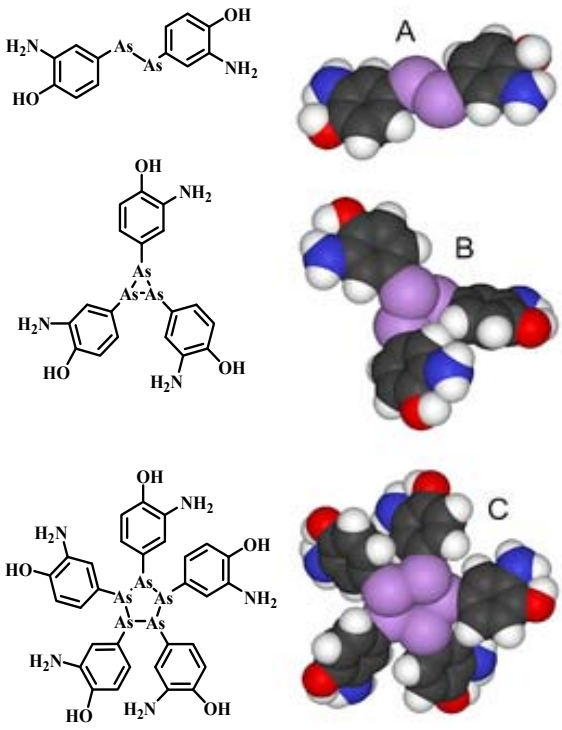


Figure 1.10: The structure of Arsphenamine has been proposed to be akin to the azobenzene (A), but mass spectral studies published in 2005 suggest that it is actually a mixture of the trimer B and the pentamer C.[160]

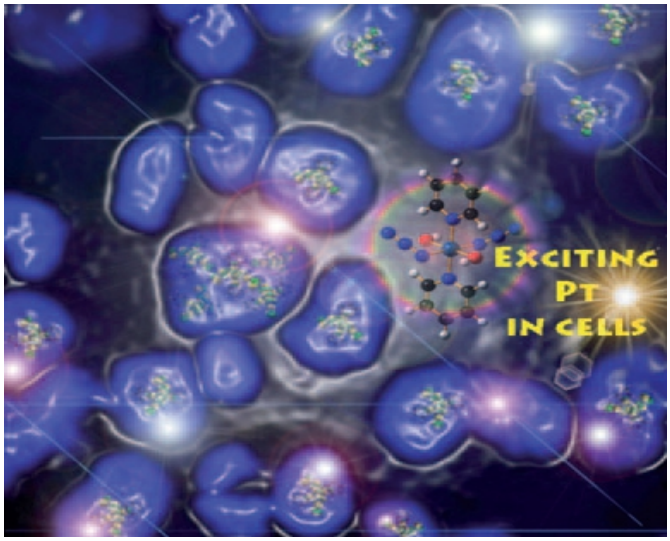


Figure 1.11: Researchers continue to search for cancer treatments that effectively destroy tumor cells while protecting surrounding healthy tissue and the body. One intriguing approach involves photoactivated drugs: an inactive precursor would be administered, then the diseased tissue could be irradiated to convert the drug into its cytotoxic form locally.[161]

Coordination chemistry of macrocyclic-based ligands has indeed been a fascinating area of current research interest to the inorganic chemists worldwide. The continued interest and quest in designing new macrocyclic ligands stem mainly from their use as: a) models for protein-metal binding sites in a substantial array of metalloproteins in biological systems, b) synthetic ionophores, c) models to study magnetic exchange phenomena, d) therapeutic reagents in chelate therapy for the treatment of metal intoxication, e) cyclic antibiotics that owe their antibiotic actions to specific metal complexation, f) guests in host-guest interactions, g) catalysts. A more recent development is the use of paramagnetic lanthanide macrocyclic complexes for enhancing contrast of magnetic resonance imaging (MRI). Recognition of the importance of complexes containing macrocyclic ligands has led to a considerable effort being invested in developing reliable inexpensive synthetic routes for these type of compounds.[162-166]

1.3.2 Suitable Imaging Characteristics of Lanthanides and their Applications in Medicine

Florescence is a useful tool for studying Eu^{+3} analogues of Gd^{+3} which facilitates investigation of coordination, water exchange and others features of such complexes. Although Eu^{3+} is a poor relaxation agent compared to Gd^{3+} and Eu^{2+}, it is an efficient luminescent species. The similarity of ionic radii allows Eu^{3+} to be used as a structural probe for corresponding Gd^{3+} analogues.[167] This aids the development of new contrast agents, as solution structures can be developed and evaluated using Eu^{3+} with less expensive equipment like fluorimeters. Binding of MRI-CAs to biomolecules and synthetic analogues can be scrutinized by luminescence studies to analyze where binding may occur. Interactions of this nature may be enhanced through rational ligand design. In our study we aim at understanding the intrinsic interaction that occurs between buffering agents e.g KHP and Eu^{+3} complexes at molecular level. In Section 1.4.8 buffers are described briefly.

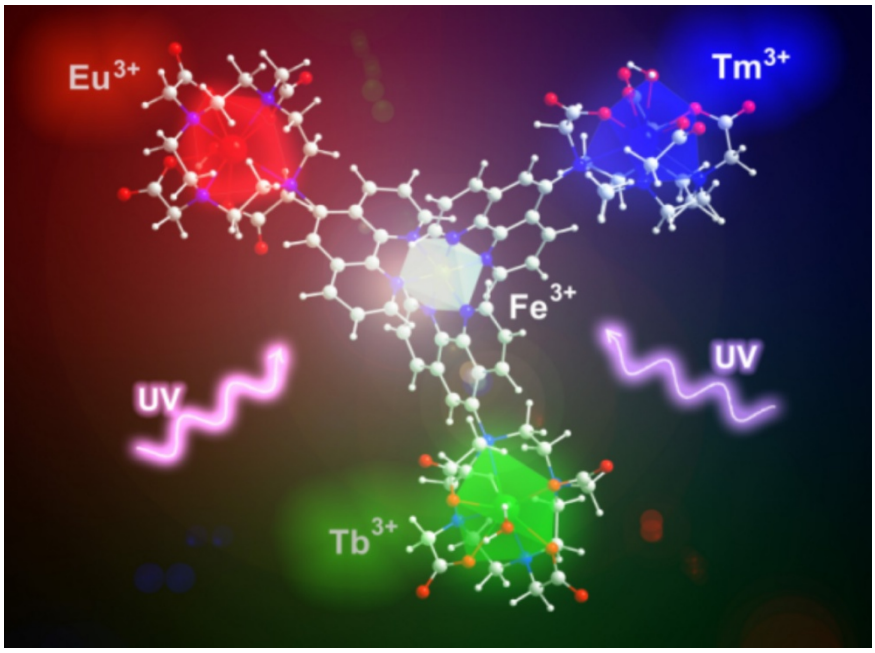


Figure 1.12: The different kinds of radiation emitted when a lanthanide is excited.[168]

Lanthanides feature significant spectral resolution due to their large Stokes shifts and narrow emission lines, and temporal resolution due to long lifetimes. This allows for the use of time-gated techniques and band pass filters to reduce interference from native or auto-fluorescence in the sample, which occurs on the nanosecond timescale.[169,170] Lanthanide complexes also do not suffer from photobleaching as organic dyes do, because lanthanides are effective quenchers of triplet states.[171] These qualities allow for the construction of robust sensors for a variety of applications. Of all the lanthanides, Eu^{3+}, Tb^{3+} and Gd^{3+} are the best ions in terms of efficient excited state population, with energy gaps of 12,300 cm^{-1} ($^5D_0 \rightarrow {}^7F_6$), 14,800 cm^{-1} ($^5D_4 \rightarrow {}^7F_0$) and 32,200 cm^{-1} ($^6P_{7/2} \rightarrow {}^8S_{7/2}$), respectively. The different kinds of radiation emitted when a lanthanide is excited is depicted in Figure 1.12. While europium and terbium both emit in the visible region, gadolinium emits in the ultraviolet, making it unfeasible for use in most sensing applications due to significant absorption and emission interference of these high-energy wavelengths. Though not suitable as luminescent sensors, Gd^{3+} complexes do have a large number of unpaired electrons ($[Xe]4f^7$) and isotropic magnetic properties. The electronic energy levels are illustrated in Figure 1.13 below. These properties, coupled to a long electron spin relaxation time of 10^{-9} s, makes this lanthanide highly NMR-active meaning active as an NMR-

relaxing agent.[172] When coordinated to one or more water molecules, Gd^{3+} enhances the water proton relaxation efficiency by lengthening the rotational correlation time.[173] Thus, many gadolinium complexes with one free binding site for solvent coordination, such as Gd(DTPA) and Gd(DOTA), have been developed for use as MRI contrast agents.[174-176] Besides providing diagnostic tools for MRI imaging, there are many other medically relevant applications of lanthanides, for example, as hypophosphatemic agents for kidney dialysis patients, as luminescent probes in cell studies, and for palliation of bone pain in osteosarcoma.[167]

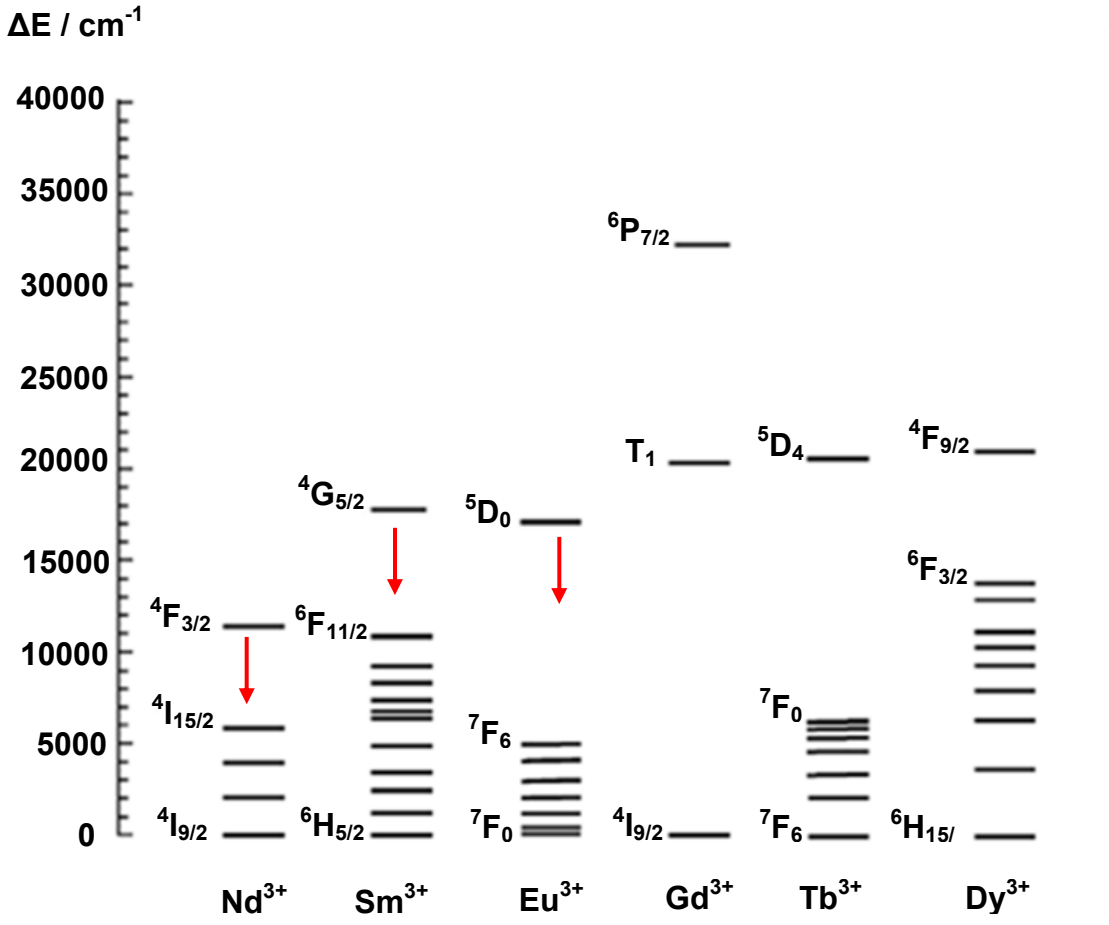


Figure 1.13: Simplified energy diagram showing the lowest lanthanide excited states and the estimated triplet state of some lanthanides where the red arrows indicate the movement of electrons from the excited to ground state.

In addition, the attachment of polyamino acids to Gd^{3+} chelates has applications in targeted imaging.[177] Some recent examples include polyornithine, polyarginine, and polylysine. Gd^{3+} chelates containing pendant phosphonate and carboxylate groups were conjugated with the positively charged groups on the polyamino acids.[177] By chemically attaching the polyamino acid to the Gd^{3+} chelate, the structure stays intact and the binding is strong enough to withstand the varying conditions of blood serum. In terms of applications, targeted imaging can also be achieved since positively charged polyamino acids selectively bind to tumor cells that have a surplus net negative charge as opposed to non-tumor cells. Accumulation of the contrast agent at the tumor site can help determine extent of tumor growth and morphology. The preceeding Section 1.4 will describe the MRI protocol, from its historical background and principle biophysical parameters to the development of more efficient MRI-CAs.

1.4 Magnetic Resonance Imaging

1.4.1 Applications of MRI

Magnetic Resonance Imaging (MRI), is a non-invasive and high resolution imaging technique and is primarily used in medical settings to produce high quality internal images of the human body. It has evolved into one of the most powerful tools in diagnostic clinical medicine and biomedical research.[8] MRI is based on the principles of nuclear magnetic resonance (NMR), a spectroscopic technique used to obtain microscopic chemical and physical information about molecules. Medical practitioners use MRI to help diagnose medical conditions and disorders of the central nervous system, brain and organ tumors, reproductive system problems, bone and joint damage or infection, breast cancer and may other diseases.[179] MRI is the method of choice because of the incredible ability to tailor the examination of the patient to the particular medical question being asked and it eliminates the need for invasive diagnostic procedures.[178] Figure 1.14 shows the versatility of examining different anatomical regions of the body.

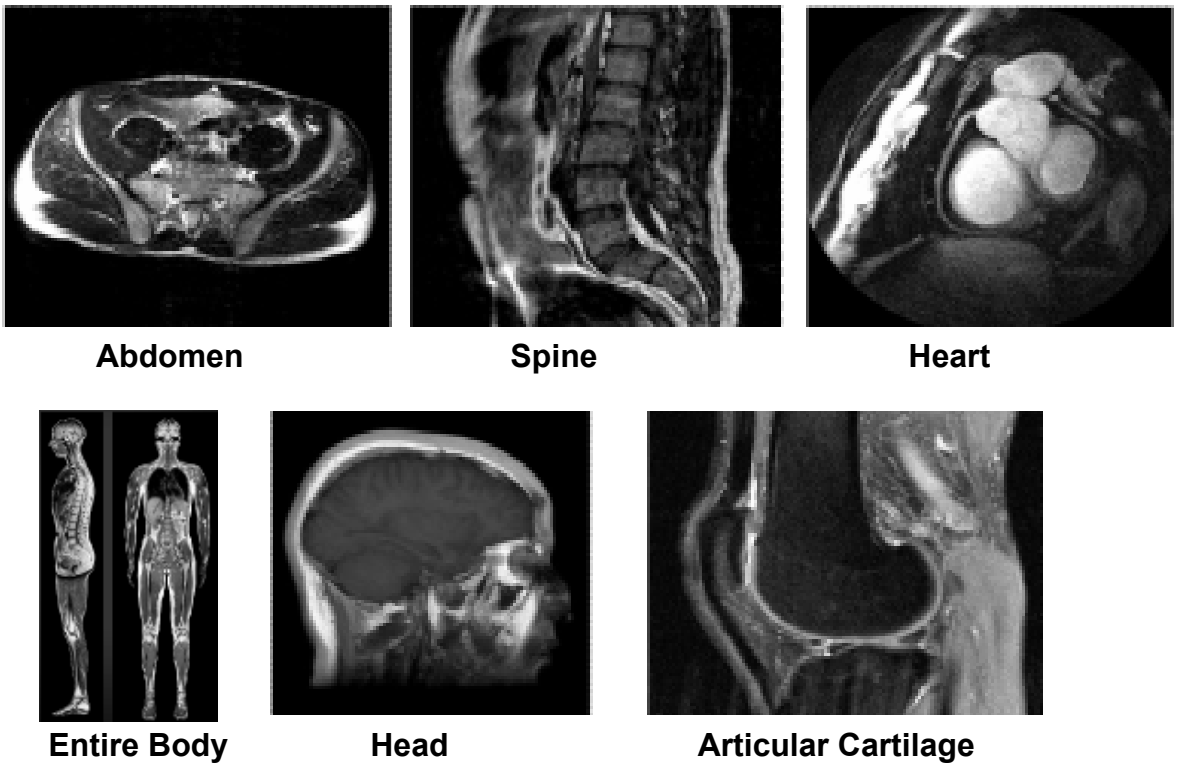


Figure 1.14: MRI scan of human abdomen, spine, head, entire body, head and articular cartilage.[178,179]

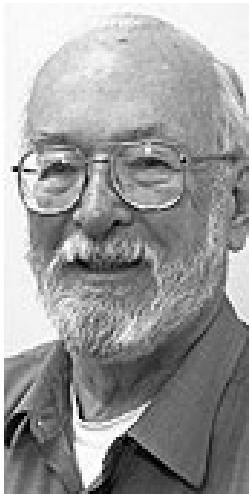
1.4.2 Historical Background

The physical principle of MRI is strongly related to the independant work of Felix Bloch and Edward Purcell for their development of NMR spectroscopy in 1946, for which they were awarded the 1952 Nobel Prize.[180-182] In the period between 1950 and 1970, NMR was developed and used for chemical and physical molecular analysis. In 1971, Raymond Damadian showed that the nuclear magnetic relaxation times of normal tissues and cancerous tissue differed, thus motivating scientists to consider magnetic resonance for detecting disease.[183]

In 1973 MRI was first demonstrated on small test tube samples by Paul Lauterbur, who used the principles of NMR with strong and weak magnetic fields to identify the position of a particular nucleus, as the strength of the field is proportional to the radiofreqency.[184] Lauterbur did not make any postulations as to the potential application for this research, although he did suggest that there was a signal difference between cancerous tissue and normal tissue. In 1975, Richard Ernst proposed MRI using phase and frequency encoding, and the fourier transform, which is the basis for current MRI techniques.[185] In 1977, Raymond Damadian demonstrated MRI of the whole body. In this same year, Peter Mansfield developed the echo-planar imaging (EPI) technique.[186,187] The *in vivo* potential of paramagnetic ions was first published in 1978, when Lauterbur *et al*. used a manganese(II) chloride solution at a dose of 0.1 mmol/kg body weight in a dog model for the differentiation of infracted and normal myocardium.[184,188] Edelstein and coworkers[189] demonstrated imaging of the body using Ernst's technique in 1980. A single image could be acquired by this technique in about five minutes. By 1986, the imaging time was reduced to about five seconds, without sacrificing too much on image quality. Recently, in 2003, the works of Lauterbur and Mansfield in the field of MRI were recognized by the Nobel Prize in Physiology and Medicine.



Raymond Damadian



Paul Lauterbur



Peter Mansfield

1.4.3 Principles of MRI

The MRI technique relies upon observation of the ^{1}H nucleus of *in vivo* water molecules, utilizing a radiofrequency pulsed technique similar that employed by conventional laboratory nuclear magnetic resonance (NMR) spectrometers. The Larmor frequency is such that when a dipole is placed in a magnetic field, a torque induced on it, called a 'magnetic moment', causes it to align with the magnetic field. For an electron, however, the magnetic moment is produced by the orbital motion of the electron about the nucleus. This produces a force, B_0, which causes the magnetic moment to precess around the direction of the magnetic field at a frequency termed the Larmor frequency (LF).

The local equilibrium magnetization M_0 is the net difference between dipoles aligned with the field and opposite to the field, but it is not directly observable because it is many orders of magnitude weaker than B_0. However, if all the dipoles that contribute to M_0 could be tipped 90°, they would all precess around the field at the same rate. Thus, the magnetization M_0 would also tip 90° and begin to precess around the main field.

Tipping over the magnetization produces a measurement, transient signal, and the tipping is accomplished by the RF pulse. During the transmit part of the basic NMR experiment, the oscillating RF current in the coil creates in the sample an oscillating magnetic field B_1 perpendicular to B_0. The field B_1 is in general several orders of magnitude smaller than B_0. Nevertheless, this causes the net magnetic field, the vector sum of B_1 and B_0, to wobble slightly around the B_0 direction. Initially M_0 is aligned with B_0, but when the net field is tipped slightly away from B_0, the magnetization M_0 begins to precess around the new net field. If the oscillation frequency B_1 is different from the precession frequency v_0, not much happens to M_0 except a little wobbling around B_0. But if the RF frequency matches the precession frequency, a resonance phenomenon occurs.

As the net magnetic field wobbles back and forth, the magnetization precesses around it in synchrony. The effect is that with each precessional rotation M_0 tips farther away from B_0, tracing out a growing spiral. After a time, the RF field is turned off, and the M_0 then continues to precess around B_0. The net effect of the RF pulse is thus to tip M_0 away from B_0, and such pulses are usually described by flip angles they produce (e.g., a 90° pulse or a 30° pulse).

The flip angle can be increased either by increasing the amplitude of B_1 of by leaving B_1 for a longer time. It is remarkable that a magnetic field as weak as B_1 can produce arbitrarily large flip angles. From an energetics point of view, tipping the net magnetization away from B_0 increases the orientational energy of the dipoles: the nuclei absorb energy from the RF pulse. This transfer of energy is possible even with small B_1 fields because B_1 oscillates at the resonant frequency of the nuclei, the precession frequency.

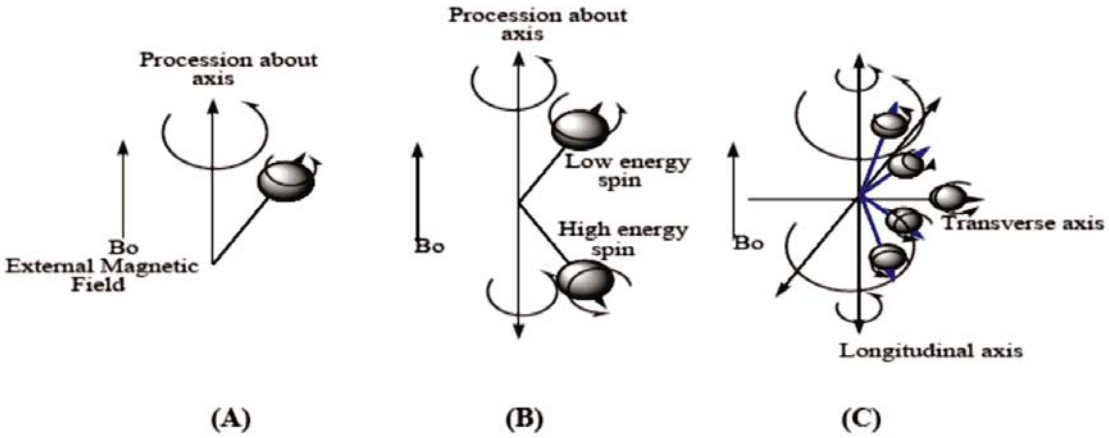


Figure 1.15: (A) Procession of protons in an external magnetic field.
(B) Proton spin energy in a magnetic field.
(C) Change in proton spin energy with increasing RF energy at the LF).[190]

In short, MRI is based on the magnetic fields of protons within the body, producing two-dimensional views of internal organs or tissues. Differentiation between biological tissues is the primary objective for imaging use in clinical diagnosis, and requires that the ^{1}H signal intensities vary depending on the tissue type.[191-194] By changing parameters, the MRI system can cause tissues in the body to take on different appearances. MRI gives a distribution of MR signal intensity resulting from the T_1 (longitudinal relaxation times – in simple terms, the time taken for the protons to realign with the external magnetic field) and the T_2 (transverse relaxation times – the time taken for the protons to exchange energy with other nuclei) of tissue water protons as indicated in Figure 1.15.[9] MRI instruments employ a gradient magnetic field, allowing ^{1}H NMR signals to be acquired as a function of three-dimensional space, with a final image consisting of a computer-reconstructed signal intensity map of the spatially encoded $^{1}H_2O$ NMR signals.

1.4.4 The biological parameters T_1 and T_2 in MRI

The relaxation process in resonance imaging is controlled by these parameters T_1 and T_2. These parameters are tissue dependant, introducing the possibility to separate different tissue types in the human body. T_2 - named the spin-spin relaxation time - is the time constant for the relaxation process in the xy-plane, whereas T_1 - named spin-lattice relaxation time - is the time constant in the z-direction. T_1 and T_2 are related to physical interaction phenomena in the tissue.[8]

T_2 effect

The T_2 effect in the relaxation process is due to dephasing of the individual proton magnetic dipole moment (MDM) because of the existence of a non-stationary magnetic field. Each proton will experience the external, stationary magnetic field B_0 along with the self-generated magnetic field of the neighboring protons. Since the angular frequency of a proton is proportional to the experienced magnetic field, the protons will precess at different frequencies, depending on the actual field. When the protons precess at different frequencies, some MDM's will be ahead and others behind compared to the ideal frequency - the Larmor frequency, resulting in a net decrease of magnetic moment in the xy-plane as time goes on. At some point the magnetic moment will become zero, when all the MDM's equalize one another. The time period from maximum value to zero is characterized by T_2. The value of T_2 depends on the mobility of the protons, since a large mobility results in an average magnetic field variation of zero, resulting in a long T_2 period.

T_1 effect

The T_1 effect in the relaxation process is due to the return of the high state protons to the low energy state. Over the time period T_1 the high state protons exchange the "extra" energy with the neighboring protons, resulting in heat and thermal energy. The value of T_1 is dependant of the proton's ability to exchange the energy.[8] However, most human tissues contain about the same

amount of water and therefore do not allow significantly large tissue differentiation on the basis of water content.[195]

Table 1.1: Examples of T_1 and T_2 values of different tissues in the brain.[8]

Tissue type	T_1 (ms)	T_2 (ms)
White Matter	871	87
Gray Matter	515	74
Cerebrospinal fluid	1900	250

The relaxation process is a result of both T_1 and T_2, and due to the exponential nature of this process some tissues might not be distinguishable, if recording the signal in the xy-plane directly. For this reason it is necessary to introduce control of the relaxation process by introducing a dependency of one of the two biological parameters in the recorded signal.

The signal intensity of various tissues in MRI could be amplified by varying the multiplicity of image acquisition parameters resulting in high intrinsic image contrast where damaged tissues can be distinguished from normal tissue. In some cases the T_1 and T_2 relaxation times of water protons may vary markedly depending on tissue type, and therefore, may be used as a source of contrast in MR images. However, these relaxation times are relatively slow (~seconds), increasing the time required to obtain clinically useful images and negatively affecting image quality. While some improvement in contrast can be made by T_1- or T_2-weighting, paramagnetic metals can shorten the T_1 or T_2 of water molecules in tissues through which they pass far more effectively for the purpose of MRI contrast.[196] The innate tissue contrast in images is not sufficient to distinguish between normal and pathogenic tissues when they produce similar signal intensity. To overcome this problem, and to enhance contrast between tissues, metal complexes are injected into the body that lead to significant improvement in the contrast of T_1-weighted and T_2-weighted MR images, by increasing the difference in the signal intensity from two types of tissue as shown in Figure 1.16 where MRI images of the brain are recorded. Figure 1.17 illustrates the advantages of using MRI-CAs as opposed to not using MRI-CAs.

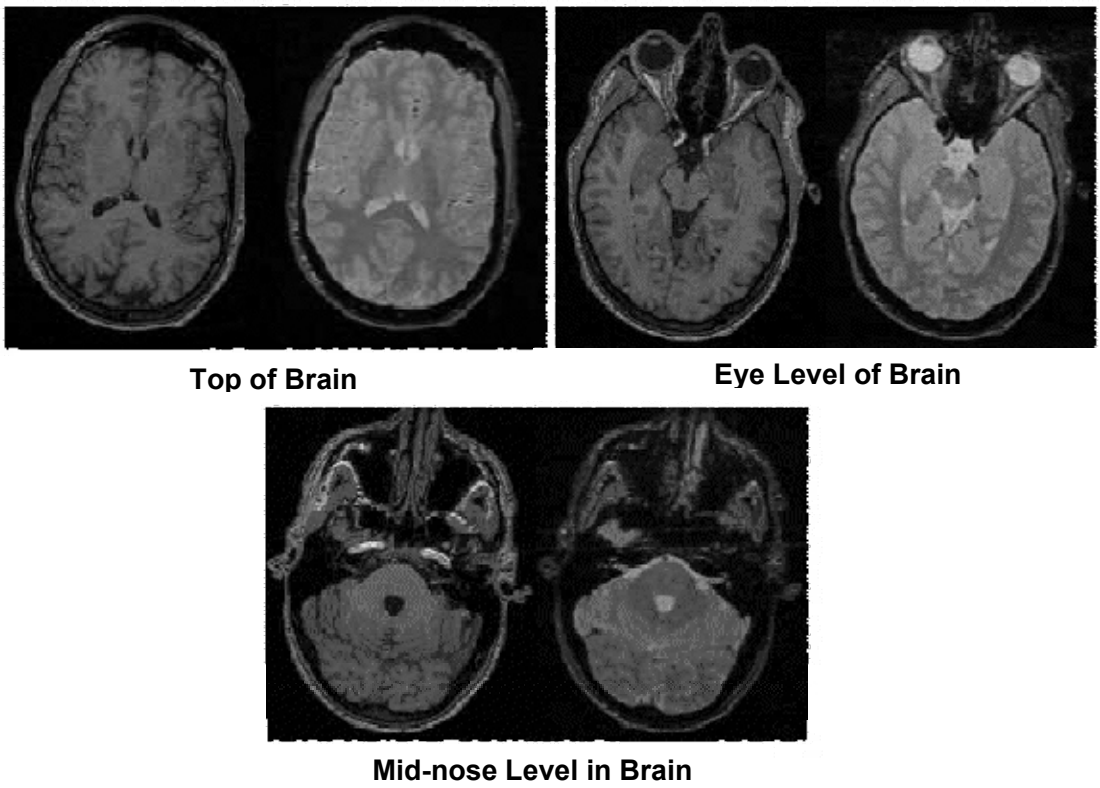


Figure 1.16: MRI images of the brain. T_1-weighted (left) and T_2-weighted (right).[196]

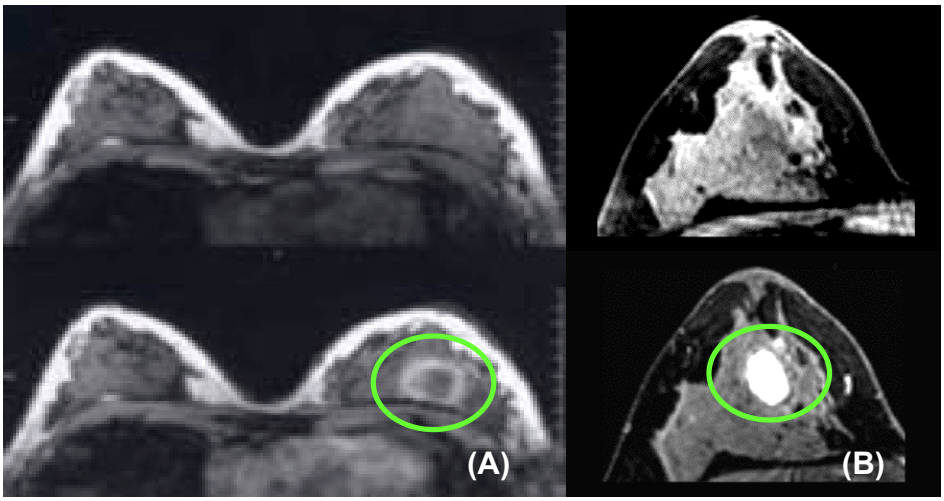


Figure 1.17: (A) Transverse fast acquisition breast MRI images at same level without contrast (upper) and with contrast (lower). The anomalies, emphasized by the green circles, show how the abnormality in the lower breast image on the right is "highlighted" by the contrast agent (gadolinium DTPA or Magnevist).
(B) MRI scans of breast without (upper) and with (lower) contrast agent (Magnevist).[197]

1.4.5 Factors related to Image Quality

Physical Factors

Improvements in image quality was made possible by the development of new equipment, software for image generation, and the design of more organ specific MRI-CAs. These combined effects significantly contributed to the improvement of the body images and thus to a much more accurate diagnosis.[196,198] Effective imaging can be achieved by: 1) increasing the sensitivity and specificity of the visualisation procedure; 2) improving the selectivity in tissue characterisation; 3) reducing intrinsic image artefacts; and more recently 4) acquiring more functional information on the image process.[199]

Chemical Factors

The general coordination chemistry of the Gd^{3+} ion lends itself to its application as a relaxation agent; fast water exchange rates are crucial for attaining high relaxivity, and the ionic radius of Gd^{3+} is ideal for fast exchange. Due to lanthanide contraction[200-204], lanthanide sizes decrease across the 4f row of the periodic table, resulting in higher coordination numbers for the early lanthanides and smaller coordination numbers for those toward the end of the series. Since the Gd^{3+} ion is situated in the middle of the row, a low energy barrier exists between the eight and nine coordinate states, favoring fluctuation between the two. However, the rate of water exchange of the Gd^{3+}, once complexed, is slowed significantly relative to that of the free ion, often to the extent that it is no longer in the optimal range for high relaxivity.

In addition, there is a significant decrease in the number of inner-sphere water molecules as they are replaced by ligating atoms in a chelating ligand. When designing new contrast agents an important trend to consider, which is related to water exchange, is the inherent decrease in proton relaxation rates with increasing magnetic field strength.[205,206] New high-field scanners (100 MHz and above) now appearing in medical facilities give better signal-to-noise ratios, and this effect becomes significant. Thus, short water residence times (or fast water exchange rates) become increasingly important at high field, with the optimal value for τ_M decreasing to about 1

ns for 2.4 T scanners (100 MHz proton Larmor frequency). Thus to attain high relaxivities at high fields, the coordination chemistry challenge involves the design of ligands that effectively chelate Gd^{3+} while limiting the decrease in the water exchange rate and reduction in *q* once the ion is bound.

1.4.6 Luminescence Lifetime Studies in the Rapid-Exchange Limit

Europium is commonly used as an analogue in the luminescence study of the hydration state of gadolinium due to their similar ionic radii (atomic radii: Eu^{3+} = 1.09 Å, Gd^{3+} = 1.08 Å) and because Gd^{3+} complexes are not susceptible to OH or OD quenching due their extremely large energy gaps between emissive and ground states. The relaxivity of a contrast agent scales linearly with the number of water molecules, *q*, that are in the first coordination sphere of the agent's metal ion.[207-216] One of many approaches to develop contrast agents with higher relaxivities has been to create complexes with larger *q*-values, producing more paramagnetically affected water molecules to exchange with the bulk solvent. Deactivation of the luminescence from excited trivalent lanthanide ions in solution occurs by means of a vibrational energy transfer process involving high-energy vibrations of solvent molecules like water and deuterium oxide shown in Figure 1.18.

Many of the early investigations of non-radiative relaxation in lanthanide systems sought to identify the nature and relative importance of these interactions.[207-216] It was established that OH oscillators of coordinated water molecules provide an efficient non radiative pathway for de-excitaion of the emissive state of certain lanthanide ions. Furthermore, these oscillators act independantly and OD oscillators of coordinated D_2O molecules are quite inefficient at accomplishing this deactivation. In 1979, Horrocks and Sudnick calibrated this effect by measuring the luminescence decay rates of a series of crystalline solids containing Eu^{3+} complexes separately prepared in H_2O and D_2O where the number of metal ion coordinated water molecules was known from X-ray diffraction studies.[217,218]

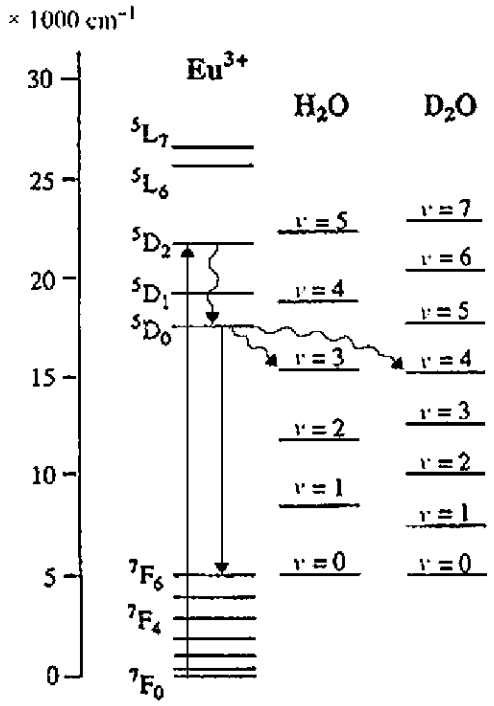


Figure 1.18: Vibrational quenching of Eu^{3+} emissive state by water. An offset has been applied so that the lowest vibrational level of OH/OD is shown at the same energy as the highest level of the ground-state manifold of the Eu^{3+}.[8]

The linear plot of the differences in the reciprocals of the excited state lifetimes in ms^{-1} (exponential decay constants) measured for the complexes crystallized in H_2O and D_2O is described by Equation 1.1:

$$q = A[\tau^{-1}_{H_2O} - \tau^{-1}_{D_2O}] \text{.....Equation 1.1}$$

where the constant A was determined to be 1.05 (water molecules·ms) for Eu^{3+} and the estimate error in the resulting approximation was *q*-value ±0.5 water molecules. Even though Equation 1.1 has proven to be very useful in the prediction of *q* for various complexes in aqueous solution, it frequently produces non-integer *q* values often greater than expected integer value. Several reasons account for this observation. First, the europium ion may form more than one type of particular complex with a particular ligand in solution. The presence of more than a single unique Eu^{3+} species in solution can easily be verified since the energy of the $^7F_0 \rightarrow {}^5D_0$ excitation transition between non-degenerate states is dependant on the identity of the atoms in

the first coordination sphere of Eu^{3+}.[219] The presence of more than one singlet peak in the $^7F_0 \rightarrow {}^5D_0$ excitation spectrum of a Eu^{3+} complex indicates multiple environments.[220] If the Eu^{3+} does exist in multiple coordination environments with different *q*-values, the *q*-value determined using Equation 1.1 depends on the rate of exchange of the Eu^{3+} between its different coordination environments. There are three possibilities namely, slow exchange, fast exchange and intermediate exchange,[221] depending on whether the rate of exchange of the Eu^{3+} between its coordination environments in slower, faster or similar to the luminescence decay rate of the excited state Eu^{3+} ion, respectively. For Eu^{3+} coordination environments containing differing numbers of first coordination sphere water molecules in the fast exchange, the *q*-value measured by Equation 1.1 will represent a concentration-weighted average of the *q*-values of each unique Eu^{3+} environment, and will typically be non-integral. The *q*-value of individual Eu^{3+} complexes in slow exchange can be determined by monitoring the luminescence decay of the corresponding $^7F_0 \rightarrow {}^5D_0$ excitation transition. It is difficult to obtain *q* values of the Eu^{3+} complexes in intermediate exchange because the luminescence decay of the excited Eu^{3+} ion is non-exponential.

Secondly, ligands containing X–H oscillators can also shorten Eu^{3+} excited state lifetimes to varying degrees. If these X–H moieties contain exchangeable hydrogen atoms, the $[\tau^{-1}_{H_2O} - \tau^{-1}_{D_2O}]$-values will be affected. Oscillators with exchangeable hydrogen atoms include alcoholic O–H and amine N–H oscillators in which the O or the N atom is directly coordinated to the metal. Amide N–H oscillators that have their carboxylic oxygen coordinated to the metal ion have also been found to shorten Eu^{3+} excited state lifetimes to a small extent. For the purpose of counting water molecules coordinated to Eu^{3+} ion, appropriate corrections need to be applied when these X–H oscillators are present.

Thirdly, the reason for non-integral and larger than expected *q*-values is that water molecules in the second coordination sphere of the Eu^{3+} ion, also called 'closely diffusing water molecules' are known to shorten luminescence lifetimes to a small extent.[222,223] Equation 1.1 is easily modified to account for the effects of X–H oscillators and water molecules beyond the first coordination sphere yielding Equation 1.2.[222,224]

$$q = A[\tau^{-1}_{H_2O} - \tau^{-1}_{D_2O} - k_{XH}] \text{ .....Equation 1.2}$$

where $k_{XH} = \alpha + \beta n_{OH} + \lambda n_{NH} + \delta n_{O=CNH}$

where n_{OH} is the number of alcoholic O–H oscillators in the first coordination sphere of Eu^{3+}, n_{NH} is the number of secondary amine N–H oscillators in the first coordination sphere of Eu^{3+}, and $n_{O=CNH}$ is the number of amide N–H oscillators in which the amide carbonyl oxygen is in the first coordination sphere of Eu^{3+}. The respective contributions of these X–H oscillators to the quenching of the $^5D_0$ state of Eu^{3+} are $\beta = 0.44$ ms^{-1}, $\gamma = 0.99$ ms^{-1} (calculated as the average of 0.759,[225] 1.0,[225] and 1.2[222]), and δ[222,223] $= 0.075$ ms^{-1}. The contribution to the q-value of a single O–H oscillator in the first coordination sphere of Eu^{3+} is calculated as half the contribution of a water molecule, i.e. $\beta = 1/(2A)$. The value α is the quenching of the excited state of Eu^{3+} by second coordination sphere water molecules.

1.4.7 Biomedical Considerations Toward the Development of MRI-CAs

Toxicity of the free Gd^{3+} used in the MRI-CAs needs to be considered. As gadolinium has a radial size approximately equal to calcium(II), competition occurs and as a result it can disrupt calcium^{2+} mediated signalling, forming strong complexes that can accumulate within the body.[188] This displacement of calcium in a physiological milieu is a driving force for many therapeutic and diagnostic applications. However, the correct choice of ligand can prevent this *in vivo* transmetallation from occurring. MRI-CAs used in the body should be biocompatible and include requirements such as rapid renal excretion, water solubility, stability in aqueous conditions, and a low osmotic potential when in solution for clinical work.[168] Also, at least one water molecule must be bound to the metal center (i.e. within the coordination sphere) and this undergoes rapid exchange with water molecules of the surrounding solution to affect the relaxation time of all the solvent protons.[155]

Factors controlling relaxivity

Relaxivity is controlled by two mechanisms that are essential to the understanding and design of contrast agents. The Solomon–Bloembergen–Morgan equations bring these important parameters together and have been outlined and discussed in previous reviews and further details by Botrill *et al.*,[226] Kowalewski *et al.*,[227] and Aime *et al.*[228] The inner sphere relaxation mechanism utilizes gadolinium and directly bound water interactions, and the outer sphere mechanism is based upon interactions between the second sphere and closely diffusing water molecules.[227] Figure 1.18 demonstrates the different parameters that need optimization for high relaxivity. These include the hydration of the metal ion, the mean residence time of the water molecule in the first coordination sphere (τ_M), and the tumbling rate of the species, which is characterized by the rotation correlation time (τ_R).[228]

Inner sphere relaxivity

The relaxivity of a contrast agent at commonly used imaging fields (0.5–1.5 T) can most effectively be controlled when the complexes are designed with the inner sphere relaxation mechanisms in mind. These mechanisms are governed by the following equation:[228]

$$R_{IP}^{IS} = \frac{Cq}{55.6} \frac{1}{T_{1M} + \tau_M} \qquad \textbf{.....Equation 2.1}$$

The Equation 2.1 shown above represents the inner sphere contribution to relaxivity, where C = molar concentration of paramagnetic compound, q = number of bound water molecules, τ_M is the mean water residence time, and T_{1M} = longitudinal relaxation time of the bound water protons.[228] T_{1M}, is controlled by the molecular rotational correlation time, τ_R, whereby slower tumbling of the contrast agents leads to faster relaxation rates, and hence relaxivity.[228]

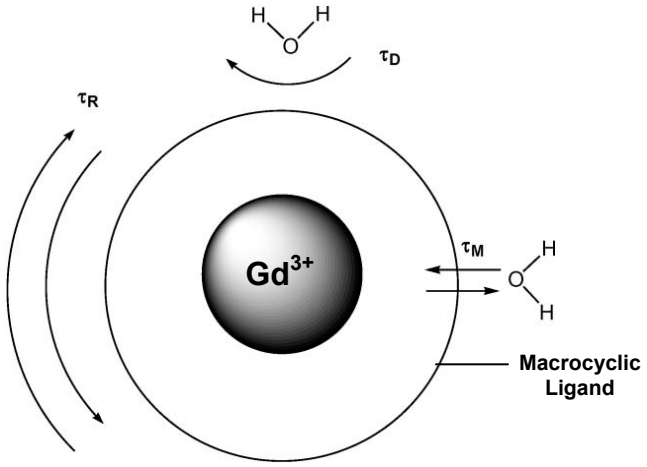


Figure 1.19: Illustration of the different parameters that require optimisation for maximum relaxivity of gadolinium contrast agents.[8]

The number of bound water molecules, *q*, is usually 1 (especially in current commercially available contrast agents) due to the octadentate chelators used for metal encapsulation.[227] These are very stable complexes, and prevent the release of the metal within the body. However, there have been recent examples of stable hepta-coordinated contrast agents containing two water molecules bound to the gadolinium.[9] This is an attractive development as higher numbers of water molecules present enhance the relaxivity of the complex. Figure 1.19 depicts the different parameters that require optimisation for maximum relaxivity of gadolinium contrast agents.[8] As mentioned previously, T_{1M} is dominated by molecular reorientation τ_R.[228] It also depends on the residence time of the bound water, τ_M, and electron paramagnetic relaxation, T_{1e} and T_{2e}. τ_D is defined as the diffusion coefficient of proximal water molecules. Aime *et al.* provide a full and detailed explanation of these factors in their recent review article.[228] In basic terms, T_{1e} and T_{2e} are frequency dependant, which means that at usual field strengths (0.5–1.5 T) τ_M, T_{1e} and T_{2e} are insignificant.[228] Hence at these fields consideration is mainly given to the molecular rotation correlation time.

Outer sphere relaxivity

Contrast agents can display relaxivity even when $q = 0$. In the absence of coordinated water molecules observed relaxivity arises from outer sphere contributions.[229] Outer sphere contributions originate from: (i) second sphere relaxation where water molecules hydrogen bonded to the carboxylate oxygen atoms are relaxed via dipolar mechanisms and (ii) outer sphere relaxation which arises due to diffusion of water molecules in the bulk near to the Gd^{3+} complex.[9,230] The parameters of importance are the electronic relaxation time of the metal, the distance of the closest approach of solvent and solute and the sum of their diffusion coefficients.[155] The outer sphere relaxivity is usually estimated by equations proposed by Freed *et al*.[231] It is important to note that this model is only an approximation for the polyaminocarboxylate ligands used in contrast agents because it does not take into account interactions of water with the complex, which for these ligands are important.[228] On the whole it seems that outer sphere contributions to relaxivity are not very well understood, and this phenomenon is somewhat overlooked when contrast agents are being developed.[9] The primary developmental focus of next-generation MRI contrast agents has been on derivatization of aminocarboxylate systems used in general practice.[232] Figure 1.20 shows some commercially available aminocarboxylate-based MRI contrast agents in current usage.

Features of compounds based on ligands such as DTPA and DOTA include inexpensive streamlined syntheses as well as adequate solubility and toxicological parameters.[233,234] The following examples illustrate several approaches toward optimizing the aminocarboxylate system en route to more efficient relaxation agents. Research efforts in new contrast-agent design are generally directed towards the optimization of one or more of the afore-mentioned relaxation parameters through ligand structural modification. For example, Merbach and co-workers have reported numerous studies that probe the factors influencing the water exchange rate of aminocarboxylate Gd^{3+} complexes.[235-239] The main explanation for increased water exchange rates is steric crowding at the water binding sites, a property that favors the release of the coordinated water molecule in a dissociative exchange process.

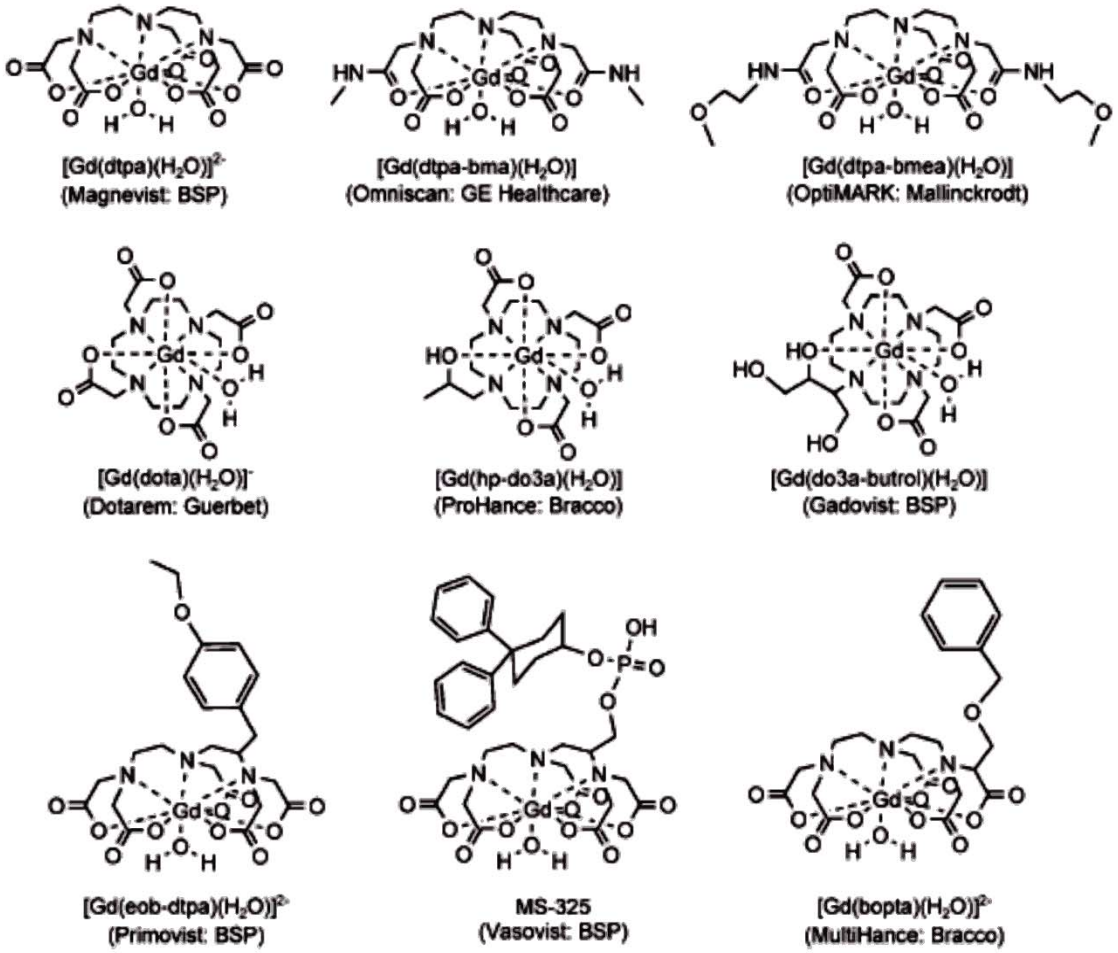


Figure 1.20: Commercial aminocarboxylate-based MRI contrast agents (Bayer Schering Parma AG).[232]

Derivatives of DTPA, shown in Figure 1.21, have been synthesized with varying numbers of carbon atoms in the ligand scaffold.

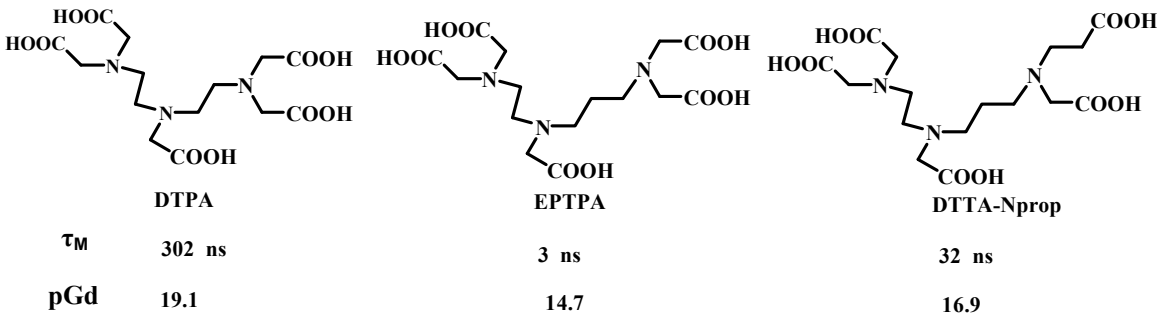


Figure 1.21: The DTPA ligand and two of its derivatives prepared for water exchange rate studies.[235,236]

As shown by the τ_M values, water exchange is accelerated in the resultant Gd^{3+} complexes, with values approaching the optimal range for high relaxivity at higher magnetic fields (60–100 MHz). This rate enhancement is achieved, however, at the cost of thermodynamic stability, as measured by the relatively low pGd* values tabulated in Figure 1.21. This phenomenon of decreased stability upon increasing water exchange rates is common for aminocarboxylate ligands and must be addressed when considering these complexes as high-relaxivity agents, particularly at the high magnetic field strengths of future clinical scanners. Increased water exchange rates for macrocyclic complexes based on [Gd(DOTA)(H_2O)] have also been reported. The pyridine-*N*-oxide derivative of DOTA illustrated in Figure 1.22 resulted in a gadolinium complex with a significantly faster water exchange rate than the parent complex (τ_M = 39 vs. 244 ns).[240] As with the linear aminocarboxylates mentioned above, the rate of increased water exchange was attributed to an increase in steric crowding.

* pGd = -log[Gd]free ; [Gd]total=1 μM, [L]total =10 μM (pH 7.4, 25 °C, 0.1 M KCl).

A monophosphinic acid derivative shown in Figure 1.22 was found to possess an even faster exchange rate, with τ_M = 16 ns.[241] Steric crowding owing to the bulky phosphinate group is given as a rationale for the increased rate, as well as a possible favorable arrangement of water molecules in a second coordination sphere. The relaxivity of this complex is 6 $mM^{-1}s^{-1}$ (20 MHz, 25 °C), an improvement over commercial agents.

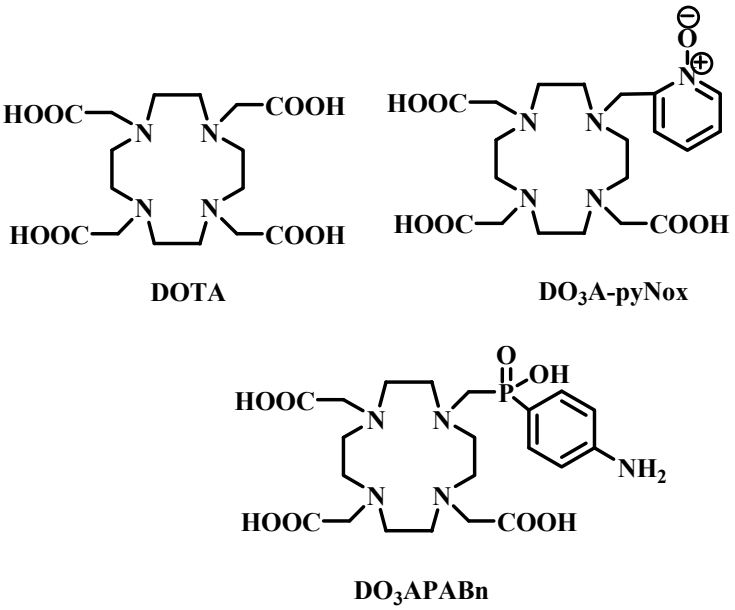


Figure 1.22: The DOTA ligand and derivatives prepared to increase water exchange rates.[240,241]

Aminocarboxylate complexes with q>1 have also been reported in efforts to achieve higher relaxivity. Relaxivity is highly dependant on q, and relaxivity values will be limited for complexes that possess only one coordinated water molecule (q=1). Two examples of q=2 complexes are depicted in Figure 1.23. In each case, DTPA complexes are tethered to a central core to produce dinuclear Gd^{3+} complexes with increased hydration numbers (q=2). The relaxivity values of $[Gd_2\{pX\text{- }(DTTA)_2\}(H_2O)_4]^{2-}$ and $[Gd_2\{mX(DTTA)_2\text{-}(H_2O)_4]^{2-}$ are 12.8 and 11.6 $mM^{-1}s^{-1}$ (20 MHz, 37 °C), respectively, and represent significant increases over that of the parent DTPA complex (r_{1p} = 4.3 $mM^{-1}s^{-1}$).[242] These values are influenced by the higher q value and (owing to increased molecular weight) by an increase in the rotational correlation time τ_R.[189]

A supramolecular approach was used to generate another dinuclear *q*=2 complex via iron terpyridine complexes derivatized with DTPA shown in Figure 1.23.[243]

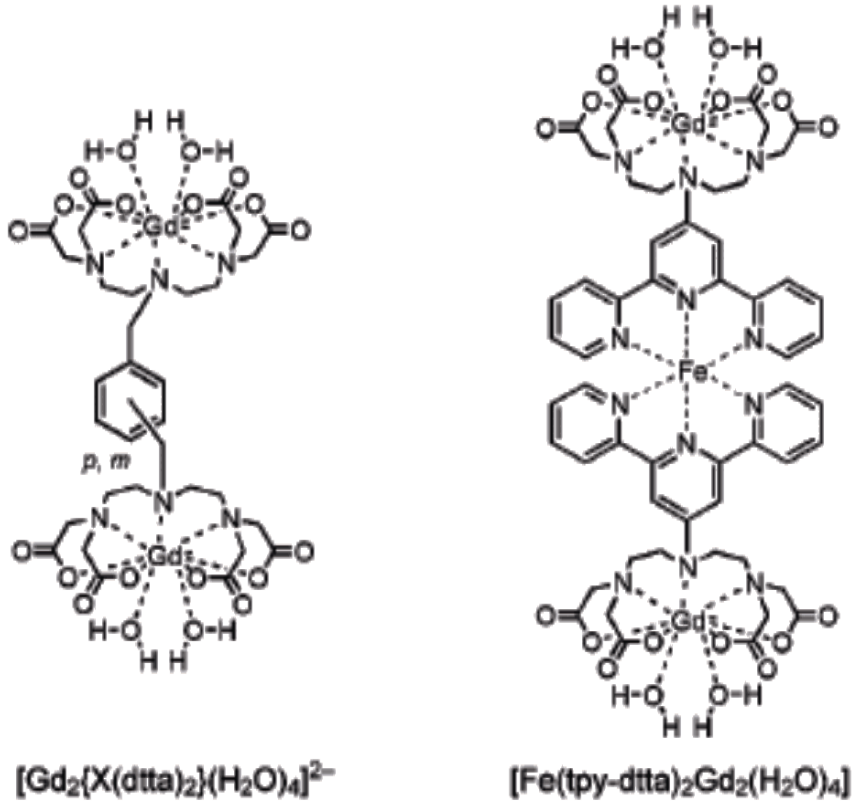


Figure 1.23: Examples of dinuclear, q=2 DTPA-based Gd^{3+} complexes proposed as improved high-relaxivity MRI contrast agents.[243]

The high relaxivity of $[Fe(tpy\text{-}dtta)_2Gd_2(H_2O)_4]$ (15.7 $mM^{-1}s^{-1}$, 20 MHz, 37 °C) is attributed to an increase in *q* as well as a long τ_R value resulting from the higher molecular weight and rigidity of the complex.[201] While the relaxometric properties of such *q*=2 compounds are improved, the thermodynamic chelate stability suffers greatly in both cases. The increase in *q* is made possible by removing a carboxylate arm of the parent DTPA to open up a metal coordination site. As is observed for increased water exchange in aminocarboxylate complexes, higher number of coordinated water molecules via a decrease of ligand denticity is accompanied by a dramatic decrease in thermodynamic stability. The pGd values for the para- and meta-substituted xylene-based complexes (16.2 and 15.1, respectively) are significantly lower than the value of 19.1 for the parent DTPA complex.[9] Even less stable is the iron terpyridine complex; its

pGd value of 10.6 represents a decrease by more than five orders of magnitude in stability relative to the DTPA-BMA complex (pGd = 15.8), the ligand with the lowest pGd value of all clinically approved agents. This effect of decreased stability resulting from increased *q* or water exchange rates raises a key concern in contrast agent design. The optimization of one parameter will often hamper that of another, making the goal of high-relaxivity of practical agents a major challenge. To achieve a practical high-relaxivity agent, the optimal combination of all relevant parameters must be accomplished while maintaining solubility and chelate stability. As an example of a gadolinium-based contrast agent not focused on traditional aminocarboxylate ligand scaffolds, Wilson and co-workers have reported several studies of Gd^{3+} encapsulated inside fullerene cages.[244-246] The peripheries of these cages are decorated with solubilizing groups to allow for application of C_{60} in aqueous media. Relaxivities ranging from about 10 to as high as 38.5 $mM^{-1}s^{-1}$ (30 MHz, 26 °C) are due entirely to second and outer-sphere relaxation, as there are no inner-sphere water molecules directly coordinated to the gadolinium ion. In solution, these "gadofullerenes" aggregate, resulting in large assemblies with long rotational correlation times and consequent high relaxivities.[9] However, practical concerns such as in vivo toxicity and deaggregation in the presence of various salts (thereby limiting the effect of long τ_R values on relaxivity)[247] may preclude considering such systems for contrast agent applications.

A second approach to MR contrast is based on magnetic polymer particles, e.g. dextran-stabilized colloidal magnetite solutions as T_2 relaxation agents for MR, was initially patented by Owen *et al.* followed by several patents on biocompatible magnetic particles.[248,249] The first product based on magnetic particle technology, AMI-25 or ferrioxidases, appeared on the market in 1995, distributed under the license as Endorem® (Laboratoire Guerbet SA, France) or Ferridex® I.V. (Berlex laboratories Inc., U.S.A. ;Tanabe, Seiyaku Company, Japan).

As mentioned earlier, the interaction of the Eu^{+3} metal center and biological buffers are examined across the pH range in this work. In the preceeding Section 1.4.8 the buffers used in this study are briefly introduced with respect to their origin, structure and properties.

1.4.8 Biological Buffers

Biological buffers are predominantly synthetic compounds serving widely to the pH stabilization and for the pH control in the pH range of 5.5–11.4.[250] They are soluble in water and have a high chemical stability and compatibility in various biological systems. Today, biological buffers are predominantly utilized as chemical agents for analytical chemistry. They are used in buffer exchange processes and as mobile phases during some chromatography steps, too.[257] These buffer compounds provide alternate buffer compounds with pK_a values near physiological conditions for biological applications.[251,252] The biological buffers are free of chromophores absorbing light above 200 nm. In spite of this, it was reported recently that some of the buffers weaken markedly the passing light under some experimental condition.[253] There have been no studies that have previously reported interactions of these biological buffers with lanthanide(III) complexes in solution specifically on whether their absence or presence changes derived physical quantities.

Good Buffers

In 1966, Good and coworkers discovered, developed and introduced a special group of zwitterionic biological buffers, called Good buffers.[254] Later, in 1980, they were patented and they also introduced a new generation of biological buffer compounds based on the zwitterionic character of Good buffers.[252] Good buffers stabilize pH of solution and they are used as protein solubilization agents in aqueous solutions too.[255] The pK_a values of these biological buffers lie at or near physiological pH area.[251,254] Popularity of using of biological buffers increased in analytical chemistry and followed two phenomena. The first being photometric detection that is accounted for using modern instrumental analytical methods. The second phenomenon is the fact that biological buffers are free of chromophores absorbing ultraviolet light above 200 nm. To ensure these biological buffers are free of chromophores they are further tested by the passing a short wavelength UV-light beam through aqueous solutions.[253,256] One of the main attributes exploited by Good buffers is the fact that the pK_a of sulfonic acids are very low. The buffers used throughout this work are tabulated in Table 1.2.

Potassium hydrogen phthalate (KHP)

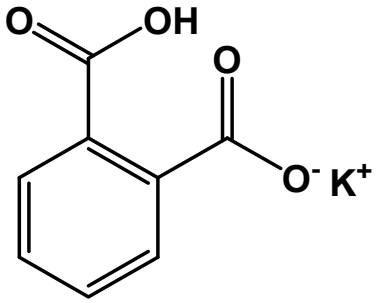
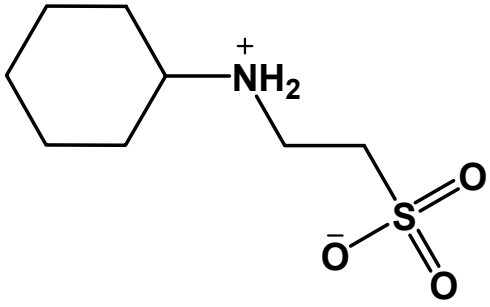
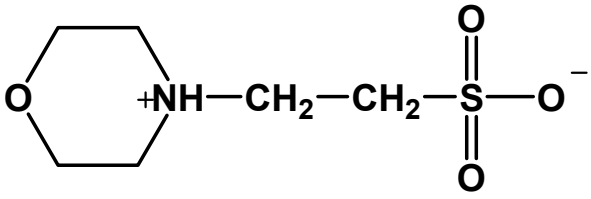
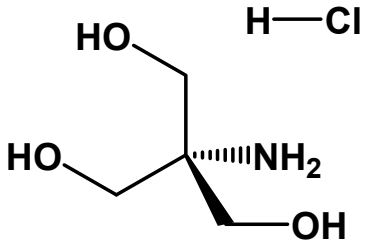
Potassium hydrogen phthalate, often called simply KHP, is an acidic salt compound. It forms white powder, colorless crystals, a colorless solution, and an ionic solid that is the mono- potassium salt of phthalic acid. The hydrogen is slightly acidic, and it is often used as a primary standard for acid-base titrations because it is solid and air-stable, making it easy to weigh accurately. It is also used as a primary standard for calibrating pH meters because, besides the properties just mentioned, its pH in solution is very stable.

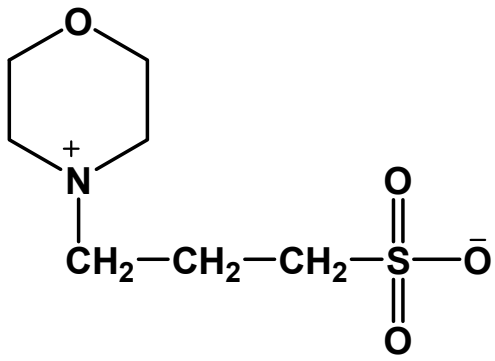
In water KHP dissociates completely giving the potassium cation (K^+) and hydrogen phthalate anion (HP^- or $Hphthalate^-$). As a weak acid hydrogen phthalate reacts reversibly with water to give hydronium (H_3O^+) and phthalate ions.

$$\mathbf{HP^- + H_2O \rightleftharpoons P^{2-} + H_3O^+}$$

KHP can be used as a buffering agent (in combination with hydrochloric acid (HCl) or sodium hydroxide (NaOH) depending on which side of pH 4.0 the buffer is to be. In acidic solutions KHP becomes phthalic acid, which is a dibasic acid, with pK_a's of 2.98 and 5.28. Phthalic acid is one of three isomers of benzenedicarboxylic acid, the others being isophthalic acid and terephthalic acid. Sometimes the term "phthalic acids" is used to refer to this family of isomers, but in the singular, "phthalic acid", refers exclusively to the *ortho*- isomer.

Table 1.2: Common Buffers Used in Study.

Buffers	Structure	pK_a at 25 °C	pH Range
Potassium hydrogen phthalate		**5.51**	**4-8**
CHES		**9.49**	**8.6 – 10.0**
MES		**6.10**	**5.5 – 6.7**
Tris/HCl		**8.3**	**7.0 – 9.0**

Buffers	Structure	pK_a at 25 °C	pH Range
MOPS		**7.20**	**6.5 – 7.9**
Multi-component buffer (1 mM CHES, 1 mM MES, 2 or 10 mM Tris, 1 mM MOPS, 1 mM and or Potassium hydrogen phthalate)			**2.0 – 10.0**

1.5 Scope and Objectives of the Research Project

The aims of this work are to enhance metal complexation of macrocyclic ligands through new structural features introduced into ligand backbones and pendant moieties using selectivity trends observed for transition metal complexes. Specifically, we planned to enhance complexation stability of lanthanides (Eu and Gd) by encapsulation of the metal within macrocyclic cavities based on cyclen with grafted cyclohexyl on pendant amino alcohol donors. The target ligands are illustrated in Figure 1.24. Initial feasibility studies toward target intermediates were carried out with the aim of finding the most suitable pathways. Many of the synthetic routes envisaged have been developed in our laboratories or have been reported by others in the scientific literature.

Target Ligands to be Synthesized

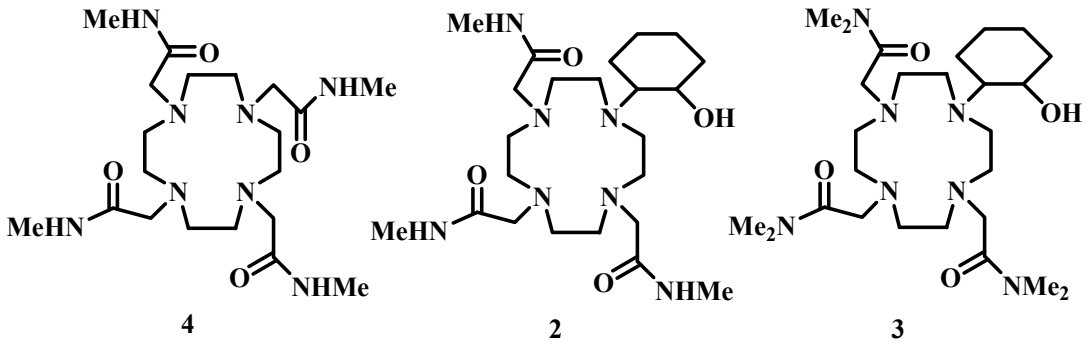


Figure 1.24: Target Ligands.

For the ligand feasibility study, three clearly distinct methodologies or possible strategic pathways taken toward the target molecules were defined as shown below in Figure 1.25, namely (i) direct alkylation, (ii) mono-protection and (iii) tri-protection methods, respectively. The success and reproducibility of any chosen path was vital in unraveling and understanding the synthetic considerations that needed to be taken into account when synthesizing mono *N*-substituted cyclen derivatives.

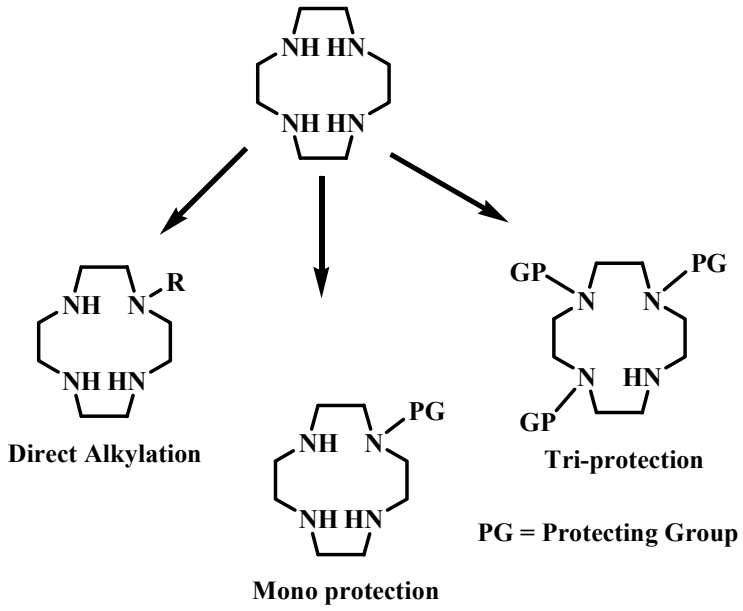


Figure 1.25: Strategic paths taken toward target molecules.

(i) In the direct alkylation path, the pendant cyclic moiety was added selectively to one of the nitrogen atoms on the cyclen backbone, followed by further alkylation with pendant acetamides to form target ligands.

(ii) Conversely, in the mono-protection strategy, one of the nitrogen's is selectively protected typically with a tosyl protection group. Once that was achieved the product was further alkylated with pendant arms to form an intermediate. This compound is further deprotected to remove the protecting group leaving an available site for attack by the pendant cyclic moiety.

(iii) In the tri-protection approach, three of the nitrogens are selectively protected typically with boron or molybdenum/tungsten derivatives. This leaves one free nitrogen site available that can be selectively alkylated with a pendant cyclic moiety. Once this is achieved, the central protecting metal can be removed using the appropriate procedures, and once cleaned further alkylated with pendant arms to form the final target ligands.

Through the different strategies mentioned and the various synthetic tools used, this demonstrates how diverse the chemistry of 1,4,7,10-tetraazamacrocycles is. The chelates to be synthesized are to take into consideration the effect of:

(i) Using different types of pendant donors.

Amide groups used as pendant donors have donor atoms that allow for the manipulation of the hydration sheath of the metal complex as well as the overall complex charge. A comparison of our findings with DOTA and DOTAM will show how changing one of the pendant donors to a pendant amino alcohol donor changes the system.

(ii) Grafting aliphatic groups such as cyclohexyl into pendant donor backbones.

The bulkier pendant moieties may allow for intramolecular interactions that favor metal encapsulation of metal ions of smaller ionic radius and an increase in exchange rate of the coordinated water molecule envisaged.

(iii) Characterize all products

All compounds from precursors, ligands and their respective metal complexes will be thoroughly analyzed using appropriate scientific instrumentation namely NMR spectroscopy, mass spectroscopy, Fourier transform infrared spectroscopy and X-ray crystallography (where possible).

(iv) *Clearly define the effects of intramolecular interactions arising from changes in ligand topology that result in enhanced Lewis acidity of the complexed metals.*

f) Studies on Eu(III) Complexes

(i) Luminescence Studies and UV-visible to determine spectroscopic pK_as, and hence elucidate the solution structure of Europium-Complexes.

(ii) Determination of q, number of coordinated water molecules to metal center, using luminescent lifetime measurements.

(iii) Investigate the solution chemistry of metal complexes using Cyclic Voltammetry.

g) The general hypotheses proposed in this study are as follows:

Introducing cyclic groups onto the macrocyclic ring nitrogens imparts greater rigidity to the macrocyclic ring that slows down the kinetics of demetalation. This occurs since the protonation of the nitrogen donor atoms in the sterically crowded macrocyclic cage becomes more difficult.

(i) Although the number of coordinated water molecules plays an important role in enhancing the performance of a contrast agent, the rate and mechanism of water exchange is equally crucial. These are intimately related to the inner-sphere solution structure and reported water exchange rates for different Gd^{3+} complexes may vary by as much as four orders of magnitude. A dissociatively activated water exchange mechanism is often suggested since it is supposed that there is no space for a second water molecule to enter before a bound water has departed in nine coordinate Gd^{3+} complexes of octadentate ligands. The greater steric crowding of the coordination polyhedron, induced by the bulkier backbones of the pendant donor atoms, is

proposed to decrease the activation energy required to reach the eight coordinate transition state thereby increasing the rate of exchange with the bulk solution.

(ii) There have been few examples of studies conducted with lanthanide complexes with commonly used buffer systems namely Good's Buffers on which earlier work have been reported. This project ultimately aims at preparing and studying new cyclen-based Ln^{3+} metal chelates exhibiting improved resolution and functionality and investigating the effects of buffer systems involving potassium phthalate (KHP). The fact that these buffers contain both NH, CH and OH oscillators and in the case of KHP a chromophore that may affect photophysical and electrochemical behavior in solution merits the need for investigation.

Chapter Two Experimental

2.1 Materials and Methods

2.1.1 General Materials

Deionised water was produced by a Millipore RO unit, and further purified by reverse osmosis using a Millipore MilliQ Ultra-Pure system (18 MΩ cm). All glassware was washed thoroughly with liquid soap, rinsed with distilled water, rinsed with commercial acetone and dried in an oven set at 100 °C. All reagents were the highest commercially available grades and used without further purification unless otherwise indicated (Section 2.1.2). However, the solvents that were utilized were appropriately dried. The reagents used are listed in Table 2.1. All masses were calculated according to exact mass range.

Table 2.1: Materials used in this study.

REAGENT	SUPPLIER	GRADE	% PURITY
Acetone	Merck	CR	
Acetonitrile	Agros-Organics	AR	
Argon	Afrox	AR	
Calcium chloride	BDH	GR	Anhydrous
Cesium carbonate	Sigma	AR	
Chloroacetyl chloride	BDH	CP	
Cyclen	Strem Chemicals	CR	
Dimethyl ammonium hydrochloride	Sigma	AR	
Chloroform-d, contains 1 % v/v tetramethylsilane	Aldrich	AR	99.8 atom % D
Diethyl ether	Aldrich	CP	
Dimethylformamide	Sigma	CP	
Deuterium oxide	Aldrich	AR	99.9 atom % D
Deuterium Chloride	Sigma	AR	
Ethanol Absolut puriss. p.a.	Aldrich	CP	
Ethyl acetate	Aldrich	CP	

REAGENT	SUPPLIER	GRADE	% PURITY
Europium triflate	Aldrich	AR	98 %
Gadolinium triflate	Aldrich	AR	98 %
Hydrochloric Acid	Saarchem	GR	32 %
Iodine, chips	Aldrich	GP	99+ %
Liquid nitrogen	Afrox	CR	
Magnesium Turnings	Riedel-de Haën	CP	≥99.5 %
Magnesium sulfate anhydrous	SaarChem	AR	uniLAB
Methyl ammonium hydrochloride	Sigma	AR	
Nitrogen gas	Afrox	AR	
Potassium chloride	Aldrich	AR	
Potassium carbonate	Sigma	AR	
Potassium dihydrogen phosphate	Merck	GR	
Potassium iodide	BDH	GR	
Potassium hydrogen phthalate	Saarchem	GR	99.995 %
Phosphorus pentoxide	Sigma	CP	
Nitric Acid Ampoule	VBH	AR	99.995%
Sodium Deuteroxide	Sigma	AR	
Sodium Hydroxide Pellets	Merck	uniLAB	
Sodium Hydroxide Ampoule (0.1 M)	VBH	AR	99.995%
Sodium nitrate	Aldrich	AR	99.995%
CHES	Sigma	AR	99 %
MOPS	Sigma	AR	99.5 %
MES	Sigma	AR	99.5 %
Tris	Merck	AR	

Key: **AR** = Analytical Reagent **CR** = Commercial Reagent
CP = Chemically Pure **GR** = General Reagent

2.1.2 Distillation of Solvents

2.1.2.1 Acetonitrile

Acetonitrile was dried by refluxing over di-phosphorus pentoxide (DPP), in an argon atmosphere. The dried solvent was stored over molecular sieves (4 Å).[257]

2.1.2.2 Ethanol

Although absolute ethanol was utilized it was further dried using 5 g of magnesium turnings and 0.5 g of iodine per 100 ml solvent. The mixture was heated until a vigorous reaction occurred and turned from yellow to clear. 1 L of ethanol was then added to the flask, and the mixture refluxed for about an hour (under an argon atmosphere), before the dried ethanol was collected.[257]

Note: The common drying agent used for the drying tubes was calcium chloride (anhydrous) as it has a large capacity for absorption of water. After use, it was stored in at oven set at 100 ºC.

2.1.3 General Analytical Characterisation Techniques

2.1.3.1 Nuclear Magnetic Resonance Spectroscopy (NMR)

^{1}H and ^{13}C NMR spectra were recorded on a Bruker Avance 300 Spectrometer operating at 300 MHz (^{1}H) and 75 MHz (^{13}C). Samples were calibrated with TMS (^{1}H) and with the triplet of $CDCl_3$ for ^{13}C at 77.00 ppm. COSY experiments were performed to elucidate complex spectra of macrocyclic chelates obtained using a Bruker 500 MHz spectrophotometer. Samples were either dissolved in D_2O or *d*-chloroform depending on the sample being analyzed. In some cases D_2O was spiked with $NaO_3S(CH_2)_3SiMe_3$ for referencing in ^{13}C spectra.

All NMR Data are found in Appendix A

2.1.3.2 Electrospray Ionization-Mass Spectroscopy (ESI-MS)

Low-resolution mass spectra were recorded on a Thermo Finnigan LXQ Mass Spectrometer. The polarity used was positive. The ionisation method used was Electrospray Ionization (ESI). Samples were prepared in de-ionised water or methanol mixtures. Elution was performed using either methanol in 0.1 % formic acid or a 50:50 methanol:water mixture in 0.1 % formic acid. The data obtained were processed using the Xcalibur Version 2.0.7 software, and are quoted as *m*/*z* values.

All MS Data are found in Appendix B

2.1.3.3 Fourier Transform Infrared Spectroscopy (FTIR)

Samples were recorded on a Bruker TENSOR 27 Standard System FT-IR spectrometer and the measurements obtained were processed using the OPUS v5.5 software. Samples of either solid or liquid were analyzed with air as a background on a diamond sampler. The signal resolution was 4 cm^{-1} and the scan range from 400-4000 cm^{-1}.

All FTIR Data are found in Appendix C

2.1.3.4 Melting Point Determination

The melting point was determined using a JM instruments (model 628) standard laboratory melting point apparatus equipped with a microscope and a heating stage.

2.1.3.5 Solid State Chemistry of Polyazamacrocycles and their Complexes with Lanthanides

2.1.3.5.1 Crystal Growth Techniques Employed

Crystal growth involves a phase change from liquid or gas to a solid, such as the precipitation of a solute from a solution or the formation of a solid from condensation of a gas. This occurs through two processes, nucleation and growth, which are favored by using supersaturated solutions and/or temperature gradients. When several molecules in solution approach each other in appropriate orientations, they form a submicroscopic nucleus upon which additional molecules may adsorb. Continued adsorption results in an ordered extended crystal structure. The probability that a crystal will form depends on the nature and concentration of the solute (i.e. the distance between solutes), as well as solvent conditions such as temperature, pH, ionic strength, viscosity, polarity, etc. To grow single crystals suitable for X-ray diffraction analysis, relatively few nuclei should be formed rather than multiple sites of nucleation that will yield microcrystalline solids.

High quality crystals may only be obtained when the rate of deposition onto a nucleation site is kept at a rate sufficiently low to allow oriented growth. A high growth rate may lead to defects in the crystal forming multibranched or dendritic crystallites through rapid growth in too many directions. As molecules in the gas phase or solvent interact with the surface of the growing crystal, they may or may not be preferentially adsorbed. That is, nucleation sites that contains steps, ledges, or surface depressions is more easily able to allow more efficient crystal growth due to the prolonged interaction of suspended molecules with the surface.

Experimentally, the successful growth of single crystals on the order of 0.01-0.1 mm is not trivial. In this work crystals were mainly grown by dissolving the solid target compounds into a minimal amount of suitable solvent (acetonitrile, ethanol) that was then allowed to slowly evaporate at room temperature to acquire good quality single crystals. In some cases however, single crystal growth was achieved by spiking the solution with a type of solvent that the solid does not necessarily dissolve in (e.g. diethyl ether). This was done to force the single crystals out of solution.

2.1.3.5.2 Solving Crystal Structures

Single-crystal determination for compounds namely polyazamacrocycles and their corresponding lanthanide complexes were carried out using a Bruker SMART Apex II diffractometer at 173 K using graphite-monochromated CuK_α radiation.[258] The data was corrected for Lorentz and polarization[259] effects and absorption using SADABS.[260] The structure was solved by use of Patterson mapping. Least squares refinement on F^2 was used for all reflections. Structure solution, refinement and the calculation of derived results was performed using the SHELXTL[261] software package. The non-hydrogen atoms were refined anisotropically. The hydrogen atoms were located and then placed in theotretical positions. Images were created using the ORTEP IV program obtained from the Cambridge Structural Database (CSD).[262]

All X-ray crystallographic Data are found in Appendix G (Data Disc)

2.2 Synthetic Aspects and Strategies of Designing Lanthanide Complexes under Standard Laboratory Conditions

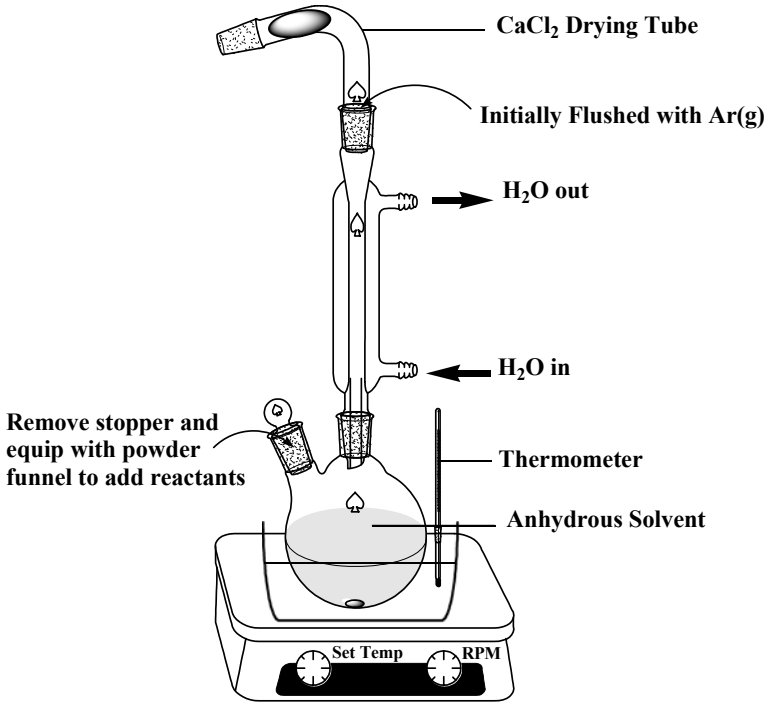
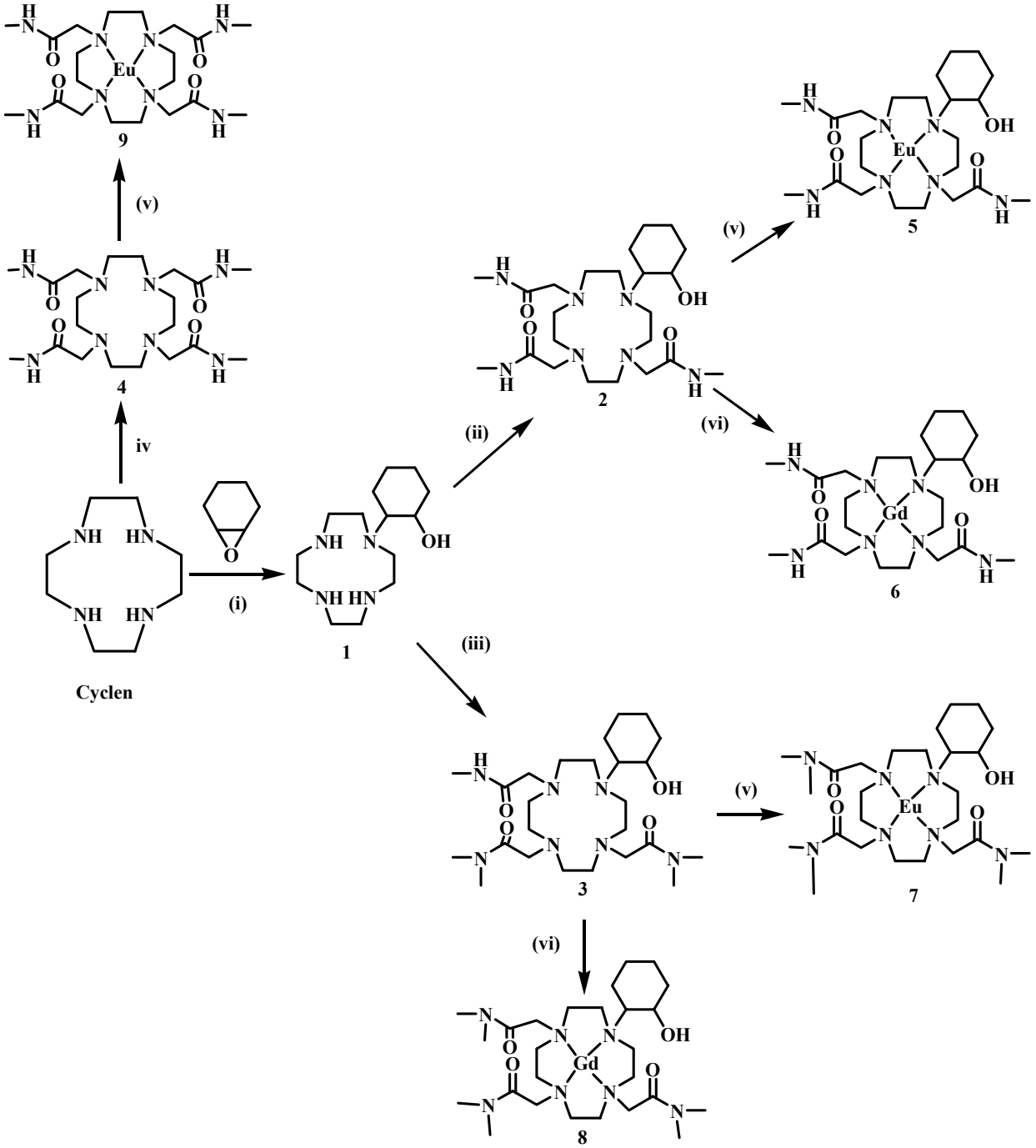


Figure 2.1: General reaction set up for all synthetic reactions in this work.

Without resorting to longer acyclic syntheses or high dilution techniques, the six membered cyclohexyl derivatives were viably obtained using a direct alkylation strategy. The general experimental set up for all synthetic reactions in this work is illustrated in Figure 2.1. It was possible to synthesize the following ligands shown earlier in Figure 1.24, and their corresponding europium and gadolinium complexes. DTMA was chosen as a target ligand merely for comparative purposes, to observe the effective differences between both moieties.

The generalized synthetic strategy is summarized in Figure 2.2 below.



(i)Dry EtOH, 80 °C, 48 hrs. (ii)Dry CH_3CN, 90 °C, N-methyl-chloroacetamide, $CsCO_3$, 10 hrs. (iii)Dry CH_3CN, 90 °C, Di-methyl-chloroacetamide, $CsCO_3$, 10 hrs. (iv) Dry EtOH, 90 °C, N-methyl-chloroacetamide, K_2CO_3, 48 hrs.(v) Dry CH_3CN, 90 °C, Europium Triflate, 90 hrs. (vi) Dry CH_3CN, 90 °C, Gadolinium Triflate, 90 hrs.

Figure 2.2: Generalized reaction conditions toward respective target molecules.

2.2.1 Synthesis of Precursor: Preparation of *N*-methyl-chloroacetamide

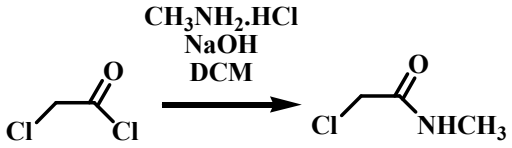


Figure 2.3: Preparation of *N*-methyl-chloroacetamide.

The reaction scheme shown in Figure 2.3 describes the synthesis of α-chloroamide and was originally based on work performed by Parker *et. al.* from chloroacetyl chloride with the appropriate amine.[263] NaOH (14.5 g, 3.63×10^{-1} mol) was in dissolved 20 ml distilled water, allowing the solution to cool to room temperature before adding 100 ml of dichloromethane. This mixture was then placed in an ice/ethanol-bath at approx 5 °C. Methylamine hydrochloride (11.9 g, 3.96×10^{-1} mol) was then added to the cooled mixture with continuous stirring. Chloroacetyl chloride (20.8 g, 1.86×10^{-1} mol) dissolved in 40 ml of dichloromethane was added in a dropwise fashion to the cooled mixture. The solution was allowed to stir for a further 2 hours. The organic layer was removed and then washed with deionised water. The organic extracts were further dried with drying agent (K_2CO_3) and collected. The solvent was removed under reduced pressure to afford the product, *N*-methyl-chloroacetamide (9.54 g, 8.91×10^{-2} mol) as a crystalline solid in 48% yield.

Empirical Formula: C_3H_6ClNO

^{1}H NMR ($CDCl_3$): δ 6.71 (s, NH, 1H), δ 4.06 (s, CH_2, 2H), δ 2.91-2.80 (d, CH_3, 3H).

^{13}C NMR ($CDCl_3$): δ 166.45 (s, CO, 1C), δ 42.53 (s, CH_2, 1C), δ 26.46 (s, CH_3, 1C).

FTIR: C-Cl_{str}: (medium, sharp) 758.09cm^{-1}, C-H_{bend} (strong, sharp) 1262 - 1410cm^{-1}, C=O_{str}: (strong, sharp) 1650.92cm^{-1}, N-H_{str}: (strong, broad) 3322.01cm^{-1}, C-H_{str}: (weak, broad) 2800-3100cm^{-1}.

Melting point (m.p) 35-37 °C

2.2.2 Preparation of *Di*-methyl-chloroacetamide

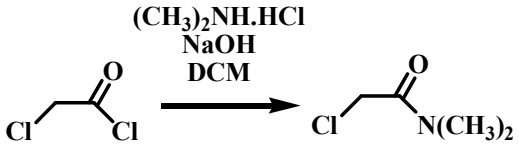


Figure 2.4: Preparation of *Di*-methyl-chloroacetamide.

The reaction scheme depicted in Figure 2.4 is based on the preceding reaction and has been modified accordingly since an oil product was isolated instead of a solid. Similarly, NaOH (7.15 g, 1.79×10^{-1} mol) was dissolved in 10 ml distilled water, allowing the solution to cool to room temperature before adding 50 ml of dichloromethane. This mixture was then placed in an ice/ethanol-bath at approx 5 °C. Dimethylamine hydrochloride (15.26 g, 1.35×10^{-1} mol) was then added to the cooled mixture with continuous stirring. Chloroacetyl chloride (10.13 g, 8.96×10^{-2} mol) dissolved in 20 ml of dichloromethane was added in a dropwise fashion to the cooled mixture. The solution was allowed to stir for a further 2 hours. The organic layer was removed and then washed with deionised water. The organic extracts were further dried with drying agent (K_2CO_3) and collected. The solvent was removed of under reduced pressure to afford the product, *Di*-methyl-chloroacetamide (9.54 g, 8.91×10^{-2} mol) as a colorless oil in 66% yield.

Empirical Formula: C_4H_8ClNO

^{1}H NMR ($CDCl_3$): δ 4.10 (s, CH_2, 2H), δ 3.11 (s, CH_3, 3H), δ 2.99 (s, CH_3, 3H).

^{13}C NMR ($CDCl_3$): δ 166.35 (s, CO, 1C), δ 41.08 (s, CH_2, 1C), δ 37.47 (s, CH_3, 1C), δ 35.79 (s, CH_3, 1C).

FTIR: C-Cl_{str}: (strong, sharp) 756.72cm^{-1}, C=O_{str}: (strong, sharp), 1639.98cm^{-1}, 2959.24cm^{-1} C-H_{str}: (medium, sharp), 1263.04- 1547.41cm^{-1}, C-H_{bend} (strong, sharp), N-H_{str} 3006.96 cm^{-1}.

2.2.2.1 Synthesis of *β*-amino alcohol Intermediate: 1-(2-Hydoxycyclohexyl)-1,4,7,10-tetraazacyclodecane (1)

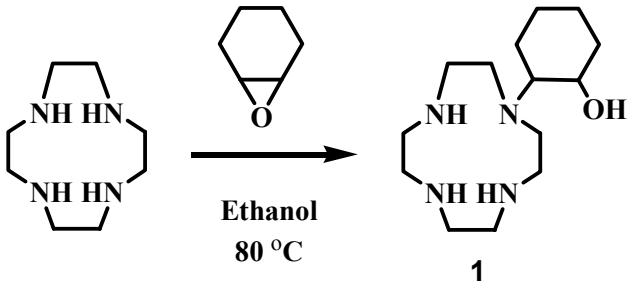


Figure 2.5: Preparation of 1-(2-Hydoxycyclohexyl)-1,4,7,10-tetraazacyclodecane (**1**).

The reaction scheme presented in Figure 2.5 is based on work originally performed in our laboratory by de Sousa *et al.*[264] and has been optimised in this work. The macrocycle, cyclen (2.3 g, 1.34×10^{-2} mol) was dissolved in 100 ml of anhydrous ethanol by stirring. Cyclohexene oxide (1.1 g, 1.12×10^{-2} mol) was added to this mixture and refluxed for 48 hrs at 80 ^{o}C under a $CaCl_2$ drying tube. On removing the solvent, a pale yellow oil was obtained. This was placed under reduced pressure affording a white amorphous solid. Trituration with minimal volume (10 ml) of cold acetone for 1 hr afforded a solid precipitate. The precipitate was filtered and purified by crystallization from hot ethyl acetate. The re-crystallization procedure was repeated until only the mono-substituted product, 1-(2-Hydoxycyclohexyl)-1,4,7,10-tetraazacyclodecane (0.9828 g, 3.64×10^{-3} mol) was isolated in 27% yield.

Empirical Formula: $C_{14}H_{30}N_4O$

^{1}H NMR (D_2O): δ 3.40-3.60 (m, CH, 1H), δ 2.90-2.40 (m, H_{cyclen}, 16H), δ 2.40-2.30 (m, CH_2, 1H), δ 2.10-1.90 (t, CH_2, 1H), δ1.90-1.80 (t, CH_2, 1H), δ 1.80-1.60 (m, CH_2, 2H).

^{13}C NMR (D_2O): δ 70.26 (s, CO, 1C), δ 64.84 (s, CH, 1C), δ 47.24 (s, CH_2, 4C), 45.48 (s, CH_2, 2C), δ 44.32 (s, CH_2, 2C), δ 33.77 (s, CH_2, 1C), δ 24.92 (s, CH_2, 1C), δ 24.06 (s, CH_2, 1C), δ 23.35 (s, CH_2, 1C).

ESI-MS (+): $[M + H]^+$ = m/z (271) and $[M + Na]^+$ = m/z (293).

m/e (relative intensity): 270.24 (100.0%), 271.25 (16.1%), 271.24 (1.5%), 272.25 (1.4%).

FTIR: N-H_{str}: (weak, broad) 2801.59-2930.50cm^{-1}, C-H_{str}: (strong, sharp) 2946.57cm^{-1}, O-H_{str}: (medium, broad) 3280.46cm^{-1}, C-H_{bend}: 1243–1410.71cm^{-1} (strong, sharp).

Melting point (m.p) 144-146 °C

2.2.3 Synthesis of *N*-substituted Cyclen based Ligands

2.2.3.1 Preparation of 1,4,7-tris[*N*-methylcarbomylmethyl]-10-2(hydroxycyclohexyl)-1,4,7,10-tetraazacyclododecane (2)

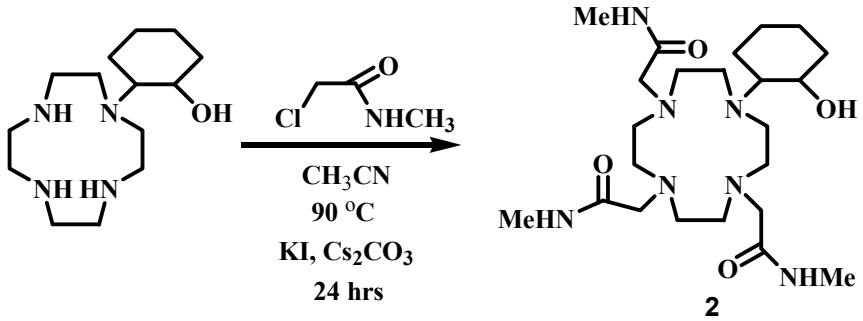


Figure 2.6: Preparation of 1,4,7-tris[*N*-methylcarbamylmethyl]-10-(2-hydroxycyclohexyl)-1,4,7,10-teraazacyclododecan (**2**).

Although two different methodologies were utilized to synthesize the above target **2** using DMF and CH_3CN as solvents, purification was easier using CH_3CN. The reaction scheme shown above in Figure 2.6 is based on work originally performed by de Tsukube *et al.*[8] and has been modified in this work. A solution of 1-(2-Hydoxycyclohexyl)-1,4,7,10-tetraazacyclodecane or Cy-cyclen (0.3032 g , 1.12×10^{-3} mol), *N*-methyl chloroacetamide (0.4025 g, 3.76×10^{-3} mol), KI (0.6646 g, 4.01×10^{-3} mol) and $CsCO_3$ (1.8185 g, 5.58×10^{-3} mol) was refluxed in dry CH_3CN (50 ml) for 24 hrs and then filtered to remove the excess metal salts. Acetonitrile was removed and the residue washed with diethyl ether to remove any unreacted Cy-cyclen. The preparation was further dried under reduced pressure. The product, 1,4,7-tris[*N*-methylcarbomylmethyl]-10-2-(hydroxycyclohexyl)-1,4,7,10-tetraazacyclododecane (0.5402 g, 1.12×10^{-3} mol) was isolated as a white powder in 99 % yield.

Empirical Formula: $C_{23}H_{45}N_7O_4$

^{1}H NMR ($CDCl_3$): δ 3.65-4.00 (m, CH_2, 4H), δ 4.14-4.25 (m, CH_2, 1H), δ 4.25-4.38 (m, CH_2, 1H), δ 4.48-4.68 (m, CH_2, 2H), δ 5.10-5.30 (m, CH_3, 9H), δ 5.30-5.51 (m, CH_2, 6H), 5.51-6.05 (m, CH_2, 14H), 6.05-6.40 (m, CH_2, 5H), 6.41-6.61 (m, CH, 2H).

^{13}C NMR ($CDCl_3$): δ 175.45 (s, CO, 1C), δ 174.19 (s, CO, 1C), δ 167.87 (s, CO, 1C), δ 68.33 (s, CH, 1C), δ 63.88 (s, CH, 1C), δ 58.70 (s, CH_2, 2C), δ 57.64 (s, CH_2, 4C), δ 51.02 (s, CH_2, 2C), δ 49.15 (s, CH_2, 2C), δ 33.08 (s, CH_2, 1C), δ 25.74 (s, CH_2, 1C), δ 24.25 (s, CH_2, 1C), δ 23.46 (s, CH_2, 1C), δ 21.74 (s, CH_3, 3C).

ESI-MS (+): $[M + H]^+$ = m/z (484), $[M + Na]^+$ = m/z (506), $[M + K]^+$ = m/z (522) and $[M + Cs]^+$ = m/z (616)

m/e (relative intensity for free ligand): 483.35 (100.0%), 484.36 (26.4%), 485.36 (4.2%), 484.35 (2.6%).

m/e (relative intensity for Na complex): 506.343 (100.0%), 507.346 (25.6%), 508.350 (3.1%), 507.340 (2.6%).

m/e (relative intensity for K complex): 522.317 (100.0%), 523.320 (25.6%), 524.315 (7.2%), 524.324 (3.1%), 523.314 (2.6%), 525.318 (1.9%).

m/e (relative intensity for Cs complex): 616.259 (100.0%), 617.262 (25.6%), 618.265 (3.1%), 617.256 (2.6%).

FTIR: C-H_{bend} (medium, sharp) 1439.83^{-1}, C=O_{str} :(strong, sharp) 1670.17cm^{-1}, N-H_{str}: (strong, broad) 2832.41^{-1}, C-H_{str}: (weak, broad) 2800-3100cm^{-1} O-H_{str}: (strong, broad) 3253.24cm^{-1}.

Melting point (m.p) 192-194 °C

2.2.3.2 Preparation of 1,4,7-tris[*N,N*-dimethylcarbamylmethyl]-10-(2-hydroxycyclohexyl)-1,4,7,10-tetraazacyclododecane (3)

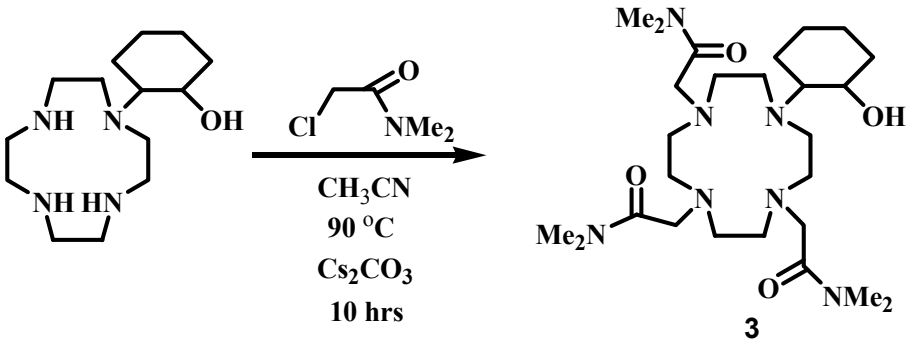


Figure 2.7: Reaction scheme showing preparation of 1,4,7-tris[*N,N*-dimethylcarbamylmethyl]-10-(2-hydroxycyclohexyl)-1,4,7,10-tetraazacyclododecane (**3**).

The reaction scheme shown above in Figure 2.7 is based on the preceding reactions to form **2** and has been modified accordingly to achieve the target **3**. A solution of 1-(2-Hydoxycyclohexyl)-1,4,7,10-tetraazacyclodecane (0.3412 g, 1.26 mmol), *Di*-methyl chloroacetamide (0.7804 g, 6.42 mmol) and $CsCO_3$ (6.0823 g, 18.67 mmol) was refluxed in dry acetonitrile (50 ml) for 10 hrs and then filtered to remove the excess $CsCO_3$. Acetonitrile was removed and the preparation was further dried under reduced pressure. The sample was completely dissolved in distilled water and the pH adjusted to <1 using concentrated hydrochloric acid. The solution was placed in an extracting funnel and extracted with dichloromethane (3 × 30 ml) to remove any excess chloroacetamides. The aqueous fraction was then frozen using liquid nitrogen and lyophilized to render the hydrochloride salt of the target **3**, a light yellow powder in 97 % yield (0.8185 g, 1.22 mmol).

Empirical Formula: $C_{26}H_{51}N_7O_4$

^{1}H NMR ($CDCl_3$): δ 3.60-4.00 (m, CH_2, 4H), δ 4.10-4.40 (m, CH_2, 2H), δ 4.45-4.70 (m, CH, 1H), δ 5.25-5.35 (m, CH_2, 3H), δ 5.35-6.35 (m, CH_3/CH_2, 36H), δ 6.40-6.90 (m, CH_2, 4H).

FTIR: C-H_{bend} (medium, sharp) 1402.87cm^{-1},C=O_{str} :(strong, sharp) 1627.94 m^{-1}, N-H_{str}: (strong, broad) 2939.51cm^{-1}, O-H_{str}: (strong, broad) 3349.30cm^{-1}.

ESI-MS (+): $[M + H]^+$ = m/z (527) and $[M + Na]^+$ = m/z (549).

m/e (relative intensity): 525.40 (100.0%), 526.40 (31.7%), 527.41 (4.3%), 527.40 (1.6%).

2.2.3.3 Preparation of 1,4,7,10-Tetrakis(methylcarbamylmethyl)-1,4,7,10 tetraazacyclodecane (4)

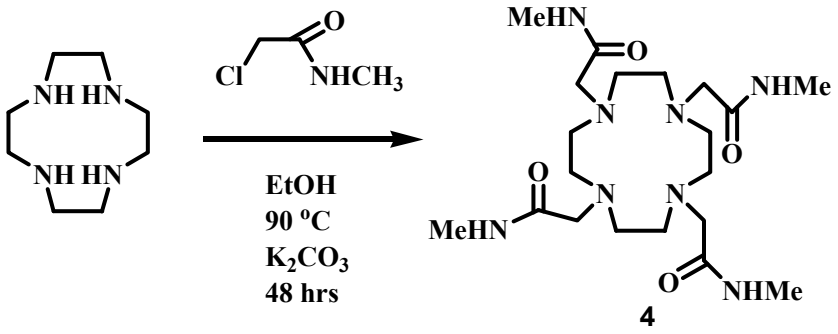


Figure 2.8: Preparation of 1,4,7,10-Tetrakis(methylcarbamylmethyl)-1,4,7,10-tetra-azacyclodecane (**4**).

This reaction scheme shown above in Figure 2.8 was based on earlier publications of Aime *et al.*[146] and Parker *et al.*[265] Cyclen (0.200 g, 7.40×10^{-4} mol) and potassium carbonate (0.6610 g, 4.79×10^{-4} mol) was placed in a two neck round-bottom flask under argon. To this, *N*-methyl chloro-acetamide (0.5500 g, 5.14×10^{-3} mol) was added followed by 20 ml of dried ethanol transferred using a gas tight syringe. (Care was taken to make sure that during the transfer process, the flask was kept under argon atmosphere). The mixture was heated to reflux for 48 hours at 90 °C. Upon cooling excess potassium carbonate was filtered off and the solvent was removed under reduced pressure. The residue was taken up in hot ethanol, cooled and filtered. The target **4** namely 1,4,7,10-Tetrakis(methylcarbamylmethyl)-1,4,7,10-tetraazacyclodecane (or simply DTMA) was further dried under reduced pressure and isolated in 100 % yield (0.3382 g, 7.41×10^{-4} mol).

Empirical Formula: $C_{20}H_{40}N_8O_4$

^{1}H NMR (D_2O): δ 2.65-2.75 (s, CH_2, 16H), δ 2.75-2.85 (s, CH_3, 12H), δ 3.05-3.25 (s, CH_2, 8H).

^{13}C NMR (D_2O): δ 177.19 (s, CO, 1C), δ 60.34 (CH_2 methylene), δ 54.59 (CH_2 cyclen ring), δ 28.20 (CH_3 acetamide arms).

ESI-MS (+): $[M + H]^+$ = m/z (457), $[M + Na]^+$ = m/z (479) and $[M + K]^+$ = m/z (495).

m/e (relative intensity of free ligand): 456.32 (100.0%), 457.32 (23.0%), 458.32 (3.9%), 457.31 (3.0%).

m/e (relative intensity of Na complex): 479.307 (100.0%), 480.310 (22.2%), 480.304 (3.0%), 481.314 (2.4%).

m/e (relative intensity of K complex): 495.281 (100.0%), 496.284 (22.2%), 497.279 (7.2%), 496.278 (3.0%), 497.288 (2.4%), 498.282 (1.6%)

FTIR: C-H_{bend} (medium, sharp) 1406.83cm^{-1},C=O_{str} : (strong, sharp) 1670.02cm^{-1}, N-H_{str}: (strong, broad) 2864.65 cm^{-1}, O-H_{str}: (strong, broad) 3345.68cm^{-1}.

Melting point (m.p) 222-224 °C

2.2.4 Synthesis of Eu^{3+} and Gd^{3+} Macrocyclic Complexes

2.2.4.1 Metal Complexation of 1,4,7-tris[*N*-methylcarbamylmethyl]-10-(2-hydroxycyclohexyl)-1,4,7,10-tetraazacyclododecane with Europium

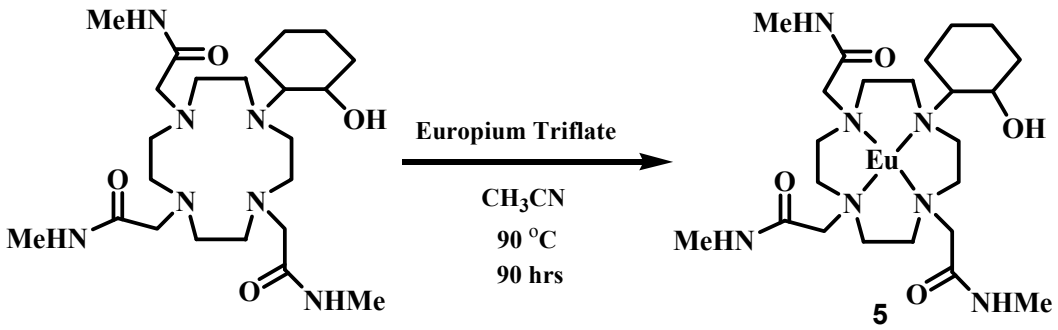


Figure 2.9: Preparation of Europium-1,4,7-tris[*N*-methylcarbamylmethyl]-10-(2-hydroxycyclohexyl)-1,4,7,10-tetraazacyclododecane (**5**).

This ligand complexation reaction scheme shown above in Figure 2.9 was based on work performed by Parker and coworkers.[265] Europium triflate (0.4141 g, 6.90×10^{-4} mol) was dissolved in dry acetonitrile to give a 0.02 M solution. 1-(2-hydroxycyclohexyl)-4,7,10-tris-(acetamide)-1,4,7,10-tetraazacyclodecane (0.300 g, 6.21×10^{-4} mol) was dissolved in dry acetonitrile to give a 0.03 M solution. This was added to the triflate solution via a dropping funnel under argon. The solutions were allowed to react in a 1.1:1 molar ratio. The mixture was refluxed at 90 °C for 90 hrs under a $CaCl_2$ drying tube. Upon completion of the reaction, the solvent was removed to dryness under reduced pressure. The crude product was redissolved in a minimal amount of dry acetonitrile to which diethyl ether was added dropwise until the solution

became turbid. Refrigeration overnight afforded Europium-1,4,7-tris[*N*-methylcarbamylmethyl]-10-(2-hydroxycyclohexyl)-1,4,7,10-tetraazacyclododecane (0.6284 g, 5.81×10^{-4} mol) and was isolated in 94 % yield as a triflate salt.

^{1}H NMR (D_2O): The spectrum showed the presence of the paramagnetic center characteristically indicated by several broad resonances appearing over a large ppm range as in the case of compound **5** these appeared at 27.785, 25.484, 22.741, 19.378 (axial protons on cyclen ring), 10.264 to -6.150 (equatorial protons on the cyclen ring and CH_3 protons of pendant arms) -6.150 to -16.768 (CH_2 protons on pendant arms).

FTIR: C-H_{bend} (weak, sharp) 1407.43 cm^{-1}, C=O_{str} :(strong, sharp) 1631.83 cm^{-1}, N-H_{str}: (weak, broad) 2949.60 cm^{-1}, C-H_{str}: (weak, broad) 2800-3100 cm^{-1} O-H_{str}: (weak, broad) 3293.37 cm^{-1}.

ESI-MS (+): $[M + 2H]^{2+}$ = m/z (318), $[M + 1TfO]^{+}$ = m/z (784), $[M + 2TfO]^{+}$ = m/z (934).

m/e (relative intensity): 785.23 (100.0%), 783.23 (86.8%), 786.23 (27.5%), 784.23 (24.0%), 787.23 (5.8%), 787.22 (4.3%), 785.22 (3.9%), 786.22 (3.6%), 784.22 (2.9%), 788.23 (1.7%)

2.2.4.2 Metal Complexation of 1,4,7-tris[*N,N*-dimethylcarbamylmethyl]-10-(2-hydroxycyclohexyl)-1,4,7,10-tetraazacyclododecane with Europium

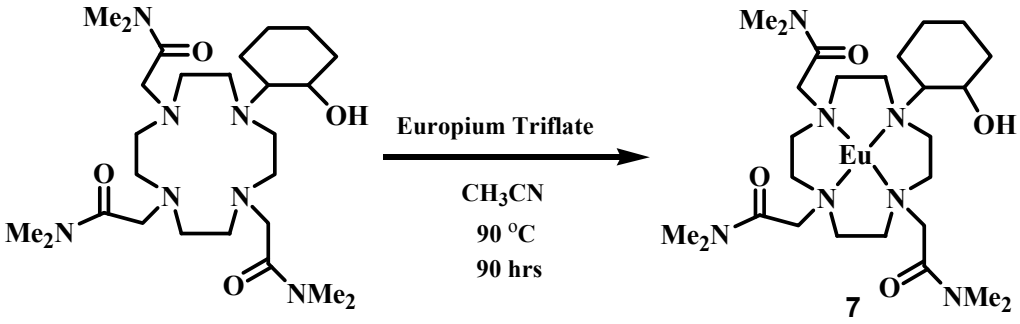


Figure 2.10: Reaction scheme showing preparation of Europium-1,4,7-tris[*N,N*-dimethylcarbamylmethyl]-10-(2-hydroxycyclohexyl)-1,4,7,10-tetraazacyclododecane (**7**).

The complexation reaction scheme shown in Figure 2.10 was based on work performed by Parker and co-workers[265] as mentioned earlier. Europium triflate (0.3485 g, 58 mmol) was dissolved in dry acetonitrile to give a 0.02 M solution. The hydrochloride salt of 1,4,7-tris[*N,N*-dimethylcarbamylmethyl]-10-(2-hydroxycyclohexyl)-1,4,7,10-tetraazacyclododecane (0.3055 g, 0.45 mmol) (**3**) was dissolved in dry acetonitrile to give a 0.03 M solution. This was added to the triflate solution via a dropping funnel under argon. The solutions were allowed to react in a 1.3:1 molar ratio. The mixture was refluxed at 90 °C for 90 hrs under a $CaCl_2$ drying tube. Upon completion of the reaction, the solvent was removed to dryness under reduced pressure. The crude product was redissolved in a minimal amount of dry acetonitrile to which diethyl ether was added dropwise until the solution became turbid. The flask was stopped and placed in the refrigerator overnight and allowed to crystallise. No crystallization occurred and the product was redissolved in acetonitrile. Further attempts to crystallize using diethyl ether and benzene were unsuccessful. The solvent was removed and further dried under reduced pressure. A minimal amount of water (5 ml) was used to redissolved the product and 20% NH_4OH was added dropwise until the solution reached a pH of 10. The solution was filtered using a celite plug to remove the excess europium as $Eu(OH)_3$. The filtrate was further frozen using liquid nitrogen and lyophilised to give a yellow oily resin. The Europium-1,4,7-tris[*N,N*-dimethylcarbamylmethyl]-10-(2-hydroxy-cyclohexyl)-1,4,7,10-tetraazacyclododecane product (**7**) isolated in 98 % yield (0.3003 g, 0.45 mmol).

^{1}H NMR (D_2O): The spectrum showed the presence of the paramagnetic center characteristically indicated by several broad resonances appearing over a large ppm range as in the case of compound **7** these appeared at 32.433, 29.149, 27.248, 22.870, (axial protons on cyclen ring), 12.443 to -9.217, (equatorial protons on the cyclen ring and CH_3 protons of pendant arms) -9.217 to -18.146, (CH_2 protons on pendant arms).

ESI-MS (+): $[M + 2H]^{2+}$ = m/z (414), $[M + 2TfO]^+$ = m/z (976), $[M + 2TfO]^+$ = m/z (976).

m/e (relative intensity): 827.27 (100.0%), 825.27 (87.2%), 828.28 (30.5%), 826.28 (27.1%), 829.28 (6.1%), 827.28 (5.3%), 829.27 (5.3%), 828.27 (4.5%), 826.27 (3.0%), 830.27 (1.4%), 830.28 (1.0%).

2.2.4.3 Metal Complexation of 1,4,7,10-Tetrakis(methylcarbamylmethyl)-1,4,7,10-tetraazacyclodecane with Europium

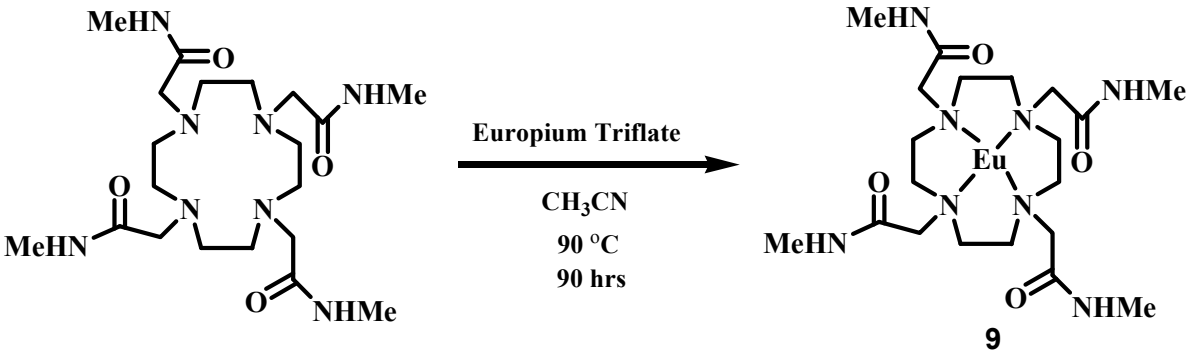


Figure 2.11: Preparation of Europium-1,4,7,10-Tetrakis-(methylcarbamylmethyl)-1,4,7,10-tetraazacyclodecane (**9**).

The complexation reaction scheme shown in Figure 2.11 toward the syhthesis of molecule **9** was successfully accomplished. Europium triflate (0.3610 g, 6.02×10^{-4} mol) was dissolved in dry acetonitrile to give a 0.02 M solution. (0.207 g, 4.54×10^{-4} mol) DTMA was also dissolved in dry acetonitrile to give a 0.03 M solution. The europium triflate and DTMA react in a 1.3:1 molar ratio. The triflate solution was placed in a flask and the DTMA solution added dropwise via a dropping funnel under argon. The solution was then refluxed at 90 °C for 90 hrs under a $CaCl_2$ drying tube. Upon completion of the reaction, the acetonitrile was removed under reduced pressure. The crude product was redissolved in a minimal amount of dry acetonitrile (5 ml) to which diethyl ether was added dropwise until the solution became turbid. Refrigeration overnight afforded the product, **9**, (0.4747 g, 4.49×10^{-4} mol) in 99% yield.

^{1}H NMR (D_2O): The spectrum showed the presence of the paramagnetic center characteristically indicated by several broad resonances appearing over a large ppm range as in the case of compound **9** these appeared at 26.908 (axial protons on cyclen ring), 7.00 to 0, (equatorial protons on the cyclen ring and CH_3 protons of pendant arms) -15.00 to 0, (CH_2 protons on pendant arm).

FTIR: C-H_{bend} (weak, broad) 1459.94cm^{-1}, N-H_{str}: (weak, broad) 2873.21cm^{-1}, O-H_{str}: (weak, broad) 3341.11cm^{-1}.

ESI-MS (+): $[M - H]^+$ = m/z (607), $[M + 1TfO]^+$ = m/z (757), $[M + 2TfO]^+$ = m/z (907)

m/e (relative intensity): 758.19 (100.0%), 756.19 (89.7%), 759.19 (27.9%), 757.19 (24.6%), 760.19 (6.8%), 758.18 (4.0%), 760.20 (2.8%), 758.20 (2.5%), 761.19 (1.2%), 759.20 (1.1%)
Melting point (m.p) 264-266 °C

2.2.4.4 Metal Complexation 1,4,7-tris[*N*-methylcarbamylmethyl]-10-(2-hydroxycyclohexyl)-1,4,7,10-tetraazacyclododecane with Gadolinium

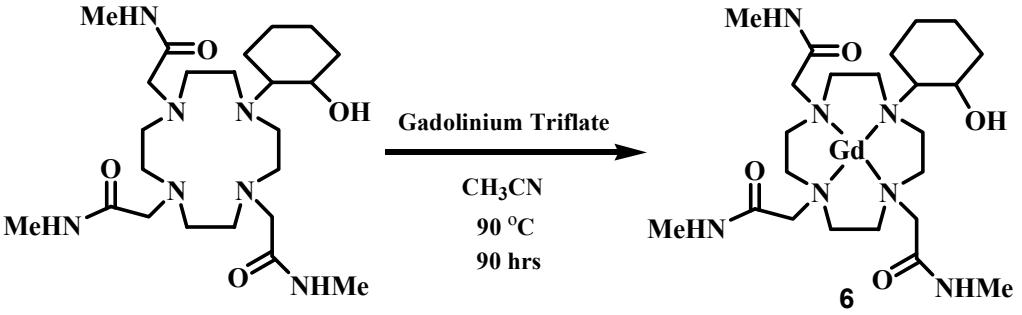


Figure 2.12: Preparation of Gadolinium-1,4,7-tris[*N*-methylcarbamylmethyl]-10-(2-hydroxycyclohexyl)-1,4,7,10-tetraazacyclododecane (**6**).

The gadolinmium complexation reaction scheme shown in Figure 2.12 adopts the same protocol as for europium complexation. Gadolinium triflate (0.4587 g, 7.58×10^{-4} mol) was dissolved in dry acetonitrile to give a 0.02 M solution. The hydrochloride salt of 1,4,7-tris[*N*-methylcarbomylmethyl]-10-2-(hydroxycyclohexyl)-1,4,7,10-tetraazacyclododecane (0.3243g, 6.71×10^{-4} mol) was also dissolved in dry acetonitrile to give a 0.03 M solution. The gadolinium triflate and ligand react in a 1.1:1 molar ratio. The triflate solution was placed in a flask and the ligand added dropwise via a dropping funnel under argon. The solution was then refluxed at 90 °C for 90 hrs under a $CaCl_2$ drying tube. Upon completion of the reaction, the acetonitrile was removed under reduced pressure. The crude product was redissolved in a minimal amount of dry acetonitrile to which diethyl ether was added dropwise until the solution became turbid. Refrigeration overnight afforded **6** (0.7341 g, 6.65×10^{-4} mol), which is a triflate salt in 99% yield.

ESI-MS (+): $[M + 2H]^{2+}$ = m/z (395), $[M + 1TfO]^{+}$ = m/z (789), $[M + 2TfO]^{+}$ = m/z (939)

2.2.4.5 Metal Complexation of 1-(2-hydroxycyclohexyl)-4,7,10-tris-(*N'*-*N'*-dimethyl-acetamide)–1,4,7,10-tetra-azacyclodecane with Gadolinium

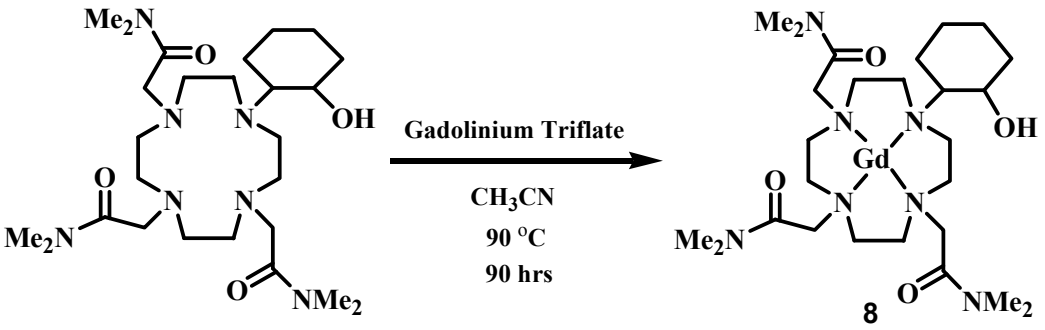


Figure 2.13: Preparation of Gadolinium-11,4,7-tris[*N,N*-dimethylcarbamylmethyl]-10-(2-hydroxycyclohexyl)-1,4,7,10-tetraazacyclododecane (**8**).

Similarly, the gadolinmium complexation reaction scheme shown in Figure 2.13 adopts the same protocol as for europium complexation. Gadolinium triflate (0.4851 g, 0.80 mmol) was dissolved in dry acetonitrile to give a 0.02 M solution. The hydrochloride salt of 1,4,7-tris[*N,N*-dimethylcarbamylmethyl]-10-(2-hydroxycyclohexyl)-1,4,7,10-tetraazacyclododecane (0.2960 g, 0.47 mmol) was also dissolved in dry acetonitrile to give a 0.03 M solution. The gadolinium triflate and ligand react in a 1.1:1 molar ratio. The triflate solution was placed in a flask and the ligand added dropwise via a dropping funnel under argon. The solution was then refluxed at 90 °C for 90 hrs under a $CaCl_2$ drying tube. Upon completion of the reaction, the acetonitrile was removed under reduced pressure. The crude product was redissolved in a minimal amount of dry acetonitrile to which diethyl ether was added dropwise until the solution became turbid. The flask was stopped and placed in the refrigerator overnight and allowed to crystallize. No crystallization occurred and the product was redissolved in acetonitrile. Further attempts to crystallize using diethyl ether and benzene were unsuccessful. The solvent was removed and further dried under reduced pressure. A minimal amount of water (5 ml) was used to redissolved the product and 20% NH_4OH was added dropwise until the solution reached a pH of 8.6. The solution was filtered through a celite plug to remove the excess gadolinium as $Gd(OH)_3$. The product, **8**, was isolated as a yellow amorphous solid in 82 % yield (0.2466 g, 0.385 mmol).

ESI-MS (+):Mol. Wt.: 682.98 $g.mol^{-1}$, $[M + 2TfO]^+$ = m/z (982).

m/e (relative intensity): 981.23 (100.0%), 979.23 (91.4%), 983.23 (81.5%), 980.26 (55.7%), 978.23 (55.2%), 982.23 (36.7%), 984.23 (30.5%), 980.23 (29.1%), 981.26 (19.7%), 985.23 (8.6%), 983.22 (8.5%), 977.23 (7.8%), 980.22 (6.8%), 981.22 (6.7%), 982.26 (5.7%), 985.24 (5.7%), 983.24 (4.8%), 982.27 (3.9%), 986.23 (2.5%), 979.22 (2.1%), 984.24 (2.0%), 983.26 (1.7%), 986.24 (1.1%)

2.3 Solution Chemistry of Complexes with Lanthanides

2.3.1 General Apparatus and Materials

2.3.1.1 pH Measurements and Calibration of pH meter

pH measurements were performed using a Metrohm 813 pH meter and a 6.0234 combination glass electrode. The instrument was calibrated against the standard N.I.S.T buffers pH 4 and pH 7 obtained from Sigma Aldrich at 25.0 °C. After calibration, the pH was tested with the pH 9 standard buffer to observe accuracy.

2.3.1.2 Preparation of Standard Solutions

A 0.1 M standard NaOH ampoule (purchased from VWR suppliers) was emptied into a dry clean 1 L volumetric flask and made up to mark. This standard solution was further used in preparation of 0.05 M NaOH standard solution by transferring 500 ml into a 1 L volumetric flask. Similarly, a 0.1 M standard HNO_3 ampoule (also purchased from VBH) was emptied into a dry clean 1 L volumetric flask and made up to mark. This standard solution was further used in preparation of 0.05 M HNO_3 standard solution by transferring 500 ml into a 1 L volumetric flask. These solutions were standardized by titrating against a known concentration of potassium hydrogen phthalate (KHP) with NaOH and then with HNO_3 with NaOH as a titrant. Each standard solution used in this study was prepared such that the ionic strength was 0.1 M; for this an appropriate amount of anhydrous $NaNO_3$ was used for ionic strength adjustment. The KHP solution was used to determine the concentrations of other standard solutions (where indicated) by means of an acid-base titration, using phenolphthalein as an indicator.

2.3.2 Luminescence Studies and UV-visible Studies: Determination of Spectroscopic pK_as of Europium Complexes in Multicomponent Buffer Solutions (MCB)

Luminescence measurements for the three target Eu^{3+} complexes were recorded using a Varian Cary Eclipse Fluorescence Spectrophotometer with software v.5.1 using Hellma quartz SUPRASIL® cells (type: 111-QS, path length = 10 mm). The excitation wavelength to be used for the luminescence study was determined from UV-Visible absorbance spectra, obtained using a Varian Cary 3E UV-Visible Spectrophotometer, using Hellma quartz SUPRASIL® cells (type: 110-QS, path length = 10 mm). Combined luminescence-absorption pH titrations were carried on solutions with absorbances < 0.3 at wavelengths ≥ λ_{ex} to avoid errors due to the inner filter effect. Luminescence spectra for the complexes were obtained by exciting at 240 nm. Points were recorded at 1 nm intervals with 0.1 s integration time. The pH was raised accordingly in 0.25 value increments across the pH range 2 to 12 using a solution of saturated NaOH and 2 ml aliquots of the solution were decanted at each pH and left to equilibrate for 96 hrs. The phosphorescence emission and absorbance spectra were then recorded as a function of pH with approximately 35-40 points per titration. Standard lease square techniques using suitable programs, namely CURVEFIT[266] or in some cases Sigmaplot[267] were used to determine deprotonation constants from absorbance and luminescence intensity data.

The experimental data were fitted using a non-linear least-squares program employing a Newton-Raphson procedure to a binding isotherm (Equations 2.1 to 2.4), which is relevant when one to four acid/base equilibria are present.

$$I_T = \frac{I_1*[H^+] + I_2*[H^+]*K_1}{K_1 + [H^+]} \quad (2.1)$$

$$I_T = \frac{I_1*[H^+]^2 + I_2*[H^+]*K_1 + I_3*K_1*K_2}{K_1*K_2 + [H^+]*K_1 + [H^+]^2} \quad (2.2)$$

$$I_T = \frac{I_1*[H^+]^3 + I_2*[H^+]^2*K_1 + I_3*[H^+]*K_1*K_2 + I_4*K_1*K_2*K_3}{K_1*K_2*K_3 + [H^+]*K_1*K_2 + [H^+]^2*K_1 + [H+]^3} \quad (2.3)$$

$$I_T = \frac{I_1*[H^+]^4 + I_2*[H^+]^3*K_1 + I_3*[H^+]^2*K_1*K_2 + I_4*[H^+]*K_1*K_2*K_3 + I_5*K_1*K_2*K_3*K_4}{K_1*K_2*K_3*K_4 + [H^+]*K_1*K_2*K_3 + [H^+]^2*K_1*K_2 + [H^+]^3*K_1 + [H^+]^4} \quad (2.4)$$

In Equations 2.1 to 2.4, I_T is the intensity at the J = 0, 1, 2, 3, and 4 monitoring wavelength, K_1 to K_4 are the acid dissociation constants and I_i is the intensity of the ith species.

2.3.2.1 Preparation of Europium Complexes in Multicomponent Buffer (MCB) with Potassium Hydrogen Phthalate (KHP)

2.3.2.1.1 Europium-1,4,7-tris[*N*-methylcarbamylmethyl]-10-(2-hydroxycyclohexyl)-1,4,7,10-tetraazacyclododecane (5)

Initially, the pH of deionised water (250-260 ml) was reduced using conc. HCl to a pH of < 2. This initial acidification of deionised water was carried out for all luminescence solution studies. Molecule **5** (0.1395 g, 5.15×10^{-4} M), KHP (0.05218 g, 1.02 mM), Tris (0.0712 g, 2.35 mM), CHES (0.0548 g, 1.06 mM), MES (0.0496g, 1.02 mM) and MOPS (0.0553 g, 1.06 mM) were carefully added to an empty A grade 250 ml volumetric flask and filled up to mark with the aforementioned acidified solution. For all luminescence studies that followed the weighing vials were re-measured to ensure the correct masses were indeed transferred and the pH was raised in

0.25 increments per pH unit using small amounts a saturated solution of NaOH to minimize the effects of dilution.

2.3.2.1.2 Europium-1,4,7,10-Tetrakis(methylcarbamylmethyl)-1,4,7,10-tetraazacyclodecane (9)

Molecule **9** (0.1368 g, 5.18×10^{-4} M), KHP (0.05218 g, 1.02 mM), Tris (0.0711 g, 2.35 mM), CHES (0.05461 g, 1.05 mM), MES (0.0499g, 1.02 mM), MOPS (0.0556 g, 1.06 mM) were carefully added to an empty A grade 250 ml volumetric flask and filled up to mark with acidified solution. Solutions were made basic by addition of small amounts of saturated NaOH in 0.25 increments per pH unit across the pH range 2 to 12.

2.3.2.2 Preparation of Europium Complexes in MCB excluding KHP

2.3.2.2.1 Preparation of Europium-1,4,7-tris[*N*-methylcarbamylmethyl]-10-(2-hydroxycyclohexyl)-1,4,7,10-tetraazacyclododecane (5)

Molecule **5** (0.1589 g, 5.87×10^{-4} M), Tris (0.0722 g, 2.38 mM), CHES (0.0564 g, 1.09 mM), MES (0.0531g, 1.09 mM), MOPS (0.0531 g, 1.08 mM) were carefully added to an empty A grade 250 ml volumetric flask and filled to mark with the acidified solution. Similarly, solutions were made basic by addition of small amounts of saturated NaOH in 0.25 increments per pH unit across the pH range 2 to 12.

2.3.2.2.2 Preparation of Europium-1,4,7-tris[*N'*-*N'*-dimethylcarbamylmethyl]-10-(2-hydroxycyclohexyl)-1,4,7,10-tetraazacyclododecane (7)

Molecule **7** (0.1650 g, 5.92×10^{-4} M), Tris (0.0721 g, 2.38 mM), CHES (0.0565 g, 1.10 mM), MES (0.0532g, 1.09 mM), MOPS (0.0533 g, 1.08 mM) were carefully added to an empty A grade 250 ml volumetric flask and filled to mark with the acidified solution. Likewise, solutions were made basic by addition of small amounts of saturated NaOH in 0.25 increments per pH unit across the pH range 2 to 12.

2.3.2.2.3 Preparation of Europium-1,4,7-tris[*N*-methylcarbamylmethyl]-10-(2-hydroxycyclohexyl)-1,4,7,10-tetraazacyclododecane Complex (5) in Water

Molecule **5** (0.1611 g, 5.95×10^{-4} M) was carefully added to an empty A grade 250 ml volumetric flask and filled to mark with the acidified solution. Again, solutions were made basic by addition of small amounts of saturated NaOH in 0.25 increments per pH unit across the pH range 2 to 12.

All Spectroscopic Data are found in Appendix E (See Data Disc)

2.3.3 Luminescent Lifetime Measurements on Europium-1,4,7-tris[*N*-methyl-carbamylmethyl]-10-(2-hydroxycyclohexyl)-1,4,7,10-tetraazacyclododecane (5): Determination of *q*

Luminescence lifetime measurements were measured using a Varian Cary Eclipse Fluorescence Spectrophotometer with software v.5.1 using a Hellma quartz SUPRASIL® cells (type: 111-QS, path length = 10 mm) in lifetime scan mode using a Phosphorescence Life Time (Short) setting with an excitation wavelength, λ_{ex} = 240 nm and the emission of Eu^{3+} complexes were detected at 580 nm. The complexes were thoroughly dried under vacuum for a day prior to the measurements. The concentrations of the solutions were *ca.* 5.00×10^{-4} M to 6.00×10^{-4} M. The lifetime data were processed using the build in software program on a Varian Cary Eclipse Fluorescence Spectrophotometer, by fitting the decay curves to a mono-exponential equation, $\boldsymbol{I = I_0^{(-\,tk\,)}}$. The natural log of the average intensity of the scans was plotted against time and the slope was used as the decay rate. This was performed in water and D_2O. All fits showed a standard deviation of < 10 %. The revised **Equation 3.1 and 3.2** was used to calculate *q* values at 580 nm.[221-224,268]

$$\boldsymbol{q = 1.11(k_{H_2O} - k_{D_2O} - 0.985)} \quad \textbf{.....Equation 3.1}$$

$$\boldsymbol{q = 1.11(k_{H_2O} - k_{D_2O} - 0.965)} \quad \textbf{.....Equation 3.2}$$

2.3.3.1.1 Preparation of Europium-1,4,7-tris[*N*-methylcarbamylmethyl]-10-(2-hydroxycyclohexyl)-1,4,7,10-tetraazacyclododecane (5) Solutions in Water (H_2O)

2.3.3.1.2 Europium-1,4,7-tris[*N*-methylcarbamylmethyl]-10-(2-hydroxycyclohexyl)-1,4,7,10-tetraazacyclododecane (5) in MCB with KHP in Water

The same solutions used for the luminescence studies in Sections 2.3.2.1.1 were utilized for this study. Specifically, the pH of the solutions analyzed were: 4.710, 5.320, 7.423, 8.172, 8.710, 9.382 and 9.484, respectively.

2.3.3.1.3 Europium-1,4,7-tris[*N*-methylcarbamylmethyl]-10-(2-hydroxycyclohexyl)-1,4,7,10-tetraazacyclododecane (5) in Water

The same solutions used for the luminescence studies in Sections 2.3.2.3 were utilized for this study. Specifically, the pH of the solutions analyzed were: 4.375, 4.795, 8.275 and 8.645, respectively.

2.3.3.2 Preparation of Europium-1,4,7-tris[*N*-methylcarbamylmethyl]-10-(2-hydroxycyclohexyl)-1,4,7,10-tetraazacyclododecane (5) Solutions in Deuterated Water (D_2O)

2.3.3.2.1 Europium-1,4,7-tris[*N*-methylcarbamylmethyl]-10-(2-hydroxycyclohexyl)-1,4,7,10-tetraazacyclododecane (5) in Multi-component Buffer with KHP

Similar to preparations in water, the pH of deuterated water (*ca.* 25-26 ml) was reduced using conc. DCl to a pH of < 2. This initial acidification of deuterated water was carried out for all luminescence lifetime studies. A six figure balance was utilized for the preparation of D_2O solutions. **5** (0.016163 g, 5.97×10^{-4} M), KHP (0.005494 g, 1.08 mM), Tris (0.0070769 g, 2.34 mM), CHES (0.005339 g, 1.03 mM), MES (0.005259g, 1.08 mM), MOPS (0.005317 g, 1.02 mM) were carefully added to an empty A grade 25 ml volumetric flask and filled up to mark with the aforementioned acidified D_2O solution. The weighing paper for each compound was re-measured to ensure the correct masses were indeed transferred. The pH was adjusted accordingly using sodium deuteroxide (NaOD) in a thermostated cell equipped with a stirrer bar

set at 25.0 ± 0.2°C. The following pH solutions were analyzed: 4.695, 5.321, 7.424, 8.174, 8.714, 9.382 and 9.485.

2.3.3.2.2 Europium-1,4,7-tris[*N*-methylcarbamylmethyl]-10-(2-hydroxycyclohexyl)-1,4,7,10-tetraazacyclododecane (5) in Deuterated Water

5 (0.016292 g, 6.02 ×10-4 M), was carefully added to an empty A grade 25 ml volumetric flask and filled up to mark with the acidified D_2O solution. Again, the weighing paper for the complex was re-measured to ensure the correct mass was indeed transferred. The pH was raised accordingly using sodium deuteroxide (NaOD) in a thermostated cell equipped with a stirrer bar set at 25.0 ± 0.2°C. The following pH solutions were analyzed: 4.375, 4.799, 8.298 and 8.646, respectively.

All Lifetime Data are found in Appendix F (See Data Disc)

2.3.4 Using Cyclic Voltammetry to Observe Solution Behavior of Europium Complexes

Cyclic voltammetry (CV) was performed using an Autolab PGSTAT10 potentiostat (EcoChemie B. V., Netherlands) and contolled by GPES (General purpose electrochemical systems, GPES AUTOLAB software, v. 4.5, Eco EcoChemie B. V., Netherlands, 1997). The scan rate was varied between 10 -1000 mV s^{-1}. A 5 mm diameter glassy carbon electrode was used as the working electrode. The electrode surface was prepared on a regular basis by polishing it with a 6 micron diamond paste followed by sonication. Ag/AgCl was used as the reference electrodes and the Pt wire as the auxiliary electrode. All CV experiments were performed on 5 cm^3 of 5.15×10^{-4} $mol.dm^{-3}$ solution of the europium complexes in 1×10^{-3} $mol.dm^{-3}$ (2×10^{-3} $mol.dm^{-3}$ for Tris) under nitrogen atmosphere in a thermostated cell (25.0 ± 0.2°C).[269, 270]

2.3.4.1 Preparation of Multi-component Buffer with Europium Complexes

2.3.4.1.1 Europium-1,4,7-tris[*N*-methylcarbamylmethyl]-10-(2-hydroxycyclohexyl)-1,4,7,10-tetraazacyclododecane (5)

The pH of the solutions were determined using a Metrohm 813 pH meter calibrated against standard buffer solutions and adjusted with HCl or NaOH, as appropriate. Initially, the pH of deionised water (250-260 ml) was reduced using conc. HCl to a pH of < 2. This initial acidification of deionised water was carried out for all cyclic voltammetry solution studies. **5** (0.1395 g, 5.15×10^{-4} M), KHP (0.05218 g, 1.02 mM), Tris (0.0712 g, 2.35 mM), CHES (0.0548 g, 1.06 mM), MES (0.0496g, 1.02 mM), MOPS (0.0553 g, 1.06 mM) were carefully added to an empty A grade 250 ml volumetric flask and filled up to mark with the acidified solution. The weighing vials were re-measured to ensure the correct masses were indeed transferred. For this electrochemical study, 100 ml of the solution was placed into a thermostated cell equipped with a stirrer bar and connected to a circulating water bath set at 25.0 ± 0.2°C. The pH was raised in 0.25 value increments accordingly using a solution of saturated NaOH and 2 ml aliquots of the solution were decanted at each pH and left to equilibrate for 96 hrs. The following pH solutions were selected and analyzed: 3.221, 6.294, 8.731 and 11.847.

2.3.4.1.2 Europium-1,4,7,10-Tetrakis(methylcarbamylmethyl)-1,4,7,10-tetraazacyclodecane (4)

Molecule **4** (0.1368 g, 5.18×10^{-4} M), KHP (0.05218 g, 1.02 mM), Tris (0.0711 g, 2.35 mM), CHES (0.05461 g, 1.05 mM), MES (0.0499g, 1.02 mM), MOPS (0.0556 g, 1.06 mM) were carefully added to an empty A grade 250 ml volumetric flask and filled up to mark with acidified solution as mentioned earlier. Similarly, the weighing vials were re-measured to ensure the correct masses were indeed transferred. As before, 100 ml of the solution was placed into a thermostated cell equipped with a stirrer bar and connected to a circulating water bath set at 25.0 ± 0.2°C. The pH was raised in 0.25 value increments accordingly using a solution of saturated NaOH and 2 ml aliquots of the solution were decanted at each pH and left to equilibrate for 96 hrs. The following pH solutions were selected and analyzed: 3.201, 6.212, 8.657 and 11.856.

All CV Data are found in Appendix H (See Data Disc)

Chapter Three Results and Discussion

3.1 Synthetic Comments

3.1.1 Synthesis of Precursors

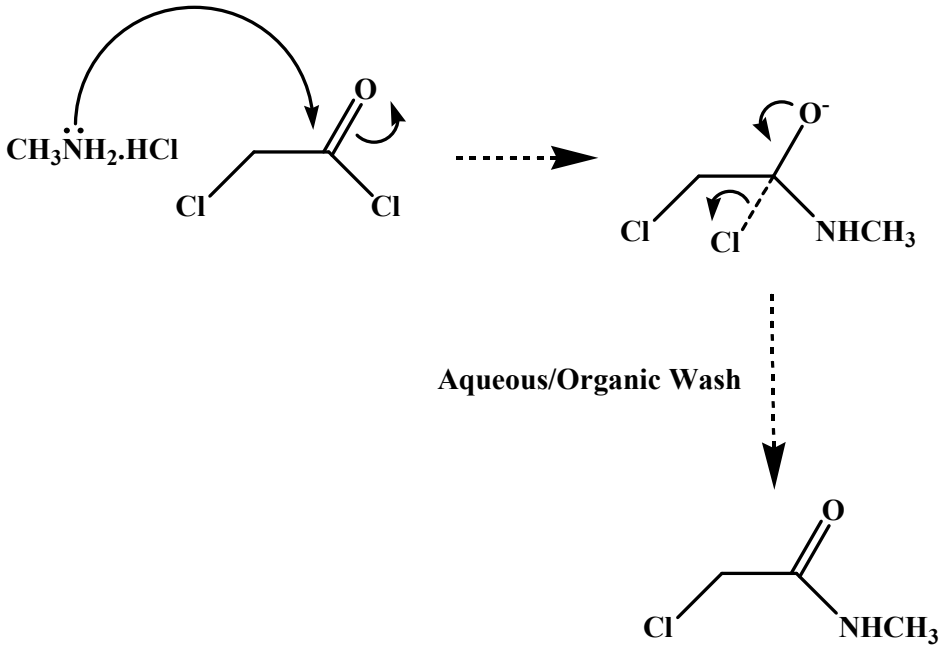


Figure 3.1: Mechanism of Reaction Toward Target Precursors.

The target product *N*-methyl-chloroacetamide was successfully synthesized by a nucleophilic acyl substitution reaction. The mechanism of reaction toward the target α-chloroacetamide is illustrated in the above reaction scheme Figure 3.1. The nucleophile methylamine hydrochloride must be deprotonated first before it adds onto the carbonyl of the chloroacetyl chloride, but initially forms a tetrahedral intermediate which was not isolated. Because the chloroacetyl chloride has a leaving group in the form of a chloride, the tetrahedral intermediate can further react by expelling the chloride. The white solid was produced in 48% yield. For the target *Di*-methyl-chloroacetamide the same mechanism applies and the product was formed in a yield of 66%. It was noted that during the synthesis care had to be taken to ensure the rate of addition of chloroacetyl chloride was slow and that the flask it was added to had been in an ice /ethanol-bath for approximately 10-15 mins prior to addition. These small changes optimized the yield and ensured exclusive formation of the product.

3.1.2 Synthesis of *β*-amino alcohol Intermediate: 1-(2-Hydoxycyclohexyl)-1,4,7,10-tetraazacyclodecane

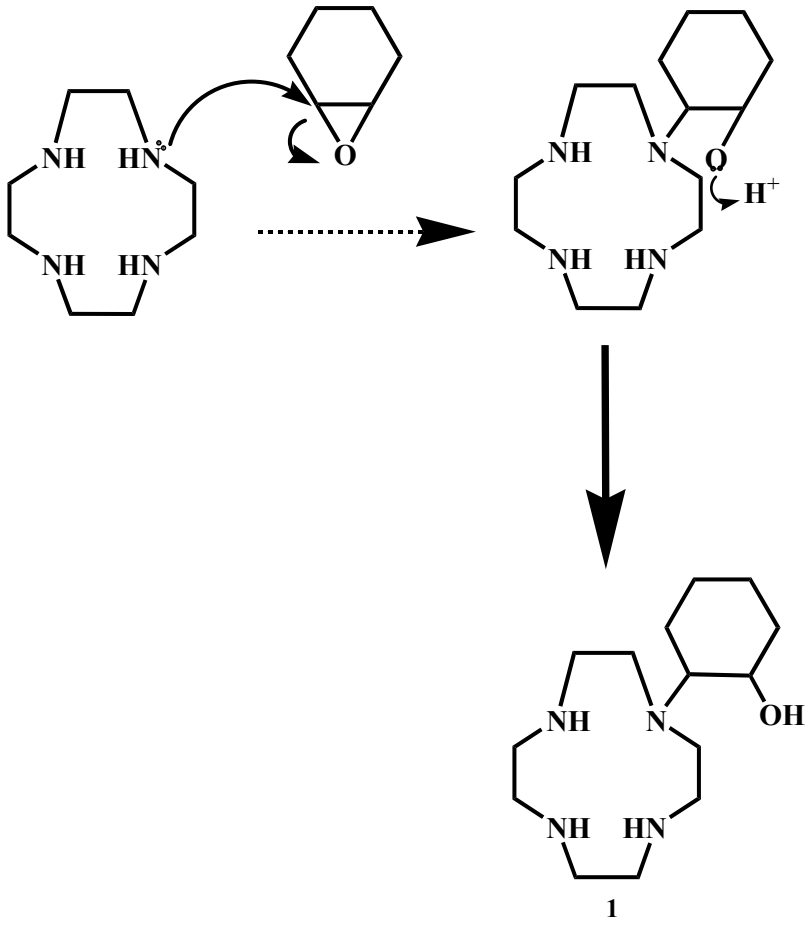


Figure 3.2: Mechanism of Reaction Toward Target Intermediate.

The target product 1-(2-hydoxycyclohexyl)-1,4,7,10-tetraazacyclodecane, **1**, was successfully synthesized by a nucleophilic addition reaction. The mechanism of reaction toward the target intermediate 1 is illustrated in the above reaction scheme in Figure 3.2. Using a 10% excess of cyclohexene oxide to the tetraazamacrocycle cyclen, adds on a single cyclohexene oxide to give the target. This is a useful result, as it leaves three nitrogen donors free for substitution with donor groups like acetamides. An amine lone pair proceeds to react with the carbocation on the epoxide alpha to the oxygen. This results in ring opening of the expoxide and formation of the *β*-amino alkoxide intermediate which further reacts with H^+ in the ethanol to form the *β*-amino alcohol. The clean white crystalline solid was needle like and produced in 27% yield. It was

noted that during the synthesis care was taken to ensure that the trituration process was executed with minimal amounts of acetone and recrystallization several times was key in achieving the product exclusively in reasonable yield. Using cold acetone or acetone at room temperature did not affect the overall yield.

3.1.3 Synthesis of *N*-substituted Cyclen based Ligands

The target ligand was successfully synthesized by base catalyzed nulceophilic addition reaction and the reaction mechanism is shown in Figure 3.3. The amine lone pairs react with the carbon alpha to the carbonyl as it is more positively charged and subsequently expels the chloride leaving group. The crystalline solid was beige/to off white color and produced in 99% yield. The *N*-methyl chloroacetamide was reacted with 1,4,7-tris[*N*-methylcarbamylmethyl]-10-(2-hydroxycyclohexyl)-1,4,7,10-tetraazacyclododecane in 3.3:1 ratio. Care was taken to wash the crude product thoroughly with diethyl ether to remove any unreacted cyclen to afford the target product exclusively. The *Di*-methyl derivative was also successfully produced employing the same mechanism in 97% yield with five equivalents of *Di*-methyl chloroacetamide. Using the same ratios for the *Di*-methyl was not adequate toward the synthesis of target **3** which resulted in mixtures of bi- and tri-substituted derivatives. The same reaction mechanism also applies to the synthesis of **4** which was a synthesized as a white crystalline solid in 100% yield. The major difference between the two preceding reactions and this one is the use of K_2CO_3 as a base and the absence of the KI which is the non participating halogen exchange agent. The product yields are much higher than those reported by Tsukube *et. al.*[68] who achieved 26% yield after purification by column chromatography.

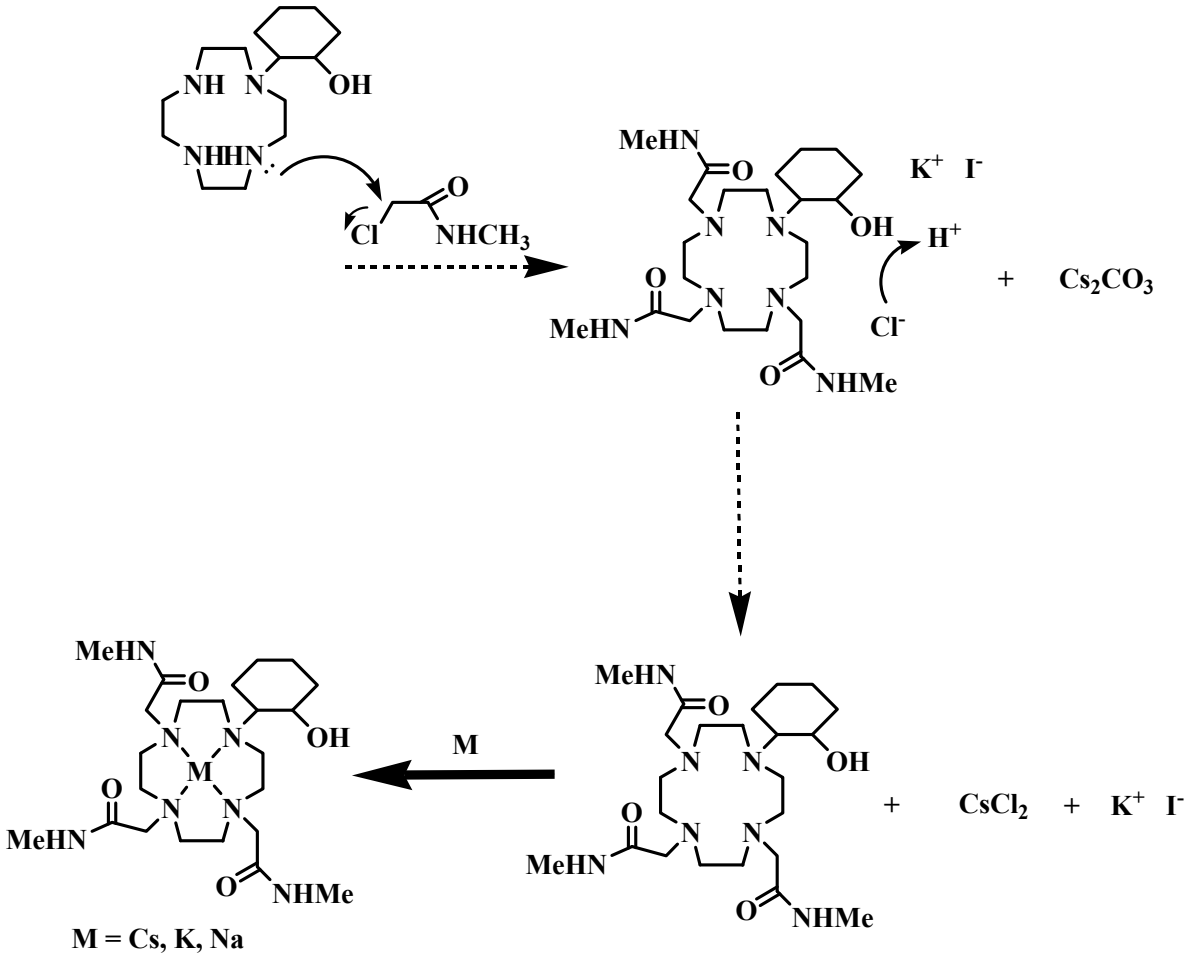


Figure 3.3: Mechanism of Reaction Toward Target Ligands.

3.1.4 Lanthanide Complexation of Target Ligands

In similar complexation reactions involving kinetically inert macrocycles, the complexation reaction proceeds through the quick formation of a metastable species leading, after a slow reorganization of the macrocycle, to thermally stable complexes. Specific stability of the complexes that have been synthesized in this study were not determined, however their specific *in vivo* inertness arises from transitory bonds between the central lanthanide metal ion and the oxygen of the cyclohexyl pendant moiety and the three pendant arms bearing carboxylate groups.

3.2 Solid State and Supramolecular Chemistry

3.2.1 Crystal Analysis Polyazamacrocyclic Ligands

3.2.1.1 Crystal Structure of 1,4,7-tris[*N*-methylcarbamylmethyl]-10-(2-hydroxy-cyclohexyl)-1,4,7,10-tetraazacyclododecane or (2):

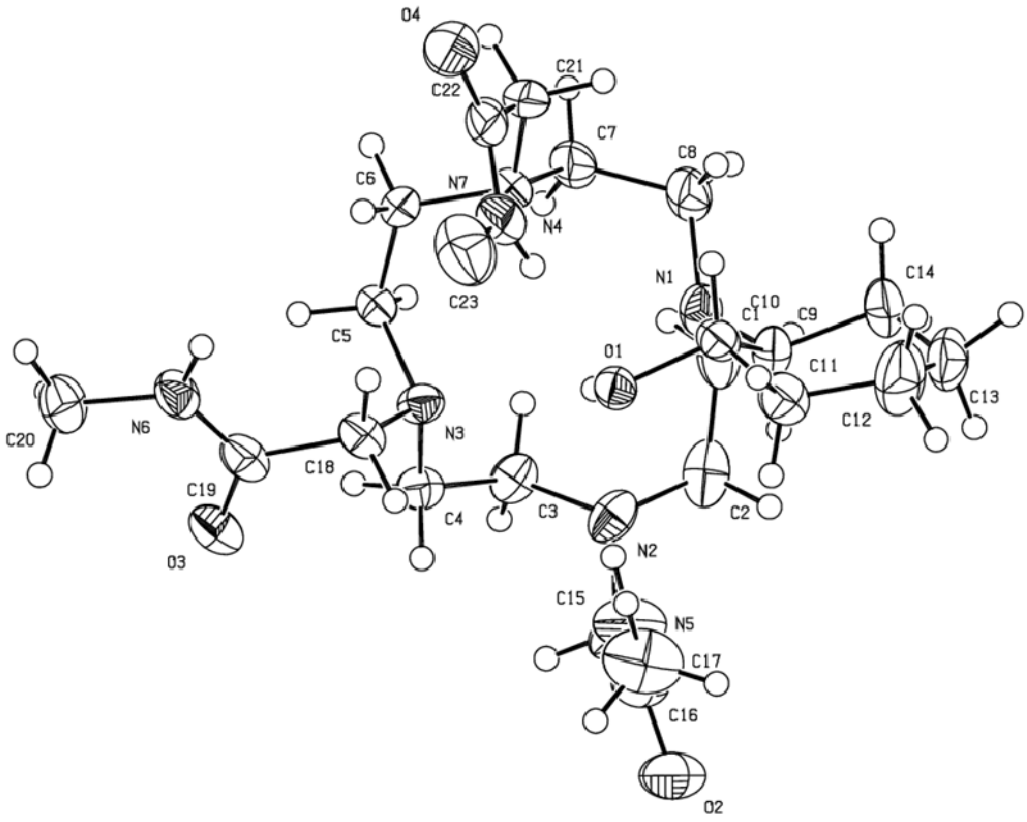


Figure 3.4: Conformation of **2** - Ortep illustration.

Molecule **2** was formed by reacting 1-(2-hydoxycyclohexyl)-1,4,7,10-tetraazacyclodecane (**1**) with excess *N*-methyl chloroacetamide by refluxing in dry DMF. Cesium carbonate was used as the base to neutralize HCl formed as a by-product and KI as a halogen exchange agent. Excess metal salts were removed by filtration and further purification of the filtrate to remove unreacted 1,4,7-tris[*N*-methylcarbamylmethyl]-10-(2-hydroxycyclohexyl)-1,4,7,10-tetraazacyclododecane was accomplished by washing in hexane and diethyl ether. Furthermore, to remove excess *N*-methyl-chloroacetamide, the pH of the solution was lowered and washed with dichloromethane a number of times. The pH of the solution was raised with NaOH and again washed with dichloromethane. To grow crystals, the water was removed by lyophilisation and a minimal

amount of dry acetonitrile (5 ml) was used to dissolve the product to which diethyl ether was added dropwise until the solution became turbid. This set up was left to slowly evaporate at room temperature to afford colourless crystals. The reported molecular structure shown in Figure 3.4 is a free chelator that crystallized with one molecule of water in the $P2_{1/c}$ space group and found to be in the monoclinic crystal system. The conformations of **2** are stabilized by multiple and cooperative intramolecular N—H···O and O—H···O hydrogen bonding interactions. The average torsion for N—C—C—N angle in the cyclen ring was determined to be 62.45°(8). The crystal data, collection and structure refinement parameters for **2** are shown in Table 3.1.

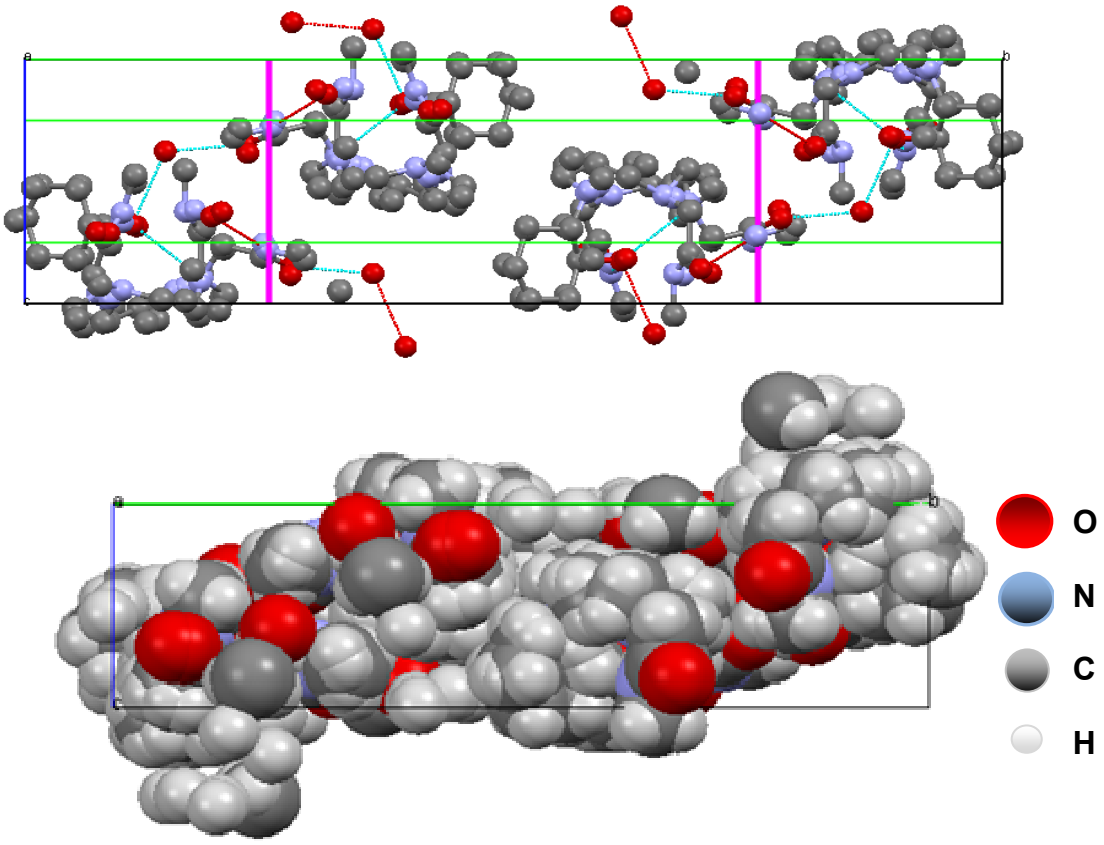


Figure 3.5: Packing of **2** in the unit cell along *a* axis- Ortep illustration.

There are four molecules within the unit cell which arrange themselves in a double helical fashion, one helix for the macrocyclic backbone and the other for acetamide arms as illustrated in Figure 3.5.

3.2.2.2 Crystal Structure of Na-1,4,7-tris[*N*,*N*-dimethylcarbamylmethyl]-10-(2-hydroxy-cyclohexyl)-1,4,7,10-tetraazacyclododecane or (3):

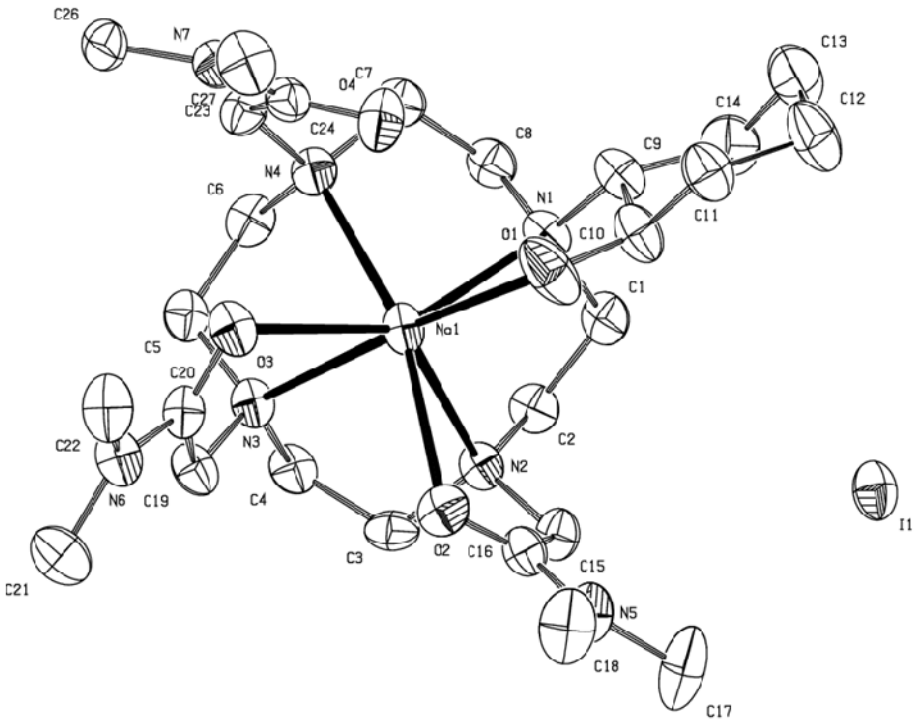


Figure 3.6: Conformation of **3** - Ortep illustration: Hydrogen atoms removed for clarity.

Molecule **3** was formed by reacting **1** with excess *Di*-methyl chloroacetamide by refluxing in dry DMF. A similar protocol to that which was adopted for the purification of **2** was also utilized for **3**. This set up was left to slowly evaporate at room temperature to afford the colourless crystals. The molecular structure illustrated in Figure 3.6 is a sodium complex of **3** that crystallized with an iodide counter ion (iodide originates from the halogen exchange agent used in the synthesis) and is in the $P2_{1/n}$ space group with monoclinic crystal system. Similarly, the conformations of molecule **3** are stabilized by multiple and cooperative intramolecular N—H···O and O—H···O hydrogen bonding interactions. The presence of the OH group on the cyclohexyl moiety is known to have an affinity for smaller metal ions like sodium.[8] The sodium ions are coordinated to the four nitrogen atoms on the cyclen, the three oxygen atoms of the carboxylic amides and to one oxygen on the cyclohexyl pendant moiety. The average Na—N

and Na—O bond lengths for the coordination of cyclen ring and oxygen donors were 2.595 Å and 2.563 Å, respectively. The average torsion for N—C—C—N angle in the cyclen ring was determined to be 60.76(5) °.

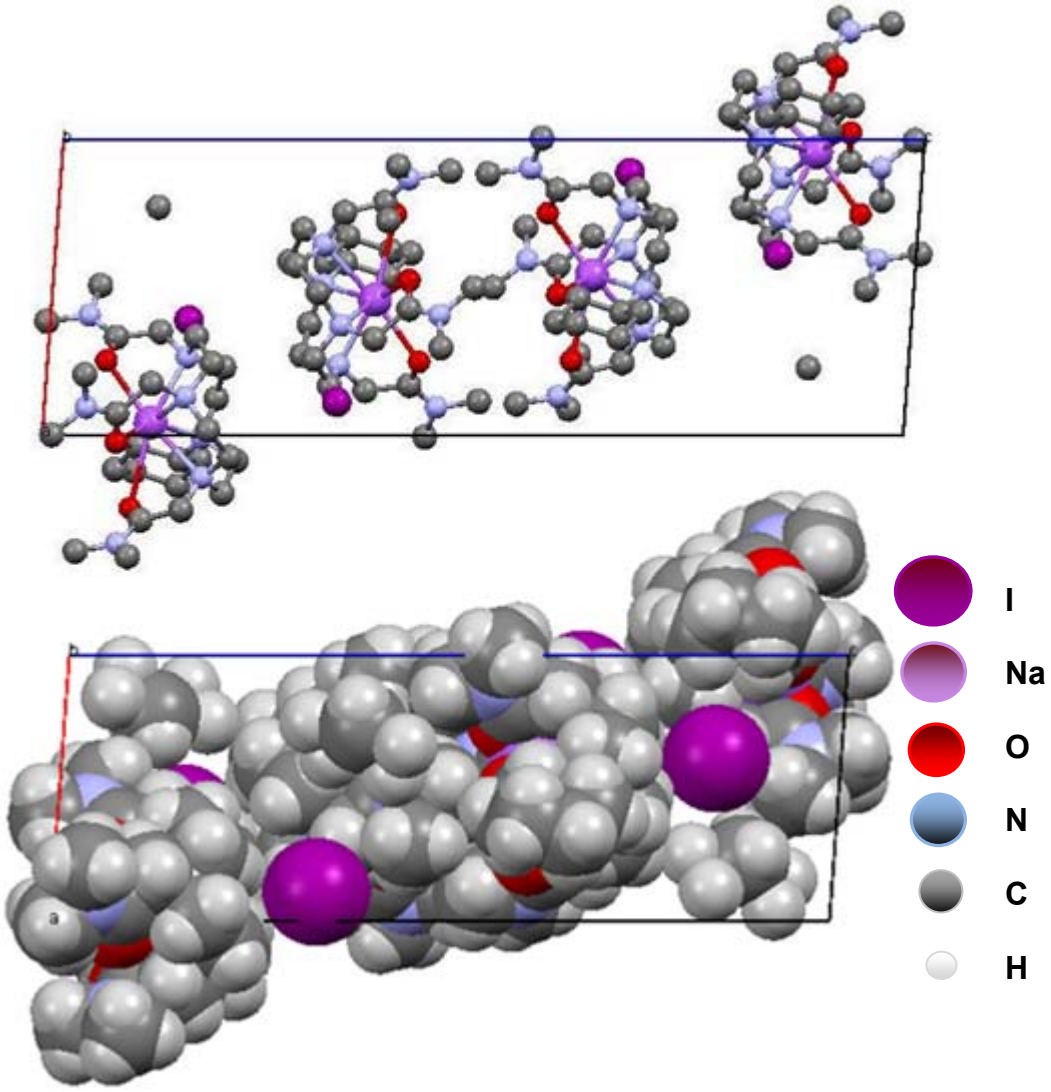


Figure 3.7: Packing of **3** in unit cell along *b* axis - Ortep illustration.

There are four molecules within the unit cell which arrange themselves in a double helical fashion, one for the macrocyclic backbone and the other for acetamide arms as illustrated in Figure 3.7. The iodide counterion also forms part of the unit cell alternating between each molecular species.

Table 3.1: Crystal Data, Collection and Structure Refinement Parameters for Ligands.

Structural formula	$C_{23}H_{45}N_7O_4$ (Molecule 2)	$C_{26}H_{50}N_7NaO_4$ (Molecule 3)
M	488.16	675.63
Crystal size (mm^3)	0.40 x 0.37 x 0.25	0.48 x 0.33 x 0.14
Crystal system	Monoclinic	Monoclinic
Space group (Z)	$P2_{1/c}$ (4)	$P2_{(1)/n}$ (4)
***a* (Å)**	9.6189(2)	9.7838(3)
***b* (Å)**	32.1984(7)	11.5254(3)
***c* (Å)**	8.6632(2)	28.5330(8
α (°)	90	90
β (°)	99.5380(10)	94.156(2)
γ (°)	90	90
Volume ($Å^3$)	2646.02(10)	3208.98(16)
Density Mg/m^3	1.225	1.398
F(000)	1066.9	1408
μ mm^{-1}	0.086	1.053
Temperature K	173(2)	173(2)
Wavelength Å	0.71073	0.71073
R_{int}	0.0283	0.0708
***θ* range (°)**	1.26 to 25.00	1.43 to 28.00
Completeness to theta	100.0 %	100.0 %
Goodness-of-fit on F^2	1.161	1.182
Unique reflections	4668	7729
***wR*2(*R*1)**	0.1847 (0.0761)	0.1352 (0.0529)

3.2.2 Polyazamacrocyclic Lanthanide Complexes

3.2.2.1 Crystal Structure of Europium-1,4,7-tris[*N*-methylcarbamylmethyl]-10-(2-hydroxycyclohexyl)-1,4,7,10-tetraazacyclododecane or (5):

Molecule **5** was formed by reacting **2** with excess europium triflate by refluxing in dry acetonitrile. The solvent was removed on the rotary evaporator and further dried under reduced pressure. A minimal amount of water (5 ml) was used to redissolve the product and 20% NH_4OH was added dropwise until the solution reached a pH of 10. The solution was filtered using a celite plug to remove the excess europium as $Eu(OH)_3$. The crude product was redissolved in a minimal amount of dry acetonitrile to which diethyl ether was added dropwise until the solution became turbid. Refrigeration overnight afforded the colourless crystallized product.

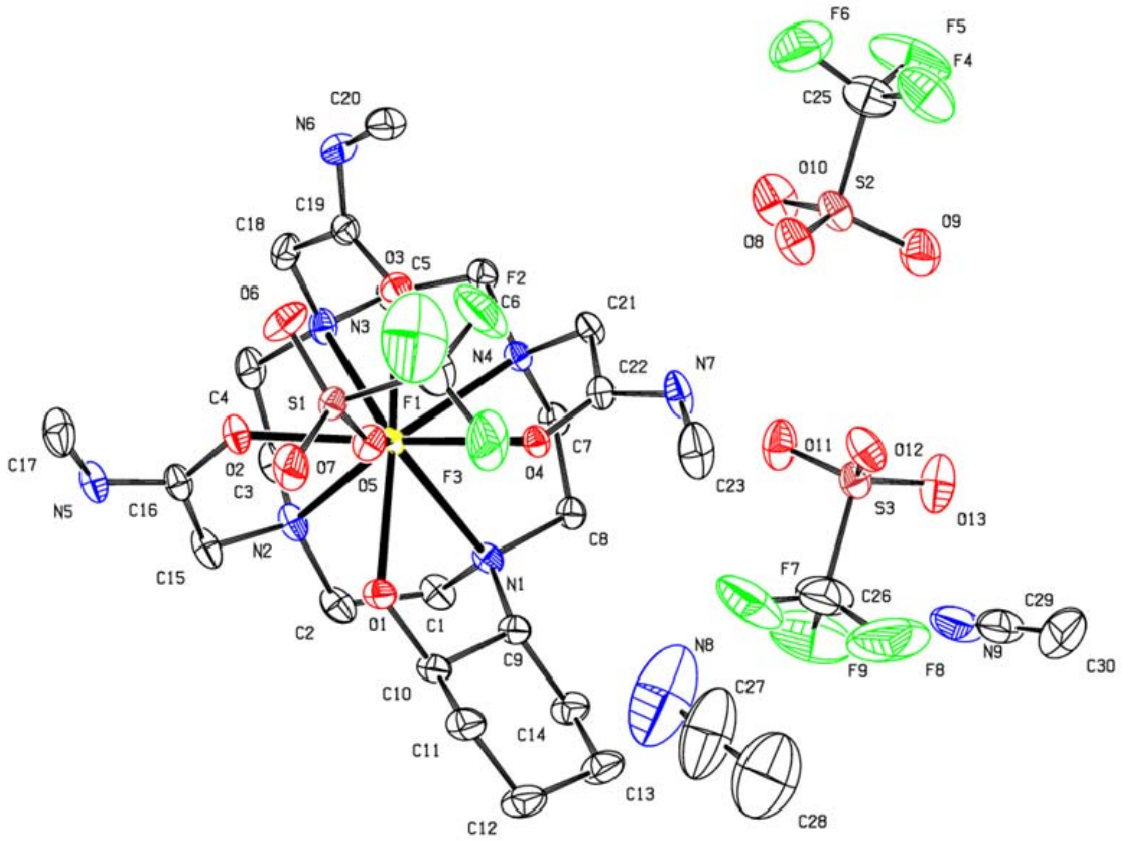


Figure 3.8: Conformation of **5** - Ortep illustration: Hydrogen atoms removed for clarity.

The molecular structure shown in Figure 3.8 is a europium complex of **2** that crystallized with three triflate counterions and two neutral acetonitrile solvent molecules and found to be in P_{-1} space group with triclinic crystal system. The central metal ion coordinated to the four nitrogens of the cyclen ring, the three oxygen atoms on the carboxylic amides and the hydroxyl group oxygen of the pendant cyclohexyl ring. In addition, one triflate anion was coordinated to the metal center. This gives rise to a nine coordinate environment as expected for Eu^{3+} azamacrocyclic type complexes. The triflate anions and the carbons on the cyclohexyl ring showed some disorder. The average Eu—N and Eu—O bond lengths for the coordination of cyclen ring and oxygen donors were 2.661 Å and 2.381 Å, respectively. A summary of selected bond distances is shown in Table 3.2.

Table 3.2: Summary of selected bond distances in **5**.

Bond Distances	Donor Type	Source	Length /Å
Eu—$N_{(1)}$	nitrogen	cyclen backbone	2.657(17)
Eu—$N_{(2)}$	nitrogen	cyclen backbone	2.656(17)
Eu—$N_{(3)}$	nitrogen	cyclen backbone	2.673(18)
Eu—$N_{(4)}$	nitrogen	cyclen backbone	2.658(16)
Eu—$O_{(1)}$	oxygen	hydroxyl group	2.408(15)
Eu—$O_{(2)}$	oxygen	carboxylic amide	2.363(15)
Eu—$O_{(3)}$	oxygen	carboxylic amide	2.380(14)
Eu—$O_{(4)}$	oxygen	carboxylic amide	2.373(14)
Eu—$O_{(5)}$	oxygen	triflate	2.443(15)

Furthermore, as mentioned earlier the lanthanide that is coordinated to a single triflate (O—Eu=2.443 Å) and the bond length is slightly larger compared to other oxygen donors, in fact it is very similar to the Eu—O distance for the hydroxyl group.

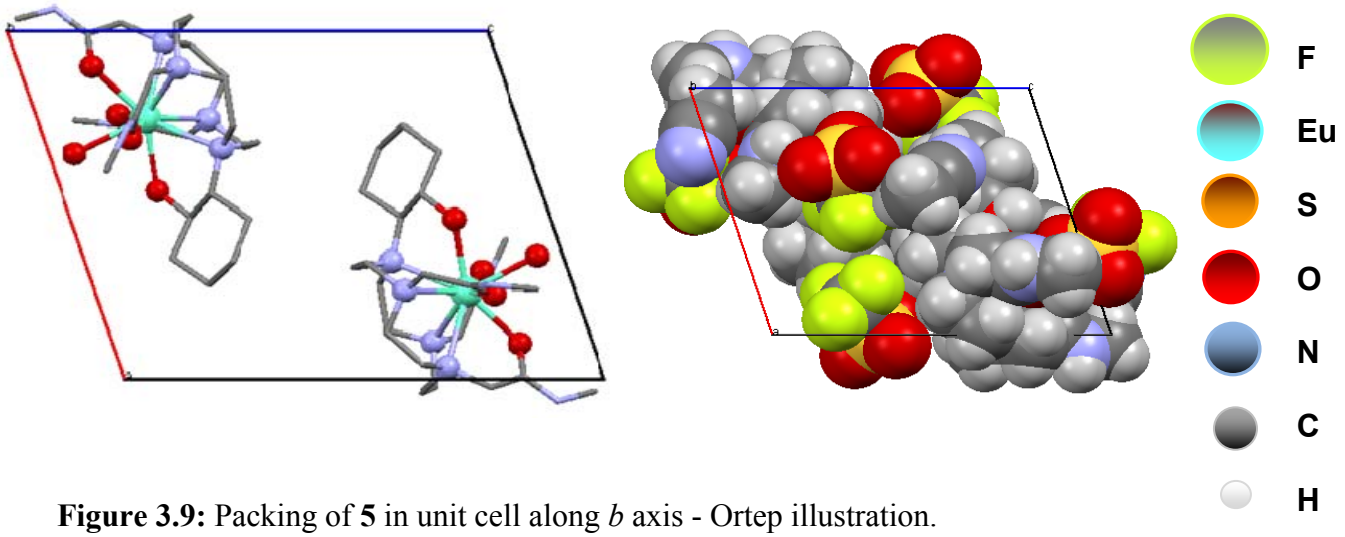


Figure 3.9: Packing of **5** in unit cell along *b* axis - Ortep illustration.

There are two molecules within the unit cell which arrange themselves in a double helical fashion, one for the macrocyclic backbone and the other for acetamide arms as illustrated in Figure 3.9. The triflate counterions also forms part of the unit cell alternating between each molecular species and also found to cap the axial position. The crystal packing is characterized by a chain structure when considering the hydrogen bond interactions between the symmetry related molecules. The complex adopts a distorted monocapped square anitiprismatic geometry in solid-state as illustrated in Figure 3.10, with an average torsion for N—C—C—N angle of 58.51°.

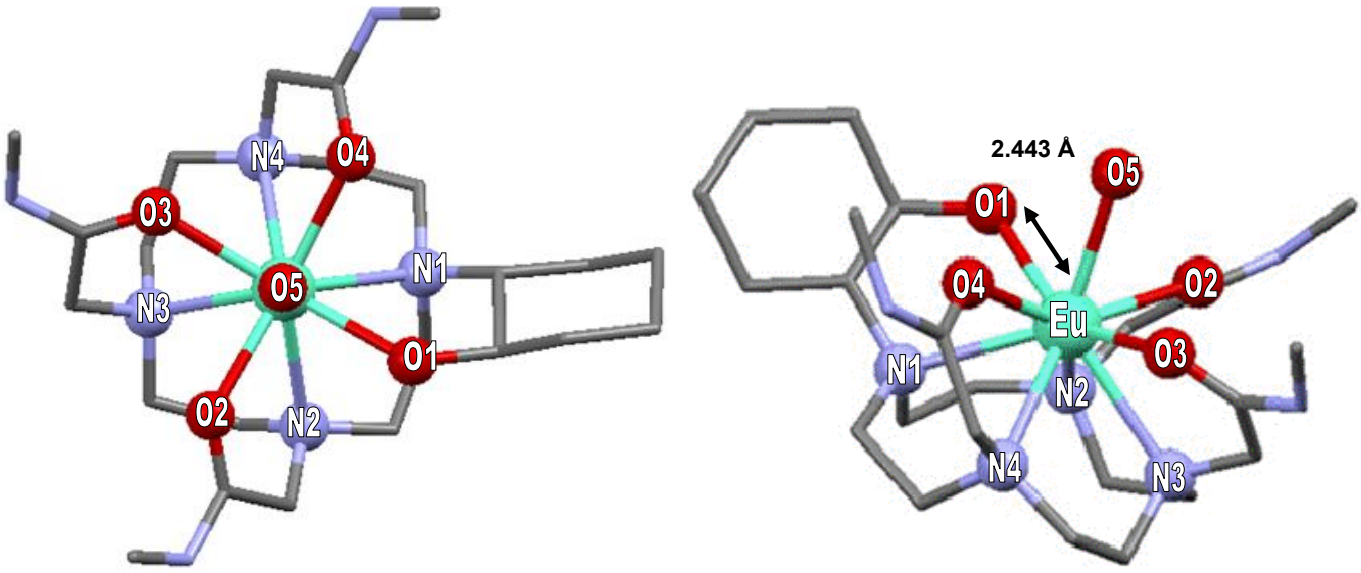


Figure 3.10: Shows the capped square anitiprismatic geometry of **5**.

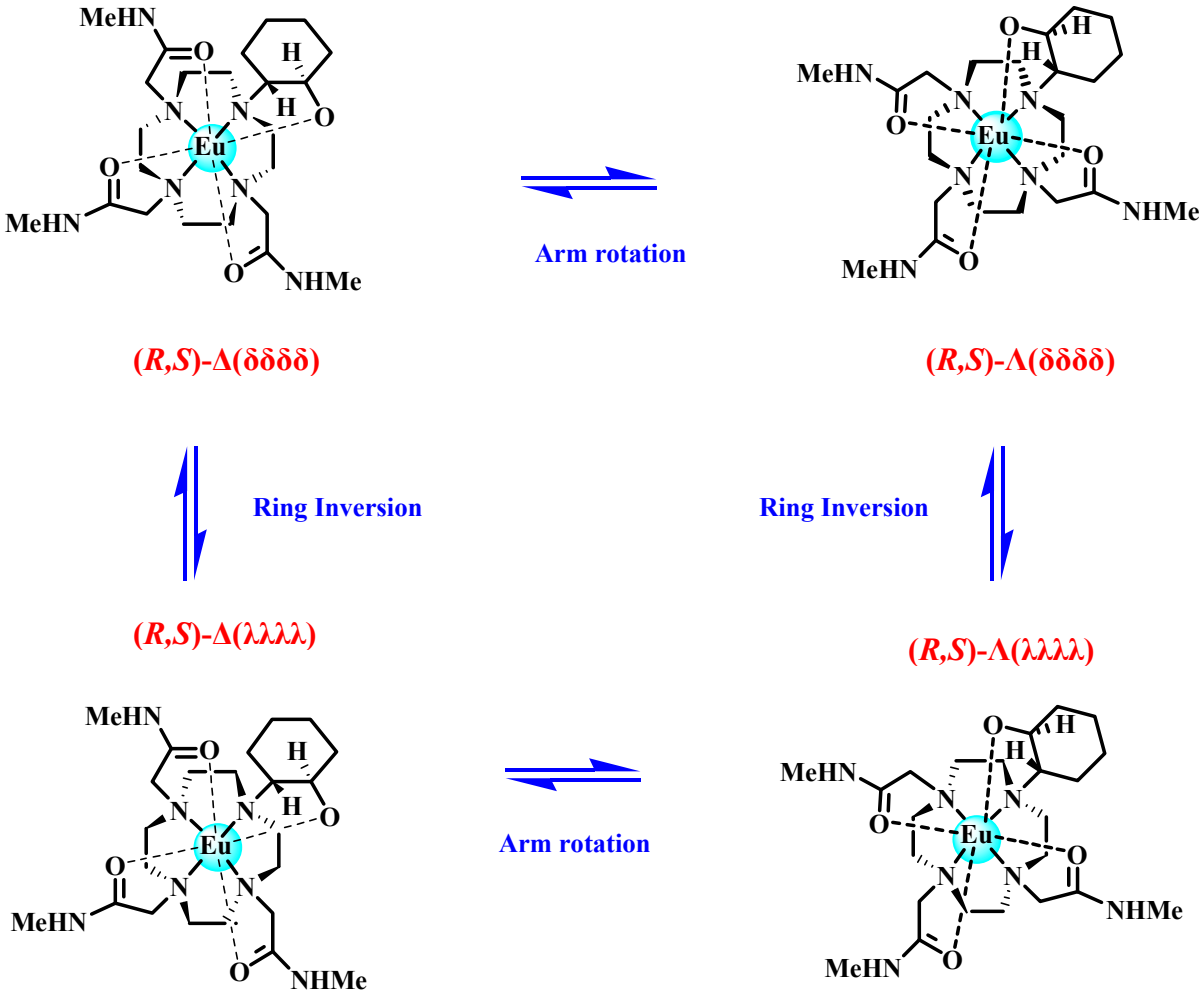


Figure 3.11: Interconversion of stereoisomers for the (*R,S*)-**5** isomer.

Molecule **5** has two stereogenic centers which give rise to 16 possible stereoisomers. The major stereoisomer isolated shown in Figure 3.8 was the (*R,S*)-Λ(δδδδ) isomer. Figure 3.11 shows a representation of the (*R,S*) isomer and can be extrapolated to the (*S,R*), (*S,S*) and (*R,R*) isomers, respectively.

3.2.2.2 Crystal Structure of Europium-1,4,7,10-Tetrakis(methylcarbamylmethyl)-1,4,7,10-tetraazacyclodecane or (9):

Molecule **9** was formed by reacting **4** with excess europium triflate by refluxing in dry acetonitrile. The solvent was removed on the rotary evaporator and further dried under reduced pressure. A minimal amount of water (5 ml) was used to redissolved the product and 20% NH_4OH was added dropwise until the solution reached a pH of 10. The solution was filtered using a celite plug to remove the excess europium as $Eu(OH)_3$. Similary, the crude product was redissolved in a minimal amount of dry acetonitrile to which diethyl ether was added dropwise until the solution became turbid. Refrigeration overnight afforded the crystallized product.

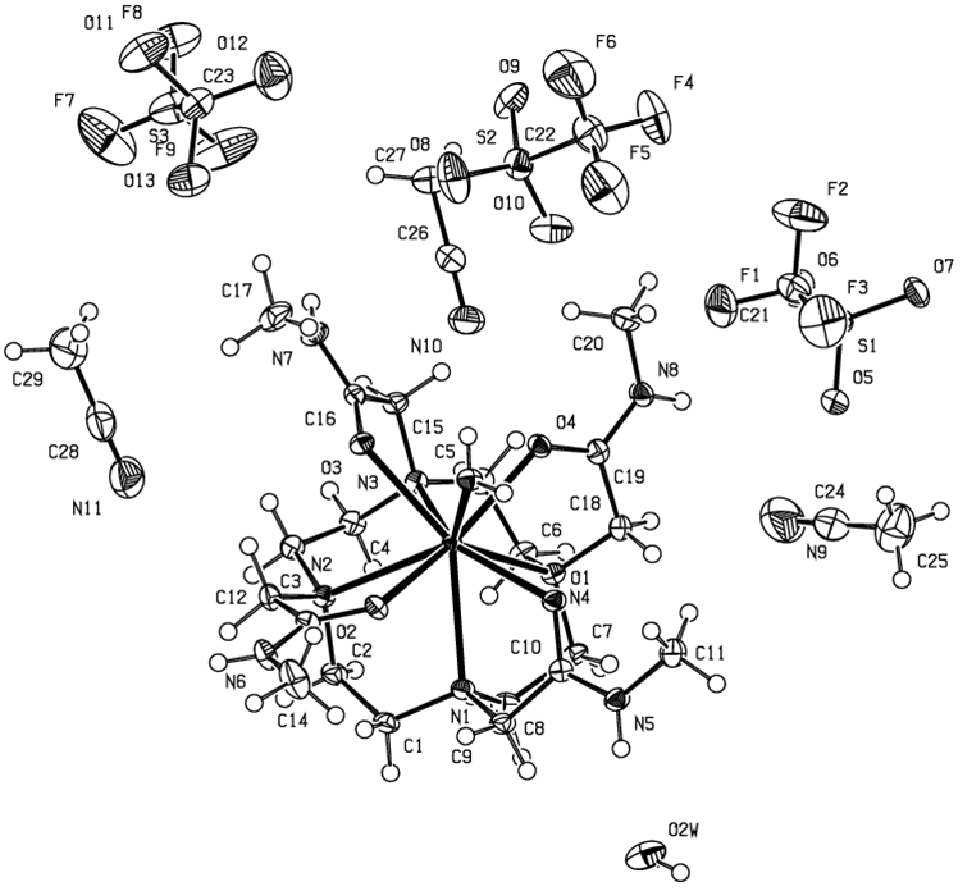


Figure 3.12: Conformation of **9** - Ortep illustration.

The determined molecular structure shown in Figure 3.12 is a europium complex of **4** that crystallized with three triflate counterions and two neutral acetonitrile solvent molecules and was found to be in P_{-1} space group with a triclinic crystal system. The central metal ion coordinated to the four nitrogens of the cyclen ring, the four oxygen donors on the carboxylic amides.

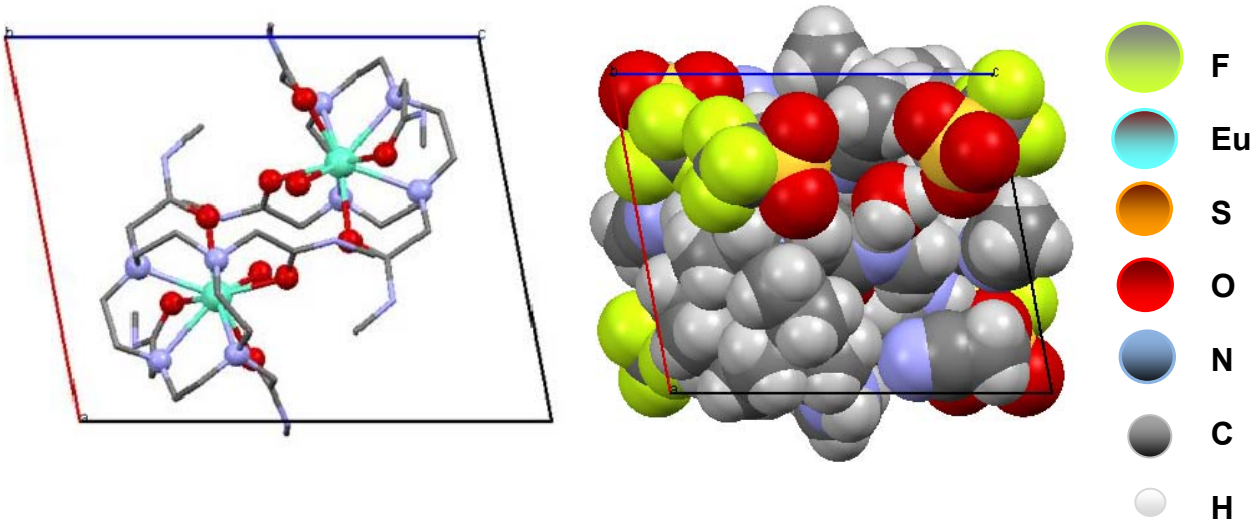


Figure 3.13: Packing of **9** in unit cell along *b* axis - Ortep illustration.

There are two molecules within the unit cell which arrange themselves in a head to tail fashion, as illustrated in Figure 3.13. The crystal packing is characterized by a chain structure when considering the hydrogen bond interactions between the symmetry related molecules. The triflate counterions also forms part of the unit cell alternating between each molecular species with water in the capping position. As in the previous europium complex **5**, this complex also gives rise to a nine coordinate environment as expected for Eu^{3+} azamacrocyclic type complexes. The average Eu—N and Eu—O bond lengths for the coordination of cyclen ring and oxygen donors were 2.650 Å and 2.388 Å, respectively. Furthermore, as mentioned earlier the lanthanide that is coordinated to a single water molecule (O—Eu=2.437Å) and the bond length is slightly larger compared to other oxygen donors. The complex adopts a distorted capped square anitiprismatic geometry in solid-state illustrated in Figure 3.14, with an average torsion for N—C—C—N angle of - 58.95°. Molecule **9** has no stereogenic centers and adopts a similar conformation as Ln-DOTA type complexes like Ln-DTMA. The major stereoisomer isolated

shown in Figure 3.12 was the Δ(λλλλ) isomer. Figure 3.15 shows a representation of the possible stereoisomers. A summary of selected bond distances is shown in Table 3.3.

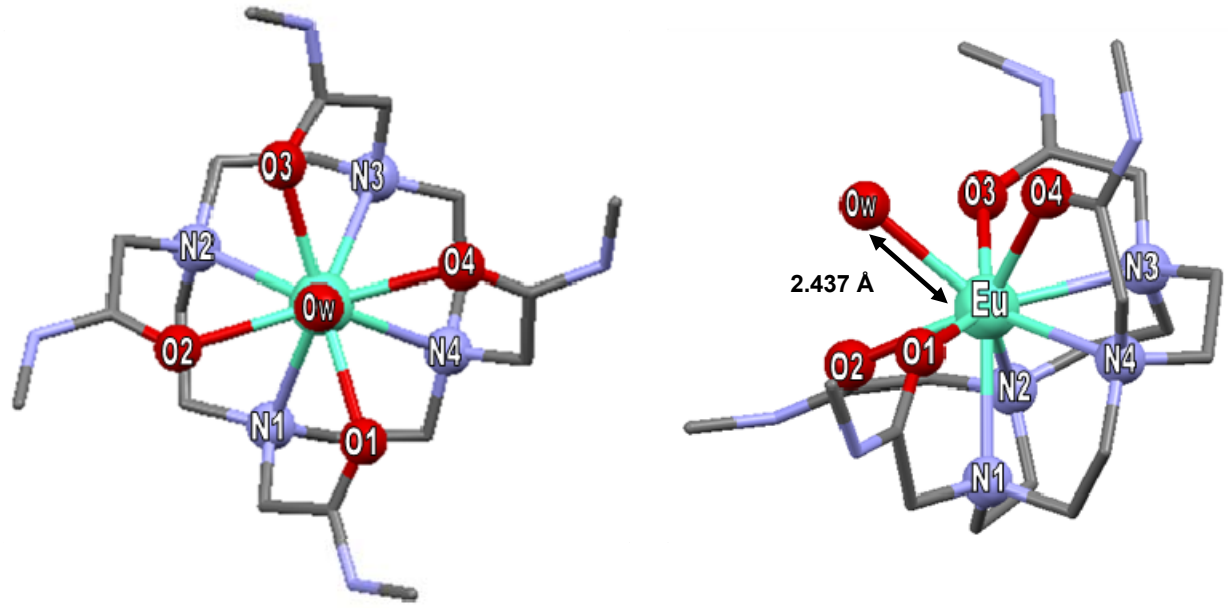


Figure 3.14: Capped square anitiprismatic geometry of **9**.

Table 3.3: Summary of selected bond distances in **9**.

Bond Distances	Donor Type	Source	Length /Å
Eu—$N_{(1)}$	nitrogen	Cyclen backbone	2.649(15)
Eu—$N_{(2)}$	nitrogen	Cyclen backbone	2.627(15)
Eu—$N_{(3)}$	nitrogen	Cyclen backbone	2.643(15)
Eu—$N_{(4)}$	nitrogen	Cyclen backbone	2.682(15)
Eu—$O_{(1)}$	oxygen	Carboxylic Amide	2.346(12)
Eu—$O_{(2)}$	oxygen	Carboxylic Amide	2.445(12)
Eu—$O_{(3)}$	oxygen	Carboxylic Amide	2.399(12)
Eu—$O_{(4)}$	oxygen	Carboxylic Amide	2.363(12)
Eu—$O_{(W1)}$	oxygen	Water Molecule	2.437(12)

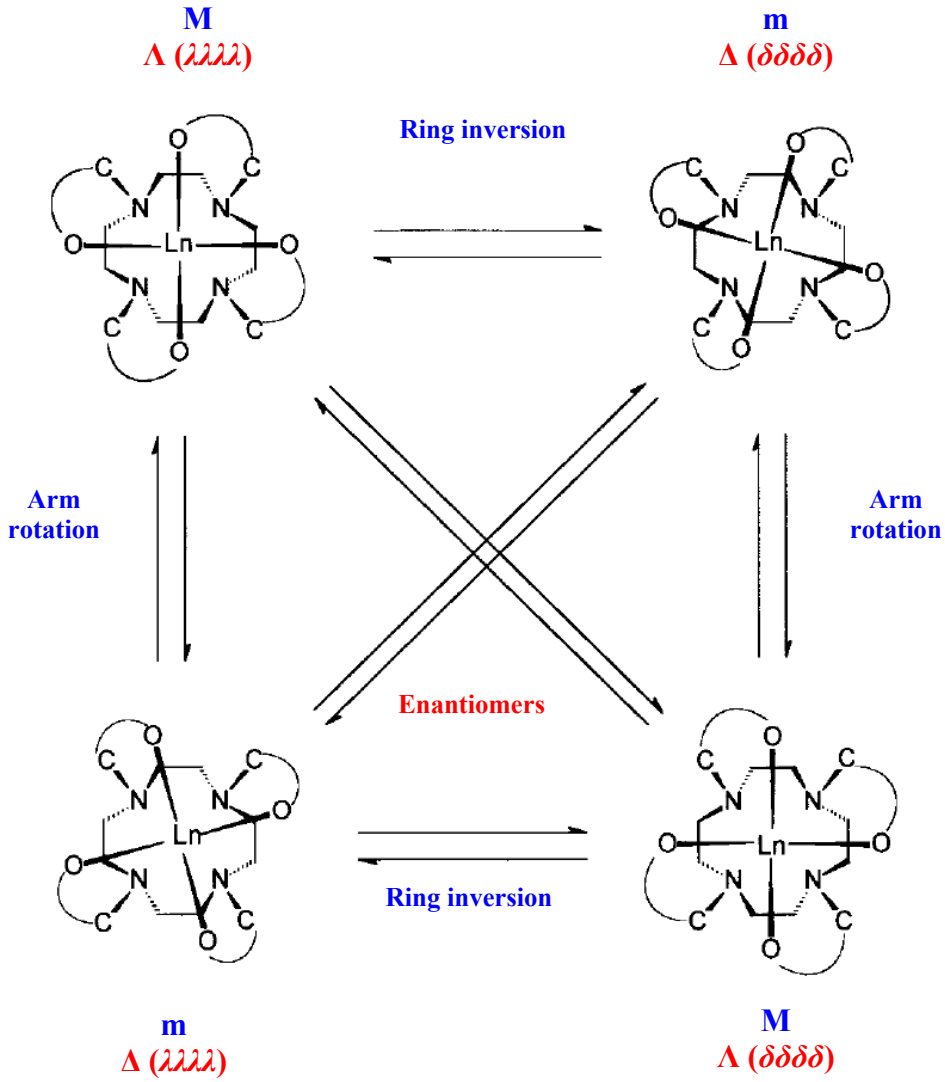


Figure 3.15: General interconversion of stereoisomers in lanthanide complexes of cyclen-based macrocylic ligands.

In some earlier work, dealing with the Gd^{3+} complex of DTMA, a distinct evaluation of water and prototropic exchange rates for a Gd coordinated solvent molecule were reported for the first time, evidencing that crystals of $[Gd(DTMA)(H_2O)][ClO_4]^{3+}.NaClO_4.3H_2O$ are made of $[Gd(DTMA)(H_2O)]^{3+}$ with sodium cations and perchlorate counter anions and crystallization water molecules. The macrocyclic ligand acts as octadentate. The metal ion is coordinated by the four nitrogens of the tetraazamacrocyclic moiety and by the amidic oxygen atoms provided

by the side arms. The ninth position of the coordination sphere is occupied by an oxygen atom of a water molecule. The Gd–N and the Gd–O amidic bond distances spanning in the ranges 2.621(5) to 2.649(6) and 2.351(5) to 2.455(5) Å, respectively, as well as the Gd–O (water) distance (2.461(5) Å) are comparable with those previously reported for analogous Gd^{3+} complexes.[273-276] The resulting polyhedron, which can be described as a distorted square antiprism,[277] capped by the water oxygen, corresponds to the usual co-ordination geometry of Gd^{3+} complexes with ligands based on the 1,4,7,10-tetraazacyclododecane structure and their stereochemical conformation is illustrated in Figure 3.15.[273-276]

The tetraaza ring has a [3333] C corners conformation,[278] with the four amidic chains in a head-to-tail relative arrangement. The four amidic nitrogen atoms have a significant sp_2 character, indicating that the usual π conjugation takes place in each amidic functional group thus enhancing the donor capability of the carbonylic oxygens. Concerning the packing, it is worth noting that the oxygen of the Gd^{3+} coordinated water molecule is very close (2.921(1) Å) to an oxygen atom of a perchlorate ion, suggesting that a strong hydrogen bond between $[Gd(DTMA)(H_2O)]^{3+}$ and a counter ion occurs. In addition the water oxygen O5 is 3.483(7) Å from a symmetry related O5 atom. Comparing the above mentioned Gd(DTMA) complex to the molecule **9** synthesized in this work, it is clear that they are very similar in terms of geometrical make up and certainly affirms the fact that Eu^{3+} can be used as a structural analogue for Gd^{3+}.

3.2.2.3 Crystal Structure of Gadolinium-1,4,7-tris[*N*-methylcarbamylmethyl]-10-(2-hydroxycyclohexyl)-1,4,7,10-tetraazacyclododecane or (6):

Molecule **6** was formed by reacting **2** with excess gadolinium triflate and the same protocol was that was adopted for the purification of **5** and **9** was also utilized for **6**. Refrigeration overnight afforded the colourless crystallized product.

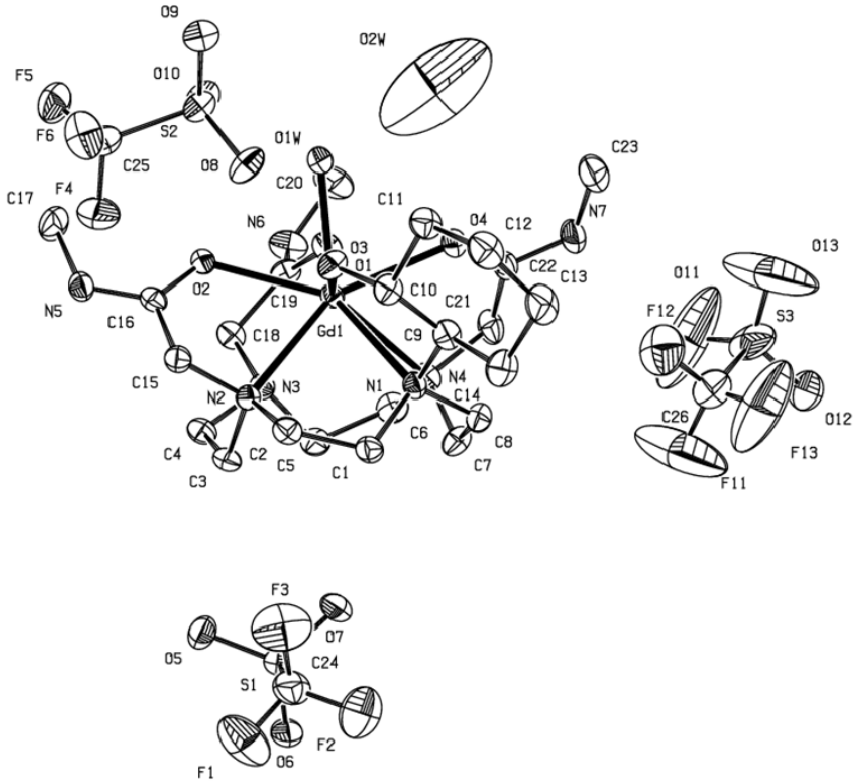


Figure 3.16: Conformation of **6** - Ortep illustration: Hydrogen atoms removed for clarity.

The molecular structure shown above in Figure 3.16 crystallized with three triflate counterions and two neutral water molecules and was found to be in Pcca space group within an orthorhombic crystal system. It adopts the same coordination geometry as complex **5** with a water molecule in the capping position giving rise to a nine coordinated polyhedron as discussed earlier. The average Gd—N and Gd—O bond lengths for the coordination of cyclen ring nitrogens and oxygen donors were 2.659 Å and 2.376 Å, respectively. A summary of selected bond distances is shown in Table 3.4.

Table 3.4: Summary of selected bond distances in **6**.

Bond Distances	Donor Type	Source	Length /Å
Gd—$N_{(1)}$	nitrogen	cyclen backbone	2.651(3)
Gd—$N_{(2)}$	nitrogen	cyclen backbone	2.625(3)
Gd—$N_{(3)}$	nitrogen	cyclen backbone	2.699(3)
Gd—$N_{(4)}$	nitrogen	cyclen backbone	2.660(3)
Gd—$O_{(1)}$	oxygen	hydroxyl group	2.440(3)
Gd—$O_{(2)}$	oxygen	carboxylic amide	2.374(3)
Gd—$O_{(3)}$	oxygen	carboxylic amide	2.336(3)
Gd—$O_{(4)}$	oxygen	carboxylic amide	2.354(3)
Gd—$O_{(W1)}$	oxygen	water molecule	2.422(3)

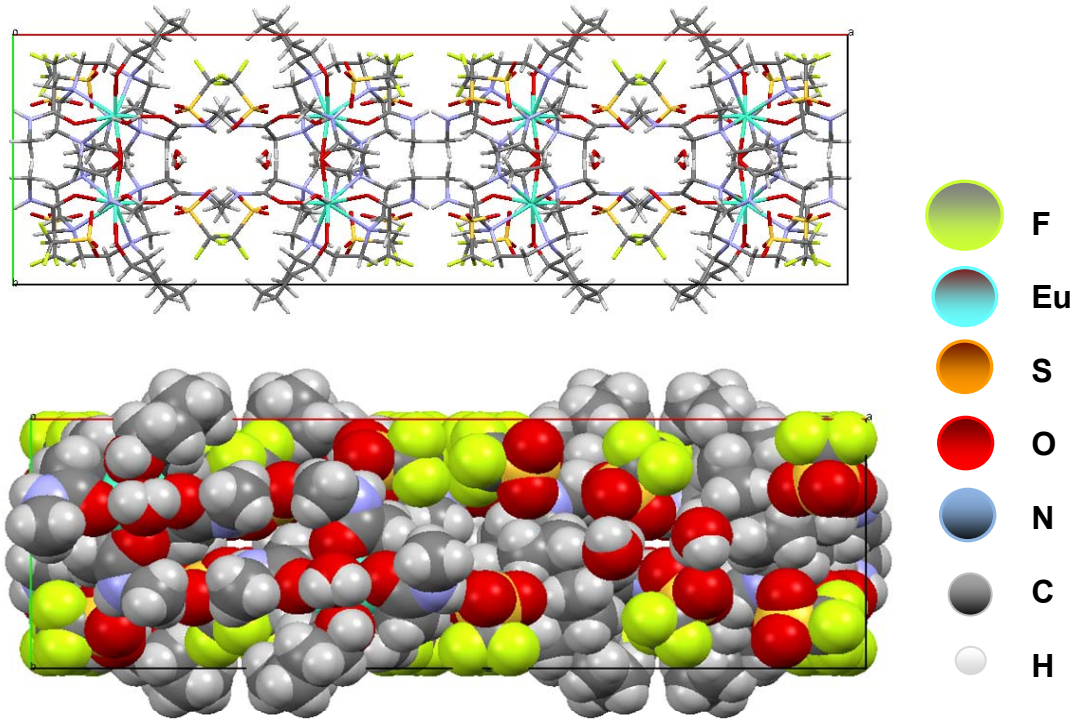


Figure 3.17: Packing of **6** in unit cell along *a* axis - Ortep illustration.

There are eight molecules within the unit cell which arrange themselves in a double helical fashion, one for the macrocyclic backbone and the other for acetamide arms as illustrated in

Figure 3.17. The triflate counterions also forms part of the unit cell alternating between each molecular species with water in the capping position.

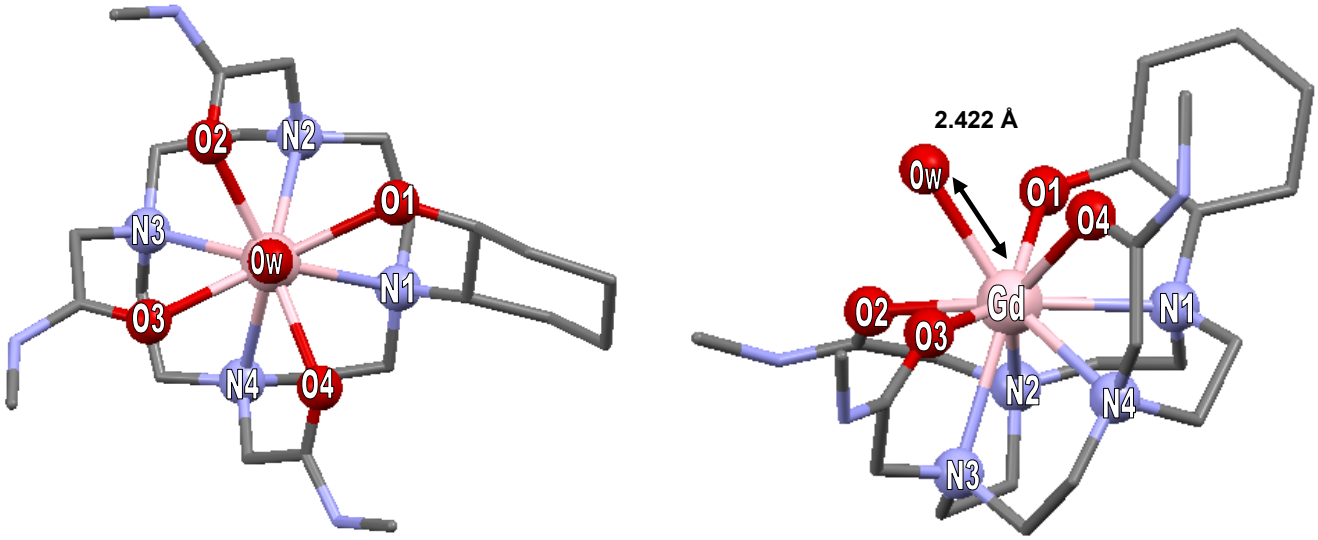


Figure 3.18: Capped square anitiprismatic geometry of **6**.

Furthermore, as mentioned earlier the lanthanide that is coordinated to a single triflate (O—Eu=2.422 Å) and the bond length is slightly larger compared to other oxygen containing donors, in fact it is very similar to the Eu—O distance for the hydroxyl group. The complex adopts a distorted capped square anitiprismatic geometry in solid-state as illustrated in Figure 3.18, with average torsion angles for N—C—C—N angle of 57.72°.

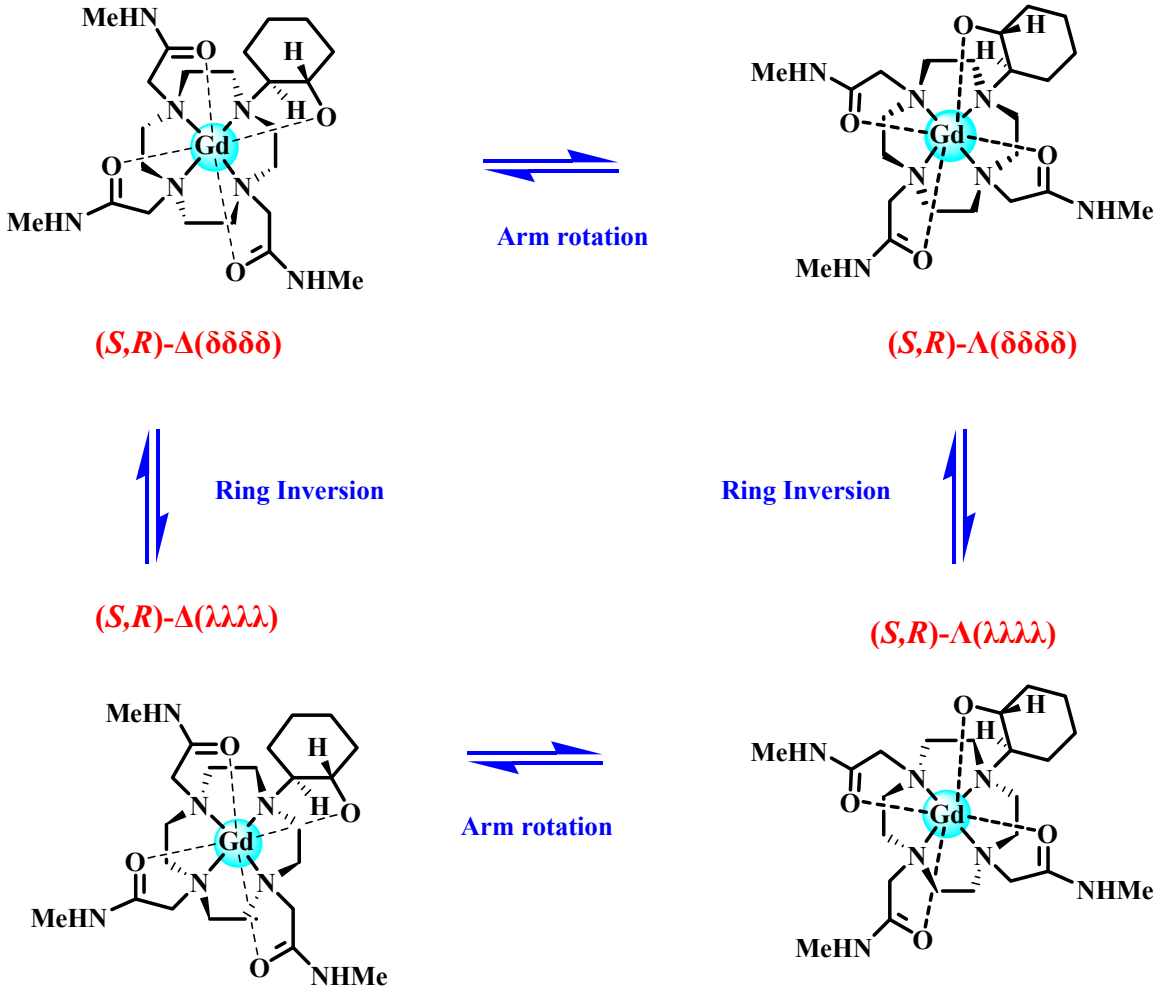


Figure 3.19: Interconversion of stereoisomers for the (*S,R*)-**5** isomer.

Similar to molecule **5,** molecule **6** has two stereogenic centers which give rise to 16 possible stereoisomers. The major stereoisomer isolated shown in Figure 3.16 was the (*S,R*)-Δ(λλλλ) isomer. Figure 3.19 shows a representation of the (*S,R*) isomer and can be extrapolated to the (*R,S*), (*S,S*) and (*R,R*) isomers, respectively

In 2006, Aime and co-workers reported the crystal structures of Gd-DOTAM and Py-DOTAM.[279] The single crystals of $[Gd(DOTAM)H_2O](CF_3SO_3)_3.3H_2O$ were grown from slow evaporation of a water solution. It crystallized with one $[Gd(DOTAM)\text{-}H_2O]^{3+}$ complex cation, three triflate counterions and three water molecules of crystallization. Its X-ray structure presents a nine coordinate Gd^{3+} ion. In the cation, the four nitrogen and four oxygen atoms form two square planes (deviations of the nitrogens and of the oxygens from their respective square

planes are 0.001 and 0.003 Å) that are parallel to each other. The gadolinium ion is 0.716(1) Å out of the oxygen plane and 1.614(1) Å from the nitrogen plane. Considering also the coordinated water molecule in the capping position, the coordination geometry of the metal ion is a capped square antiprism with the twist angle between the two planes of the nitrogen and oxygen comparable to the values found in Ln-DOTA complexes.[280] The Gd–O_w bond distance is 2.394(3) Å in their complex somewhat shorter than that reported for $[Gd(DTPA)H_2O]^{2+}$ 2.507(10)[281] $[Gd(DOTA)H_2O]^{3+}$ 2.458(3) Å[282], but comparable with $[Gd(DO3A)H_2O]^{3+}$ 2.429 Å[283] with the same capped square antiprism geometry. The Gd–O carboxylate bond distances are in the range 2.372(3) to 2.388(4) Å and the Gd–N 2.638(4) to 2.671(4) Å comparable to those found in the previously quoted $[Gd(DO3A)H_2O]^{3+}$. The numerous hydrogen acceptor–donor atoms determine the molecular packing. The crystals of compound $[Gd(DOTAM)H_2O].(CF_3SO_3^-)_3.0.5H_2O.CH_3CN$ were obtained by slow diffusion of water in acetonitrile. It crystallizes with two independant Gd complex molecules as asymmetric units. The geometry around Gd^{3+} ions is a typical capped square antiprism with a twist angle between the two square planes of the four coordinated nitrogen and the four oxygens. In general, the supramolecular structures in our study are very similar to those previously reported in literature and/or are in current use as MRI-CAs with respect to their bond distances, bond angles, torsion angles and general arrangement of the coordination polyhedron. Of vital importance is that a single capping position in all lanthanide complexes were reported, a much needed feature ensuring occupancy by a single water molecule from the body which enhances contrast between diseased and healthy tissue.

Table 3.5: Crystal Data, Collection and Structure Refinement Parameters for Complexes.

Structural formula	$C_{58}H_{99}Eu_2F_{18}N_{17}O_{26}S_6$ (molecule 5)	$C_{26}H_{49}F_9GdN_7O_{15}S_3$ (molecule 6)	$C_{29}H_{53}EuF_9N_{11}O_{15}S_3$ (molecule 9)
M	2288.82	1124.15	1214.96
Crystal size (mm^3)	0.47 x 0.28 x 0.15	0.45 x 0.15 x 0.04	0.33 x 0.23 x 0.09
Crystal system	Triclinic	Orthorhombic	Triclinic
Space group (Z)	P-1 (1)	Pcca (8)	P-1 (2)
***a* (Å)**	11.8523(2)	41.2383(6	12.8612(2)
***b* (Å)**	13.4938(2)	13.1777(2)	14.1272(3)
***c* (Å)**	15.4748(3)	15.5431(2)	14.4666(3)
α (°)	70.5800(10)	90	82.4570(10)
β (°)	70.7790(10)	90	77.2400(10)
γ (°)	81.9570(10)	90	68.4760(10)
Volume ($Å^3$)	2202.72(7)	8446.5(2)	2381.13(8)
Density Mg/m^3	1.725	1.768	1.695
F(000)	1158	4536	1232
μ mm^{-1}	1.672	1.829	1.556
Temperature K	173(2)	173(2)	173(2)
Wavelength Å	0.71073	0.71073	0.71073
R_{int}	0.0338	0.0756	0.0436
***θ* range (°)**	1.46 to 28.00	1.55 to 28.00	1.45 to 28.00
Completeness to θ	100.0 %	99.9 %	100.0 %
Goodness-fit on F^2	1.044	0.895	1.066
Unique reflections	10633	10218	11490
***wR*2(*R*1)**	0.0624 (0.0234)	0.076 (0.0384)	0.0555 (0.0222)

3.3 Solution Chemistry of Europium Complexes

3.3.1 Luminescence Studies and UV-vis Studies of Europium Complexes: Determination of Spectroscopic pK_as

Ligand field effects are normally studied through photophysical measurements of the metal ion, either absorption or emission. For lanthanide ions the amount of information that can be obtained from these studies is limited by shielding of the 4f-orbitals by the 5d-orbitals. As a result of this shielding the effect of the ligand field is small relative to spin-orbital coupling (~100 cm^{-1} *versus* ~2000 cm^{-1}). As a consequence, the emission spectra of lanthanide ions are characterized by sharp emission bands that correspond to the Russell-Saunders (spin orbit coupling) states of the ground state. Figure 3.20 illustrates different lanthanide excitation and electronic states when associated with an antenna. Information about the ligand field is contained within these sharp emission bands and can therefore only be clearly discerned at higher spectral resolutions. Under Laporte selection rules f-f transitions are forbidden; nevertheless, some transitions are permitted under electric or magnetic dipole selection rules through the mixing of 5d and 4f orbitals that arises from distortions of the coordination sphere by vibrational motion. As a consequence the intensities of f-f transitions remain low.

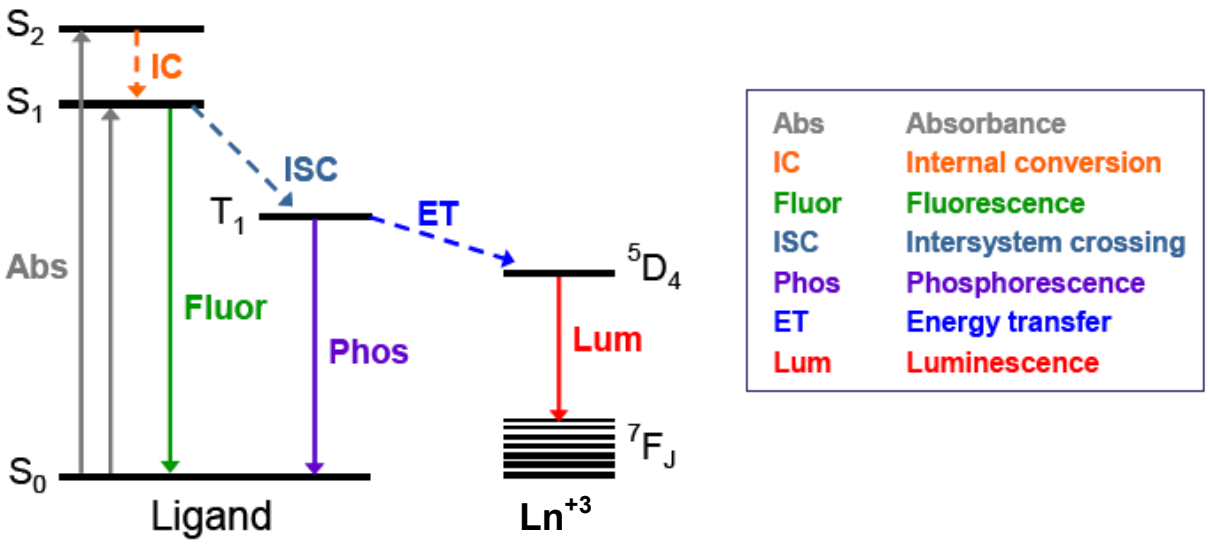


Figure 3.20: Diagram explaining lanthanide excitation and electronic states when associated with an antenna.[284]

3.3.1.1 Europium-11,4,7-tris[*N*-methylcarbamylmethyl]-10-(2-hydroxycyclohexyl)-1,4,7,10-tetraazacyclododecane (5) in MCB with KHP

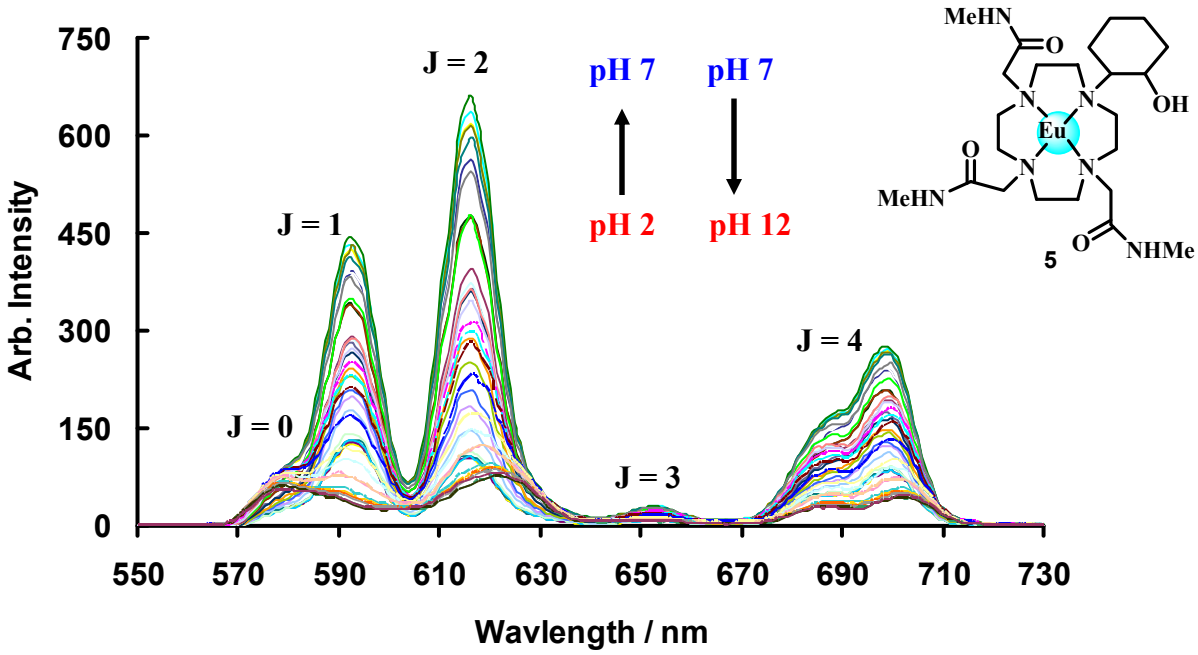


Figure 3.21: Variation of intensity for emission spectrum of **5** in MCB with KHP upon titration with NaOH.

Figure 3.21 depicts the variation of intensity for emission spectrum of **5** in multicomponent buffer (MCB) with KHP upon titration with NaOH. The variation of lanthanide emission was found to be most intense in the physiological pH range between pH 6 to 8 for J = 0, 1, 2, 3 and 4. In general for all J bands a bell shaped profile was observed. From the non-linear least square fits shown in Figure 3.22 it was found that two protonation equilibria arise which corresponds to the deprotonation phthalate carboxylate which was followed by the deprotonation of the metal-bound water molecule. The mean values were calculated and found to be $pK_1 = 4.67 \pm 0.06$ and $pK_2 = 8.69 \pm 0.12$, respectively. Using UV-vis spectroscopy an absorbance band was observed at $\lambda = 270$ nm, which corresponds to the characteristic phthalate π to π^* transition, and was monitored shown in Figure 3.23. Similarly, a plot of absorbance versus pH shown in Figure 3.24 was fitted using an iterative procedure for a three pK_a fit model as it showed the best fit. The protonation equilibria using UV-vis spectroscopy was found to be $pK_1 = 2.84 \pm 0.24$, $pK_2 = 5.11 \pm 0.10$ and $pK_3 = 11.12 \pm 0.62$, respectively. The first two equilibria observed for UV-vis

spectroscopy corresponded to the deprotonation of the phthalate carboxylates and agrees well with the known pK_as of the carboxylates found in phthalate[285] which are pK_1 = 2.98 and pK_2 = 5.28, respectively. However, the value pK_3 = 11.12 ± 0.62 is likely to be caused by working at high pH which results in demetalation of the complex. Precipitation of Eu^{3+} follows and the formation of Eu-phthalate complexes or Eu-hydroxides that are insoluble and could explain the slight increase in absorbance at high pH.

Figure 3.24 illustrates the proposed protonation equilibria and explains the modulation observed for **5** in MCB with KHP upon titration with NaOH. The phthalate moiety coordinates in a unidentate fashion and the coordination number of nine is preserved. Between pH 2 and pH 4.7 the intensity of the emission bands increases due to the binding of the phthalate carboxylate which gradually deprotonates and coordinates with the metal center this further enhances the intensity signal via an energy transfer mechanism transferred from the S_1 and possibly T_1 state of the phthalate moiety to the triplet state of the lanthanide.[286] Although it is well known that the phthalate moiety can coordinate in a bidentate fashion with tri substituted cyclen derivatives[287], however in molecule **5** the nona-coordinated polyhedron is fully occupied. In addition, if phthalate were to bind in a bidentate fashion, the formation of a 7-membered ring chelate results which is highly unstable as it energetically unfavorable.[288] As the pH increases to about 7 an increase in emission intensity is observed. At high pH > 7, it is proposed that the cyclohexyl group re-coordinates to the metal center and consequently displaces of the phthalate moiety causing an overall decrease in emission intensity.

Although the metal-bound water molecule undergoes dissociative exchange with bulk water at a rate of $>10^7$ s^{-1} at 298 K, it is very difficult to substitute it in aqueous media. So far, only addition of excess fluoride has been shown to be displace the metal bound water molecule,[143] e.g., for $[EuDOTAMPh]^{3+}$ and to a partial extent in $[Eu(DOTA)(H_2O)]^-$. In the fluoride-bound species, the complex seemed to adopt a preferred twisted square anti prismatic structure possibly formed via the TSAP mono-aqua species. However, for molecules where q = 2 or 3, the water molecule is readily displaced by addition of ligating anions, especially chelating species (e.g., lactate, citrate, malonate, succinate).[289,290,291,292] Such reactions may be monitored by following the enhancement of luminescence emission intensity and lifetime as bound water molecules

efficiently quench the excited state of, e.g., Yb^{3+}, Nd^{3+}, Eu^{3+}, and Tb^{3+} species. In the case of Eu^{3+} complexes, the change in the form of the emission spectrum also characterizes this process, since a marked decrease in intensity was observed which shows that the phthalate is no longer coordinated to the metal ion. This displacement can also then be extrapolated to complex **9** where the amidic pendant arm re-coordinates in a similar fashion.

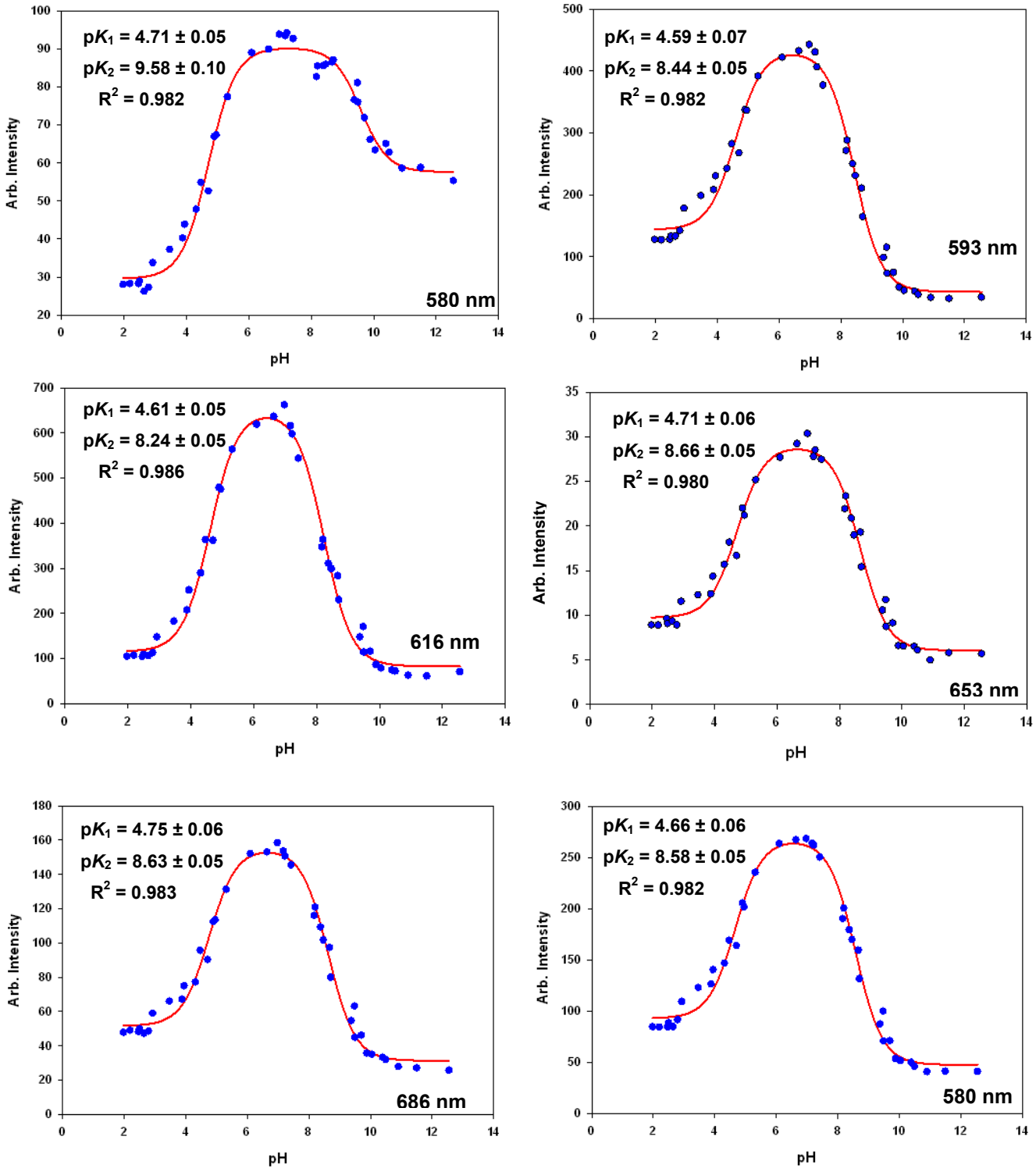


Figure 3.22: Non-linear least square fits for **5** in MCB with KHP corresponding to J = 0, 1, 2, 3 and 4.

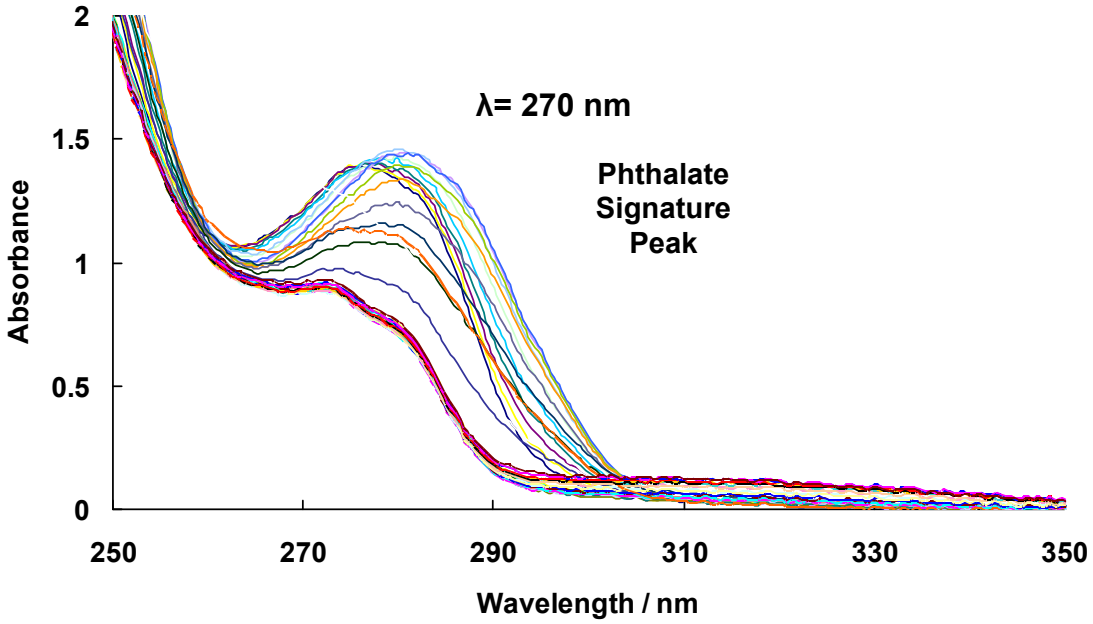


Figure 3.23: Variation in absorbance of **5** in MCB with KHP upon titration with NaOH.

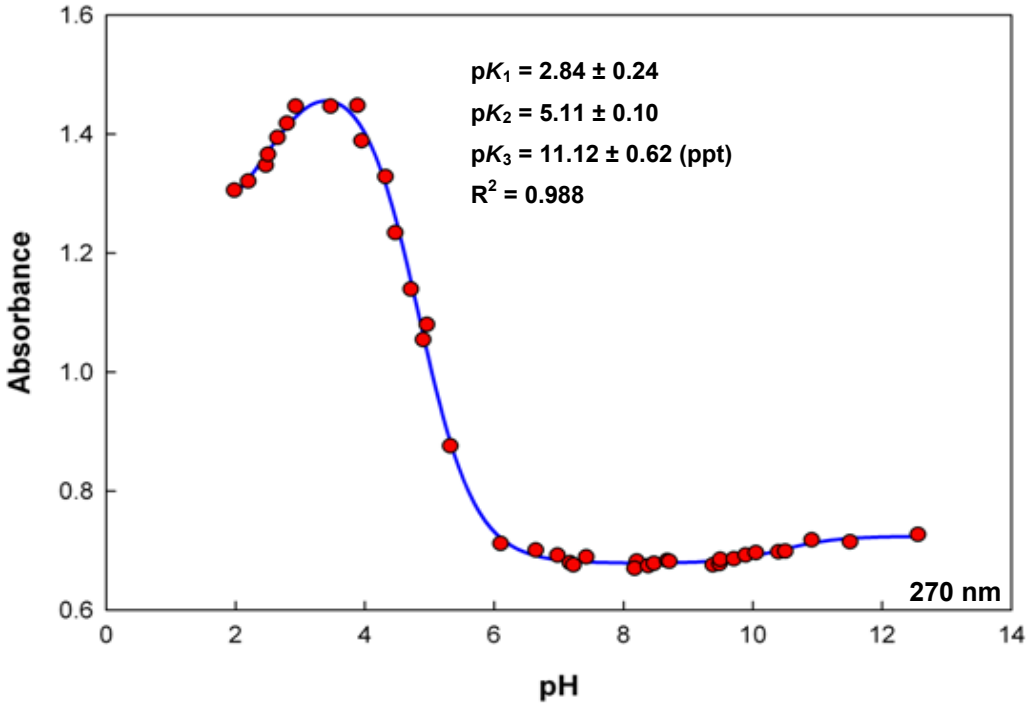


Figure 3.24: Non-linear least square fit for **5** in MCB with KHP corresponding monitoring at λ = 270 nm across pH range.

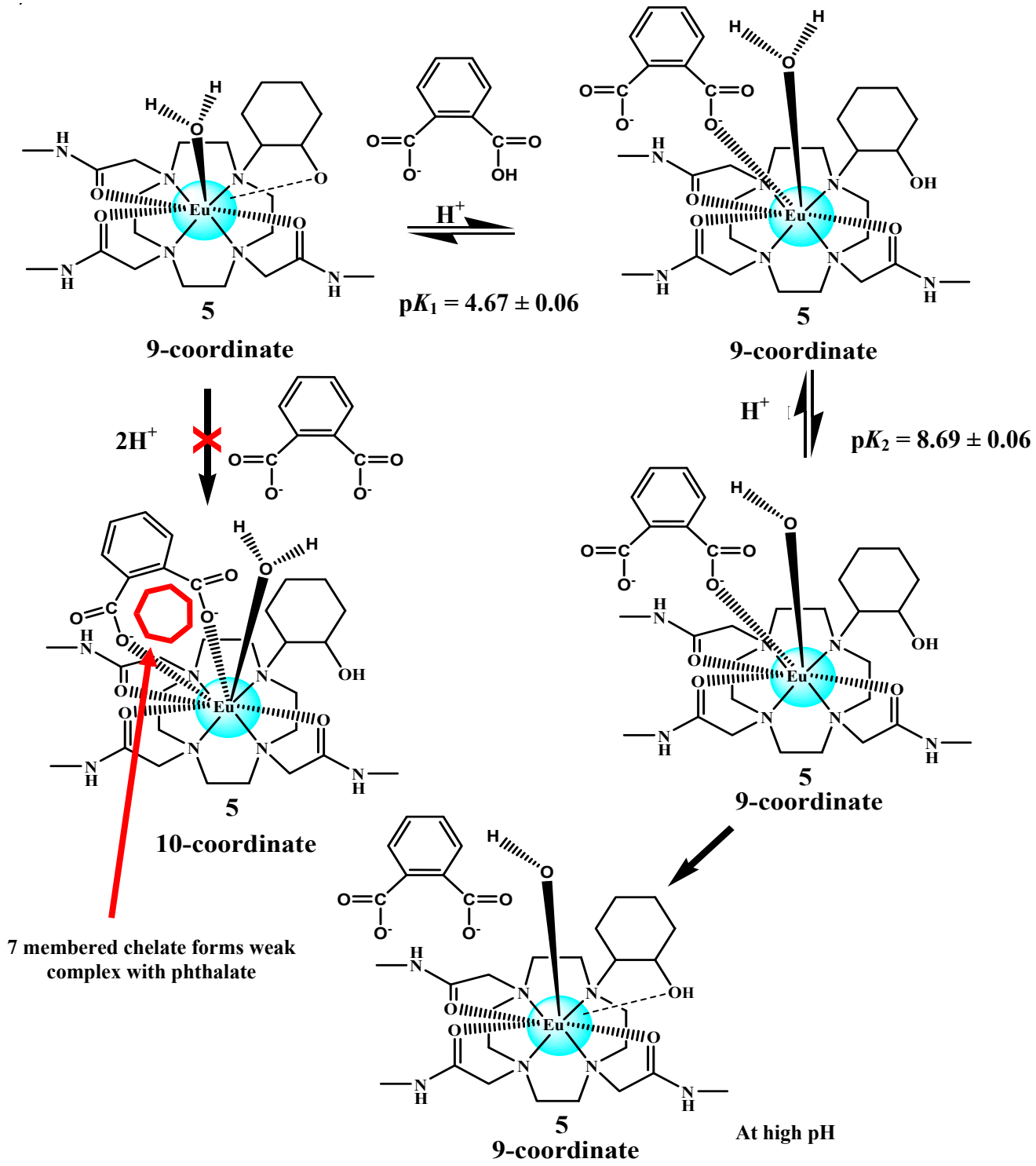


Figure 3.25: Proposed protonation equilibrium for **5** in MCB with KHP upon titration with NaOH.

3.3.1.2 Europium-1,4,7,10-Tetrakis-(methylcarbamylmethyl)-1,4,7,10-tetraazacyclodecane Complex (9) in MCB with KHP

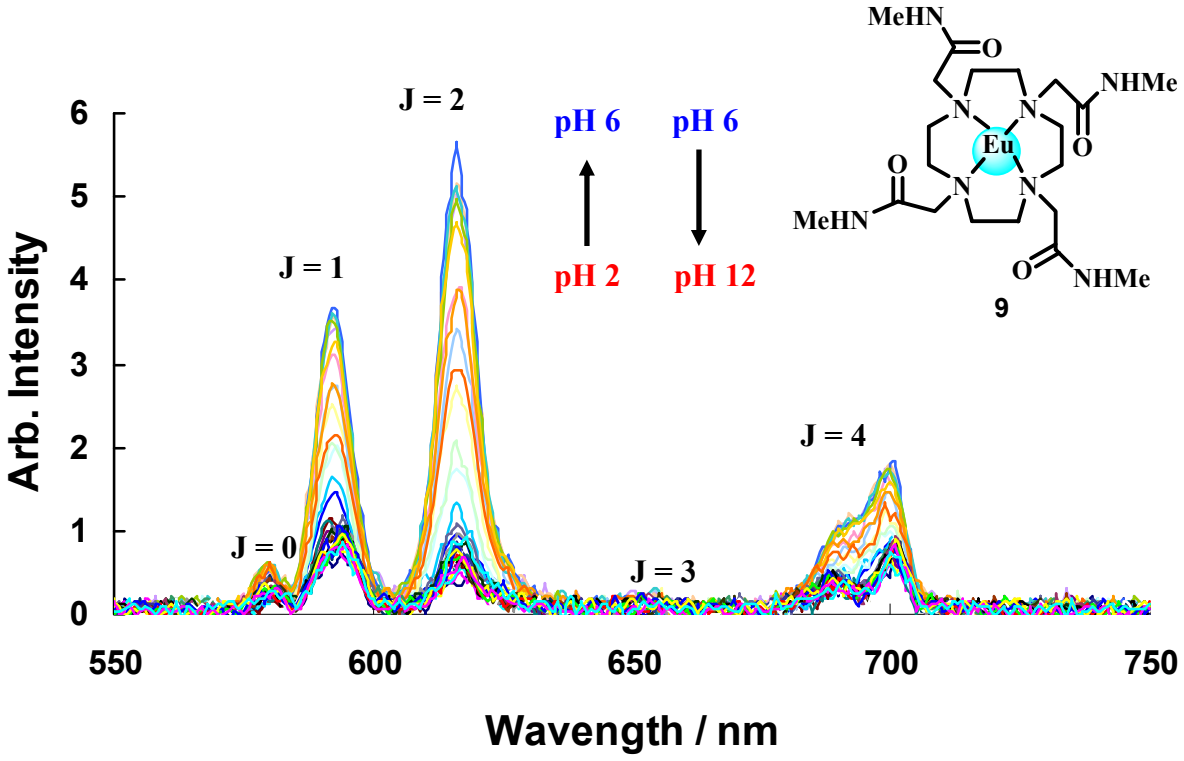


Figure 3.26: Variation of intensity for emission spectrum of **9** in MCB with KHP upon titration with NaOH.

Figure 3.26 depicts the variation of intensity for emission spectrum of **9** in multicomponent buffer (MCB) with KHP upon titration with NaOH. The variation of lanthanide emission was found to be most intense in the pH range between pH 5 and 7 for J = 0, 1, 2, 3 and 4. Similarly, for all J bands a bell shaped profile was observed from pH 4 to about pH 8. From the non-linear least square fits shown in Figure 3.27 it was found that two protonation equilibria arise which corresponds to the deprotonation phthalate carboxylate, followed by the deprotonation of the metal-bound water molecule. The mean values were calculated and found to be $pK_1 = 4.99 \pm 0.63$ and $pK_2 = 7.30 \pm 0.11$, respectively. Using UV-vis spectroscopy an absorbance band was observed at $\lambda = 280$ nm which corresponds to the characteristic phthalate π to π^* transition shown in Figure 3.28.

A plot of absorbance versus pH shown in Figure 3.29 was fitted using an iterative procedure for a two pK_a fit model as it showed the best fit. The protonation equilibria using UV-vis spectroscopy was found to be pK_1 = 2.55 ± 0.16 and pK_2 = 4.97 ± 0.02, respectively. The equilibria observed for UV-vis spectroscopy corresponded to the deprotonation of the phthalate carboxylates. Figure 3.30 illustrates the proposed protonation equilibria and explains the modulation observed for complex **9** in MCB with KHP upon titration with NaOH. The same argument for **5** applies to **9**, the difference being that the amidic arm displaces the water molecule.

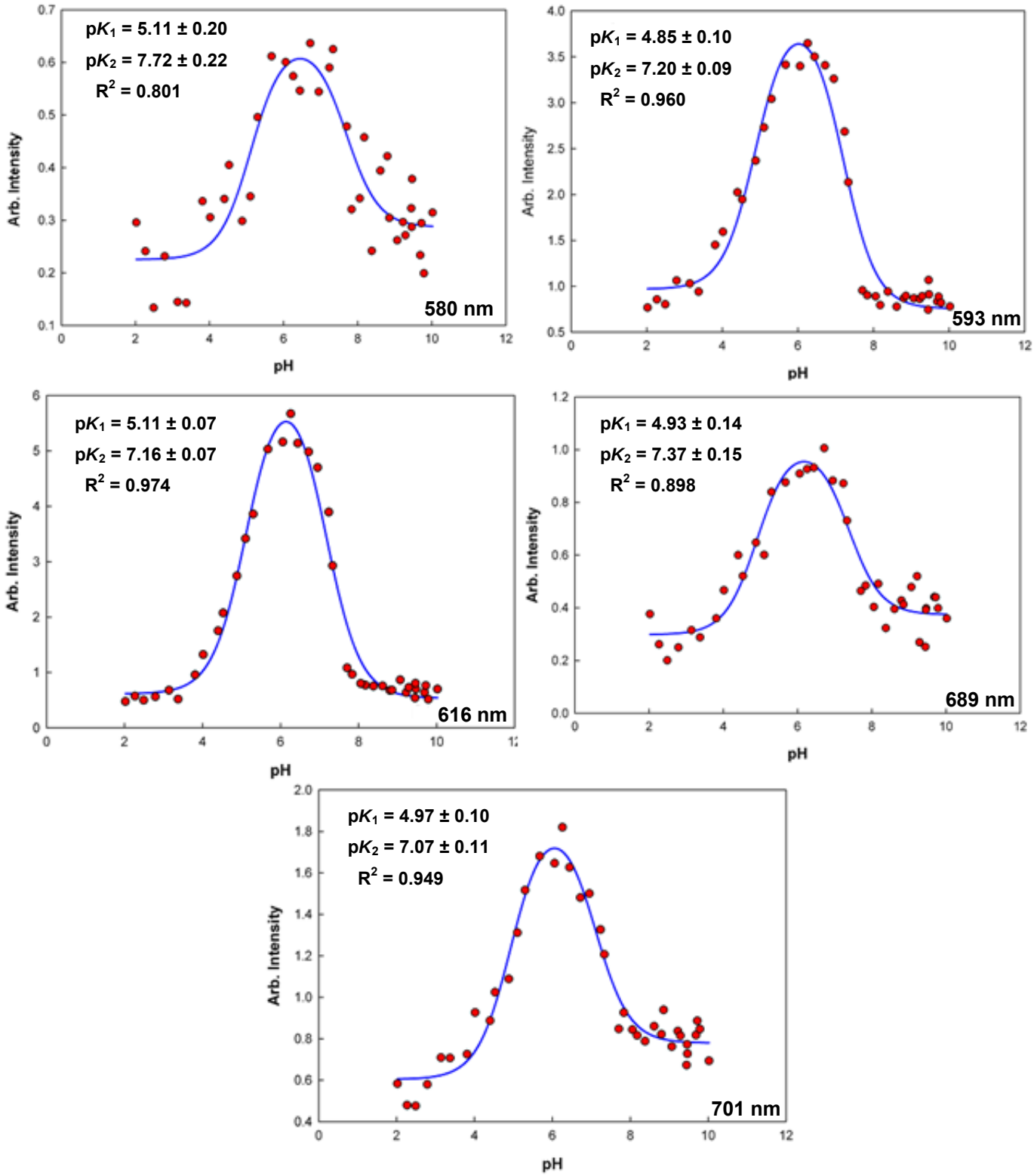


Figure 3.27: Non-linear least square fits for **9** in MCB with KHP corresponding to J = 0, 1, 2, 3 and 4.

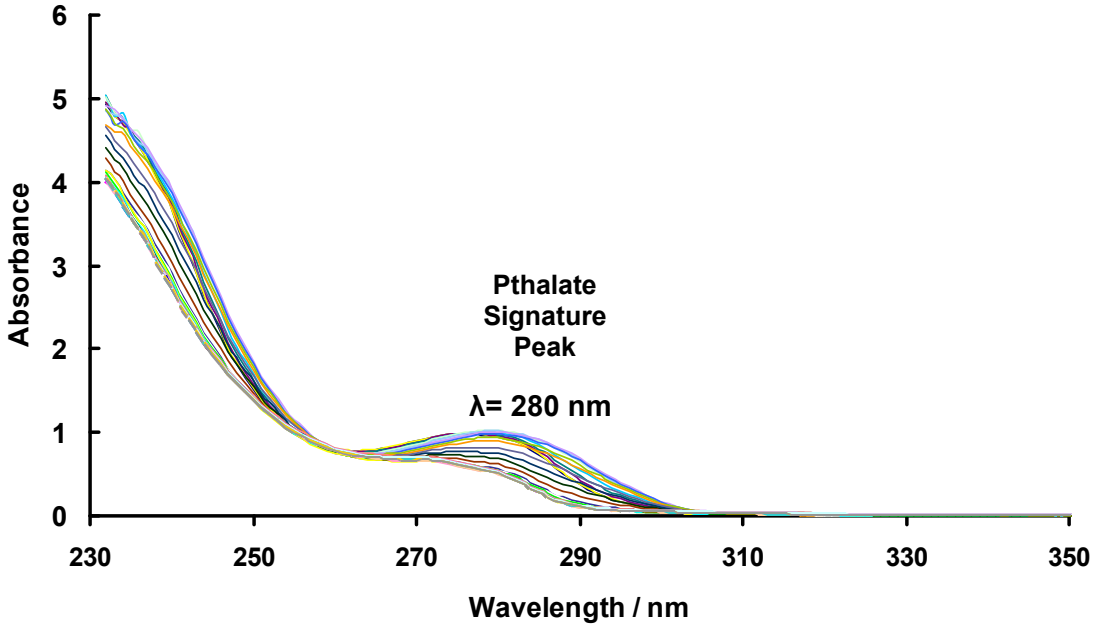


Figure 3.28: Variation in absorbance of **9** in MCB with KHP upon titration with NaOH.

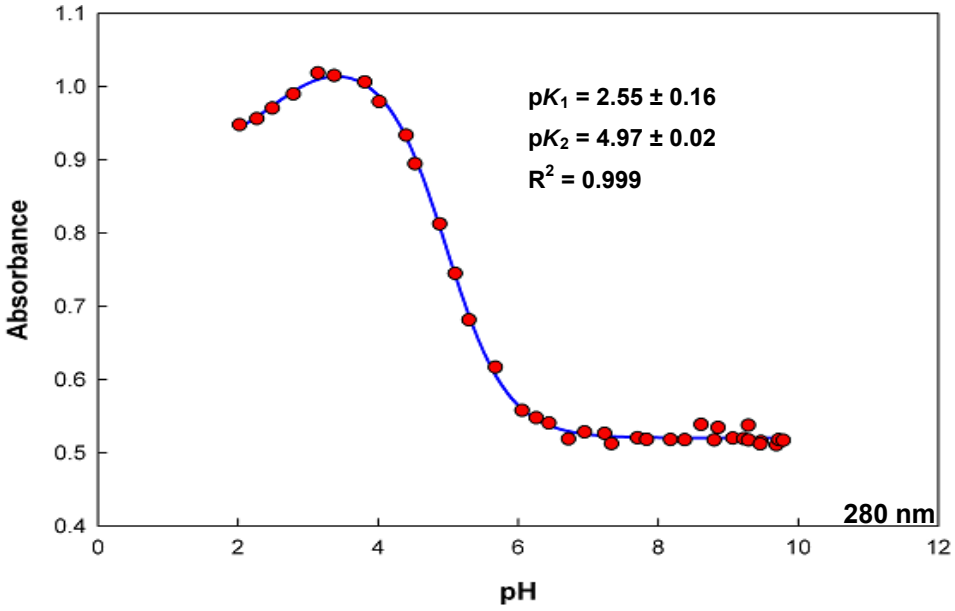


Figure 3.29: Non-linear least square fit for **9** in MCB with KHP corresponding to monitoring at λ = 280 nm across pH range.

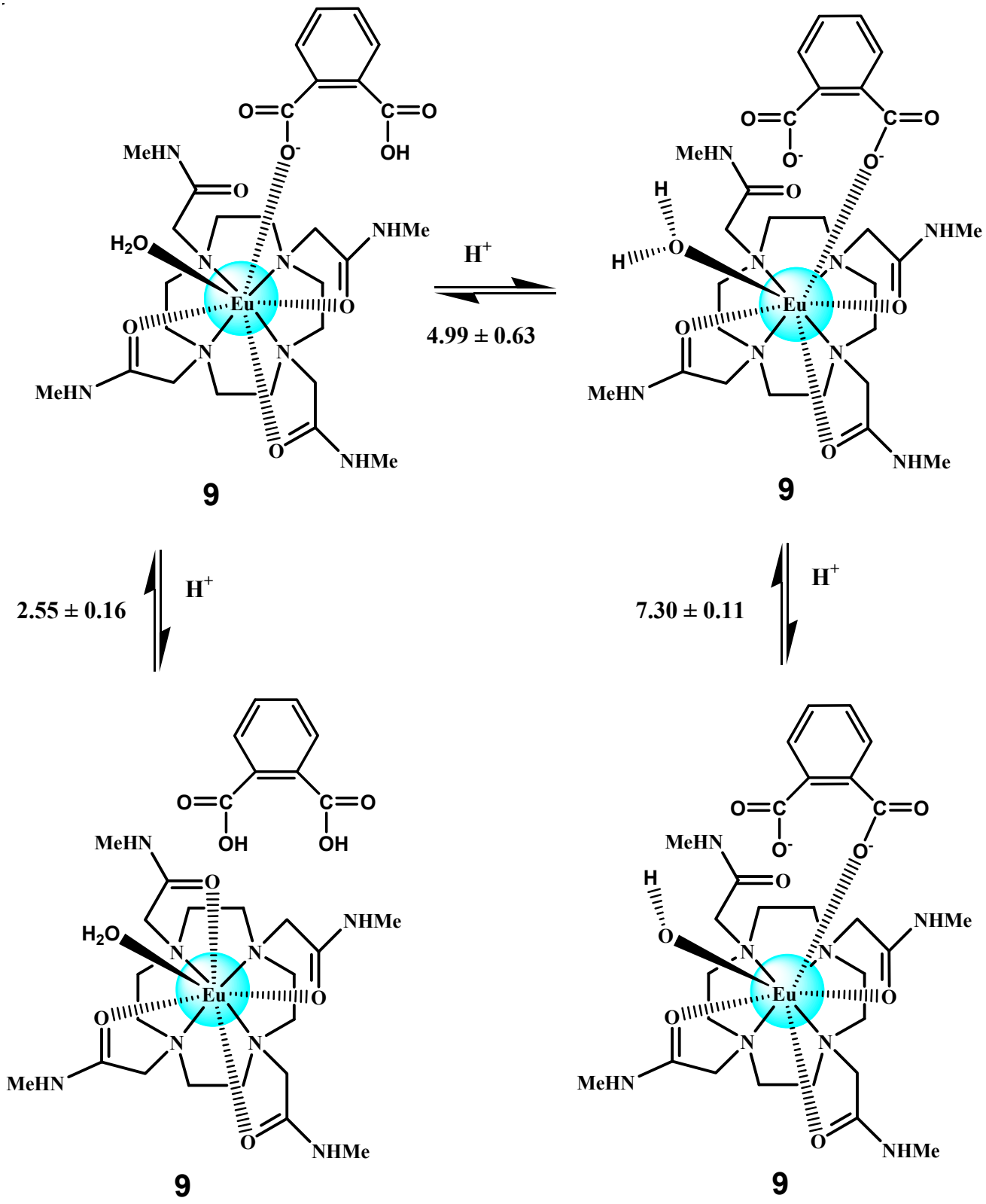


Figure 3.30: Proposed protonation equilibrium for **9** in MCB with KHP upon titration with NaOH.

3.3.1.3 Europium-1,4,7-tris[*N*-methylcarbamylmethyl]-10-(2-hydroxycyclohexyl)-1,4,7,10-tetraazacyclododecane (5) in MCB without KHP

Figure 3.31 depicts the variation of intensity for emission spectrum of **5** in MCB without KHP upon titration with NaOH. The variation of lanthanide emission was found to be constant from pH 2 to 8 for J = 0, 1, 2, 3 and 4. However, for the band J = 0 (580 nm) the intensity increased after pH 8 while the others decreased substantially. From the non-linear least square fits shown in Figure 3.32 it was found that only one protonation equilibrium existed which corresponds to the deprotonation of metal-bound water molecule. The mean pK_a for all J bands were calculated and mean pK_1 was found to be 9.04 ± 0.07. Using UV-vis spectroscopy an absorbance band was observed at λ = 308 nm where the change in absorbance was monitored shown in Figure 3.33. Similarly, a plot of absorbance versus pH shown in Figure 3.34 was fitted using an iterative procedure. For the absorbance band at λ = 308 nm, it was observed that the absorbance between pH 2 and 8 remained between 0.03 to 0.05 absorbance units and increased to 0.13 at pH 11. Only one protonation equilibrium existed and the mean value was found to be pK_1 = 9.02 ± 0.10 which agreed well with that found when fitting the luminescence data. Figure 3.35 illustrates the proposed protonation equilibrium for **5** in MCB excluding KHP upon titration with NaOH.

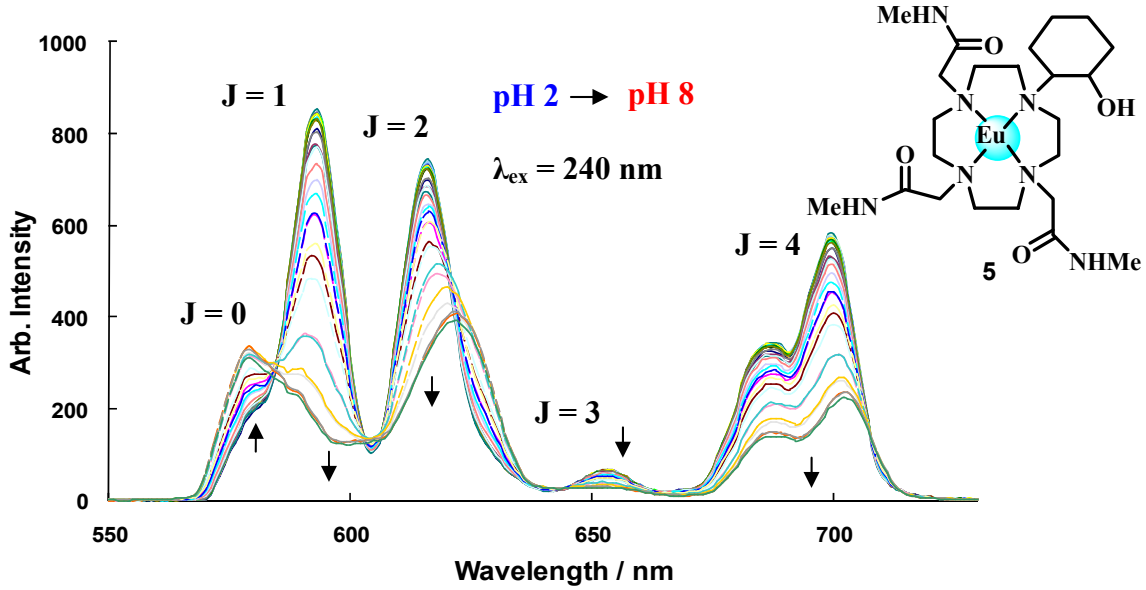


Figure 3.31: Variation of intensity for emission spectrum of **5** in MCB excluding KHP upon titration with NaOH.

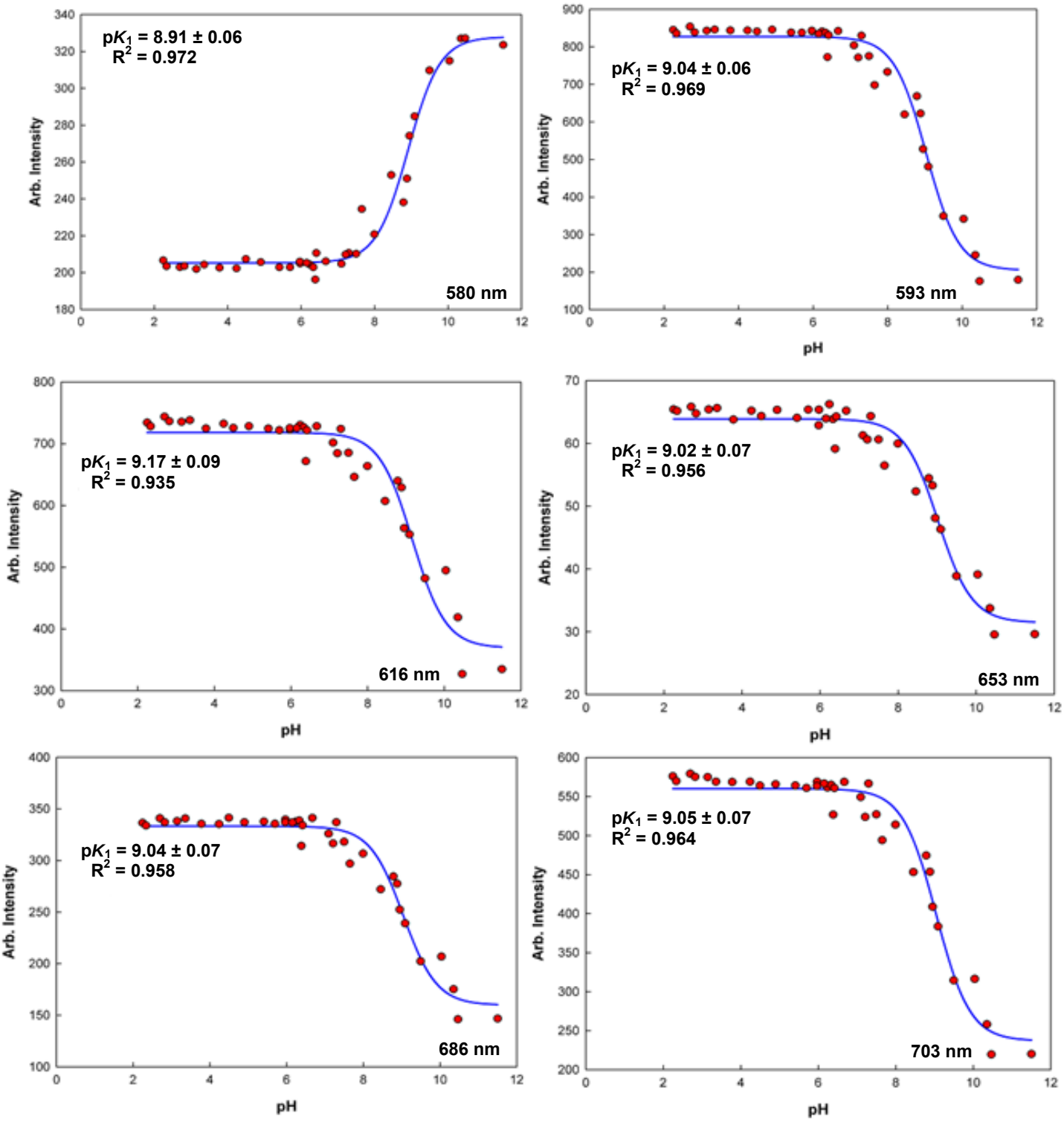


Figure 3.32: Non-linear least square fits for variation of emission band intensity as a function of pH for **5** in MCB excluding KHP corresponding to J = 0, 1, 2, 3 and 4.

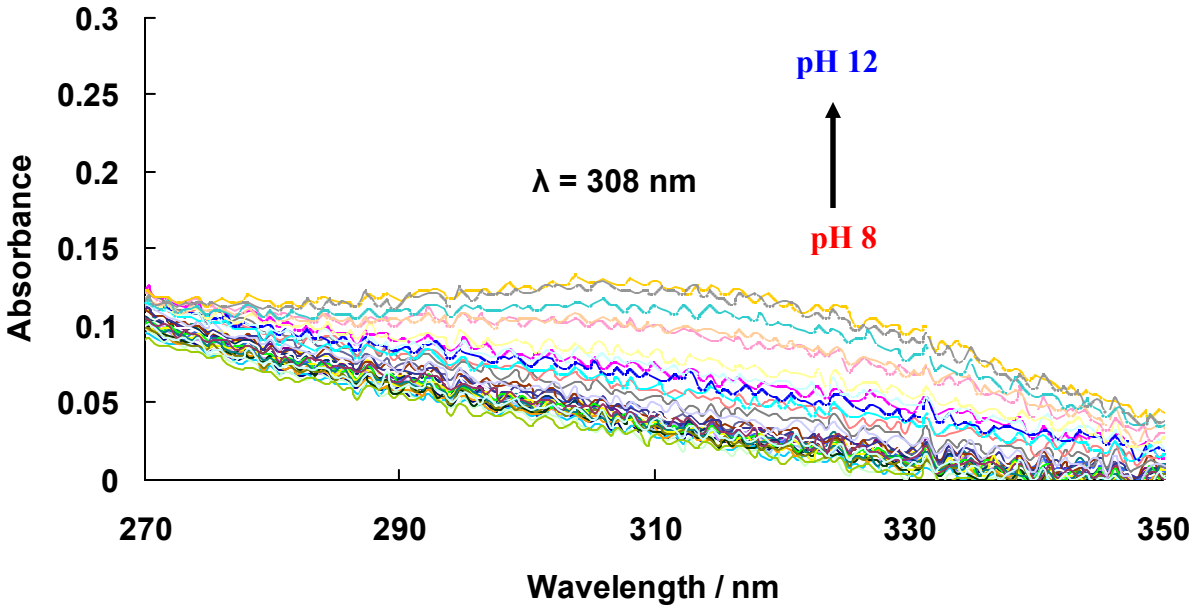


Figure 3.33: Variation in absorbance of **5** in MCB excluding KHP upon titration with NaOH.

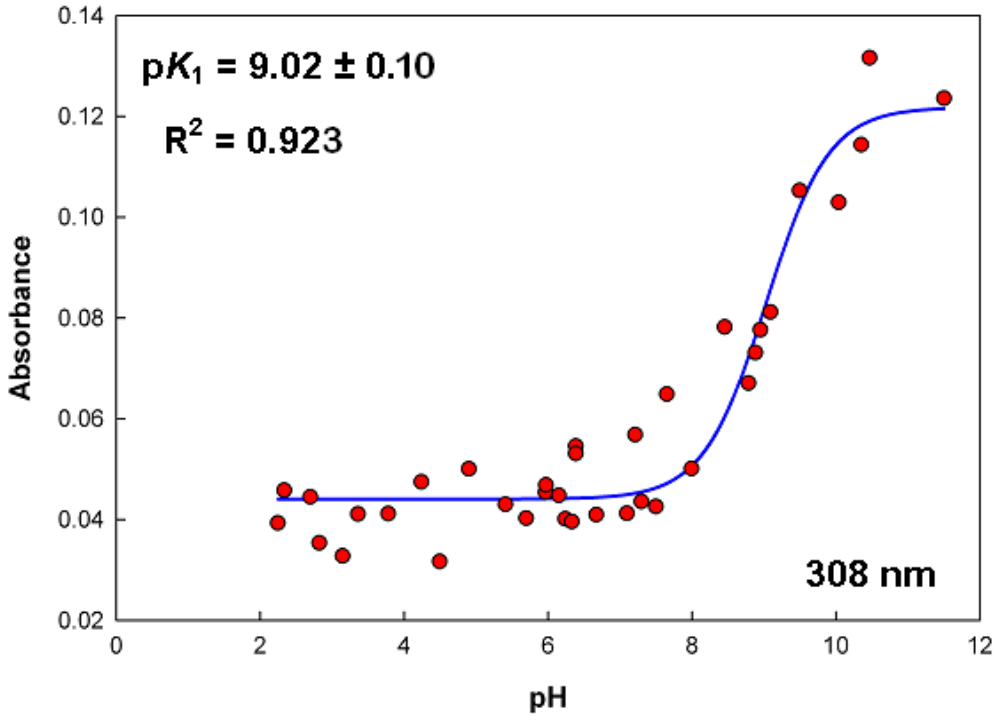


Figure 3.34: Non-linear least square fit for variation of absorbance band intensity as a function of pH for **5** in MCB excluding KHP corresponding to monitoring at λ = 308 nm.

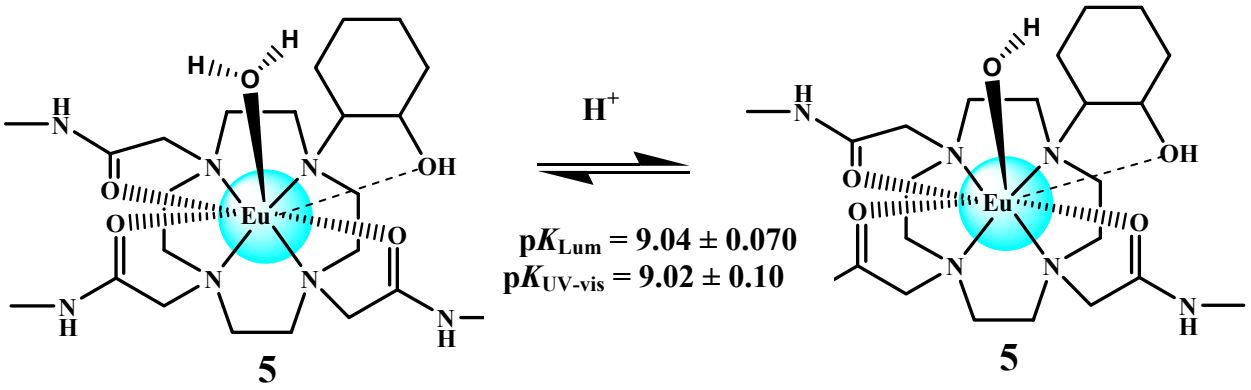


Figure 3.35: Proposed protonation equilibrium for complex **5** in MCB excluding KHP upon titration with NaOH.

3.3.1.4 Europium-1,4,7-tris[*N*,*N*-dimethylcarbamylmethyl]-10-(2-hydroxycyclohexyl)-1,4,7,10-tetraazacyclododecane (7) in MCB without KHP

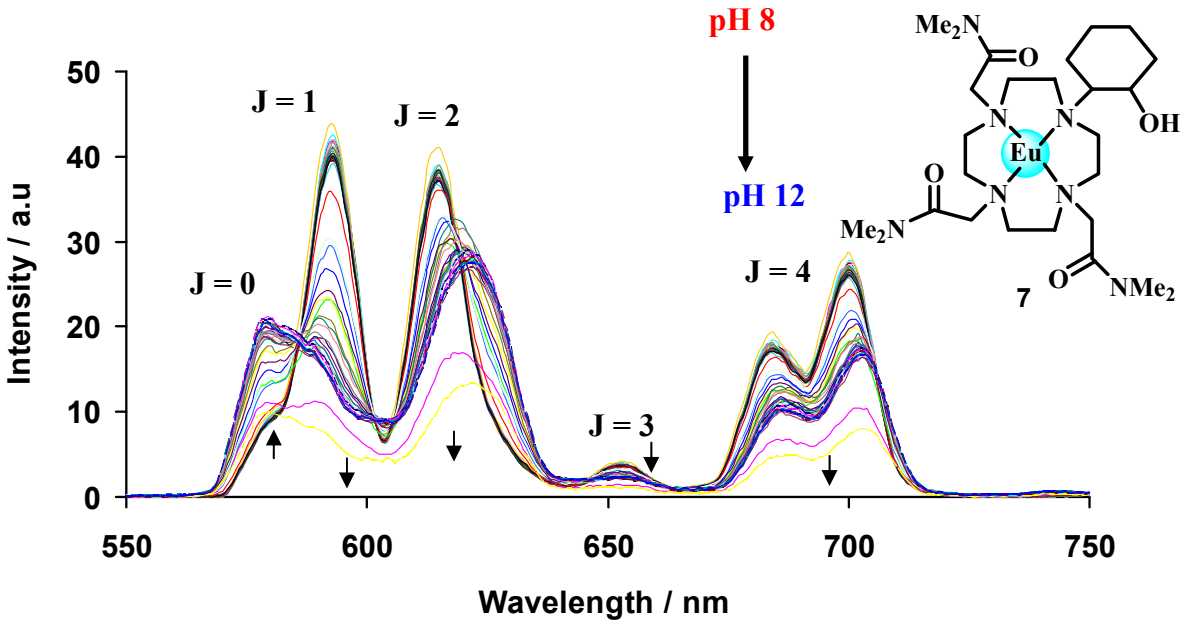


Figure 3.36: Variation of intensity for emission spectrum of **7** in MCB excluding KHP upon titration with NaOH.

Figure 3.36 depicts the variation of intensity for emission spectrum of **7** in MCB without KHP upon titration with NaOH. The variation of lanthanide emission was found almost identical to **5** which was found to be unchanged from pH 2 to 8 for J = 0, 1, 2, 3 and 4. Similarly, the band J =

0 (580 nm) increased after pH 8 while the other J bands decreased substantially. From the non-linear least square fits shown in Figure 3.37 it was found that only one protonation equilibrium existed which corresponds to the deprotonation of the metal-bound water molecule, the mean value was calculated and found to be pK_1 = 8.22 ± 0.08. This value compared to that of **5** was understandably lower. This was attributed to the inductive effects of the methyl groups on the acetamide arms in **7**. The mean pK_1 could not be confirmed using UV-vis spectroscopy where the change in absorbance was monitored at λ = 263 nm shown in Figure 3.38. As can be observed there is no definable spectroscopic pK_a only scatter due to the absence of phthalate in solution shown on Figure 3.39. Figure 3.40 illustrates the proposed protonation equilibrium for **7** in MCB excluding KHP upon titration with NaOH which could only be elucidated using the luminescence data.

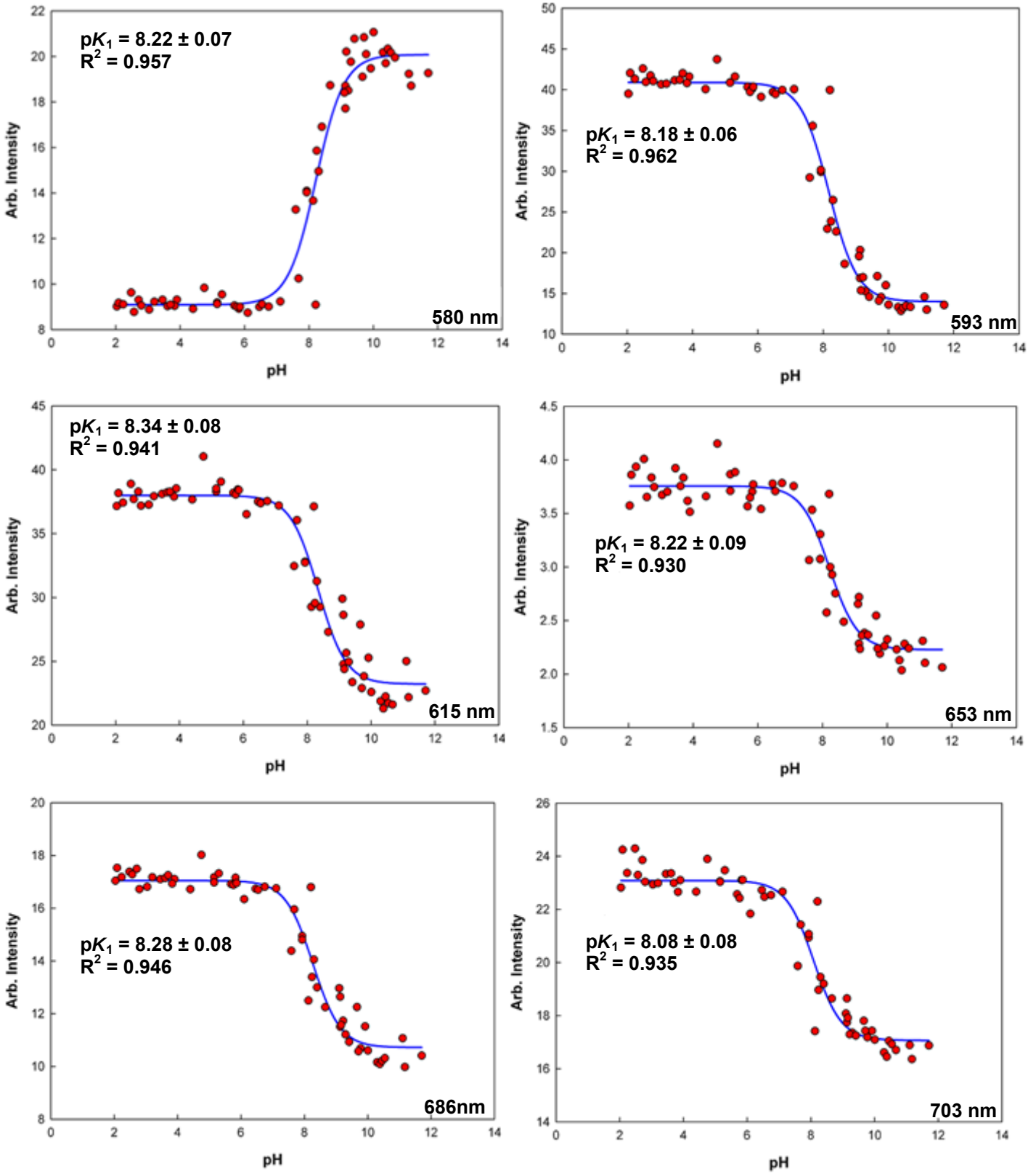


Figure 3.37: Non-linear least square fits for **7** in MCB excluding KHP corresponding to J = 0, 1, 2, 3 and 4.

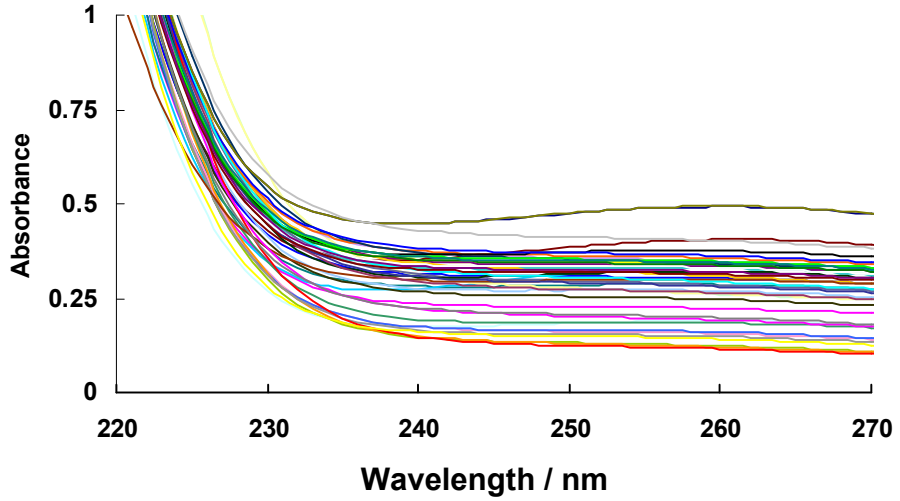


Figure 3.38: Variation in absorbance of complex **7** in MCB excluding KHP upon titration with NaOH.

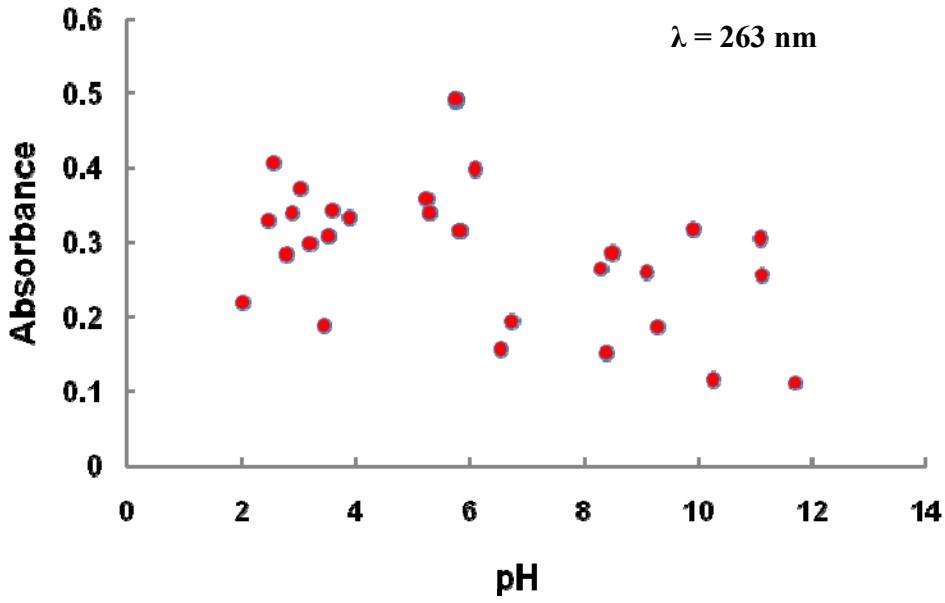


Figure 3.39: Scatter of the absorbance (λ = 263 nm) observed for **7** in MCB excluding KHP across pH range from 2 to 12.

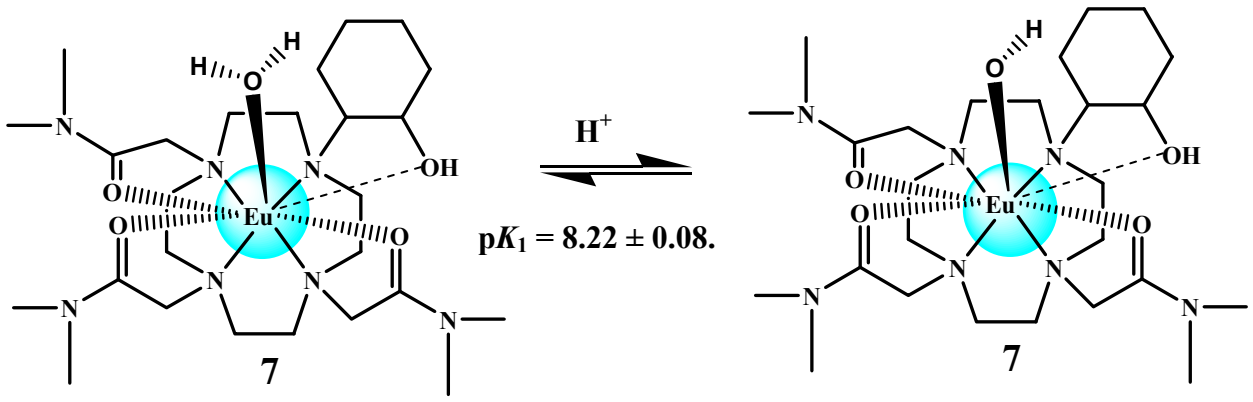


Figure 3.40: Proposed protonation equilibrium for **7** in MCB excluding KHP upon titration with NaOH.

3.3.1.5 Europium-1,4,7-tris[*N*-methylcarbamylmethyl]-10-(2-hydroxycyclohexyl)-1,4,7,10-tetraazacyclododecane (5) in Water

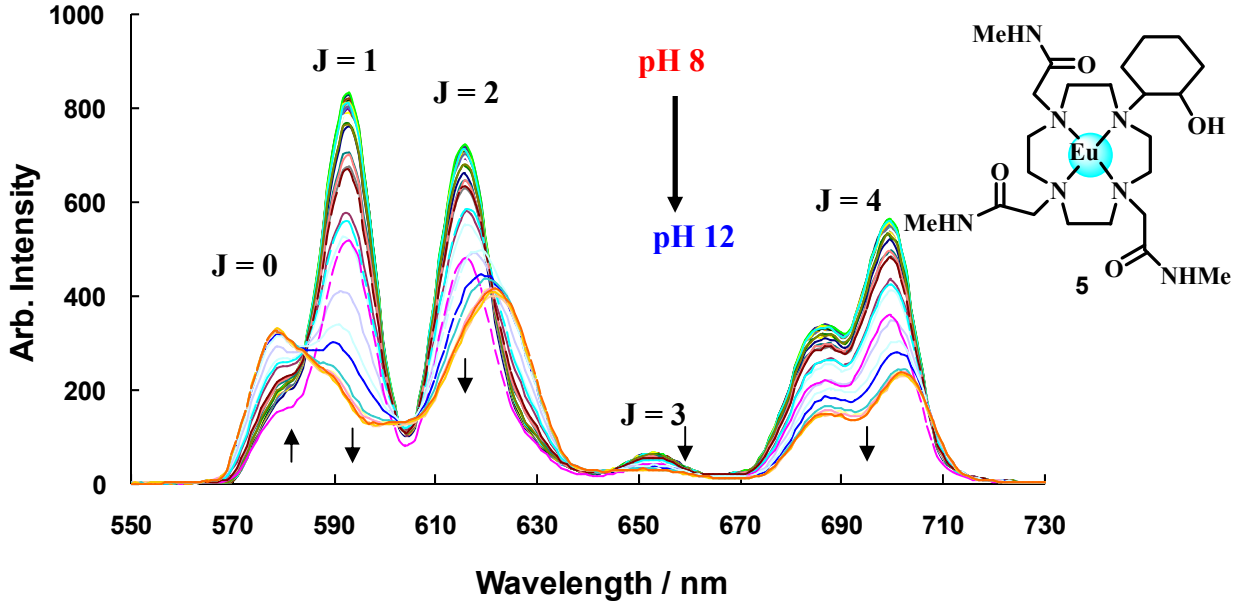


Figure 3.41: Variation of intensity for emission spectrum of **5** in water upon titration with NaOH.

Figure 3.41 depicts the variation of intensity for emission spectrum of **5** in water upon titration with NaOH. The variation of lanthanide emission was found to be constant from pH 2 to 8 for

J = 0, 1, 2, 3 and 4. The J = 0 (580 nm) band increased after pH 8 while the others decreased substantially. From the non-linear least square fits shown in Figure 3.42 it was found that only one protonation equilibrium existed which corresponds to the deprotonation of metal-bound water molecule where $pK_1 = 8.69 \pm 0.07$. This was further confirmed using UV-vis spectroscopy where the change in absorbance at $\lambda = 313$ nm was monitored shown in Figure 3.43. A plot of absorbance versus pH shown in Figure 3.44 was fitted using an iterative procedure. Similar to the behavior of the band J = 0 (580 nm) between pH 2 and 8 in luminescence, the absorbance band observed in UV-vis spectroscopy at $\lambda = 313$ nm remained relatively unchanged between 0.03 to 0.05 absorbance units and increased to 0.13 at pH 11. Again only one protonation equilibrium existed and the mean pK_a was found to be $pK_1 = 8.69 \pm 0.07$ which agreed well with luminescence fits. Figure 3.45 illustrates the proposed protonation equilibrium for **5** in water upon titration with NaOH.

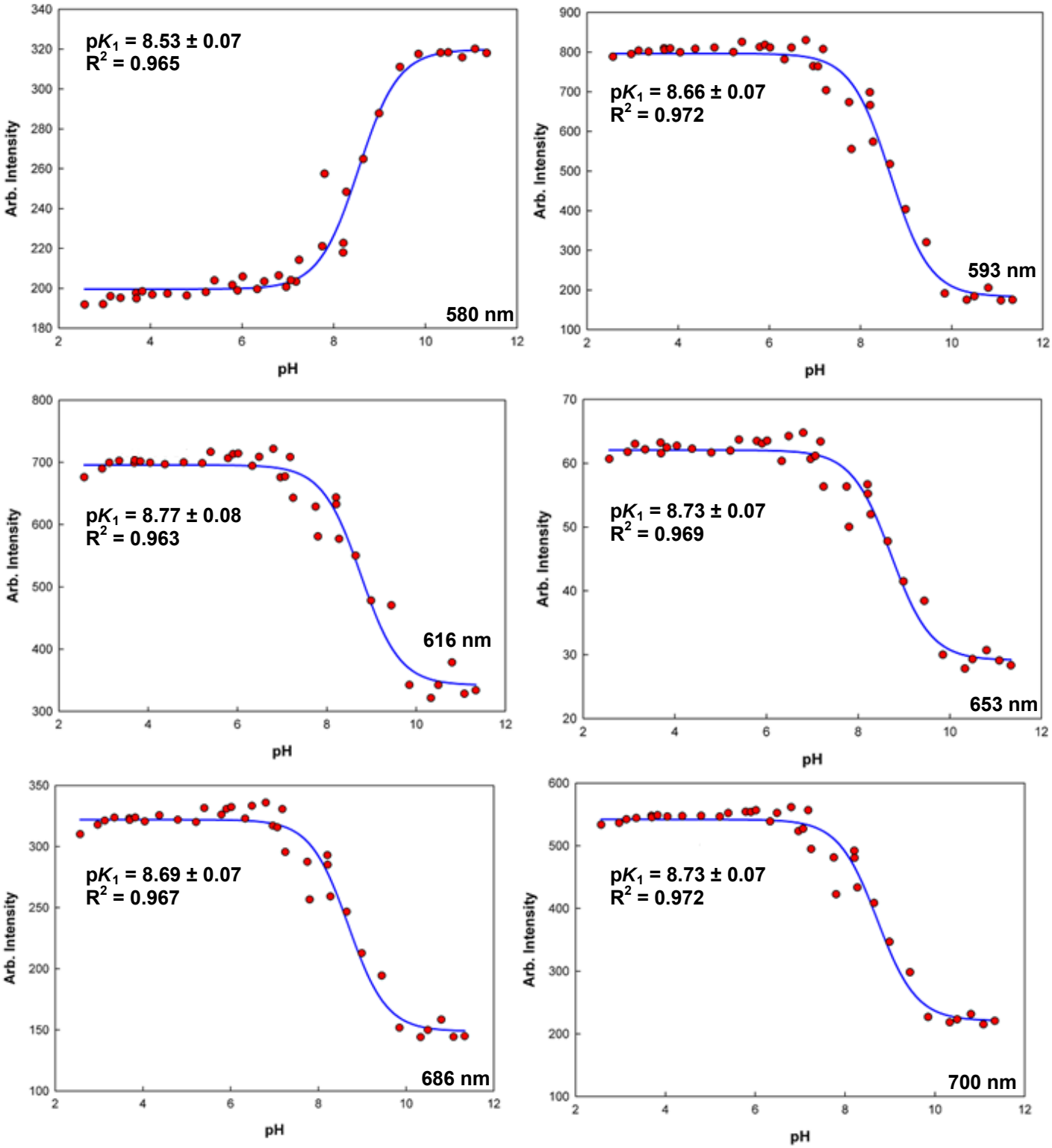


Figure 3.42: Non-linear least square fits for complex **5** in water corresponding to J = 0, 1, 2, 3 and 4.

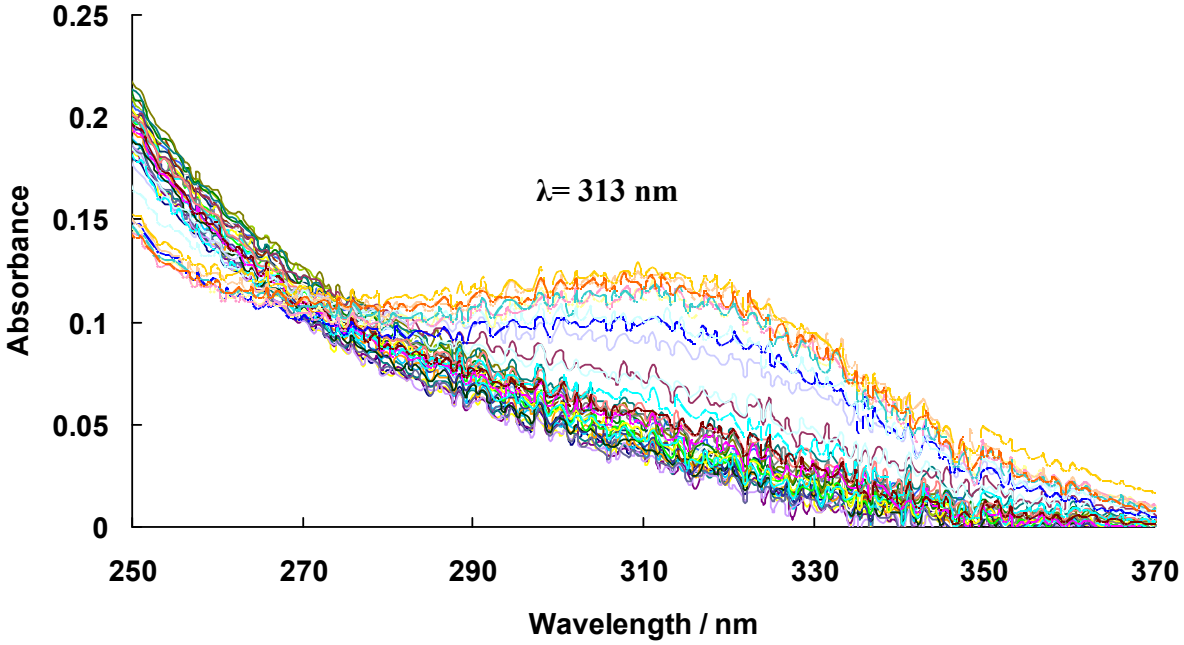


Figure 3.43: Variation in absorbance of **5** in water upon titration with NaOH.

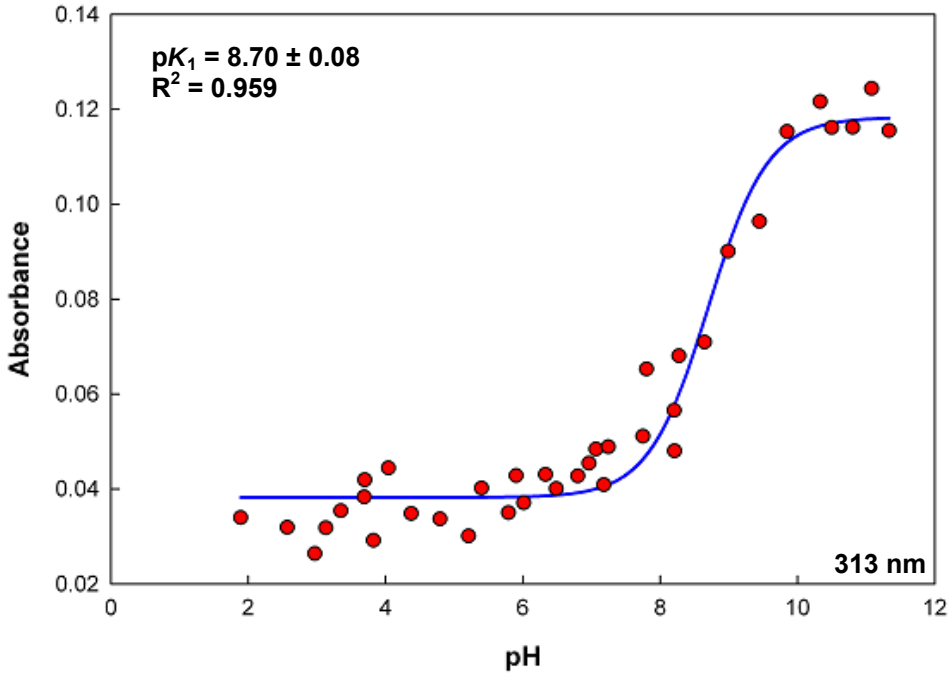


Figure 3.44: Non-linear least square fit for **5** in water corresponding monitoring at λ = 313 nm across pH range.

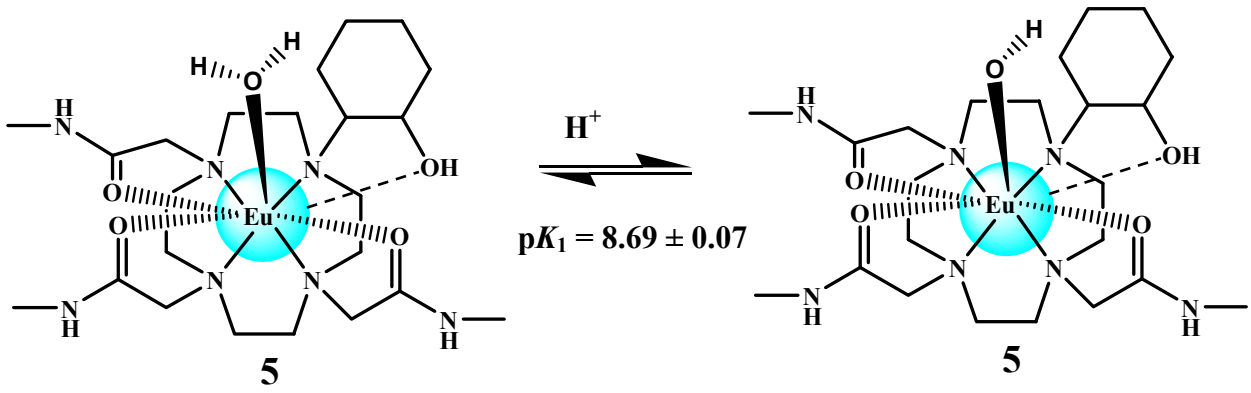


Figure 3.45: Proposed protonation equilibrium for **5** in water upon titration with NaOH.

3.3.2 Lifetime Studies- Determination of *q* for Europium-1,4,7-tris[*N*-methylcarbamyl-methyl]-10-(2-hydroxycyclohexyl)-1,4,7,10-tetraazacyclododecane (5)

The Eu^{3+} ion is an attractive candidate for studying transitions of the 4f electrons because the emissive $5D^0$ state (λ = 580 nm), being non-degenerate, is not split by the ligand field. This means that transitions from $5d^0$ to the $7f^J$ manifold exhibit ligand field patterns arising solely from the degeneracy of the *J*-state of the 7f ground state. The number of water molecules in the inner-coordination sphere (*q*) was indirectly determined by measuring the fluorescent lifetimes of **5** in H_2O and D_2O.

In general, the OH oscillators present on the coordinated water molecule are efficient quenchers of the excited state. Although quenching by OH oscillators may be minimized by using octa- or nonadentate ligands, amide and amine NH oscillators are more prone to quenching in these systems.[293] However O-D oscillators are largely ineffective at quenching fluorescence, therefore it is possible to indirectly determine the number of water molecules in both coordination spheres by comparing the fluorescence lifetimes in H_2O and D_2O.[220] The intensity and lifetime of lanthanide emissions were investigated, and has been found to be sensitive to the local ionic or chiral environment by the perturbation of the singlet, triplet, or lanthanide excited states.

Nearby water molecules in the outer coordination sphere also quench the excited state, albeit to a lesser extent because of their relative distance from the metal center. The effect of distance on the efficiency of vibrational deactivation follows an approximate r^{-6} dependence. For an OH

oscillator that is 2.9 Å from a Ln^{3+} ion, the effect can be assumed to be 100% efficient (i.e., a typical Ln water proton distance from crystallographic analyses of aqua species. Then at a distance of 3.6 Å, the process may be calculated to be 25% efficient and 8% at 4.5 Å.[8] These distances approximate to second- and outer-sphere hydration values and highlight the quenching effect of unbound water molecules. As a consequence, an improved method for assessing the hydration states of Eu, Yb, and Tb complexes has emerged, accounting for the effect of exchangeable XH oscillators and of closely diffusing waters,[222,8] This relationship between the fluorescent lifetimes was modeled in Equation 3.1 and 3.2.[222,224,268]

Furthermore, the relaxation through O-D oscillators is less efficient because only the higher harmonics overlap with the metal excited state, and the Frank-Condon overlap factor is less favorable. There is also an additional contribution of solvent based quenching from the second-sphere as mentioned by Sudnick *et al.*,[268] as the quenching effect is still observable in complexes without coordinated solvent molecules. The coordination of lanthanide complex is a largely ionic interaction and hence the solution hydration states of Eu^{3+} will provide results close to that of Gd^{3+}.

Equations under consideration:

$$q = A[\tau^{-1}_{H_2O} - \tau^{-1}_{D_2O}] \text{.....Equation 1.1}$$

$$q = A[\tau^{-1}_{H2O} - \tau^{-1}_{D2O} - k_{XH}] \text{ .....Equation 1.2}$$

$$\text{where } k_{XH} = \alpha + \beta n_{OH} + \lambda n_{NH} + \delta n_{O=CNH}$$

k_{XH}	given	α	β	γ	δ
0.985		0.31	0.45	0.99	0.075
			n=1	n=0	n=3
0.965		0.31	0.44	0.99	0.075
			n=1	n=0	n=3

$$q = 1.11(k_{H2O} - k_{D2O} - 0.985) \text{ .....Equation 3.1}^{224,268}$$

$$q = 1.11(k_{H2O} - k_{D2O} - 0.965) \text{ .....Equation 3.2}^{222}$$

As mentioned earlier the reason for non-integral and larger than expected q-values is that water molecules in the second coordination sphere of the Eu^{3+} ion, also called 'closely diffusing water molecules' are known to shorten luminescence lifetimes to a small extent.[222,223] Equation 1.1 is easily modified to account for the effects of X–H oscillators and water molecules beyond the first coordination sphere yielding Equation 1.2.[222,224]

$$q = A[\tau^{-1}_{H_2O} - \tau^{-1}_{D_2O} - k_{XH}] \quad \text{.....Equation 1.2}$$

$$\text{where } k_{XH} = \alpha + \beta n_{OH} + \lambda n_{NH} + \delta n_{O=CNH}$$

where n_{OH} is the number of alcoholic O–H oscillators in the first coordination sphere of Eu^{3+}, n_{NH} is the number of secondary amine N–H oscillators in the first coordination sphere of Eu^{3+}, and $n_{O=CNH}$ is the number of amide N–H oscillators in which the amide carbonyl oxygen is in the first coordination sphere of Eu^{3+}. The respective contributions of these X–H oscillators to the quenching of the $^5D_0$ state of Eu^{3+} are $\beta = 0.44$ ms^{-1}, $\gamma = 0.99$ ms^{-1} (calculated as the average of 0.759,[225] 1.0,[225] and 1.2[222]), and δ[222,223] $= 0.075$ ms^{-1}. The contribution to the q-value of a single O–H oscillator in the first coordination sphere of Eu^{3+} is calculated as half the contribution of a water molecule, i.e. $\beta = 1/(2A)$. The value α is the quenching of the excited state of Eu^{3+} by second coordination sphere water molecules.

3.3.2.1 Europium-1,4,7-tris[*N*-methylcarbomylmethyl]-10-2(hydroxycyclohexyl)-1,4,7,10-tetraazacyclododecane (5) in MCB with KHP

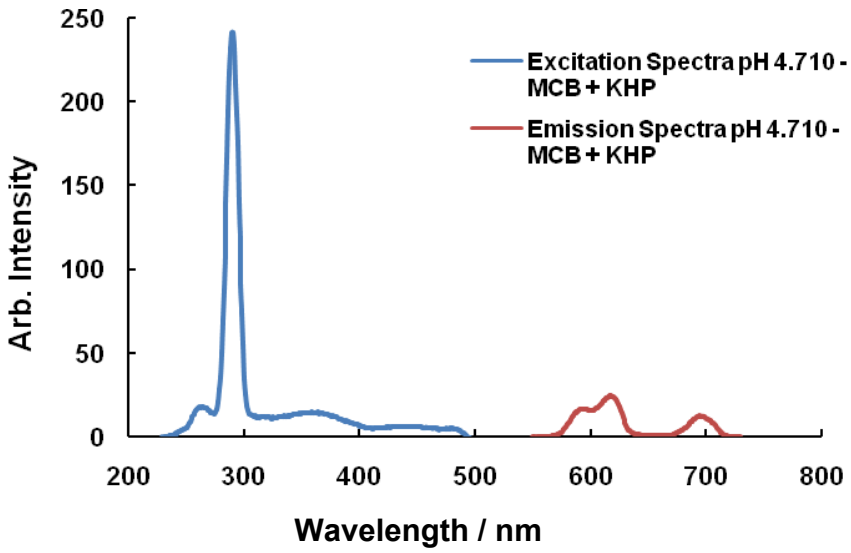


Figure 3.46: Eu^{3+} $^7F_0 \rightarrow {}^5D_0$ excitation and emission spectra of complex **5** containing 1 mM KHP in MCB at 25 ºC.

Table 3.6: Eu^{3+} Excited State Lifetimes of 5 in MCB with KHP.

pH	k_{H_2O}	τ_{H_2O} / ms	k_{D_2O}	τ_{D_2O}/ ms
4.710	3.149	0.3176	0.569	1.758
5.32	3.12	0.3205	0.568	1.761
7.423	2.849	0.3510	0.601	1.664
8.172	2.592	0.3858	0.637	1.570
8.71	2.799	0.3573	0.808	1.238
9.382	2.953	0.3386	0.971	1.030
9.484	2.727	0.3667	1.115	0.900

From the emission spectrum shown in Figure 3.46 it was possible to determine the appropriate wavelength of excitation (240 nm). Table 3.6 shows the Eu^{3+} Excited State Lifetimes of 5 in

MCB with KHP which are the parameters used for the estimation. The hydration number (q) obtained for **5** shown in Table 3.7 in water and deuterated water in MCB with KHP decreases from pH 4.710 to pH 9.484 and range from 1.77 to 0.70 using Equation 3.1[224,268] and from 1.79 to 0.72 using Equation 3.2[222], respectively. The pH points selected were taken before and after the respective pK_as determined using luminescence spectroscopy.

Table 3.7: q values determined at 580 nm for **5** in MCB with KHP.

pH	q values Eq. 3.1	q values Eq. 3.2
4.710	1.77	1.79
5.32	1.74	1.76
7.423	1.40	1.42
8.172	1.08	1.10
8.71	1.12	1.14
9.382	1.11	1.13
9.484	0.70	0.72

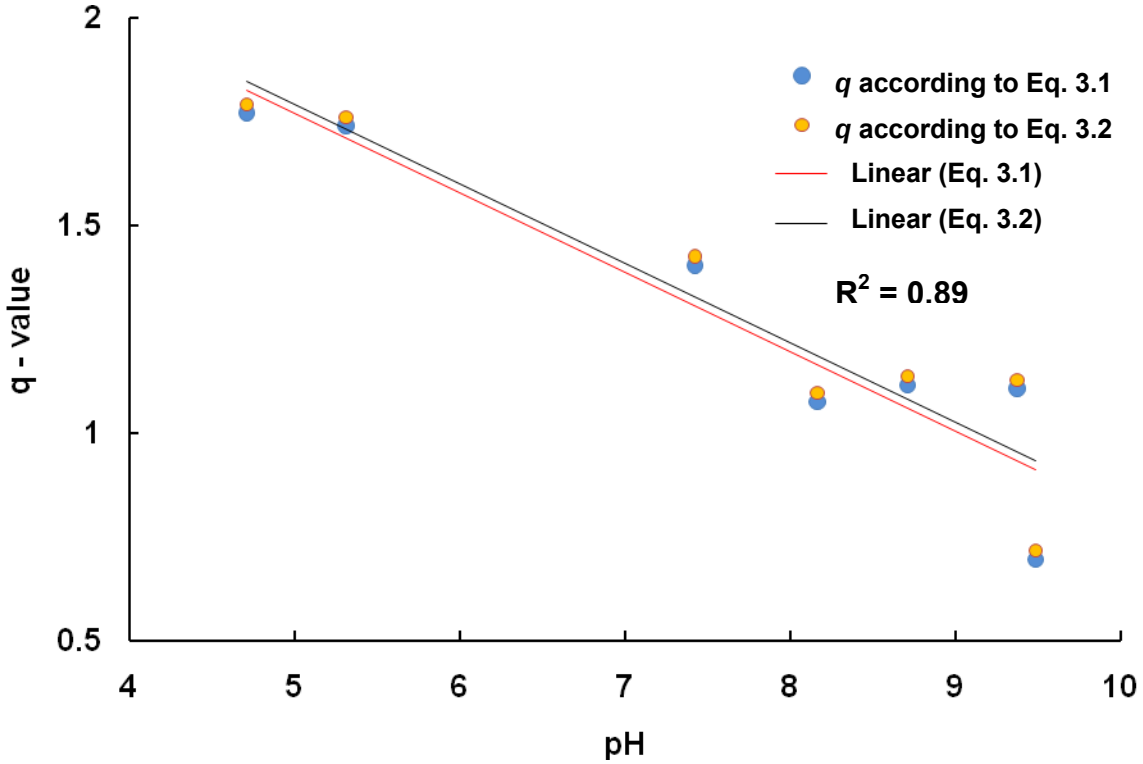


Figure 3.47: Change in q value for **5** across the pH range 4.710 to 9.484.

3.3.2.2 Europium-1,4,7-tris[*N*-methylcarbomylmethyl]-10-2(hydroxycyclohexyl)-1,4,7,10-tetraazacyclododecane (5) in Water

Table 3.8: Eu^{3+} Excited State Lifetimes of 5 in water.

pH	k_{H_2O}	τ_{H_2O} / ms	k_{D_2O}	τ_{D_2O}/ ms
4.375	2.374	0.4212	0.556	1.800
4.795	2.331	0.4290	0.559	1.789
8.275	2.453	0.4077	0.987	1.013
8.645	2.392	0.4181	0.924	1.082

Table 3.8 shows the Eu^{3+} Excited State Lifetimes of molecule **5** in water. The hydration number (q) obtained for **5** shown in Table 3.9 in water and deuterated water from pH 4.375 and 8.645 range from 0.94 to 0.55 using Equation 3.1[224,268] and from 0.95 to 0.56 using Equation 3.2[222], respectively. Again, the pH points selected were taken before and after the pK_a for the hydrolysis of water coordinated to the metal center determined using luminescence spectroscopy.

Table 3.9: q values determined at 580 nm for **5** in water.

pH	q values Eq. 3.1	q values Eq. 3.2
4.375	0.94	0.95
4.795	0.88	0.90
8.275	0.55	0.56
8.645	0.55	0.56

Of particular significance is that a single water molecule is coordinated to the metal center corroborating the results obtained from solid state analyses. It is an important feature when designing a potential MRI-CAs as it increases the difference in contrast between normal and diseased tissue.

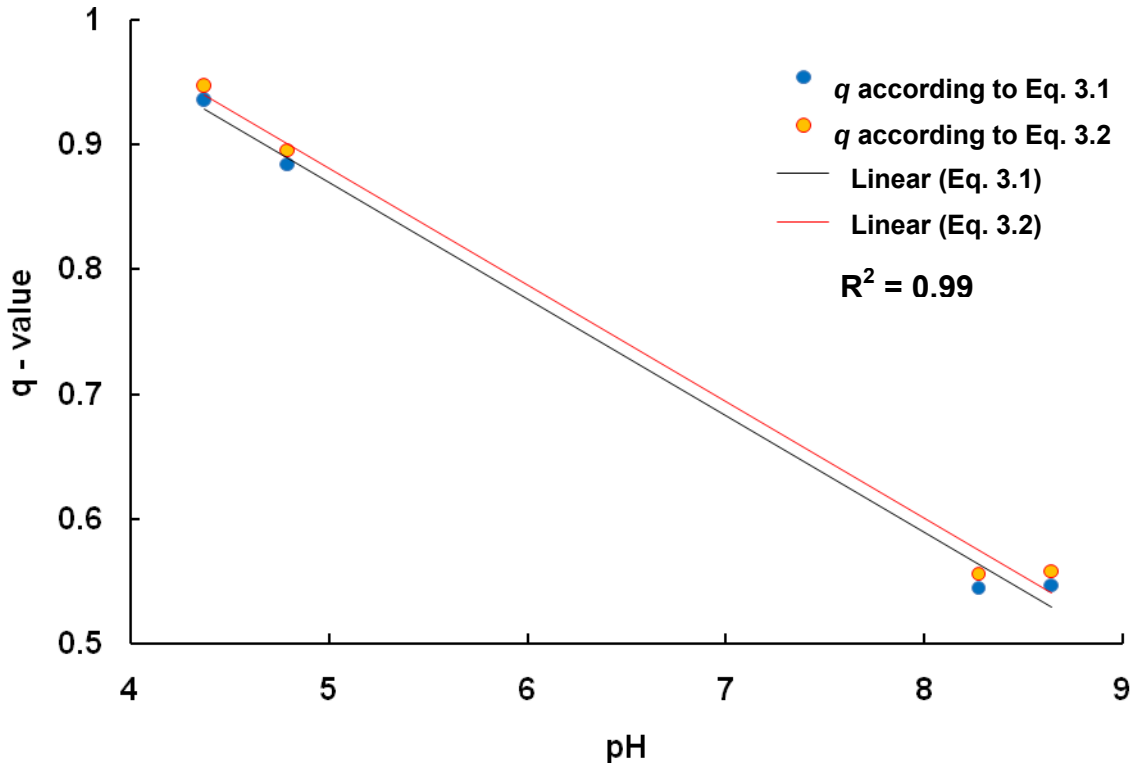


Figure 3.48: Change in *q* value for **5** across the pH range 4.375 to 8.645.

3.4 Cyclic Voltammetry of Eu-complexes across pH Range

In a typical cyclovoltammetric experiment a stationary working electrode is dipped into an electrolyte solution. In order to minimize the ohmic resistance a three electrode arrangement is preferable. In this methodology, the current passes between the working electrode and a counter electrode. The potential of the working electrode relative to the reference electrode is varied linearly with time with sweeps between 100 $mV.s^{-1}$ to 1000 $mV.s^{-1}$. The current is recorded as a function of potential shown in Figure 3.49. Cyclic voltammetry was performed in order to determine the reduction potentials of the **5** and **9** complexes at selected points across the pH range 2 to 12.

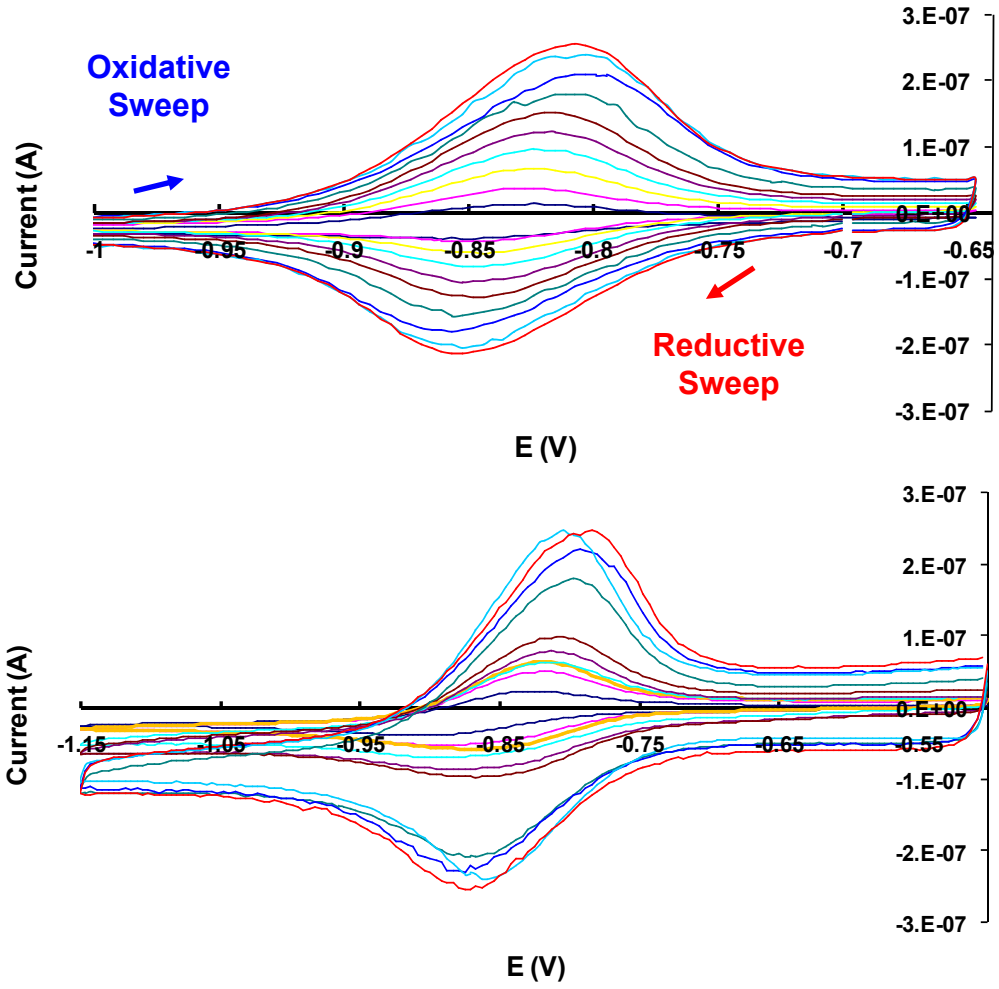


Figure 3.49: Cyclic voltammograms of **5** (top) and **9** (bottom) at pH 6.294 and pH 6.212, when scanned from (100-1000mV).

Provided the rate of electron transfer at the electrode is very fast (which corresponds to an absence of an inhibition), the concentration of the oxidised and reduced species at the electrode surface is dictated by the Nernst equation. Under these circumstances the electrode reaction is said to be reversible.

The cyclic voltammograms (CV) of **5** and **9** were investigated at different scan rates between pH 3 and 11. Figure 3.50 illustrates cyclic voltograms of **5** (red) and **9** (blue) at pH 6.294 and 6.212, respectively. The plot of $E_{1/2}$ versus pH shown in Figure 3.51 illustrates the change in the midpoint potential across the pH range. At low pH between the pH 3 to 6.5, both complexes have an $E_{1/2}$ = -0.83 V however at about pH 8.8 complex **5** has an $E_{1/2}$ = -0.83 V while complex **9** has an $E_{1/2}$ = -0.79 V. At high pH > 10, different electrochemical behavior for both complexes are observed where **5** has an $E_{1/2}$ = -1.01 V and **9** has $E_{1/2}$ = -1.00 V (versus Ag/AgCl), respectively.

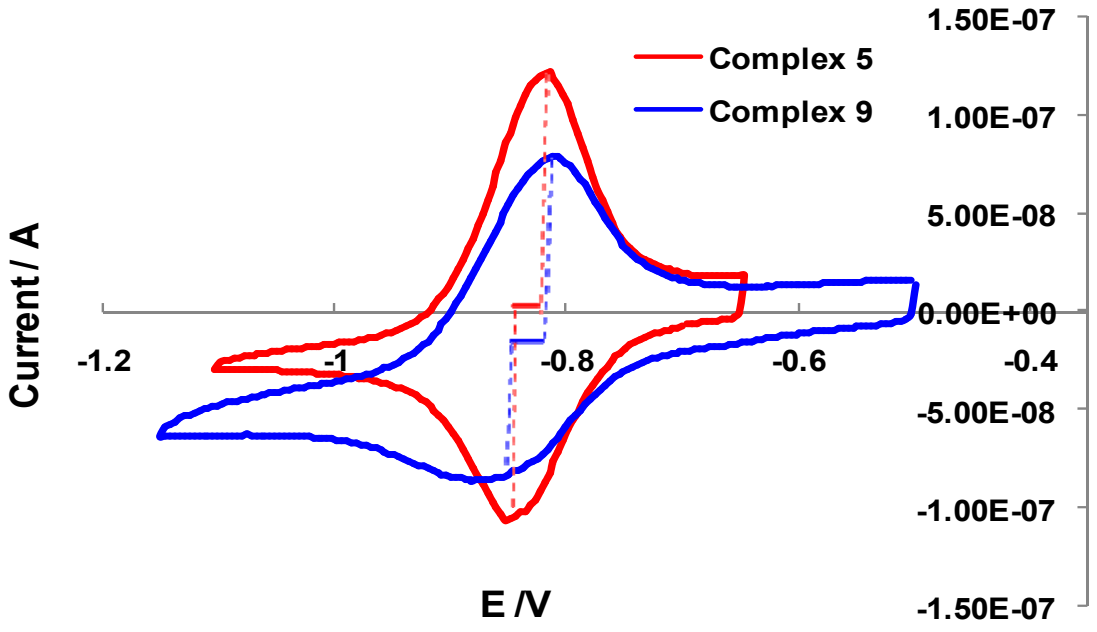


Figure 3.50: Cyclic voltammograms of **5** (in red) and **9** (in blue) at pH 6.294 and 6.212, respectively.

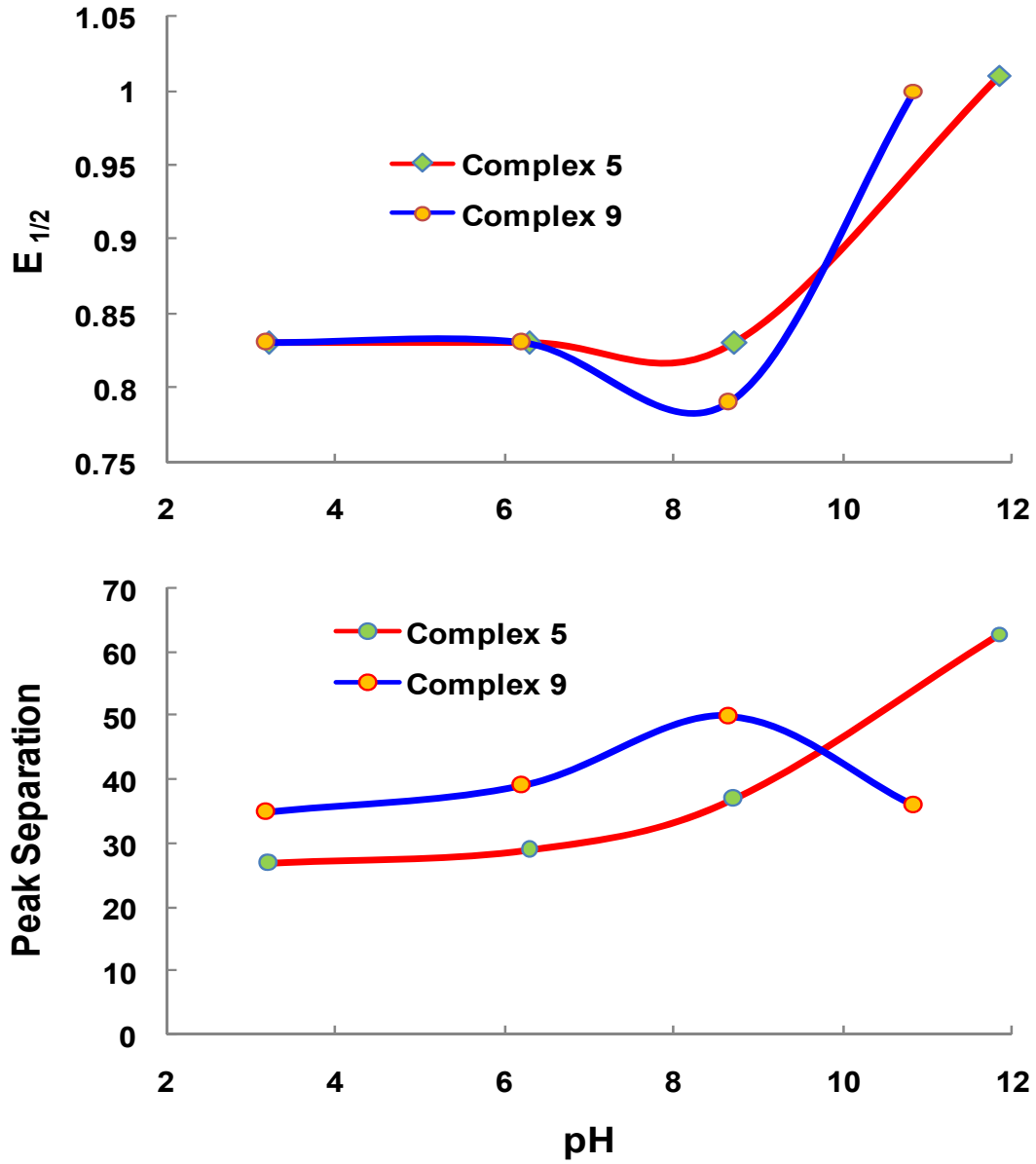


Figure 3.51: Showing $E_{1/2}$ (top) and Peak separation (bottom) versus pH for **5** (red) and **9** (blue).

The peak separation for both complexes behave differently. For a fully-reversible, diffusion-controlled, one-electron reduction, the separation between the cathodic and anodic waves should be 57 mV at 298 K and independant of the scan rate.[270] However, if it is below 57 mV its shows quasi reversible behavior. From Figure 3.52 it is deduced that the electrode reactions in both complexes are quasi reversible at low pH between 3 and 8.8. However at high pH > 10, complexes **5** and **9** have peak separation of 63 mV and 36 mV, respectively. At high pH > 11.5,

the lanthanide ion in complex **5** protrudes out of the macrocyclic cavity, whereas in complex **9** at about pH 10.9 it is still within the cavity of the macrocycle. In the oxidative sweep and reductive sweep, only a distinct wave for both complexes are observed. Usually a well defined symmetrical voltammogram arises from a single electrochemically active species.

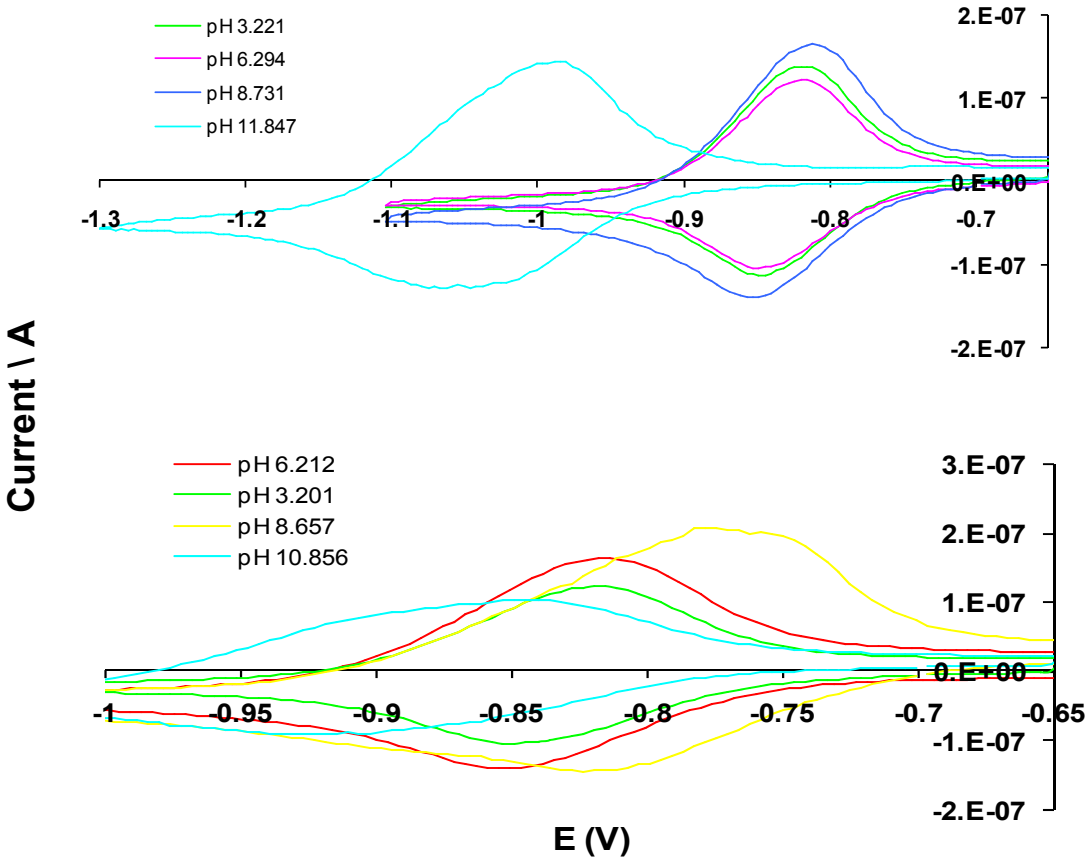


Figure 3.52: Change in potential observed of selected pH points in **5** (top) and **9** (bottom) at constant current versus Ag/AgCl.

The above voltammograms show that the metal is encapsulated within the complexes between pH 3 to 10, however above pH 11 the complex is demetalated and results in the change in potential as shown in Figure 3.52. This result shows that there exists a quasi reversible system for both complexes which is highly dependant on the pH of the system.

Reduction: $[EuL]^{3+} + e^- \longrightarrow [EuL]^{2+}$

Oxidation: $[EuL]^{2+} \longrightarrow [EuL]^{3+} + e^-$

Nicholson *et. al.*[270] have extended the theory of cyclic voltammetry to include electron transfer reactions which is described by the absolute rate equation not shown here. The results of his theoretical calculations have made it possible to use cyclic voltammetry to measure standard rate constants for electron transfer. Thus a system that appears reversible at one scan rate may be made to exhibit kinetic behavior at other scan rates, as indicated by increased separation of cathodic and anodic peak potentials. The standard rate constant is determined for electron transfer by plotting the log of the peak cathodic current, log i_c^p, against the log of the scan rate, log *v*. The slope is used to determine whether the electrochemical reduction is under diffusion control (slope close to 0.5) or is adsorbed on the electrode (slope close to1.0). As shown in Figure 3.53 complex **5** and **9** show a slope close to 1.0 ± 0.09 and 0.93 ± 0.086, respectively, which means the reduction in complexes are not diffusion controlled but the redox active species are adsorbed on the electrode surface.

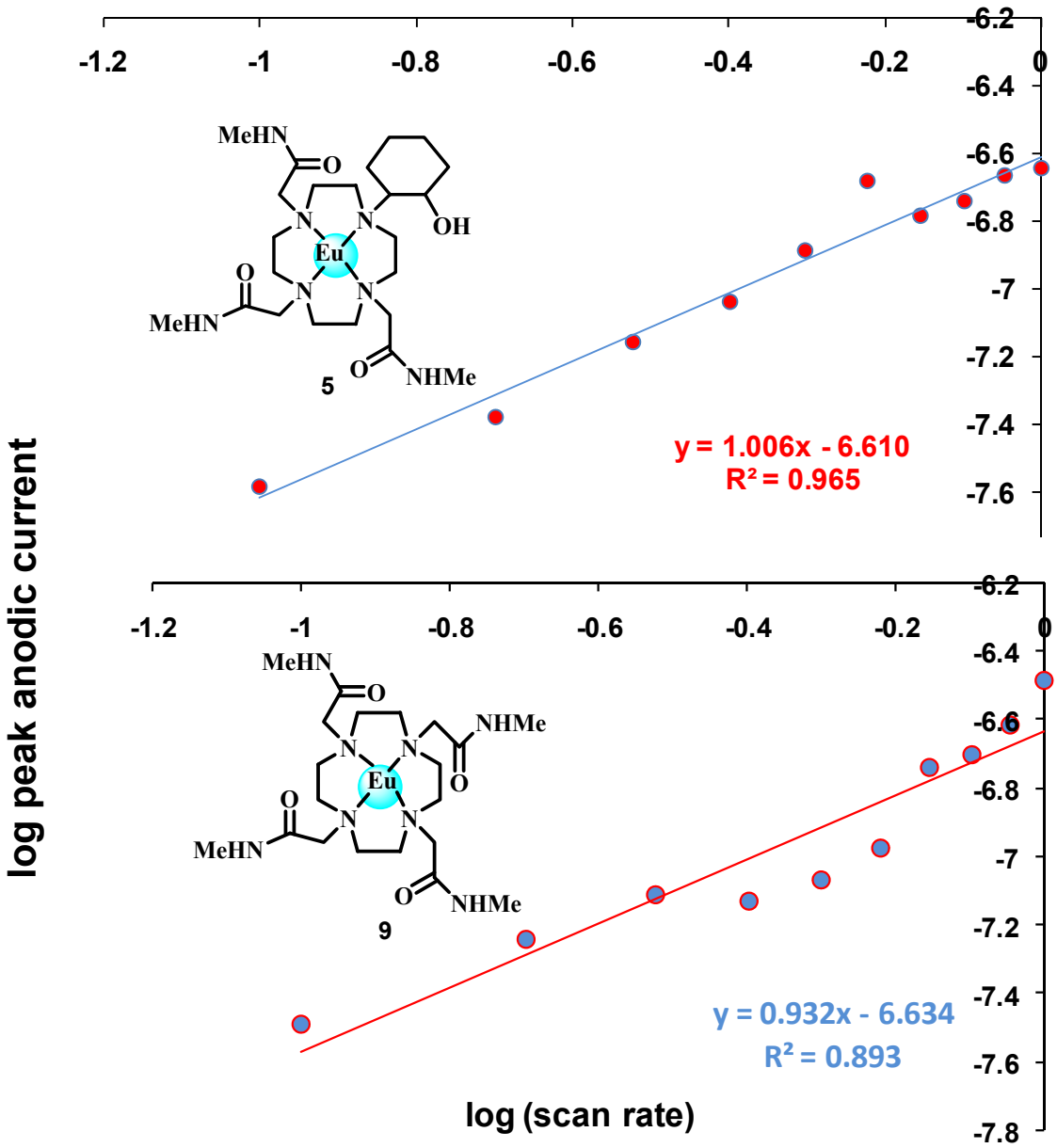


Figure 3.53: Plots obtained using Nicholson Method to determine whether electrochemical reaction is diffusion controlled for **5** and **9**.

3.5 Discussion

Synthetic Aspects

A complete summary of precursors, intermediates, ligands and lanthanide complexes used in this study is provided in Figure 3.54. The two target precursor chloroacetamides were easily synthesized in reasonable yield with no mixtures being formed.[263] These molecules were characterized using conventional methods (*see appendices A, B and C*) which confirmed their chemical identity and purity. The yields obtained compare well with literature.[263] The ring opening reaction of cyclohexeneoxide with cyclen was harnessed to introduce the cyclohexyl group.[264] The synthesis of the *β*-amino alcohol intermediate, [1-(2-Hydoxycyclohexyl)-1,4,7,10-tetraazacyclodecane or molecule **1**], was synthesized in lower yield as previously reported by de Sousa *et. al.*[264] using the direct alkylation strategy. The reason for this decrease can be attributed to the number of recrystallizations it underwent to achieve a pure crystalline product with no traces of starting material or mixtures of bis or tri-substituted cyclen. Molecule **1** was characterized using NMR ($^{1}H/^{13}C$, COSY, C-H correlation – *see appendix A*), ESI-MS (*see appendix B*) and FTIR (*see appendix C*) which confirmed its chemical identity unequivocally. Furthermore, purity was confirmed using its melting point of 145 ºC to make certain all samples were pure and homogenous. Two new octadentate macrocyclic ligands were prepared using the mono substituted 2-hydroxy-cyclohexyl-cyclen with amidic arms introduced by *N*-alkylation at the three available positions on the cyclen backbone. The choice of pendant groups originated from the fact that hydroxyalkyl pendant groups are activated by metal ion coordination to become potent nucleophiles[294-297] while amide groups slow down demetalation of complexes.[298,299] The amide ligand **2**, 1,4,7-tris[*N*-methylcarbamylmethyl]-10-(2-hydroxycyclohexyl)-1,4,7,10-tetraazacyclododecane,[68] the *N*,*N*-dimethyl analogue **3**, 1,4,7-tris[*N,N*-dimethylcarbamylmethyl]-10-(2-hydroxycyclohexyl)-1,4,7,10-tetraazacyclododecane[68] and the secondary amide **4,** 1,4,7,10-Tetrakis(methylcarbamylmethyl)-1,4,7,10-tetraazacyclodecane also commonly known as DTMA[146,265] were prepared using established procedures involving the alkylation of molecule **1** with the appropriate α-haloamide derivative. Although two different methodologies were used toward the synthesis the ligands **2** and **3**,

Tsukube and co-workers[68] method was found to be most useful for high yields (< 95 %) and reproducible preparations. All *N*-substituted cyclen based ligands were characterized using conventional methods as described earlier. The lanthanide complexes were prepared in anhydrous acetonitrile by reaction with the lanthanide trifluoromethanesulfonate (triflate) salt, and purified by recrystallization. Complexation reactions with Eu^{3+} and Gd^{3+} were successfully achieved using the method developed by Parker and co-workers[265] and resulted in high yields of complex being isolated. All target molecules were characterized using conventional methods (*see appendices A, B and C*) and X-ray crystallography was utilized when possible. The ^{1}H NMR spectra for Eu^{3+} complexes are understandably complex as the ligands in question lack C_4 symmetry and give rise to 16 possible isomers. However, other useful information can be deduced concerning the coordination geometry of these Eu^{3+} complexes. Many studies on related lanthanide complexes of carboxylate or amidic origin have revealed that two major diastereomers are present in solution namely the capped square antiprism and the twisted-square antiprism structure.[136,152] Both asymmetrical complexes **5** and **7** gave rise to four non-equivalent axial ring resonances that shifted to higher frequency compared to other resonances (*see appendices A18 and A22)*. The presence of resonances in the 10 to 25 ppm range suggested that there was a mixture of two major isomers present.[300] In general, the syntheses of Ln-based polyazamacrocycles are very feasible and can be prepared quantitatively. The reproducibility and high yields achieved in this work makes these newly synthesized complexes commercially viable as the reactions are atom economical.

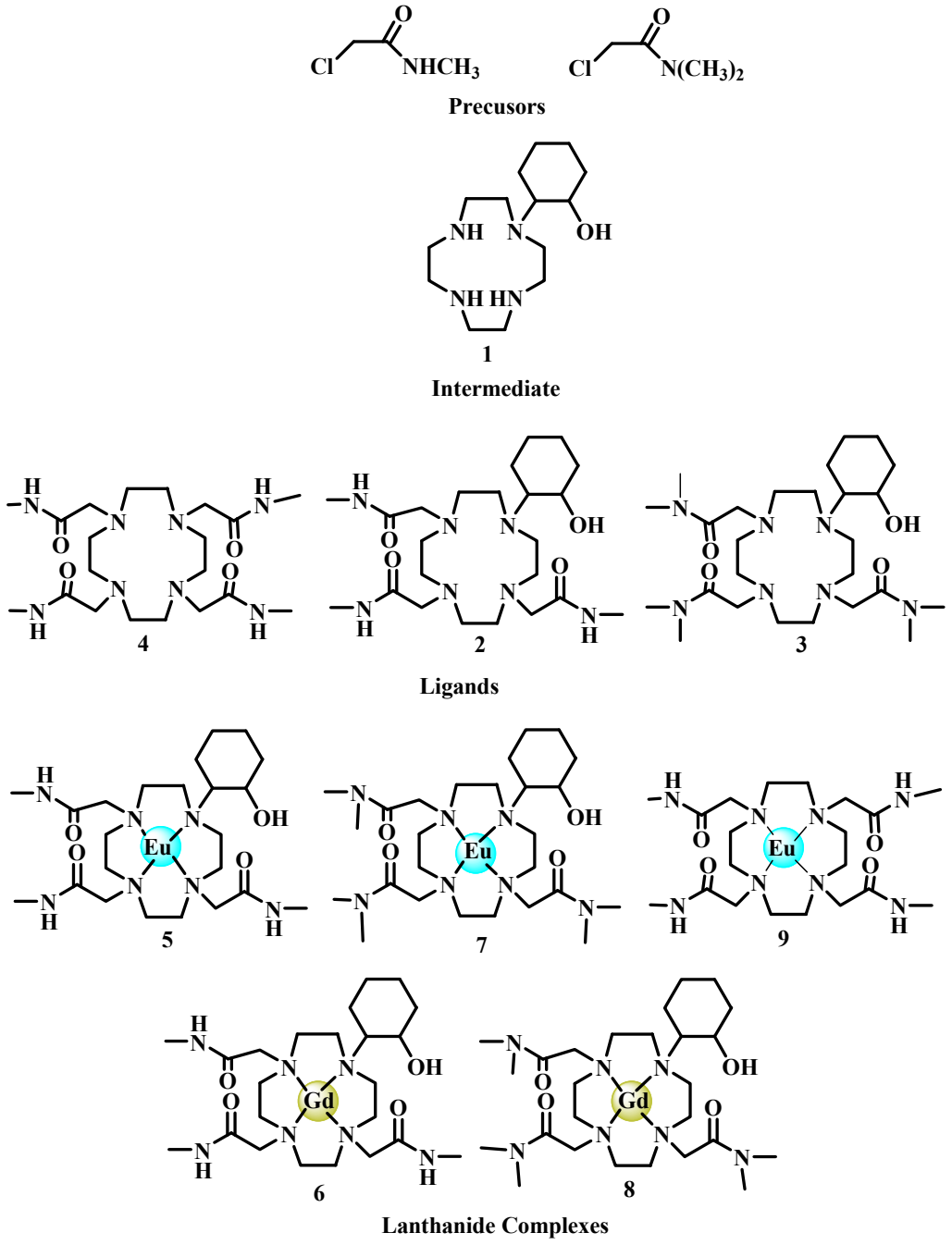


Figure 3.54: Target molecules in the study.

Supramolecular Chemistry

Molecule **2** was isolated as a free base whereas molecule **3** was isolated as a sodium complex. They both formed in the monoclinic crystal system and found to be in the $P_{21/c}$ and $P_{21/n}$ space group, respectively (see Figure 3.4, 3.6 and Table 3.1). Both crystals are stabilized by multiple and cooperative intramolecular N—H···O and O—H···O hydrogen bonding interactions. The average torsion angles N—C—C—N in the cyclen ring for molecule **2** and **3** were 62.45 º and 60.76 º, respectively. The use of Na^+ as a substitute for lanthanide ions in X-ray crystallography has been previously demonstrated by other work performed by Govenlock and co-workers, as the ion is of similar size and thereby a similar coordination requirement.[301] The decrease in average torsion angles for molecule **3** can be attributed to the presence of sodium in the macrocyclic cavity which through electrostatic interactions draws the donor atoms closer to the metal center. The average Na—N (2.595 Å) and Na—O (2.563 Å) bond lengths for molecule **3** confirm this argument. Comparing the average metal to donor distances in the sodium complex with the complexes **5** and **6**, where Eu—N (2.661 Å), Eu—O (2.381 Å) and Gd—N (2.659 Å), Gd—O (2.376 Å), respectively, and found them to very close to eachother and to the sodium-donor distances in **3**.

Three lanthanide complexes are reported where each adopts a capped square anitiprismatic geometry.[143] Molecule **2** formed crystals with both europium and gadolinium to give molecule **5** and **6**, respectively. They both formed in the triclinic and orthorhombic crystal system and found to be in the P_{-1} and Pcca space groups, respectively. The central lanthanide ion coordinates to the four nitrogens of the cyclen ring, the three amide oxygens and the hydroxyl group oxygen of the pendant cyclohexyl ring giving rise to an octadentate system which further coordinates to either water[302] as in the case of molecule **5** or a triflate as in the case of molecule **6** to form a nine coordinate polyhedron. For molecule **5,** the average Eu—N and Eu—O bond distances within the cyclen ring were 2.661 Å and 2.381 Å, respectively. In addition the bond distance between the oxygen from the triflate in the capping position and the central europium metal, Eu—O_{TfO^-}, was 2.443 Å. However, for molecule **6,** the average Gd—N and Gd—O bond distances within the cyclen ring were 2.659 Å and 2.376 Å, respectively. In addition, the bond distance between

the oxygen from the water in the capping position and the central gadolinium metal, Gd—O_W, was 2.442 Å. The closeness of the geometrical parameters between molecule **5** and **6** further demonstrate that Eu^{3+} can be used as a structural probe for corresponding Gd^{3+} analogues. The geometry about the lanthanide ions for molecules **5** and **6** is a distorted capped square antiprism.[143]

Similarly, molecule **4** formed a crystal with europium to give molecule **9**, which is formed in the triclinic crystal system and found in the P_{-1} space group. Molecule **9** also has a nine coordinate environment which arises from coordination to four nitrogens of the cyclen ring, the four oxygen donors on the carboxylic amides and an additional water molecule which caps the macrocycle. It thus assumes a similar distorted capped square anitiprism geometry. For molecule **9,** the average Eu—N and Eu—O bond distances within the cyclen ring were 2.650 Å and 2.388 Å, respectively. In addition, the bond distance between the oxygen from the water in the capping position and the central europium metal, Eu—O_W, was 2.437.

Although the study of the solid-state structure gives the exact information about conformation, bond distances and bond angles potentially important interactions between the complex and its environment is given more accurately from the study of solution structure and specifically the interaction with solvent water molecules and buffering agents which better mimic conditions within the human body.

Spectroscopic pK_as

Table 3.10: Summary of Spectroscopic pK_a Determination.

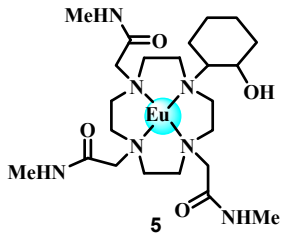
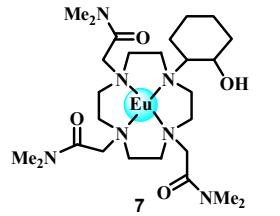
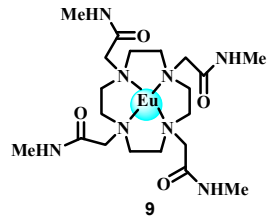
Compound Name	pK_as in Water	Mean pK_as in MCB without KHP	pK_as in MCB with KHP
 5	pK_1 = 8.69 ± 0.07 **UV-vis** pK_1 = 8.70 ± 0.08	pK_1 = 9.04 ± 0.07 **UV-vis** pK_1 = 9.02 ± 0.10	pK_1 = 4.67 ± 0.06 pK_2 = 8.69 ± 0.06 **UV-vis** pK_1 = 2.84 ± 0.24 pK_2 = 5.11 ± 0.10 pK_3 = 11.12 ± 0.62*
 7		pK_1 = 8.22 ± 0.07 **UV-vis** * pK_as could not be verified.	
 9			pK_1 = 4.99 ± 0.63 pK_2 = 7.30 ± 0.11 **UV-vis** pK_1 = 2.55 ± 0.16 pK_2 = 4.97 ± 0.02

Table 3.10 provides a summary of the spectroscopic results obtained using luminescence and UV-vis spectroscopy. The proposed protonation equilibrium of **5** and **9** in MCB with KHP is depicted Figure 3.25 and Figure 3.30, respectively. The non-linear least squares fit results clearly illustrate the profound effect that KHP has on the overall outcome of each experiment. The phthalate moiety clearly behaves as an antenna for both **5** and **9**, which results in enhanced

* invalid pK_a caused by precipitation of europium ions at high pH

emission in the acidic region and decreases after pH 7, which can be attributed to the displacement of pthlalate as the cyclohexyl moiety or amidic oxygen re-coordinates to the metal center, thus modulating the emission of europium complexes across the pH range for both complex **5** and **9**. Comparing the pK_a for the deprotonation of water in **5** and **9** in MCB with KHP, the pK_a for **5** was observed to be larger. This increase can be attributed to the hydrophobic nature of the bulky cyclohexyl pendant. For **5** and **9**, the Eu—O bond length for the coordination of the cyclohexyl oxygen donor is 2.409 Å and 2.389 Å, respectively. From this it could be deduced that there is not a major difference in coordination environment in **5** and **9**. The cyclohexyl group is merely a substitute for the weakest amidic oxygen interaction as can be seen from the bond distances. Although it could be pointed out that the average Eu—O bond length of amidic oxygen donors in **9** is 2.372 Å compared to 2.381 for **5**. This small change is negligible in the bigger scheme of things. Thus by incorporating the cyclohexyl moiety into the ligand architecture the coordination polyhedron was not changed to any great extent. It could be argued that the cyclohexyl group elicits compression on the metal center effectively making the metal smaller which increases the pK_a of the metal bound water molecule by increasing its bond length as illustrated in Figure 3.55. The fact is that cyclohexyl moiety in **5** binds more strongly to the metal center than the acetamide counterparts in **9** causing an increase in pK_a. In addition, it is proposed that the bulky hydrophobic nature of the cyclohexyl moiety that plays a certain role in causing an increase in pK_a of the metal bound water molecule. In general for **5**, it can be observed that it is the hydrophobic nature of cyclohexyl group and ionic like character of the tautomeric amidic arms that leads to a higher pK_a value for the hydrolysis of water coordinated to the metal center being observed. This result agrees well with the hypothesis and this could facilitate fast water exchange when applied to MRI.

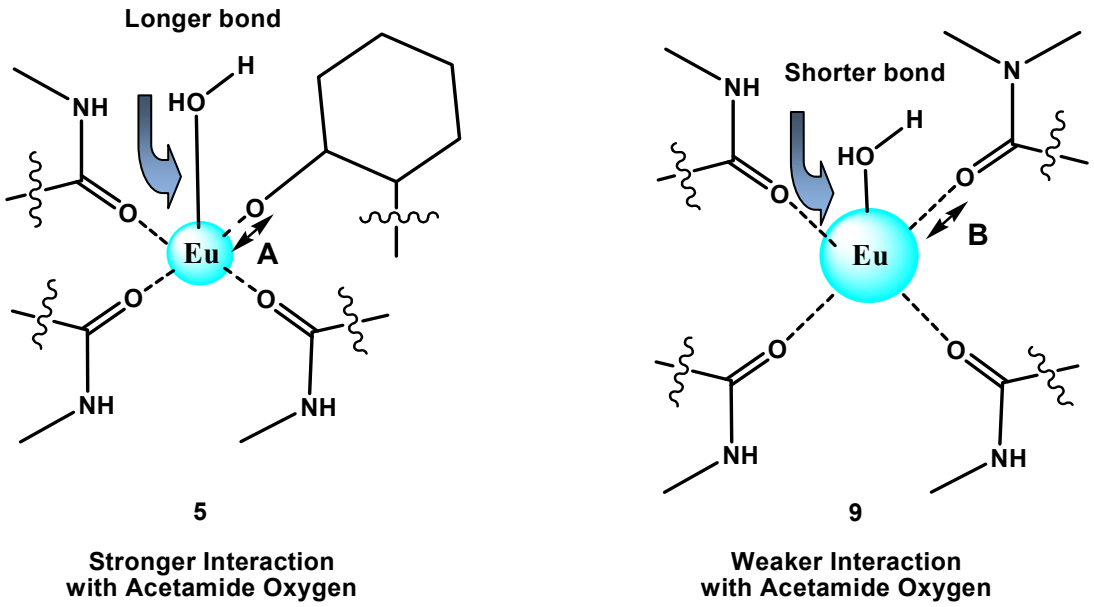


Figure 3.55: Metal compression induced by cyclohexyl moiety causes an increase in pK_a value c of water molecule attached to europium metal center.

The proposed protonation equilibrium of **5** and **7** in MCB excluding KHP is depicted Figure 3.35 and Figure 3.40, respectively. Comparing the pK_a for the hydrolysis of water in **5** and **7** in MCB excluding KHP, again it was observed that the pK_a for **5** is larger. This is possibly due to the weaker inductive effect of **7** and stronger tautomeric effect of **5**. The mere fact that the deprotonation of **7** is not possible and only relies on weaker inductive interaction brought about by the methyl groups on C=O—Eu bond making the Eu—$O_{(W)}$ bond much stronger as illustrated in Figure 3.56. However, for **5** which can be deprotonated it is proposed that the tautomers of the amidic pendant arms form a much stronger C=O—Eu interaction and the presence of a methyl group also contributes with a weaker inductive effect. The net effect results in an increased pK_a of the coordinated water molecule.

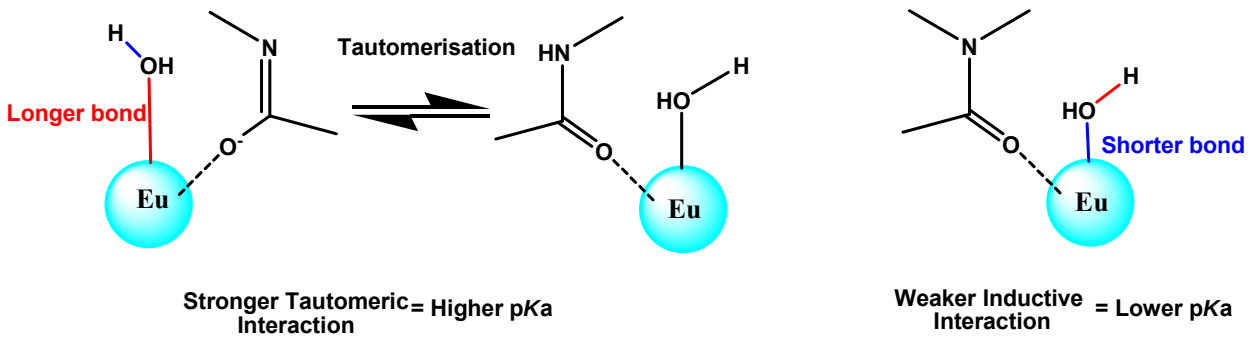


Figure 3.56: Inductive effects can cause a decrease in pK_a value of water molecule attached to lanthanide metal center.

Examining the proposed protonation equilibrium of **5** in water only, depicted in Figure 3.45, it is evident that the other biological buffers do not change the pK_a corresponding to the deprotonation of water from the central metal significantly, taking experimental error into account. The modulation of luminescence and absorbance spectra of **5** in water compared to **5** in MCB without KHP across the pH range was very similar. Their respective weighted pK_a values were found to be pK_1 = 8.69 ± 0.07 and pK_1 = 9.04 ± 0.07, and confirms that although Goods buffers do not coordinate to the metal center, its presence in solution has negligible effects in terms of the actual pK_a values obtained.

Overall the results obtained spectroscopically show that these newly developed complexes do show potential as MRI-CAs since their intensity is highest within the physiological pH range. However, incorporating the cyclohexyl moiety onto the cyclen backbone or using the *di*-methylated acetamide arms instead of the *N*-methylated had a negligible influence on the overall hydrolysis of the metal-bound water molecule. In addition, the phthalate moiety clearly behaves as an antenna and is modulated by the change in pH. Designing a system which incorporates the phthalate moiety into the ligand structure as a potential MRI-CA would be the next step in the right direction.

***q* Values**

The presence of the metal-bound water molecules coordinated to complex **5** in MCB with KHP and water only were observed by evaluating the hydration number (q) using the luminescence methods described earlier, where the rate constant for radiative decay (k) of the $^5D_0$ excited state of Eu^{3+} are measured in H_2O and D_2O.[216-224,268] The details of which are tabulated in Table 3.7 and Table 3.9. From these results it can be seen that whether in water or in MCB with KHP the central metal has single water molecule coordinated to the metal center a very important feature inherent to MRI-CAs. Considering the chemical environment in samples containing the phthalate moiety it is understandable why there is a q value that tends to 2 at low pH < 4.9. Unidentate coordination of phthalate, as illustrated in Figure 3.58, at low pH permits formation of hydrogen bonds with water molecules in the outer coordination sphere, the hydrogen of the outer sphere water molecule then hydrogen bonds to the oxygen of the cyclohexyl moiety. The outer sphere water molecule could also bond to other water molecules that are in close proximity. At higher pH > 7 further phthalate deprotonation alters the hydrogen bonding array to accommodate hydrogen bonded outer-sphere water. The q values obtained show a decrease as pH is increased. It is the above mentioned phenomena which result in an overall decrease in OH oscillators in the coordination polyhedron. From the results obtained it is clear that phthalate moiety coordinates with the central Eu^{3+} ion in a unidentate fashion and the central metal indeed maintains a coordination number of nine.

The q values corroborate well with luminescence spectroscopic data which shows two valid spectroscopic pK_as, corresponding to the phthalate deprotonation followed by the deprotonation of the metal-bound water molecule and where the mean pK_a value was found to be pK_1 = 4.67 ± 0.06 and pK_2 = 8.69 ± 0.12, respectively.

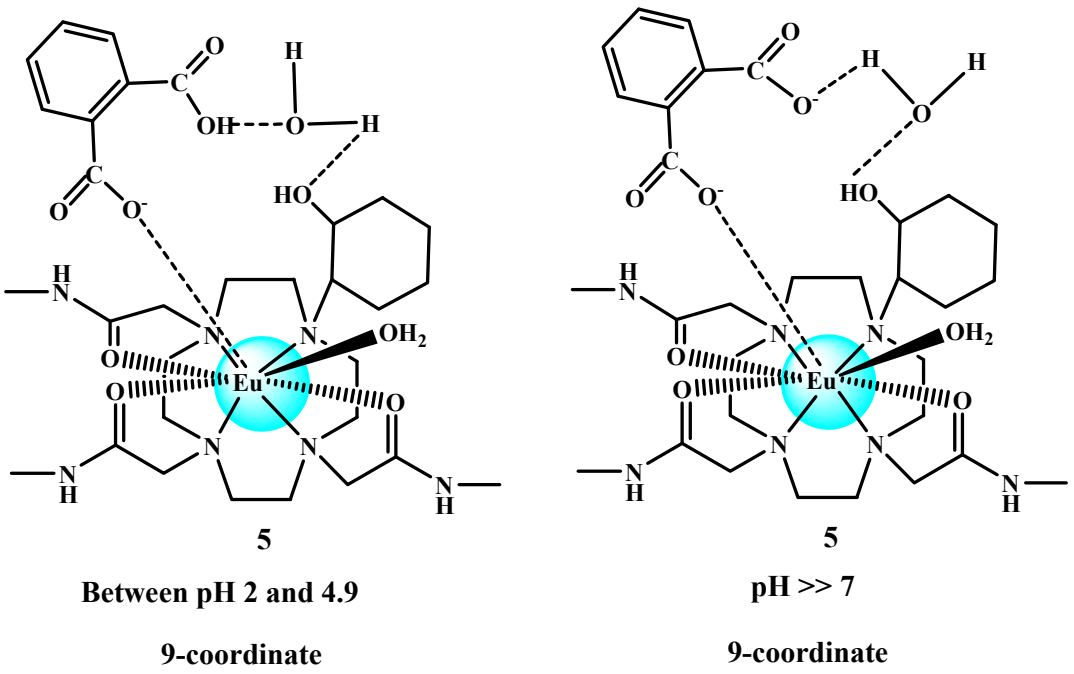


Figure 3.57: The proposed coordination environment of **5** in the presence of KHP.

It is proposed that if phthalate were to bind in a bidentate fashion it will result in the formation of a 7-membered ring chelate, which is highly unstable and will immediately result in the displacement of the metal-bound water molecule. At low pH < 4.9, the negatively charged oxygen atom of the phthalate moiety has a much stronger ionic interaction as compared to the neutral cyclohexyl group and initially causes the cyclohexyl moiety to be displaced. At high pH >7, it is proposed that the opposite occurs where the cyclohexyl group displaces the phthalate resulting in a decrease in emission intensity as observed in the luminescence studies. The slight increase in *q* is attributed to the hydrogen bonding elicited by the cyclohexyl moiety which interacts with outer sphere water molecules. There exists a closely linear relationship between *q* values and the number of protons lost during hydrolysis due to an increase in pH. Figure 3.57 illustrates how the europium metal center maintains its coordination number of nine. Overall, the slight increase in *q* at high pH which should be close to 0.5, is brought about by outer sphere hydrogen bonding between the phthalate and cyclohexyl moiety with outer sphere water molecules.

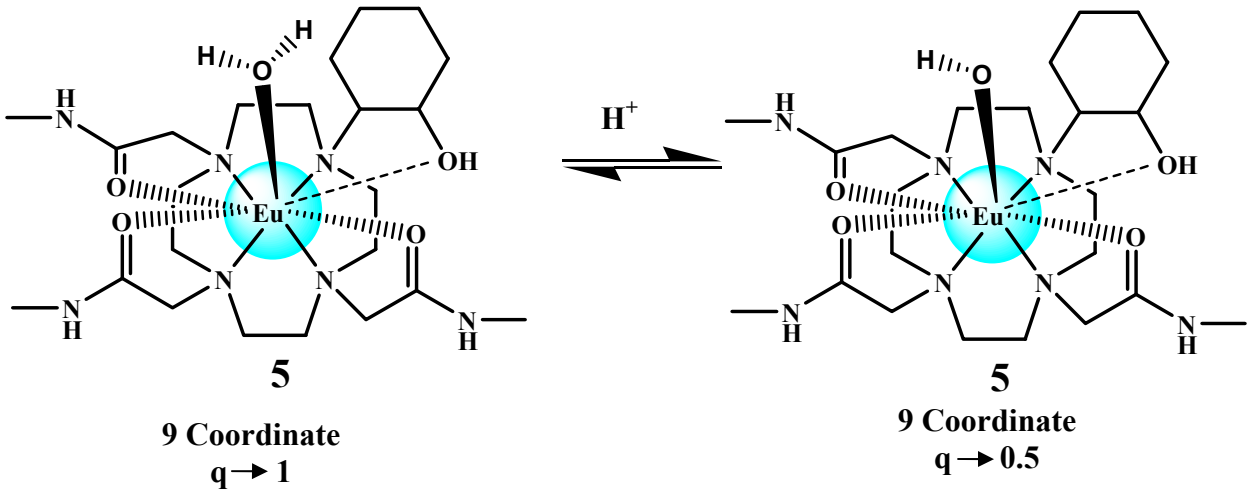


Figure 3.58: The proposed coordination environment of **5** in water remains unchanged.

The presence of the metal-bound water molecules coordinated to complex **5** in water was evaluated. At low pH the *q* value is close to one since there is a water molecule coordinated to the metal center. As the pH is increased and this water molecule is deprotonated the value of *q* tends to 0.5. The decrease in *q* is attributed to the deprotonation the metal-bound water molecule. Figure 3.58 shown above illustrates the proposition and the plot of *q* value versus pH shown in Figure 3.48 shows there exists a linear relationship between *q* and the number of protons lost during hydrolysis. For the non-linear least square fit of this relationship the R^2 was found to be 0.99. In summary the results obtained suggests the presence of a single water molecule and the unidentate coordination of phthalate in solution.

Cyclic Voltammetry

Finally, the electrochemical behavior of complex **5** and **9** across the pH range were investigated using cyclic voltammetry (CV). The mid-point reduction potential $E_{1/2}$ of a $Eu^{3+}L/Eu^{2+}L$ redox couple gives direct information on the redox stability of the Eu^{2+} state: a less negative $E_{1/2}$ indicates higher resistance of the $E^{2+}L$ to oxidation.[303] A well defined symmetrical voltammogram is observed for both complexes and it is deduced that there can only be a single electrochemically active species. The results for **5** show that the metal is encapsulated between pH 3 to 10 ($E_{1/2}$ = -0.83 V), however above pH 11 the complex is demetalated ($E_{1/2}$ = -1.01 V). The results for **9** show that the metal is encapsulated between pH 3 to 10 (-0.83 V), however above pH 10.5 the complex is also demetalated (-1.0 V).

The midpoint potential is related to the ratio of the thermodynamic stabilities of the $E^{3+}L$ and $Eu^{2+}L$ given by Equation 3.3 below.[304]

$$\Delta E_{1/2} = E_{1/2,\text{complexed}} - E_{1/2,\text{uncomplexed}} = \frac{RT}{F} \ln \frac{K_{Eu^{2+}}}{K_{Eu^{3+}}} \quad \text{……..Equation 3.3}$$

The peak separations for both complexes are different. At low pH, between 3 and 8.8 both complexes are quasi reversible and show a peak separation of < 57 mV. However at high pH > 10, complex **5** and **9** have peak separations of 63 mV and 36 mV, respectively. It is proposed that at high pH > 11.5 that the lanthanide ion in complex **5** protrudes out of the macrocyclic cavity, whereas in complex **9** at about pH 10.9 it is still within the cavity of the macrocycle. This is a major difference and is attributed to the increased resistance of **9** to be demetalated due to the four amidic arms which become deprotonated and hold onto the metal more tightly. In the case of **5**, the weaker interaction of the cyclohexyl group allows less resistance to demetalation. From the study of $E_{1/2}$ across the pH range it is clear that the hydrolysis of the metal-bound water molecule, the coordination and displacement of the phthalate moiety does not significantly affect the electrochemistry of the metal center.

At high pH, the slightly less negative value of **9** ($E_{1/2}$ = -1.0) compared to **5** ($E_{1/2}$ = -1.01) shows that **9** is not readily oxidized. This result shows that complex **5** is less resistant to oxidation as compared to complex **9**, meaning that incorporating the cyclohexyl moiety into the macrocyclic backbone shows no major contribution in terms of complex stability.

The standard rate constant is determined for electron transfer by plotting the log of the peak cathodic current, log i_c^p, against the log of the scan rate, log *v*. The slope is close to 1.0 for both complexes investigated, which means the reductions in both complexes are not diffusion controlled but the redox active species are adsorbed on the electrode surface. The electrochemical results shows that the metal remains encapsulated for most of the pH range and only becomes toxic free metal above pH 11, which is why molecule **5** could be an ideal candidate for MRI-CA development.

Chapter Four Conclusions and Future work

4.1 Concluding Remarks

In this focused study the spectroscopic and electrochemical properties of paramagnetic lanthanide polyazamacrocyclic complexes in solution were studied across the pH range. Systematic research in the field of MRI contrast media focuses on the development of complexes with higher efficiency (relaxivity) and new functionalities which target specific organs and diseases. In this work some of these interaction parameters are assessed and used to understand their structure-property relations that exist in solid and solution state. So far, there are no studies that report interactions of lanthanide complexes in which a *β*-amino alcohol pendants are involved. This study is a first of its kind and the results obtained agree with theory for the most part. Firstly, the mono-substituted *β*-amino alcohol cyclen intermediate was successfully isolated, followed by *N*-alkylation with the appropriate α-haloamide derivative to produce **2** and **3** in high yields and reproducibility. Ligand **4** was successfully synthesized for comparative purposes. Complexation of these ligands afforded us the target complexes shown in Figure 3.54.

Three lanthanide crystal structures are reported with each adopting a nona-coordinated polyhedron with a capped square anitiprismatic geometry. It is observed that the mean Ln—O bond distances for amidic oxygen donors decrease in length when going from complex **9** to the newly synthesized asymmetric hydroxy-cyclen-based complexes. The complexes showed almost no disorder using crystallization by slow evaporation techniques. Although the differences in bond length is very small this result confirms that the metal compression induced by the cyclohexyl moiety induces stronger bonding to the oxygen donors of the acetamide arms which translates into the oxygen donor in the capping positions having a longer Ln—O bond length. The longer Ln—O bond observed in the capping position promotes the hydrolysis of the metal bound water molecule which facilitates fast water exchange when applied to MRI. In addition similarity of geometrical parameters between molecule **5** and **6** further demonstrate that Eu^{3+} can be used as a structural probe for corresponding Gd^{3+} analogues.

The spectroscopic behavior of the Eu-complexes in MCB with KHP were investigated across the pH range and found that the phthalate moiety clearly behaves as an antenna and modulates the emission. Comparing the pK_a for the metal-bound water molecule in **5** and **9** in MCB with KHP, it was observed that the pK_a for **5** was larger. This increase can be attributed to the hydrophobic nature of the bulky cyclohexyl moiety. In general for **5**, it can be observed that it is both compression induced by cyclohexyl moiety and ionic like character of tautomeric arms that leads to a higher pK_a value for the hydrolysis of water coordinated to the metal center being observed. At low pH < 4.9, the phthalate behaves like an antenna and transfers energy from the S_1 and T_1 energy level to the lanthanide triplet state resulting in an enhanced emission. At high pH > 7, the phthalate is displaced by either the cyclohexyl group in the case of **5** or one of the amidic arms in the case of **9** as the pH is increased further. The spectroscopic behavior of **5** and **7** in MCB excluding KHP showed that the pK_a for **5** was again larger. This is possibly due to the weaker inductive effect of **7** and stronger tautomeric effect of **5**. Examining the spectroscopic behavior of **5** in water only showed that that the other biological buffers do not interact with the metal center. The results show that these Goods buffers namely; CHES, MES, MOPS and Tris do not coordinate to the metal directly and the minute difference in pK_a observed could be due experimental error or conditions.

The hydration number (q) for complex **5** in MCB with KHP and aqueous solution were evaluated. For the former investigation with KHP, at low pH it was found that the q value that tends to 2 and at high pH tends to 0.5. It is proposed that at low pH the phthalate anion coordinates in a unidentate fashion and displaces the cyclohexyl moiety. This coordination permits hydrogen bonding between the phthalate and cyclohexyl moiety with outer sphere water molecules. It is this specific interaction that causes q to increase since the number of OH oscillators around the polyhedron increases.

At higher pH > 7, the phthalate is further hydrolyzed, and again hydrogen bonds to neighboring water molecules where q now tends to 1.4. This is followed by the hydrolysis of the metal-bound water molecule which decreases the q value substantially. The q values obtained agreed well with the proposition that the phthalate moiety coordinates with the central Eu^{3+} ion in a unidentate fashion. It is proposed that if phthalate were to bind in a bidentate fashion it will

result in the formation of a 7-membered ring chelate which is highly unstable and will immediately result in the displacement of the metal-bound water molecule as mentioned earlier. Following from the argument used in the luminescence study, it is proposed that at high pH the cyclohexyl group displaces the phthalate. In the latter study in aqueous solution, complex **5** behaves as predicted. At low pH the q value is close to one since there is a water molecule coordinated to the metal center. As the pH is increased and this water molecule is deprotonated, the value of q tends to 0.5.

Finally, the electrochemical behavior of complex **5** and **9** across the pH range were investigated using cyclic voltammetry (CV). The results show that there is only one electrochemical species in solution and that the metal is encapsulated within the complexes between pH 3 to 10, however above pH 10.5 the complex is demetalated. It was determined that the reductions in both complexes are not diffusion controlled but the electrochemically active species are adsorbed on the electrode surface. In addition, the $E_{1/2}$ for both complexes across the pH range was determined, which showed that **9** is more resistant to demetalation than **5**. It was demonstrated that incorporating the cyclohexyl group into the macrocyclic backbone does not really increase complex stability. The hypothesis that by incorporating the bulkier backbone of the cyclohexyl ring onto cyclen, causes a decrease in the activation energy required to reach the eight coordinate transition state thereby increasing the rate of exchange with the bulk solution cannot be disproved. However, the increase in the Ln—O bond length is not due to the steric effects of cyclohexyl moiety instead it's the hydrophobic nature of the cyclohexyl group which is possibly causing this increase in pK_a of the metal bound water molecule. Overall the findings for all investigation sheds does some light into this subject matter and explains the behavior of these types of systems in solution which can be corroborated using supramolecular chemistry.

4.2 Futurework

Clearly more work will be required if the complete relationship between spectroscopic, electrochemical and coordination environment is to be elucidated. Nonetheless, the work presented herein lays the foundation for future projects. Starting with the ligand architecture, where the size of the ring and number the β-amino cyclic moieties can be altered and optimized to get the best possible metal encapsulation. Furthermore, the type of pendant arms could also be changed to hydroxymates which have been shown to have better relaxivity than their amidic counterparts. The solution chemistry can be further investigated using a plethora of anionic chromophores including lactate, citrate, malonate and salicylic acid derivatives. Generally, in scientific research it is clear that an answer to a question gives birth to new questions. The next step towards powerful imaging involves specific recognition between the Gd^{3+} complex and a target of interest. A more holistic view on the current subject matter, namely the development of MRI contrast agents, would be incomplete without relaxometric investigations of these types of systems with gadolinium, to access its feasibility and practicality in its application in early diagnosis.

References

1. Steed, J. W.; Atwood, J. L.; *Supramolecular Chemistry*, Second Edition, John Wiley and sons, London, United Kingdom, **2009**. p 2.
2. Jousselme, B.; Blanchard, P.; Levillain, E.; Delaunay, J.; Allain, M.; Richomme, P.; Rondeau, D.; Gallego-Planas N.; Roncali, J., *J. Am. Chem. Soc.*, **2003**, 125, 1363.
3. Larsen, F. K.; Mcinnes, E. J. L.; Mkami, H. E.; Rajaraman, G.; Rentschler, E.; Smith, A. A.; Smith, G. M.; Boote, V.; Jennings, M.; Timco G. A.; Winpenny, R. E. P., *Angew. Chem., Int. Ed.*, **2003**, 42, 101.
4. Bretonniere, Y.; Mazzanti, M.; Pecaut J.; Olmstead, M. M., *J. Am. Chem. Soc.*, **2002**, 124, 9012.
5. Bell, Z. R.; Jeffery, J. C.; McCleverty J. A.; Ward, M. D., *Angew. Chem., Int. Ed.*, **2002**, 41, 2515.
6. Sokol, J. J.; Shores M. P.; Long, J. R., *Inorg. Chem.*, **2002**, 41, 3052.
7. Sun, W. Y.; Kusukawa T.; Fujita, M., *J. Am. Chem. Soc.*, **2002**, 124, 11570.
8. Merbach, A. E.; Toth, E., *The Chemistry of Contrast Agents in Medical Magnetic Resonance Imaging*; Eds.; Wiley: New York, **2001**, chapters 1, 2, 3 and 4.
9. Caravan, P.; Ellison, J. J.; McMurray, T. J.; Lauffer, R. B. *Chem. Rev*. **1999**, 99, 2293.
10. Peters, J. A.; Huskens, J.; Raber, D. J., *Prog. Nucl. Magn. Reson. Spectrosc.*, **1996**, 28, 283.
11. Baker, B. F.; Khalili, H.; Wei, N.; Morrow, J. R., *J. Am. Chem. Soc.*, **1997**, 119, 8749
12. Amin, S. A.; Voss, D. A., Jr.; Horrocks, W. DeW., Jr.; Morrow, J. R., *Inorg. Chem.*, **1996**, 35, 7466.
13. Sherry, A. D.; Brown, R. D., III; Geraldes, C. F. G. C.; Koenig, S. H.; Kuan, K.-T.; Spiller, M., *Inorg. Chem.*, **1989**, 28, 620.
14. Dietrich, B.; Viout, P.; Lehn, J.-M. *Macrocyclic Chemistry*, VCH: Weinheim, **1993**.
15. Hancock, R. D.; Martell, A. E.*Chem. Rev.*, **1989**, 89, 1875.
16. Bernhardt, P. V.; Lawrance, G. A. *Coord. Chem. Rev.*, **1990**, 104, 297.
17. Micheloni, M., *J. Coord. Chem.*, **1988**, 18, 3.
18. Hancock, R. D., *In Crown Compounds*; Cooper, S. R., Ed.; VCH: New York, **1992**; pp 167-90.

19. Hancock, R. D.; Pattrick, G.; Wade, P. W.; Hosken, G. D. *Pure Appl. Chem.*, **1993**, 65, 473.
20. Alexander, V., *Chem. Rev.*, **1995**, 95, 273.
21. Parker, D., *In Crown Compounds*; Cooper, S. R., Ed.; VCH: New York, **1992**; pp 51-67.
22. Kumar, K.; Tweedle, M. F., *Pure Appl. Chem.*, **1993**, 65, 515.
23. Jurisson, S.; Berning, D.; Wei, J.; Dangshe, M. *Chem. Rev.*, **1993**, 93, 1137.
24. Strem chemical suppliers' cyclen (1) prices: $213-290 (U.S.) per gram-(March, **1996**), $46 (U.S.) per gram-(March, **2011**).
25. Lumetta, G. J.; Rapko, B. M.; Garza, P. A.; Hay, B. P.; Gilberson, R. D.; Weakley, T.; Hutchison, T. J. R., *J. Am. Chem. Soc.*, **2002**, 124, 20.
26. http://xray.tamu.edu/crystal_structure.php-last accessed 22/03/2011
27. Izatt, R. M.; Bradshaw, J. S.; Nielsen, S. A.; Lamb, J. D.; Christensen, J., *J. Chem. Rev.,***1985**, 85**,** 271.
28. Alexander, V., *Chem. Rev.*, **1995**, 95, 273.
29. Silversides, J. D.; Allan C. C.; Archibald S., *J. Dalton Trans*., **2007**, 9**,** 971.
30. Inoue, M. B.; Villegas C. A.; Asano, K.; Nakamura, M.; Inoue, M.; Fernando, Q., *Inorg. Chem.,* **1992**, 31, 2480.
31. Menon, S. C.; Panda, A.; Singh, H. B.; Butcher, R. J., *Chem. Commun.,* **2000**,143.
32. Clifford, T.; Danby, A. M.; Lightfoot, P. D.; Richens, T. R.; Hay, W., *J. Chem. Soc. Dalton Trans.,* **2001**, 240.
33. Song, B.; Storr, T.; Liu, S.; Orvig, C., *J. Inorg. Chem.,* **2002**, 685.
34. Mishra, A. K.; Chatal, J. F., *New J. Chem.,* **2001**, **25,** 336.
35. Tonei, D. M.; Ware, D. C.; Brothers, P. J.; Plieger, P. G.; Clark, G. R., *Dalton Trans.,* **2006**, 152.
36. Chandra, T.; Kraft, B. J.; Huffman, J. C.; Zalesk, J. M., *Inorg. Chem.,* **2003**, 42, 5158.
37. Hancock, R. D.; Martell, A. E., *Chem. Rev.*, **1989**, 89, 1875.
38. Busch, D. H., *Chem. Rev.*, **1993**, 93, 847.
39. Hay, B. P.; Hancock, R. D., *Coord. Chem. Rev.*, **2001**, 212, 61.
40. Schneider, H.-J.; Yatsimirsky, A., *Principles and Methods in Supermolecular Chemistry*; John Wiley and sons, New York, **2000.**

41. Kimura, E.; Aoki, S.; Koike, T.; Shiro, M., *J. Am. Chem. Soc.*, **1997**, 119, 3068.
42. Aoki, S.; Honda, Y.; Kimura, E., *J. Am. Chem. Soc.*, **1998**, 120, 10018.
43. Aoki, S.; Sakurama, K.; Matsuo, N.; Yamada, Y.; Takasawa, R.; Tanuma, S.-I.; Shiro, M.; Takeda, K.; Kimura, *E. Chem. Eur. J.*, **2006**, 12, 9066.
44. Subat, M.; Woinaroschy, K.; Anthofer, S.; Malterer, B.; Koenig, B., *Inorg. Chem.*, **2007**, 46, 4336.
45. Dischino, D. D.; Delaney, E. J.; Emswiler, J. E.; Gaughan, G. T.; Prasad, J. S.; Srivastava, S. K.; Tweedle, M. F., *Inorg. Chem.*, **1991**, 30, 1265.
46. Halfen, J. A.;Young, V. G., Jr., *Chem. Commun.*, **2003**, 2894.
47. Ratnakar, S. J.; Alexander, V., *Eur. J. Inorg. Chem.*, **2005**, 19, 3918.
48. Boldrini, V.; Giovenzana, G. B.; Pagliarin, R.; Palmisano, G.; Sisti, M., *Tetrahedron Lett.*, **2000**, 41, 6527.
49. Yoo, J.; Reichert, D. E.; Welch, M., *Chem. Commun.*, **2003**, 766.
50. Gasser, G.; Belousoff, M. J.; Bond, A. M.; Spiccia, L., *Inorg. Chem.*, **2007**, 46, 3876.
51. Gasser, G.; Belousoff, M. J.; Bond, A. M.; Kosowski, Z.; Spiccia, L., *Inorg. Chem.,* **2007**, 46, 1665.
52. Chaux, F.; Denat, F.; Espinosa, E.; Guilard, R., *Chem. Commun.*, **2006**, 5054.
53. Rohovec, J.; Gyepes, R.; Cisarova, I.; Rudovsky, J.; Lukes, I., *Tetrahedron Lett.*, **2000**, 41, 1249.
54. Anda, C.; Bencini, A.; Berni, E.; Ciattini, S.; Chuburu, F.; Dancsi, A.; Giorgi, C.; Handel, H.; le Baccon, M.; Paoletti, P.; Tripier, R.; Turcry, V.; Valtancoli, B., *Eur. J. Inorg. Chem.*, **2005**, 11, 2044.
55. Yaouanc, J. J.; Le Bris, N.; Le Gall, G.; Clement, J. C.; Handel, H.; des Abbayes, H., *J. Chem. Soc., Chem. Commun.*, **1991**, 206.
56. Filali, A.; Yaouanc, J. J.; Handel, H., *Angew. Chem. Int. Ed. Engl.*, **1991**, 30, 560.
57. Bernard, H.; Yaouanc, J. J.; Clement, J. C.; des Abbayes, H.; Handel, H., *Tetrahedron Lett.*, **1991**, 32, 639.
58. Bender, J. A.; Meanwell, N. A.; Wang, T., *Tetrahedron*, **2002**, 58, 3111.
59. Li, C.; Wong, W.-T. *Tetrahedron Lett.*, **2002**, 43, 3217.
60. Massue, J.; Plush, S. E.; Bonnet, C. S.; Moore, D. A; Gunnlaugsson, T., *Tetrahedron Letters*, **2007,** 48, 8052.

61. Kimura, E.; Aoki, S.; Koike, T.; Shiro, M., *J. Am. Chem. Soc.*, **1997**, 119, 3068.
62. Kruper, W. J.; Rudolf, P. R.; Langhoff, C. A.; *J. Org. Chem.*, **1993**, 58, 3869.
63. Chaumeil, H.; Handel, H.; *Eur. Polym. J.*, **1991**, 3, 269.
64. Helps, I. M.; Parker, D.; Morphy, J. R.; Chapman, J., *Tetrahedron*, **1989**, 45, 219.
65. Gardinier, I.; Bernard, H.; Chuburu, F.; Roignant, A.; Yaouanc, J. J.; Handel, H.; *Chem. Commun.*, **1996**, 2157.
66. Patinec, V.; Yaouanc, J. J.; Clémemt, J C.; Handel, H.; des Abbayes, H.; *Tetrahedron Lett.*, **1995**, 36, 79.
67. Martell, A. E.; Hancock, R. D.; Motekaitus, R. J., *Coord. Chem. Rev.*, **1994**, 133, 39.
68. Tsukube, H., Mizutani, Y., Shinoda, S., Okazaki, Y., Tadokoro, M., Kori, K., *Inorg. Chem.*, 38, **1999**, 15, 3506.
69. Holden, N. E., In *IUPAC General Assembly*; US Department of Energy: Brisbane, Australia, **2001**.
70. Haxel, G. B.; Hedrick, J. B.; Orris, G. J.; US Geological Survey, **2002**, pp 1-4.
71. Arnaudneu, F., *Chem. Soc. Rev.*, **1994**, 23, 235.
72. Bünzli, J.-C. G., *Journal of Alloys and Compounds*, **2006**, 408-412, 934.
73. Cotton, S., *Lanthanide and Actinide Chemistry*; John Wiley & Sons Ltd.: West Sussex, England, **2006**, p 1-15.
74. Galgano, F.; Favati, F.; Caruso, M.; Scarpa, T.; Palma, A., *LWT - Food Science and Technology*, **2008**, 41, 1808.
75. Taylor, S. R.; McLennan, S. M. In *Metal Ions in Biological Systems: The Lanthanides and Their Interrelations with Biosystems*; Sigel, A., Sigel, H., Eds.; Marcel Dekker, Inc.: New York, **2003**; Vol. 40, pp 1-38.
76. Yan, C. W., Gadolinium Complexes containing Polyaminocarboxylate ligands for the use in Magnetic Resonance Imaging Contrast Agents, PhD Thesis submitted to the University of Hong Kong, **2005**, 225.
77. Pandya, S.; Yu J.; Parker D., *Dalton Trans.*, **2006**, 2757.
78. Hart, A. J.; Jensen, P.; Plush, S. E.; Kruger, P. E.; Gunnlaugsson, T., *Inorg. Chem.*, **2006**, 45, 23, 9465.
79. Maffeo D.; Williams, J. A. G., *Inorg. Chim. Acta*, **2003**, 355, 127.
80. Dadabhoy, A.; Faulkner, S.; Sammes, P. G., *J. Chem. Soc., Perkin Trans 2*, **2002**, 348.

81. Beeby, A.; Faulkner, S.; Parker D.; Williams, J. A. G., *J. Chem. Soc., Perkin Trans. 2*, **2001**, 1268.
82. Dioury, F.; Sylvestre, I.; Siaugue, J.-M.; Wintgens, V.; Ferroud, C.; Favre-Reguillon, A.; Foos, J.; Guy, A., *Eur. J. Org. Chem.*, **2004**, 4424.
83. Viguier R. F .H.; Hulme, A.N., *J. Am. Chem. Soc.*, **2006**, 128, 11370.
84. Vicinelli, V.; Ceroni, P.; Maestri, M.; Balzani, V.; Gorka, M.; Vogtle, F., *J. Am. Chem. Soc.*, **2002**, 124, 6461.
85. Hebbink, G. A.; Grave, L.; Woldering, L. A.; Reinhoudt D. N.; van Veggel, F. C. J. M., *J. Phys. Chem.*, **2003**, 107, 2483.
86. Werts, M. H. V.; Verhoeven J. W.; Hofstraat, J. W., *J. Chem. Soc., Perkin Trans. 2*, **2000**, 433.
87. Faulkner, S.; Carrie, M.-C.; Pope, S. J. A.; Squire, J.; Beeby A.; Sammes, P. G., *Dalton Trans.*, **2004**, 1405.
88. Beeby, A.;. Dickins, R. S.; Fitzgerald, S.; Govenlock, L. J.; Maupin, C. L.; Parker, D.; Riehl, J. P.; Siligardi, G.; Williams, J. A. G., *Chem. Commun.*, **2000**, 1183.
89. Werts, M. H. V.; Verhoeven J. W.; Hofstraat, J. W., Geurts, F. A. J., *Chem. Phys. Lett.*, **1997**, 276, 196.
90. Faulkner S.; Pope, S. J. A., *J. Am. Chem. Soc.*, **2003**, 125, 10526.
91. Sambrook, M. R.; Curiel, D.; Hayes, E. J.; Beer, P. D.; Pope S. J. A.; ; Faulkner, S., *New J. Chem.*, **2006**, 30, 1133.
92. Senechal-David, K.; Pope, S. J. A.; Quinn, S.; Faulkner, S.; Gunnlaugsson, T., *Inorg. Chem.*, **2006**, 45, 10040.
93. Casnati, A.; Sansone, F.; Sartori, A.; Prodi, L.; Montalti, M.; Zaccheroni, N.; Ugozzoli, F.; Ungaro, R., *Eur. J. Org. Chem.*, **2003**, 1475.
94. Yang, C.; Fu, L.-M.; Wang, Y.; Zhang, J.-P.; Wong, W.-T.; Ai, X.-C.; Qiao, Y.-F.; Zou, B.-S.; Gui, L.-L., *Angew. Chem., Int. Ed.*, **2004**, 43, 5010.
95. Pope, S. J. A.; Kenwright, A. M.; Boote V. A.; Faulkner, S., *Dalton Trans.*, **2003**, 3780.
96. Skinner, P. J.; Beeby, A.; Dickins, R. S.; Parker, D.; Aime S.; Botta, M., *J. Chem. Soc., Perkin Trans. 2*, **2000**, 1329.
97. Blair, S.; Lowe, M. P.; Mathieu, C. E.; Parker, D.; Senanayake, P. K.; Kataky, R., *Inorg. Chem.*, **2001**, 40, 5860.

98. Bobba, G.; Frias J. C.; Parker, D., *Chem. Commun.*, **2002**, 890.

99. Song, B.; Wang, G.; Tan M.; Yuan, J., *J. Am. Chem. Soc.*, **2006**, 128, 13442.

100. Schwierking, J. R.; Menzel, L.W.; Menzel, E. R., *The Scientific World*, **2004**, 4, 948.

101. Evans, C. H., *Biochemistry of the Lanthanides*; Plenum Press: New York, 1990.

102. Platas-Iglesias, C.; Piquet, C.; Andre, N.; Bünzli, J. C. G., *J. Chem. Soc.,Dalton Trans,* **2001**, 3048.

103. Andre, N.; Scopelleti, R.; Hopgartner, G.; Piquet, C.; Andre, N.; Bünzli, J. C. G., *Chem. Commun.*, **2002**, 214.

104. Parker, D.; Dickins, R. S.; Puschmann, H.; Crossland, C.; Howard, J. A. K., *Chemical Reviews*, **2002**, 102, 1977.

105. Faulkner, S.; Matthews, J. L. *Applications of coordination chemistry: Comprehensive coordination chemistry II*, 2nd ed.; Elsevier: Amsterdam, **2003**.

106. Petoud, S.; Cohen, S. M.; Bünzli, J.-C. G.; Raymond, K. N., *J. Am. Chem. Soc.*, **2003**, 125, 13324.

107. Gritmon, T. F.; Goedken, M. P.; Choppin, G. R. *J. Inorg. and Nucl. Chem.*, **1977**, 39, 2021.

108. Gritmon, T. F.; Goedken, M. P.; Choppin, G. R., *J. Inorg. and Nucl. Chem.*, **1977**, 39, 2025.

109. Leonard, J. P.; Nolan, C. B.; Stomeo, F.; Gunnlaugsson, T.; *Top. in Curr. Chem.* **2007**, 281, 1.

110. Suarez, S.; Mamula, O.; Scopelliti, R.; Donnio, B.; Guillon, D.; Terazzi, E.; Piguet, C.; Bünzli, J. C. G., *New J. of Chem.,* **2005**, 29, 1323.

111. Horrocks Jr., W. D., *Science*, **1979**, 206, 1194.

112. Bunzli, J. C. G.; Wessner, D., *Hel. Chimi. Acta*, **1981**, 64, 582.

113. Bulman, R. A. In *Metal Ions in Biological Systems: The Lanthanides and Their Interrelations with Biosystems*; Sigel, A., Sigel, H., Eds.; Marcel Dekker, Inc.: New York, **2003**; Vol. 40, pp 39-67.

114. Cotton, F. A.; Wilkinson, G., *Advanced Inorganic Chemistry*; John Wiley and Sons: New York, **1988**.

115. Van der Ende, B.; Aarts, L.; Meijerink, A., *Phys. Chem. Chem. Phys.*, **2009**, 11, 11081.

116. Parker, D.; Williams, J. A. G. In *Metal Ions in Biological Systems: The Lanthanides and*

Their Interrelations with Biosystems; Sigel, A., Sigel, H., Eds.; Marcel Dekker, Inc.: New York, **2003**; Vol. 40, pp 233-280.

117. Dieke, G. H., Crosswhite, H. M. *Applied Optics*, **1963**, 2, 675-686.
118. Parker, D.; Williams, J. A. G., *J. Chem. Soc.-Dalton Trans.,* **1996**, 18, 3613.
119. Bünzli, J.-C. G. *Lanthanide probes in life, chemical and earth sciences: Theory and practice*; Elsevier: New York, **1989**.
120. Sabbatini, N.; Guardigli, M.; Lehn, J. M., *Coord. Chem. Rev.*, **1993**, 123, 201.
121. Carnall, W. T. In *Handbook on the Physics and Chemistry of Rare Earths*; Gschneider, K. A., Eyring, L., Eds.; North Holland Pub. Co.: Amsterdam, **1998**; Vol. 25, pp 508.
122. Walsh, B. M., In *Advances in Spectroscopy for Lasers and Sensing*; Di Bartolo, B., Forte, O., Eds.; Springer: The Netherlands, **2006**, pp 403-433.
123. Bünzli, J.-C. G.; Chopin, G. R., *Lanthanide Probes in Life, Chemical and Earth Sciences: Theory and Practice*; Elsevier: New York, **1989**.
124. Richardson, F. S., *Chem. Rev.*, **1982**, 82, 541-552.
125. Bunzli, J. C. G. In *Metal Ions in Biological Systems*; Sigel, A., Sigel, H., Eds.; Marcel Dekker: Zurich, **2004**; Vol. 42, pp 39.
126. Johnson, D. A., *J. of Chem. Ed.*, **1980**, 57, 475.
127. Desreux, J. F., *Inorg. Chem.*, **1980**, 19, 1319.
128. Spirlet, M. R.; Rebizant, J.; Desreux, J. F.; Loncin, M. F., *Inorg. Chem.*, **1984**, 23, 359.
129. Dubost, J.-P.; Leger, M.; Langlois, M.-H.; Meyer, D.; Schaefer, M. *C. R. Acad. Sci., Ser. 2*, **1991,** 312, 349.
130. Chang, C. A.; Francesconi, I. C.; Malley, M. F.; Kumar, K.; Gougoutas, J. Z.; Tweedle, M. F.; Lee, D. W.; Wilson, L. J., *Inorg. Chem.*, **1993**, 32, 3501.
131. Aime, S.; Barge, A.; Botta, M.; Fasano, M.; Ayala, J. D.; Bombieri, G., *Inorg. Chim. Acta*, **1996**, 246, 423.
132. Koenig, S. H.; Brown, R. D., III *Prog. Nucl. Magn. Reson. Spectrosc*., **1991**, 22, 487.
133. Kumar, K.; Tweedle, M. F. *Pure Appl. Chem.*, **1993**, 65, 515.
134. Corey, E. J.; Bailar, J. C., Jr. *J. Am. Chem. Soc.*, **1959**, 81, 2620.
135. Beattie, J. K., *Acc. Chem. Res.,* **1971**, 4, 253.
136. Aime, S.; Botta, M.; Ermondi, G., *Inorg. Chem.*, **1992**, 31, 4291.
137. Morrow, J. R.; Amin, S.; Lake, C. H.; Churchill, M. R., *Inorg. Chem.*, **1993**, 32, 4566.

138. Chin, K. O.; Morrow, J. R.; Lake, C. H.; Churchill, M. R., *Inorg. Chem.* **1994**, 33, 656.
139. Aime, S.; Batsanov, A. S.; Botta, M.; Howard, J. A. K.; Parker, D.; Senanayake, K.; Williams, G. *Inorg. Chem.*, **1994**, 33, 4696.
140. Kang, S. I.; Ranganathan, R. S.; Emswiler, J. E.; Kumar, K.; Gougoutas, J. Z.; Malley, M. F.; Tweedle, M. F., *Inorg. Chem.*, **1993**, 32, 2912.
141. de Martino Norante, G.; Di Vaira, M.; Mani, F.; Mazzi, S.; Stoppioni, P., *J. Chem. Soc., Chem. Commun.*, **1990**, 438.
142. Di Vaira, M.; Mani, F.; Stoppioni, P., *J. Chem. Soc., Dalton Trans.*, **1992**, 1127.
143. Aime, S.; Botta, M.; Fasano, M.; Marques, M. P. M.; Geraldes, C. F. G. C.; Pubanz, Merbach, D. A. E., *Inorg. Chem.*, **1997**, 36, 2059.
144. Woods, M.; Kovacs, Z.; Zhang, S.; Sherry, A. D., *Angew. Chem., Int. Ed.*, **2003**, 42, 5889.
145. Hoeft, S.; Roth, K., *Chem. Rev.*, **1993**, 126, 869.
146. Woods, M.; Aime, S.; Botta, M.; Howard, J. A. K.; Moloney, J. M.; Navet, M.; Parker, D.; Port M.; Rousseaux, O., *J. Am. Chem. Soc.*, **2000**, 122, 9781.
147. Dunand, F. A.; Aime, S.; Merbach, A. E., *J. Am. Chem. Soc.*, **2000**, 122, 1506.
148. Port, M.; Rousseaux, O.; Raynal, I.; Woods, M.; Parker, D.; Moreau, J.; Rimbault, J.; Pierrard, J.-C.; Aplincourt, M., *Acad. Radiol.*, **2002**, 9 Suppl 2, S300.
149. Aime, S.; Barge, A.; Bruce, J. I.; Botta, M.; Howard, J. A. K.; Moloney, J. M.; Parker, D.; de Sousa A. S.; Woods, M., *J. Am. Chem. Soc.*, **1999**, 121, 5762.
150. Aime, S.; Barge, A.; Botta, M.; de Sousa A. S.; Parker, D., *Angew. Chem., Int. Ed.*, **1998**, 37, 2673.
151. Di Bari, L.; Pintacuda, G.; Salvadori, P., *Eur. J. Inorg. Chem.*, **2000**, 75.
152. Howard, J. A. K.; Kenwright, A. M.; Moloney, J. M.; Parker, D.; Woods, M.; Port, M.; Navet, M.; Rousseau, O., *Chem. Commun.*, **1998**, 1381.
153. Aime, S.; Botta, M.; Ermondi, G.; Terreno, E.; Anelli, P. L.; Fedeli F.; Uggeri, F., *Inorg. Chem.*, **1996**, 35, 2726.
154. Aime, S.; Botta, M.; Terreno, E., in *Advances in Inorganic Chemistry*, ed. v. Eldik, R., Elsevier, Amsterdam, **2005**, vol. 57, chapter 4.
155. Aime, S.; Botta, M.; Fasano, M.; Terreno, E., *Chem. Soc. Rev.*, **1998**, 27, 19.
156. Woods, M.; Botta, M.; Avedano, S.; Wang, J.; Sherry A. D., *Dalton Trans*, **2005**, 3837.

157. Brunton, L.; Lazo, J., *Goodman and Gilman: The pharmacological basis of therapeutics*, 11th edition, McGraw Hill Co., New York, **2006**.
158. Gielen, M.; Tiekink, E. R. T., *Metallotherapeutic Drugs and Metal-based diagnostic agents: The use of metals in medicine*, John Wiley and sons, England, **2005**, 511.
159. Lloyd, N.C.; Morgan, H. W.; Nicholson, B. K.; Ronimus, R. S., *Angew. Chem. Int. Ed. Engl.*, **2005**, 44, 941.
160. Kelland, L. R.; Farell, N. P., *Platinum-based Drugs in Cancer Therapy*, Humanna Press Inc., New Jersey, **2000**.
161. Farrer, N. J.; Woods, J. A.; Salassa, L.; Zhao, Y.; Robinson, K, S.; Clarkson, G.; Mackay, F. S.; Sadler P. J., *Angew. Chem. Int. Ed.*, **2010**, 49, 8905.
162. Melson, G. A., Ed. *Coordination Chemistry of Macrocyclic Compounds;* Plenum: New York, **1979**.
163. Izatt, R. M., Christensen, J. J., Eds. *Synthesis of Macrocycles: The Design of Selective Complexing Agents, Progress in Macrocyclic Chemistry;* Wiley-Interscience: New York, **1987**; Vol. 3.
164. Lindoy, L. F. *The Chemistry of Macrocyclic Ligand Complexes;* Cambridge University Press: Cambridge, **1989**.
165. Dalley, N. K. In *Synthetic Multidentate Macrocyclic Compounds;* Izatt, R. M., Christensen, J. J., Eds.; Academic Press: New York, **1978**.
166. Elst, L. V.; Roch, A.; Gillis, P.; Laurent, S.; Botteman, F.; Bulte, J. W. M.; Muller, R. N., *Magn. Reson. Med.*, **2002**, 47, 1121.
167. Caravan, P.; Cloutier, N. J.; Greenfield, M. T.; McDermid, S. A.; Dunham, S. U.; Bulte, J. M. W.; Amedio, J. C.; Looby, R. J.; Supkowski, R. M.; Horrocks, Jr. W. D.; McMurray, T. J.; Lauffer, R. B., *J. Am. Chem. Soc.*, **2002**, 124, 3152.
168. http://www.sparkle.pro.br/sites/default/files/lanthanide-complexes-rgb.png-last accessed 22/03/2011
169. Lakowicz, J. R., *Principles of Fluorescence Spectroscopy*, 3 ed.; Springer Science and Business Media, LLC: Singapore, **2006**.
170. Gassner, A.-L.; Duhot, C.; Bunzli, J. C. G.; Chauvin, A. S., *Inorg. Chem.,* **2008**, 47, 7802.
171. Bottrill, M.; Kwok, L.; Long, N. J., *Chem. Soc. Rev.*, **2006**, 35, 557.

172. Eisinger, J.; Shulman, R. G.; Blumberg, W. E., *Nature*, **1961**, 192, 963.
173. Lauffer, R. B., *Chem. Rev.,* **1987**, 87, 901-927.
174. Sherry, A. D.; Brown, R. D.; Geraldes, C. F. G. C.; Koenig, S. H.; Kuan, K.-T.; Spiller, M., *Inorg. Chem.*, **1989**, 28, 620.
175. Bousquet, J. C.; Saini, S.; Stark, D. D.; Hahn, P. F.; Nigam, M.; Wittenberg, J.; Ferrucci, J.,J. T., *Radiology*, **1988**, 166, 693.
176. Bassett, A. P.; Steven, W. M.; Glover, P. B.; Lewis, D. J.; Spencer, N.; Parsons, S.; Williams, R. M.; De Cola, L.; Pikramenou, Z., *J. Am Chem. Soc.*, **2004**, 126, 9413.
177. Basak, B.; Bhattacharyya, U. K.; Laskar, S., *Amino Acids*, **1993**, 4, 193.
178. http://www.radiologyinfo.org/en/info.cfm?pg=bodymr – last accessed 22/03/2011
179. http://mrsrl.stanford.edu/~brian/intromr – last accessed 22/03/2011
180. Bloch, F., *Phys. Rev.*, **1946**, 70, 460.
181. Bloch, F.; Hansen, W. W.; Packard, M., *Phys. Rev.*, **1946**, 70, 474.
182. Purcell, E. M.; Torrey, H. C.; Pound, R. V., *Phys. Rev.*, **1946**, 69, 37.
183. Damadian, R. V., *Science*, **1971**, 171, 1151.
184. Lauterbur, P. G., *Nature*, **1973**, 242, 190.
185. Kumar, A.; Welti, D.; Ernst, R. R.. *J. Magn. Reson.*, **1975**,18, 69.
186. Mansfield P.; Grannell, P. K., *J. Phys.*, **1973**, C 6, L422.
187. Mansfield, P., *J. Phys*., **1977**,C 10, L55.
188. Lauterbur, P. C.; Jacobsen, M. J.; Rudin, A. M., Augmentation of the water proton spin-lattice relaxation in tissues by the in vivo injection of manganous ion., Book of abstracts, 19th Experimental Nuclear Magnetic Conference, April **1978**: B-19.
189. Edelstein, W. A.; Hutchison, J. M. S.; Johnson, G; Redpath, T., *Phys. Med. Biol.*, **1980**, 25, 751.
190. Mishra, A., Design, synthesis and characterization of smart MR contrast agents sensitive to pH/calcium changes during neural activity, Thesis submitted to the University of Tübingen, **2004**.
191. Committee on the Mathematics and Physics of Emerging Dynamic Biomedical Imaging: Mathematics and Physics of Emerging Biomedical Imaging, National Research Council, Institute of Medicine, Academy Press, Washington DC, **1996**, Chapter 4.
192. Tweedle, M. F., Bünzli, J. C; Choppin, G. R. (Eds.), *Lanthanide Probes in Life:*

Chemical and Earth Science- Theory and Practice, Elsevier, Amsterdam, **1989**, p. 127.

193. Mansfield, P.; Morris, P. G., NMR Imaging in Biomedicine, Academic Press, New York, **1982**, Chapter 2.
194. Choppin, G. R; Schaab, K. M., *Inorg. Chim. Acta.*, **1996**, 252, 299.
195. Tombach, B.; Reimer, P., *Curr. Med. Chem.*, **2005**, 12, 2795.
196. http://rsb.info.nih.gov/ij/images/– last accessed 1/03/2012
197. http://www.mriwestmorris.com– last accessed 22/03/2011
198. Krause, W., In *Topics in Current Chemistry–Contrast Agent I–Magnetic Resonance Imaging*, Springer-Verlag, **2002**.
199. Zhang, Z.; Nair, S. A.; McMurray, T. J., *Curr. Med. Chem.*, **2005**, 12, 751.
200. Lorusso, V.; Pascolo, L.; Fernetti, C.; Anelli, P. L.; Uggeri, F.; Tiribelli, C., *Curr. Pharm. Design*, **2005**, 11, 4079.
201. Baisch, U.; Dell'Amico, D. B.; Calderazzo, F.; Labella, L.; Marchetti, F.; Merigo, A., *Eur. J. Inorg. Chem.*, **2004**, 1219.
202. Goldschmidt, V. M.; Barth, T.; Lunde, G., Skrifter Norske Videnskaps Akademi i Oslo, *I. Mater.-NaturV*. Klasse, **1925**, 59.
203. Seitz, M.; Oliver, A. G.; Raymond, K. N., *J. Am. Chem. Soc.*, **2007**, 129, 11153.
204. Yao, J. Y.; Deng, B.; Sherry, L. J.; McFarland, A. D.; Ellis, D. E.; Van Duyne, R. P.; Ibers, J. A., *Inorg. Chem.*, **2004**, 43, 7735.
205. Hallenga, K.; Koenig, S. H., *Biochemistry*, **1976**, 15, 4255.
206. Koenig, S. H.; Schillinger, W. S., *J. Biol. Chem.*, **1969**, 244, 3283.
207. Kropp, J. L.; Windsor, M. W., *J. Chem. Phys.*, **1963**, 39, 2769.
208. Kropp, J. L.; Windsor, M. W., *J. Chem. Phys.*, **1965**, 42, 1599.
209. Kropp, J. L.; Windsor, M. W., *J. Chem. Phys.*, **1966**, 45, 761.
210. Freeman, J.; Crosby, G. A.; Lawson, K. E., *J. Mol. Spectrosc.*, **1964**, 13, 399.
211. Dawson, W. R.; J. L. Kropp, J. L.; Windsor, M. W., *J. Chem. Phys.*, **1966**, 45, 2410.
212. Heller, A., *J. Am. Chem. Soc.*, **1966**, 88, 2058.
213. Haas Y.; Stein, G., *J. Phys. Chem.*, **1971**, 75, 3668.
214. Haas Y.; Stein, G., *J. Phys. Chem.*, **1971**, 75, 3677.
215. Haas Y.; Stein, G., *J. Phys. Chem.*, **1972**, 76, 1093.
216. Stein G.; Wurzberg, E., *J. Chem. Phys.*, **1975**, 62, 208.

217. Horrocks, Jr. W. D.; Sudnick, D. R., *J. Am. Chem. Soc.*, **1979**, 101, 334.
218. Horrocks, Jr. W. D.; Sudnick, D. R., *Acc. Chem. Res.*, **1981**, 14, 384.
219. Frey, S. T.; Horrocks, Jr. W. D., *Inorg. Chim. Acta.*, **1995**, 229, 383.
220. Horrocks, Jr. W. D.; Sudnick, D. R., Science, **1979**, 206, 1194.
221. Horrocks, Jr. W. D.; Arkle, V. K.; Liotta, F. J.; Sudnick, D. R., *J. Am. Chem. Soc.*, **1983**, 105, 3455.
222. Beeby, A.; Clarkson, I. M.; Dickins, R. S.; Faulkner, S.; Parker, D.; Royle, L.; de Sousa, A. S.; Williams, J. A. G.; Woods, M., *J. Chem. Soc., Perkin Trans.*, **1999**, 493.
223. Dickins, R. S.; Parker, D.; de Sousa, A. S.; Williams, J. A. G., *Chem. Commun.*, **1996**, 697.
224. Supkowski, R. M., Horrocks, Jr. W. D., *Inorg. Chem.*, **1999**, 38, 5616.
225. Anelli, P. L.; Balzani, V.; Prodi, L.; Uggeri, F., *Gazz. Chim. Ital.*, **1991**, 121, 359.
226. Botrill, M.; Kwok, L.; Long, N. J., *Chem. Soc. Rev.*, **2006**, 35, 557.
227. Kowalewski, J.; Nordenskioeld, L.; Benetis, N.; Westlund, P. Q., *Prog. Nucl. Magn. Reson. Spectrosc.*, 1**985**, 17.
228. Aime, S.; Botta, M.; Terreno, E., *Adv. Inorg. Chem.*, **2005**, 57, 173.
229. Aime, S.; Batsanov, A. S.; Botta, M.; Howard, J. A. K.; Parker, D.; Senanayake, K.; Williams, G., *Inorg. Chem.*, **1994**, 33, 4696.
230. Botta, M.; *Eur. J. Inorg. Chem.*, **2000**, 399.
231. Freed, J. H., *J. Chem. Phys.*, **1978**, 68, 4034.
232. Werner, E. J.; Datta, A.; Jocher, C. J.; Raymond, K. N., *Angew. Chem. Int. Ed.*, **2008**, 47, 8568.
233. Cacheris, W. P.; Quay, S. C.; Rocklage, S. M., *Magn. Reson. Imaging*, **1990**, 8, 467.
234. Desreux, J. F.; Barthelemy, P. P., *Nucl. Med. Biol.*, **1988**, 15, 9.
235. Helm, L.; Merbach, A., *Chem. Rev.*, **2005**, 105, 1923.
236. Jázberényi, Z.; Sour, A.; Tóth, É.; Benmelouka, M.; Merbach, A., *Dalton Trans.,* **2005**, 2713.
237. Laus, S.; Ruloff, R.; Tóth, É.; Merbach, A., *Chem. Eur. J.*, **2003**, 9, 3555.
238. Powell, D. H.; Dhubhghaill, O. M. N.; Pubanz, D., Helm, L.; Lebedev, Y. S; Schlaepfer, W.; Merbach, A., *J. Am. Chem. Soc.*, **1996**, 118, 9333.
239. Tóth, É.; Burai, L.; Brücher, E.; Merbach, A., *J. Chem. Soc. Dalton Trans.*, **1997**, 1587.

240. PolSsěk, M.; Rudovský, J.; Hermann, P.; Lukeš, I.; Vander Elst, L. ; Muller, R. N., *Chem. Commun.*, **2004**, 2602.
241. Rudovský, J.; Kotek, J.; Hermann, P.; Lukeš, I.; Mainerob, V.; Aime, S., *Org. Biomol. Chem.*, **2005**, 3, 112.
242. Costa, J.; Tóth, É.; Helm, L.; Merbach, A., *Inorg. Chem.*, **2005**, 44, 4747.
243. Costa, J.; Ruloff, R.; Burai, L.; Helm, L.; Merbach, A., *J. Am. Chem. Soc.*, **2005**, 127, 5147.
244. Bolskar, R. D.; Benedetto, A. F.; Husebo, L. O.; Price, R. E.; Jackson, E. F.; Wallace, S.; Wilson, L. J.; Alford, J. M., *J. Am. Chem. Soc.*, **2003**, 125, 5471.
245. Sitharaman, B.; Bolskar, R. D.; Rusakova, I.; Wilson, L. J., *Nano Lett.*, **2004**, 4, 2373.
246. Tóth, É.; Bolskar, R. D; Borel, A.; Gonzalez, G.; Helm, L.; Merbach, A. E.; Sitharaman, B.; Wilson, L. J., *J. Am. Chem. Soc.*, **2005**, 127, 799.
247. Laniado, M.; Weinmann, H-J.; Schorner, W.; Felix, R.; Speck, U., *Physiol. Chem. Med.*, NMR, **1984**, 16, 157.
248. Owen, C. S.; Silvia, J. C.; d Angelo, L.; Liberti, P., Magnetic polymer particles, Patent EP0516198, publication date December 2, **1992**; priority dates October 4, **1985** and September 16, **1986.**
249. Owen, C. S.; Silvia, J. C.; d Angelo, L.; Liberti, P., *Magnetic polymer particles*, Patent US4795698, publication date January 3, **1989**; priority dates October 4, **1985** and September 16, **1986**.
250. Sigma-Aldrich catalogue **2011-2012**.
251. http://www.jtbaker.com/biopharm/biopharm_buffer_bio.html_last accessed 12/02/2012.
252. Ferguson, W.J.; Braunschweiger, K.I.; Braunschweiger, W.R.; Smith, J.R.; McCormick, J.J.; Wasman C.C.; Jarvis, N.P.; Bell, D.H; Good, N.E, *Anal. Biochem*., **1980**, 104, 300.
253. Vespalec, R.; Vlčková, M.; Horáková, H., *Journal of Chromatography A*, **2004**, 1051, 75.
254. Good, N.E.; Winget, G.D.; Winter, W.; Connolly, T.N.; Izana, K.; Singh, R.M.M., *Biochemistry*, **1966**, 5, 467.
255. Hames, B.D.; Rickwood, D., *Gel Electrophoresis of Proteins*, OIRL Press, Oxford, 2nd Ed., **1990**, 153.
256. Beynon, R.J.; Easterby, J.S., *Buffer Solutions: The basics*. OIRL Press, Oxford, **1996**,

Vol. 69 – 70, 74, 78, p.48.

257. Armarego, W. L. F, and Chai, C. L. L., Purification Of Laboratory Chemicals, Butterworth-Heinemann, Cornwall, Great Britain (**2003**).
258. Bruker (**2005a**). Apex2, Version 2009.1-0. Bruker AXS Inc., Madison, Wisconsin, USA.
259. Bruker (**2005b**). SAINT+. Version 7.60A. (includes XPREP and SADABS) Bruker AXS Inc., Wisconsin, USA.
260. Bruker (**1999**). SHELXTL. Version 5.1 (includes XS, XL, XP, XSHELL) Bruker AXS Inc., Wisconsin, USA.
261. Farrugia, L. J, *J. Appl. Cryst.*, **1997**, 30, 565.
262. Spek, A. L, *J. Appl. Cryst.*, **2003**, 36, 7.
263. Parker, D.; Williams, J. A. G., *J. Chem. Soc. Perkin Trans. 2*, **1995**, 1305.
264. De Sousa A. S.; Hancock, R. D.; Reibenspies, J. H., *J. Chem. Soc. Dalton Trans.*, **1997**, 939.
265. Kataky, R.; Matthes, K. E.; Nicholson, P. E.; Parker, D., *J. Chem. Soc. Perkin Trans. 2*, **1990**, 1425-1432.
266. Perry, C. B, University of the Witwatersrand, Johannesburg, South Africa.
267. SigmaPlot for Windows, V. 11. Dundas Software, Germany, **1999**.
268. Supkowski, R. M.; Horrocks, Jr. W. D., *Inorg. Chem. Acta.*, **2002**, 340, 44.
269. Gosser, D. K.; *Cyclic Voltammetry: Simulation and Analysis of Reaction Mechanisms*, VCH, New York, **1993**, 43.
270. Nicholson, R. S., *Anal. Chem.*, **1965**, 37, 1351.
271. Beeby, A.; Dickins, R. S.; Faulkner, S.; Parker, D.; Williams, J. A. G., *Chem. Commun.* **1997,** *15,* 1401.
272. Martell, A. E.; Hancock, R. D., *Metal Complexes in Aqueous Solutions*, Plenum Press, New York, **1996**.
273. Konings, M. S.; Dow, W. C.; Love, D. B.; Raymond, K. N.; Quay, S. C. , Rocklage, S. M., *Inorg. Chem.*, **1990**, 29, 1488.
274. Kang, S. I.; Ranganathan, R. S.; Emswiler, J. E.; Kumar, K.; Gougoutas, J. Z.; Malley, M. F.; Tweedle, M. F., *Inorg. Chem.*, **1993**, 32, 2912.
275. Chang, C. A.; Francesconi, L. C.; Malley, M. F.; Kumar, K.; Gougoutas, J. Z.; Tweedle, M. F.; Lee, D. W.; Wilson, L. J., *Inorg. Chem.*, **1993**, 32, 3501.

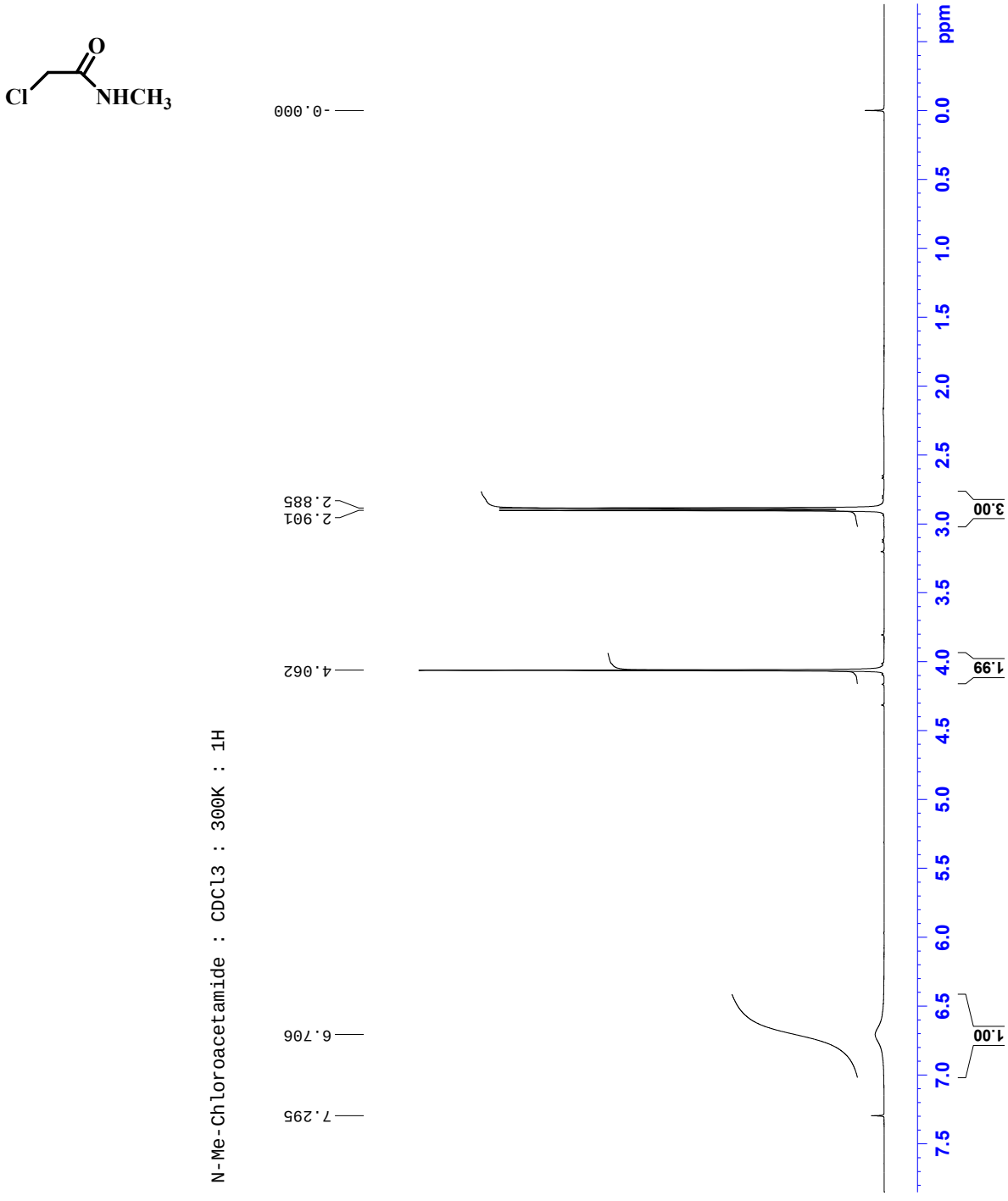
276. Dubost, J.-P.; Leger, J.-M.; Langlois, M.-H.; Meyer, D.; Schaefer, M., *C.R. Acad. Sci.*, *Ser. II*, 1991, 312, 349.
277. Guggenberger, I. J.; Muetterties, E. L., *J. Am. Chem. Soc.*, **1976**, 98, 7221.
278. Bernal, I., *Stereochemical and Stereophysical Behavior of Macrocycles*, Elsevier, Amsterdam, **1987**, p. 87.
279. Bombieri, G.; Marchini, N.; Ciattini, S.; Mortillaro, A.; Aime, S., *Inorg. Chim. Acta*, **2006**, 359, 3405.
280. F. Benetollo, G. Bombieri, L. Calabi, S. Aime, M. Botta, *Inorg. Chem.*, **2003**, 42, 148.
281. Kumar, K.; Chang, C.A.; Francesconi, L.C.; Dischino, D.D.; Malley, M.F.; Gougoutas, J.Z.; Tweedle, M.F., *Inorg. Chem.*, **1994**, 33, 3567.
282. Dubost, J.P.; Leger, J.M., Langlois, M.H., Meyer, D., Schaefer, M., *M.C.R.I. Academie Sci., Ser. II Univers.*, **1991**, 312, 349.
283. Aime, S.; Anelli, P.L.; Botta, M.; Fedeli, F.; Grandi, M.; Paoli, P.; Uggeri, F., *Inorg. Chem.*, **1992**, 31, 2422.
284. Basak, B.; Bhattacharyya, U. K.; Laskar, S., *Amino Acids*, **1993**, 4, 93-196.
285. Hall, H.K., Jr. *J. A.m. Chem. Soc.* **1957**, *79*, 5441.Turro, N. J., Modern Molecular Photochemistry, University Science Books, Mill Valley, CA., **1991**, Chapter 9.
286. Jain, A.; Yadav, K.; Mohapatra, M.; Godbole, S. V.; Tomar, B. S., *Spectrochimica Acta Part A*, **2009**, 72, 1122.
287. Park, K. K.; Jung, E. C.; Cho, h.-R.; Kim, W. H, *Spectrochimica Acta Part A*, 73, **2009**, 615.
288. Bruce, J. I.; Dickins, R. S.; Govenlock, L. J.; Gunnlaugsson, T.; Lopinski, S.; Lowe, M. P.; Parker, D.; Peacock, R. D.; Perry, J. J. B.; Aime, S.; Botta, M., *J. Am. Chem. Soc.* **2000**, 122, 9674.
289. Aime, S.; Barge, A.; Botta, M.; Howard, J. A. K.; Lowe, M. P.; Moloney, J. M.; Parker, D.; de Sousa, A. S., *Chem. Commun*., **1999**, 1047.
290. Dickins, R. S.; Gunnlaugsson, T.; Parker, D.; Peacock, R. D., *Chem. Commun*., **1998**, 1643.
291. Kimpe, K.; D'Olieslager, W.; Gorlier-Walrand, C.; Figuerinha, A.; Kovacs, Z.; Geraldes, C. F. G. C., *J. Alloys Compd*., **2001**, 323, 828.
292. Salama, S.; Richardson, F. S., *Inorg. Chem.*, **1980**, 84. 512.

293. Morrow, J. R.; Aures, K.; Epstein, D., *J. Chem. Soc., Chem. Commum.*, **1995**, 2431.
294. Kimura, E.; Kodama, Y.; Koike, T.; Shiro, M., *J. Am. Chem. Soc.*, **1995**, 117, 8304.
295. Schneider, H.-J.; Rammo, J.; Hettich, R., Angew. Chem., *Int. Ed. Engl.*, **1993**, 32, 1716.
296. Young, M. J.; Wahnon, D.; Hynes, R. C.; Chin, J., *J. Am. Chem. Soc.*, **1995**, 117, 9441.
297. Amin, S. A.; Voss, D. A., Jr.; Horocks, W. DeW., Jr.; Lake, C. H.; Churchill, M. R.; Morrow, J. R., *Inorg. Chem.*, **1995**, 34, 3294.
298. Amin, S. A.; Morrow, J. R.; Lake, C. H.; Churchill, M. R.; *Angew. Chem., Int. Ed. Engl.*, **1994**, 33, 773.
299. Lowe, M. P.; Parker, D., Chem. Commun., 2000, 707.
300. Govenlock, L. J.; Howard, J. A. K.; Moloney, J. M.; Parker, D.; Peacock, R. D.; Siligardi, G., *J. Chem. Soc. Perkin Trans. 2*, **1999**, 2415.
301. Parker, D.; Puschmann, H.; Batsanov, A. S; Senanayake, K., *Inorg. Chem.*, **2003**, 42, 8646.
302. Burai, L.; Toth, E.; Moreau, G.; Sour, A.; Scopelliti, R.; Merbach, A. E., *Chem. Eur. J.*, **2003**, 9, 6, 1394.
303. Eckardt, D, Holleck, L. Z.; *Z. Elektrochem.*, **1955**, 59, 202.

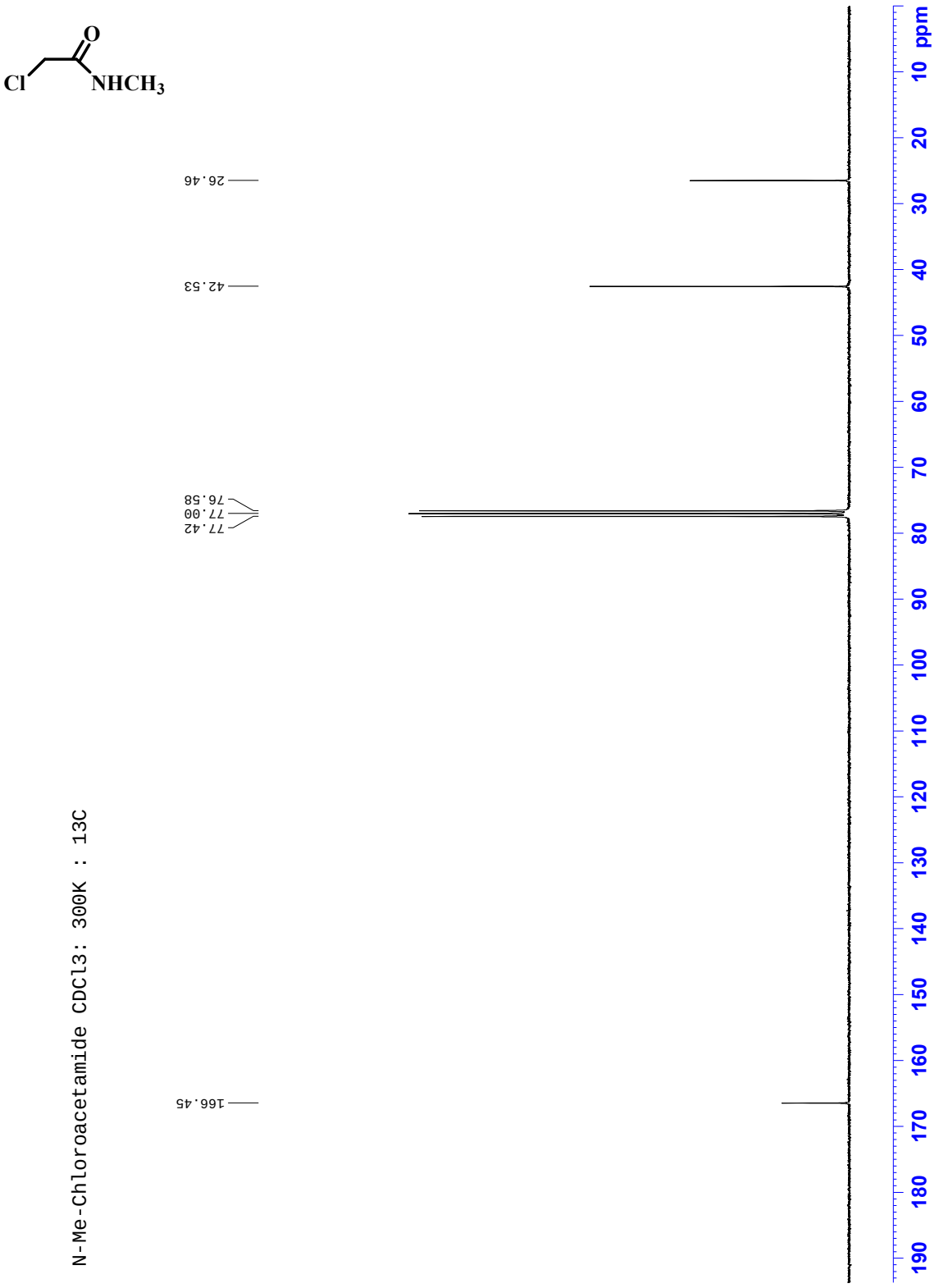
Appendices

A NMR

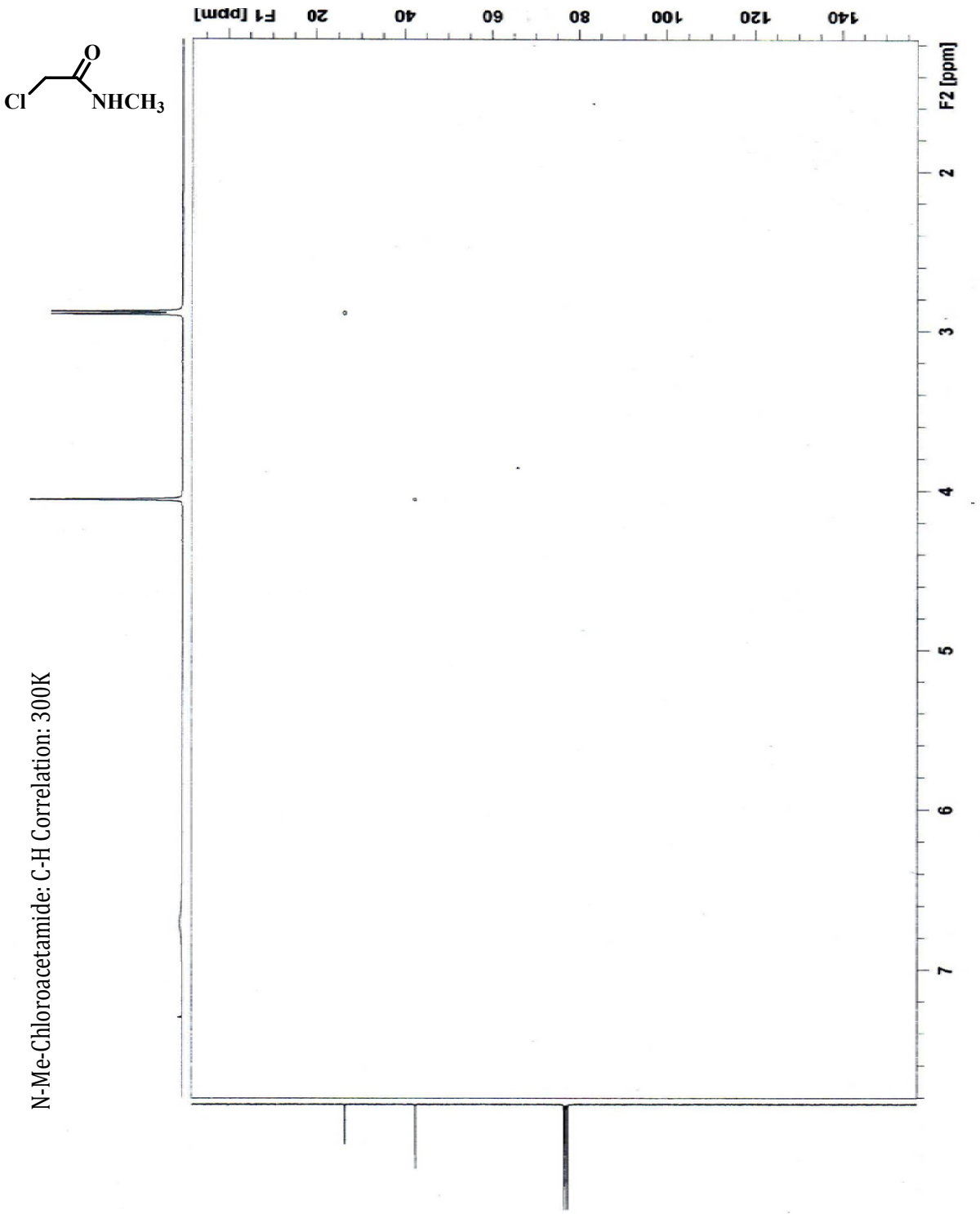
A1: *N*-Me-chloroacetamide – ^{1}H



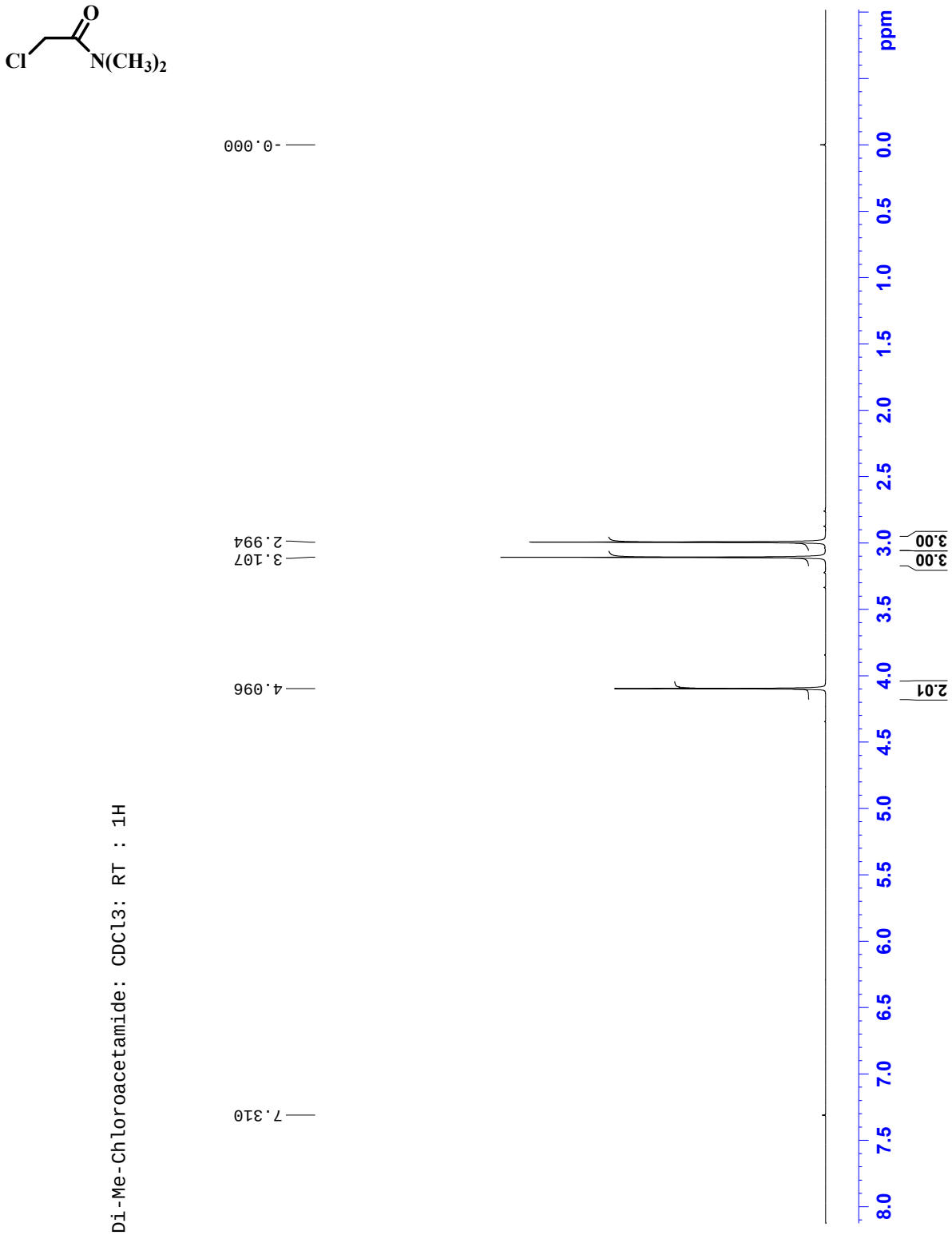
A2: *N*-Me-chloroacetamide - ^{13}C



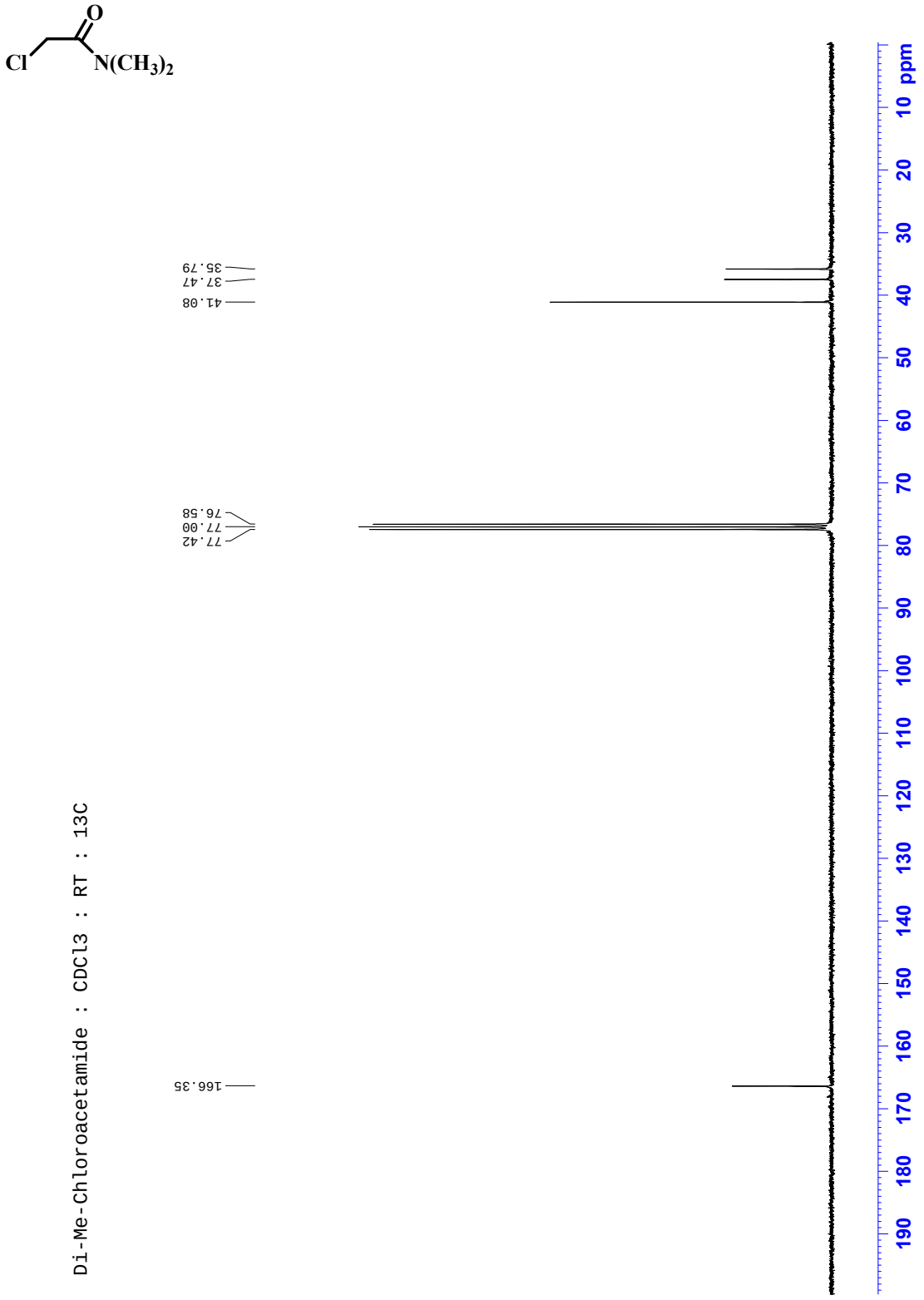
A3: *N*-Me-chloroacetamide – C-H correlation



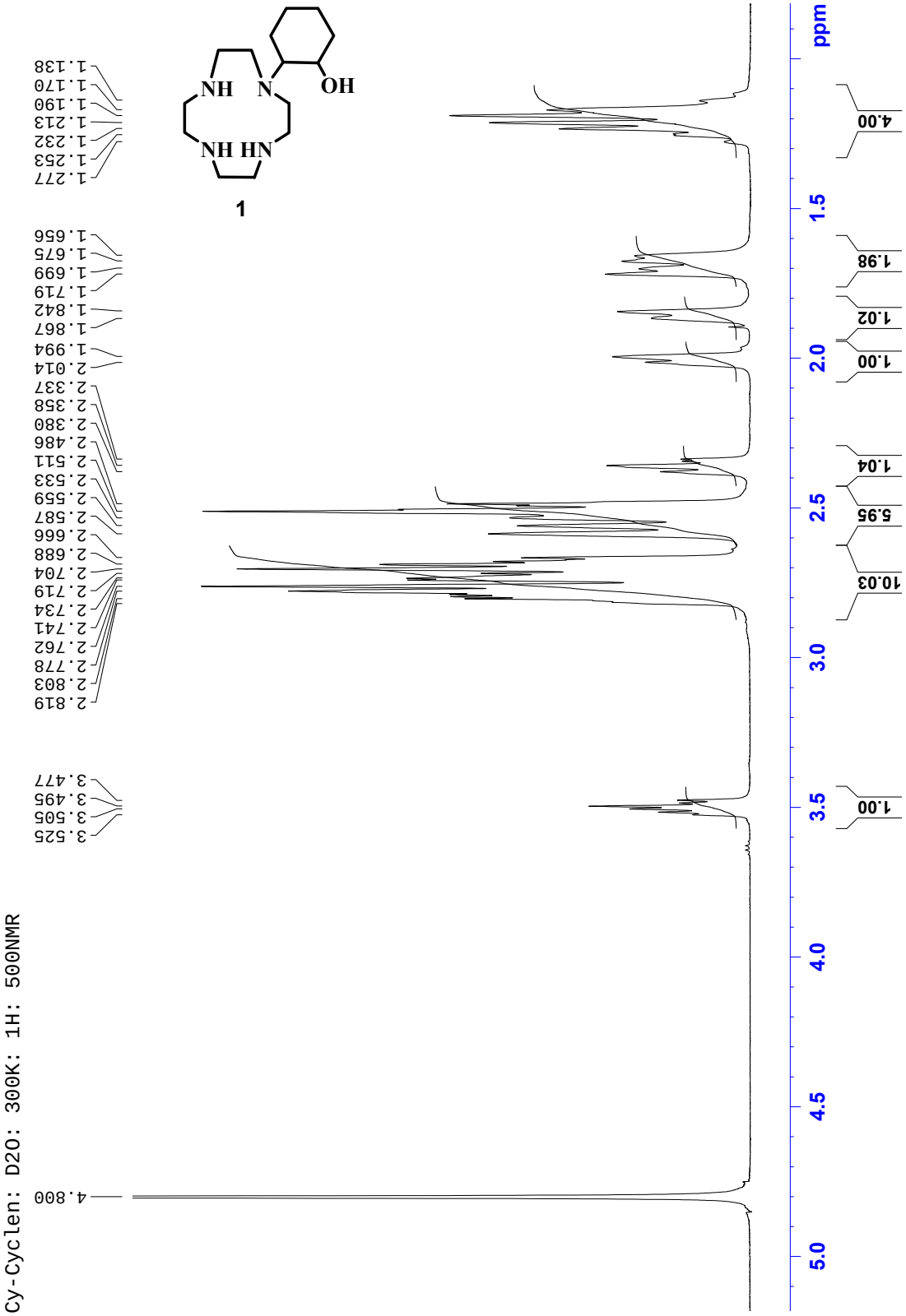
A4: *Di*-Me-chloroacetamide – ^{1}H



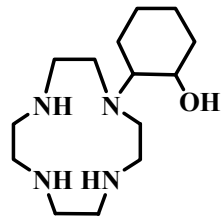
A5: *Di*-Me-chloroacetamide – ^{13}C



A6: 1-(2-Hydroxycyclohexyl)-1,4,7,10-tetraazacyclodecane (1) – ^{1}H

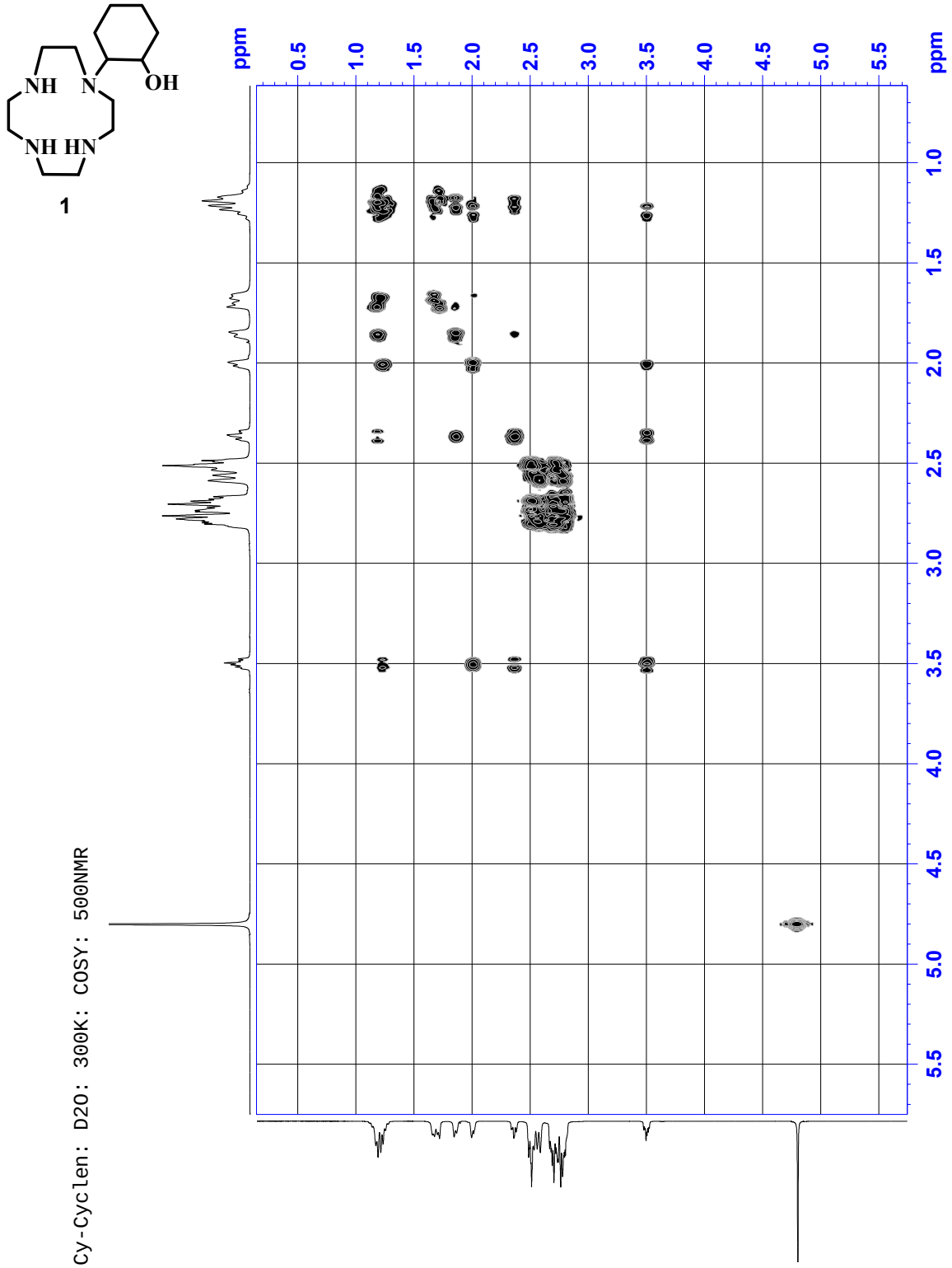


A7: 1-(2-Hydroxycyclohexyl)-1,4,7,10-tetraazacyclodecane (1) – ^{13}C

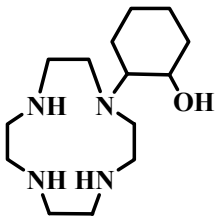


1

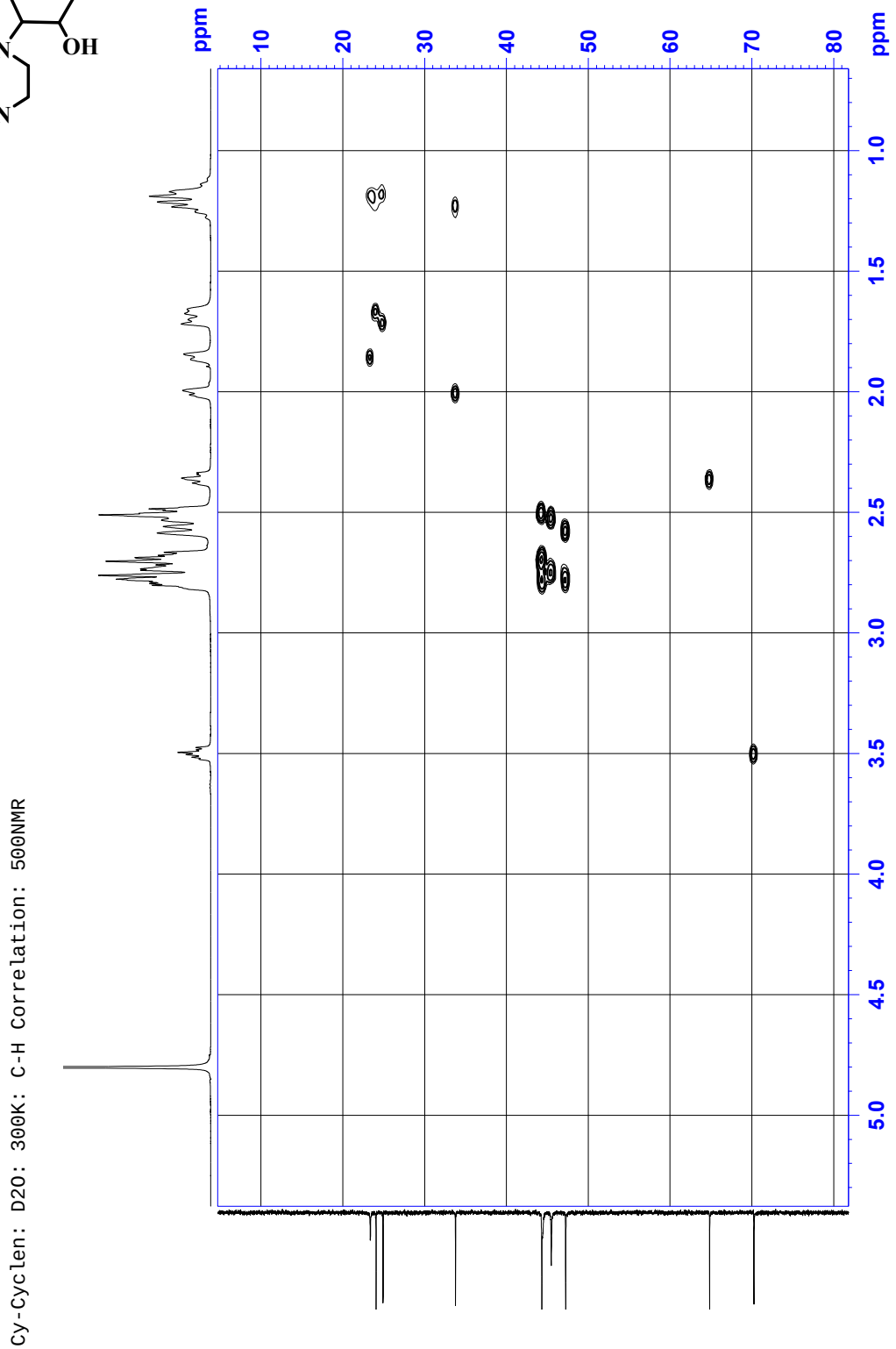
A8: 1-(2-Hydroxycyclohexyl)-1,4,7,10-tetraazacyclodecane (1) – COSY



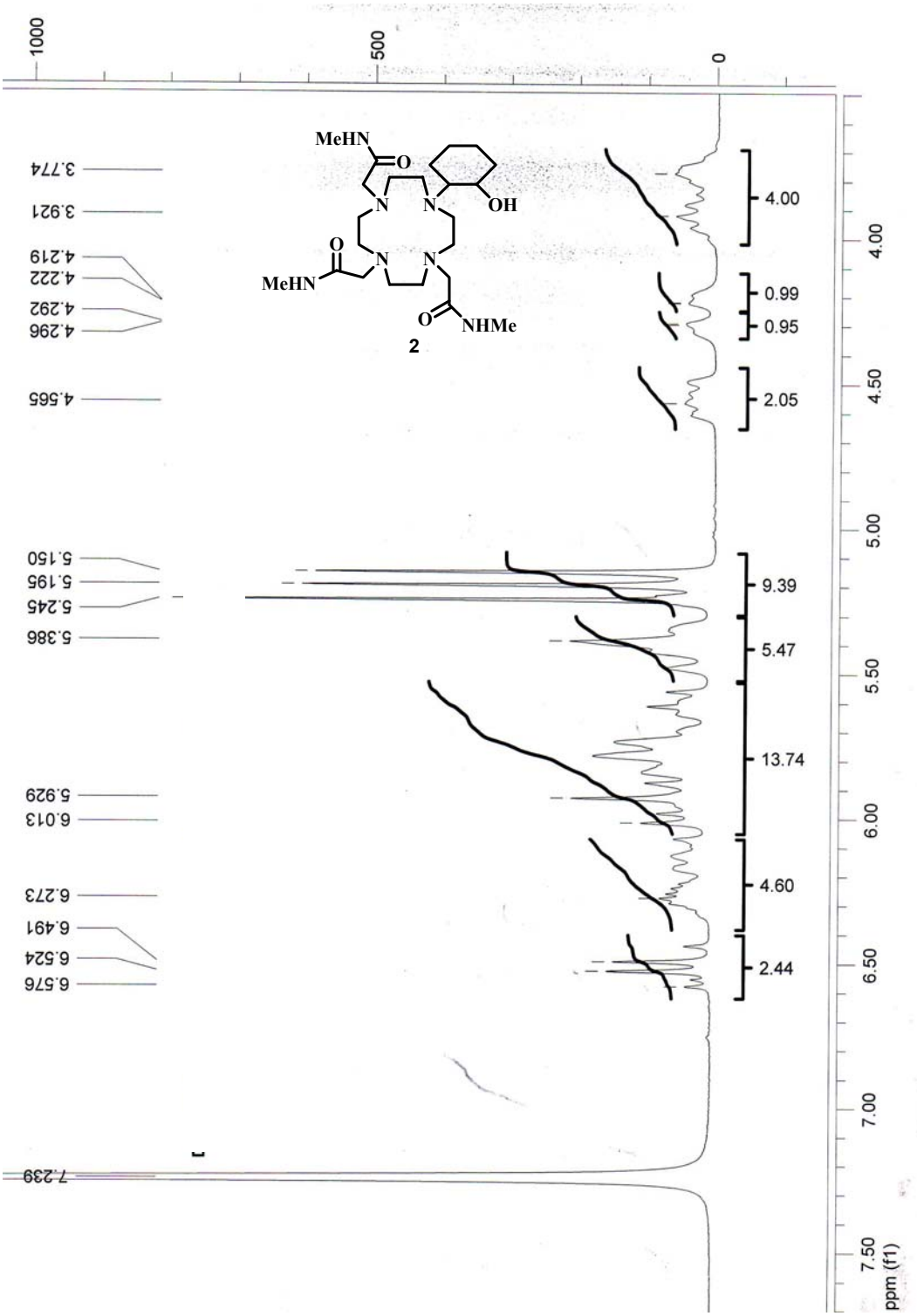
A9: 1-(2-Hydroxycyclohexyl)-1,4,7,10-tetraazacyclodecane (1) – C-H correlation



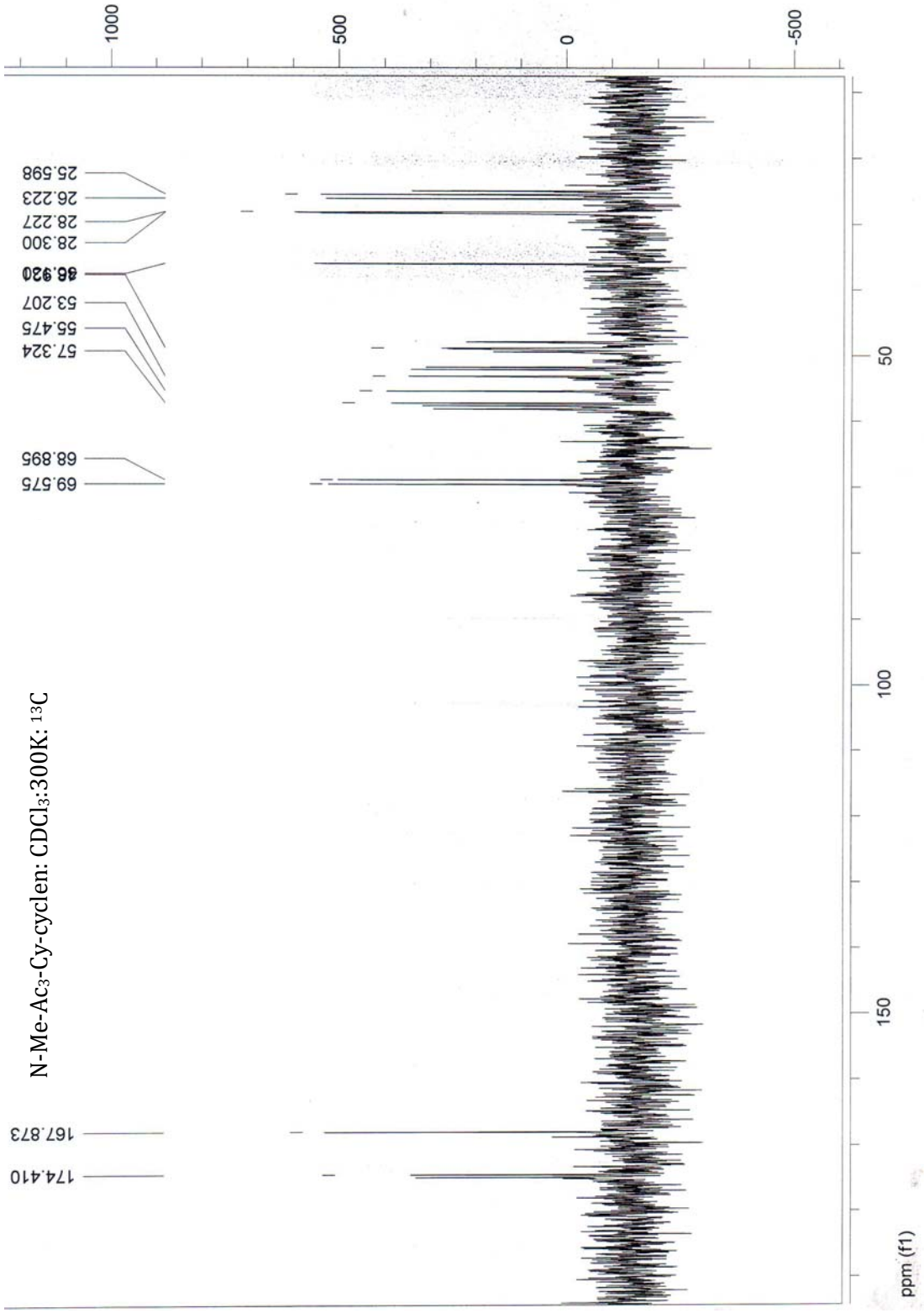
1



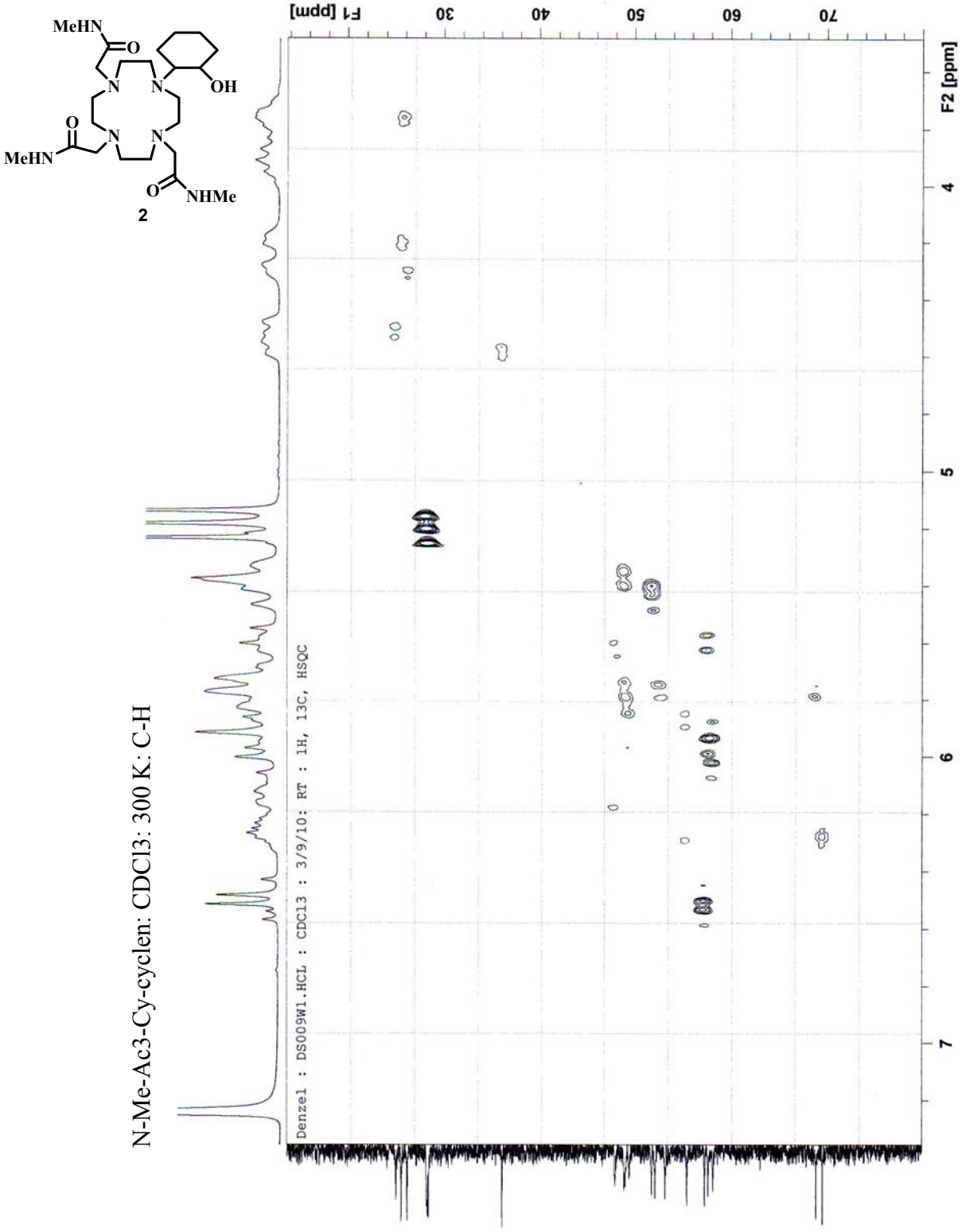
A10: 1,4,7-tris[*N*-methylcarbamylmethyl]-10-(2-hydroxycyclohexyl)-1,4,7,10-tetraazacyclododecane (2) -^{1}H



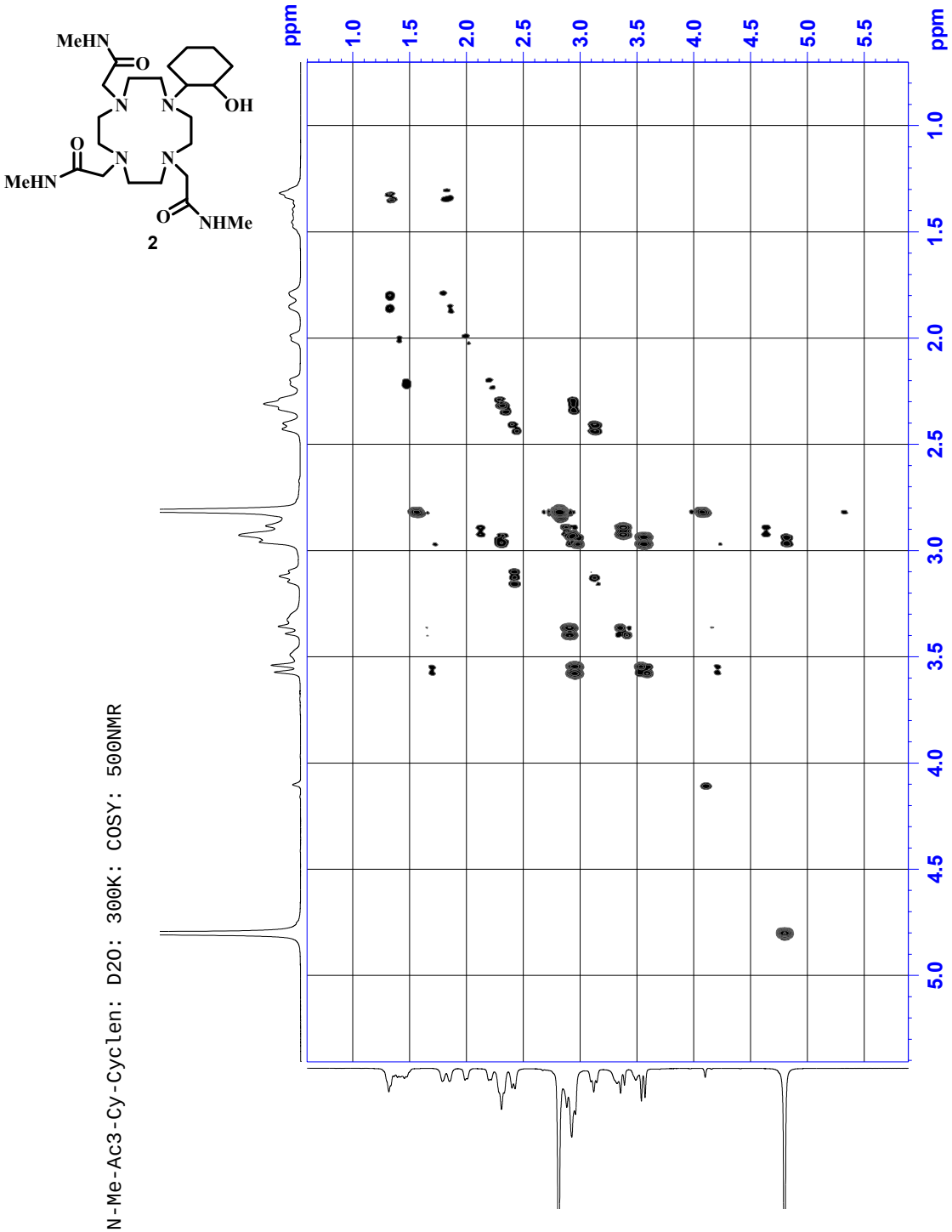
A11: 1,4,7-tris[*N*-methylcarbamylmethyl]-10-(2-hydroxycyclohexyl)-1,4,7,10-tetraazacyclododecane (2) ^{13}C



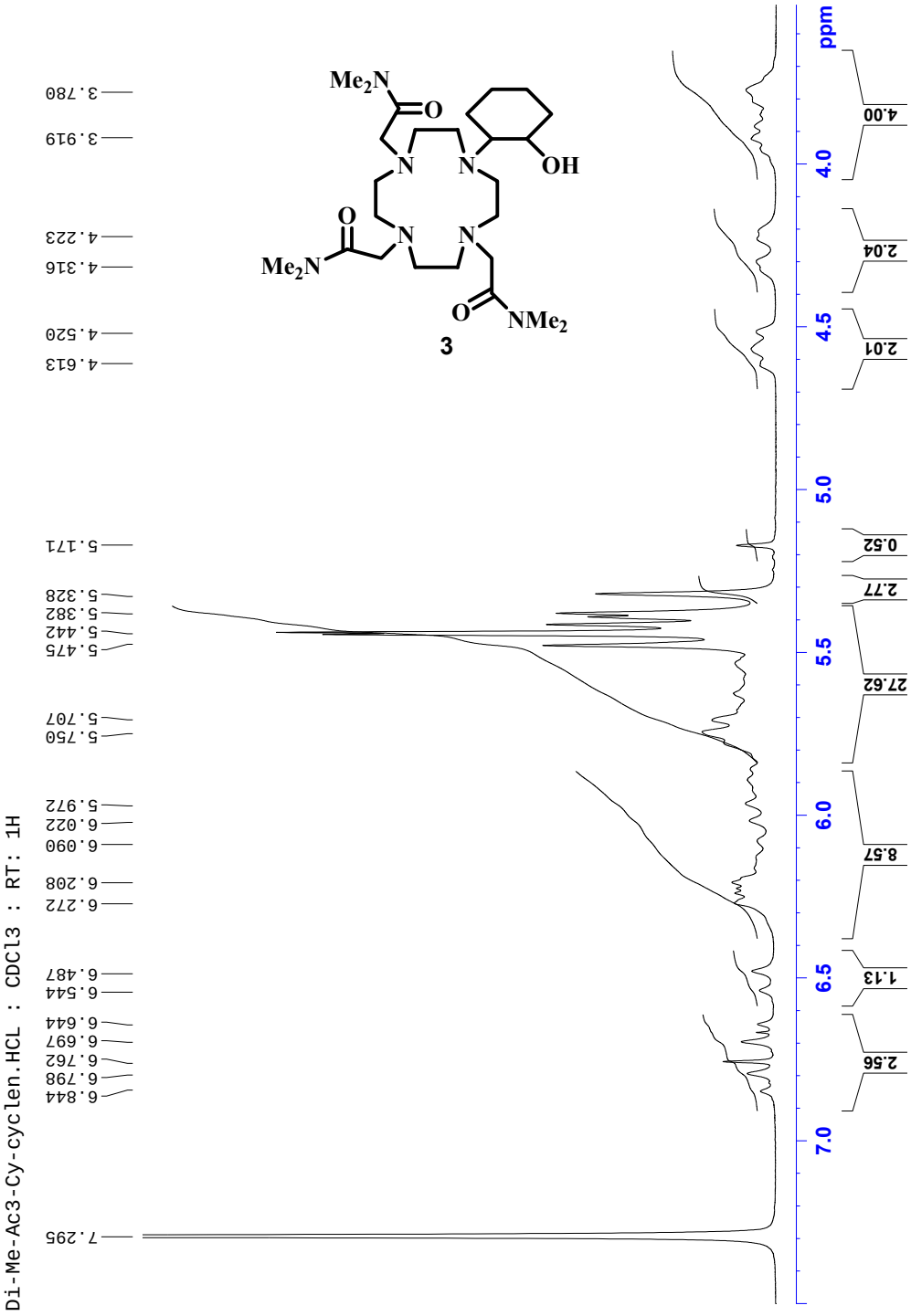
A12: 1,4,7-tris[*N*-methylcarbamylmethyl]-10-(2-hydroxycyclohexyl)-1,4,7,10-tetraazacyclododecane– C-H correlation



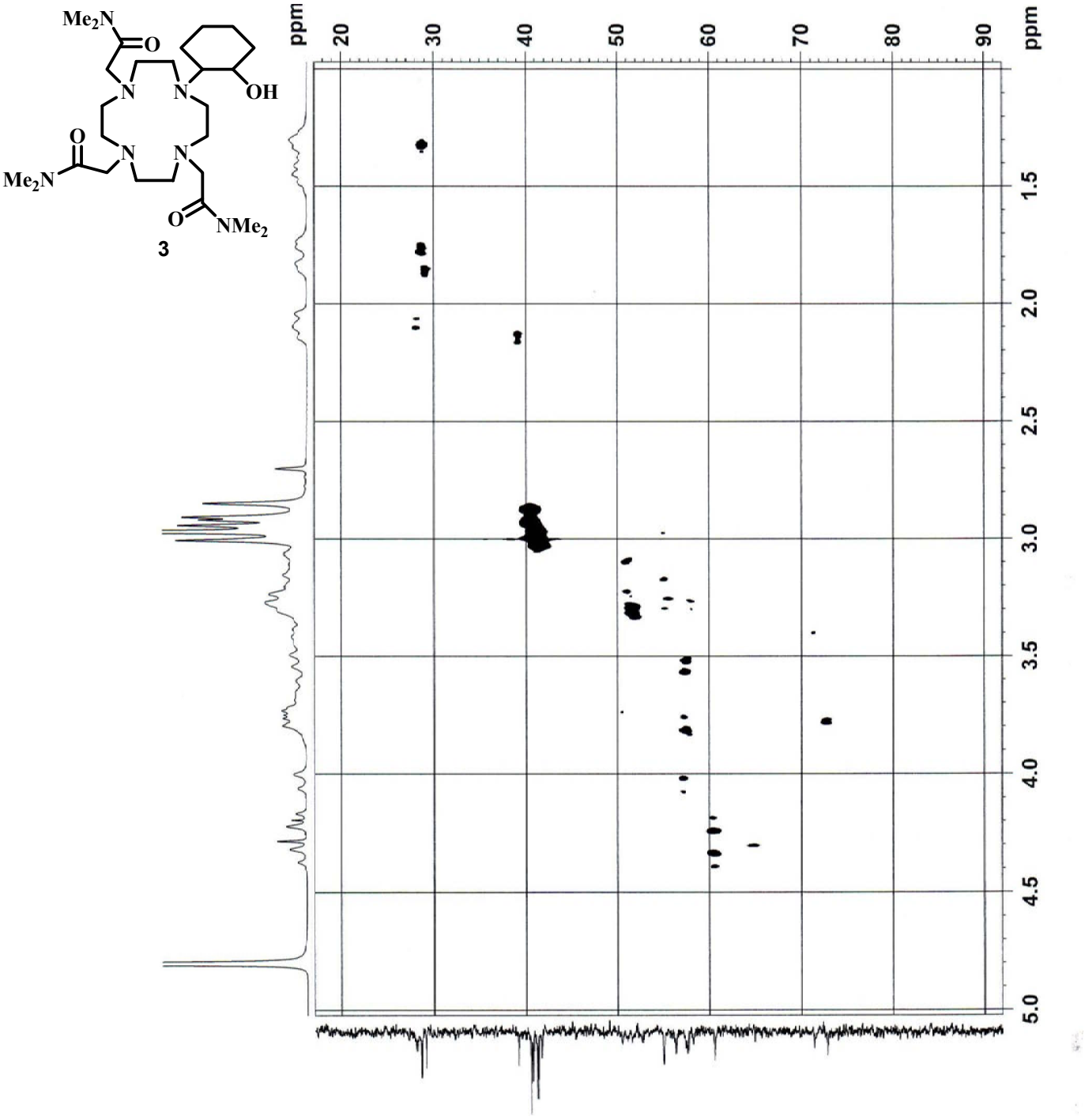
A13: 1,4,7-tris[*N*-methylcarbamylmethyl]-10-(2-hydroxycyclohexyl)-1,4,7,10-tetraazacyclododecane (2) – COSY in D_2O



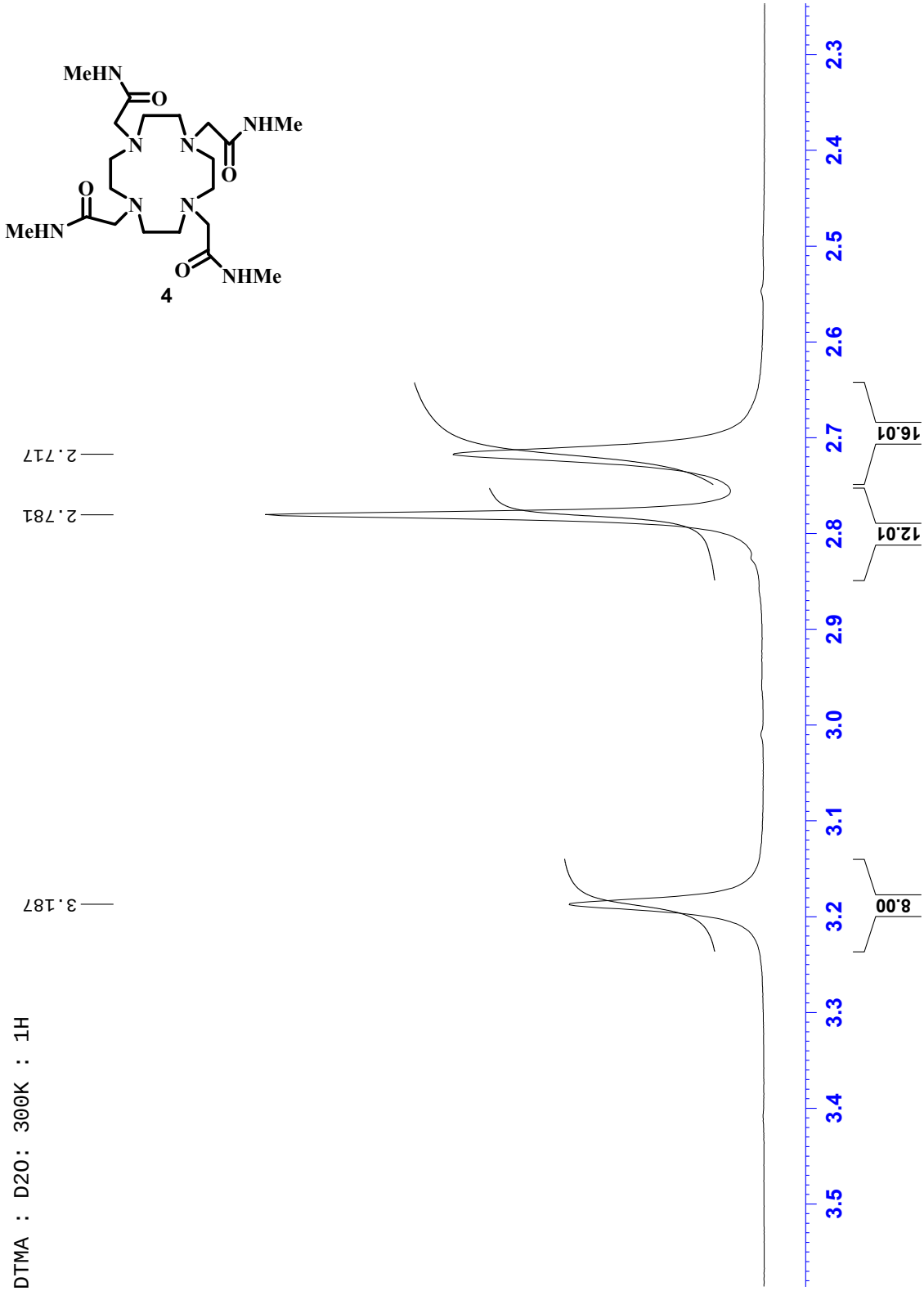
A14: 1,4,7-tris[*N*,*N*-dimethylcarbamylmethyl]-10-(2-hydroxycyclohexyl)-1,4,7,10-teraazacyclododecan (3) – ^{1}H



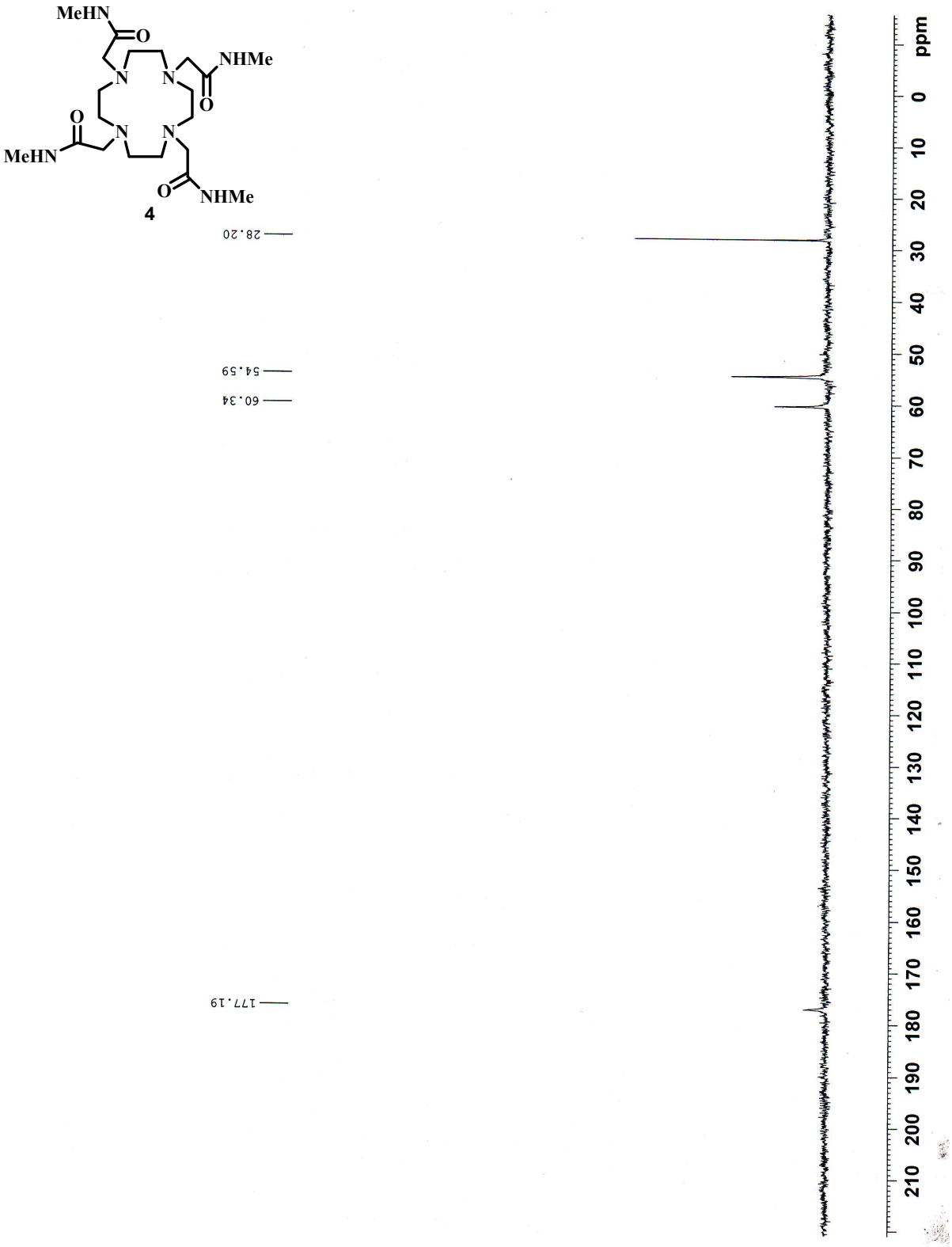
A15: 1,4,7-tris[*N*,*N*-dimethylcarbamylmethyl]-10-(2-hydroxycyclohexyl)-1,4,7,10-teraazacyclododecan (3) – C-H correlation



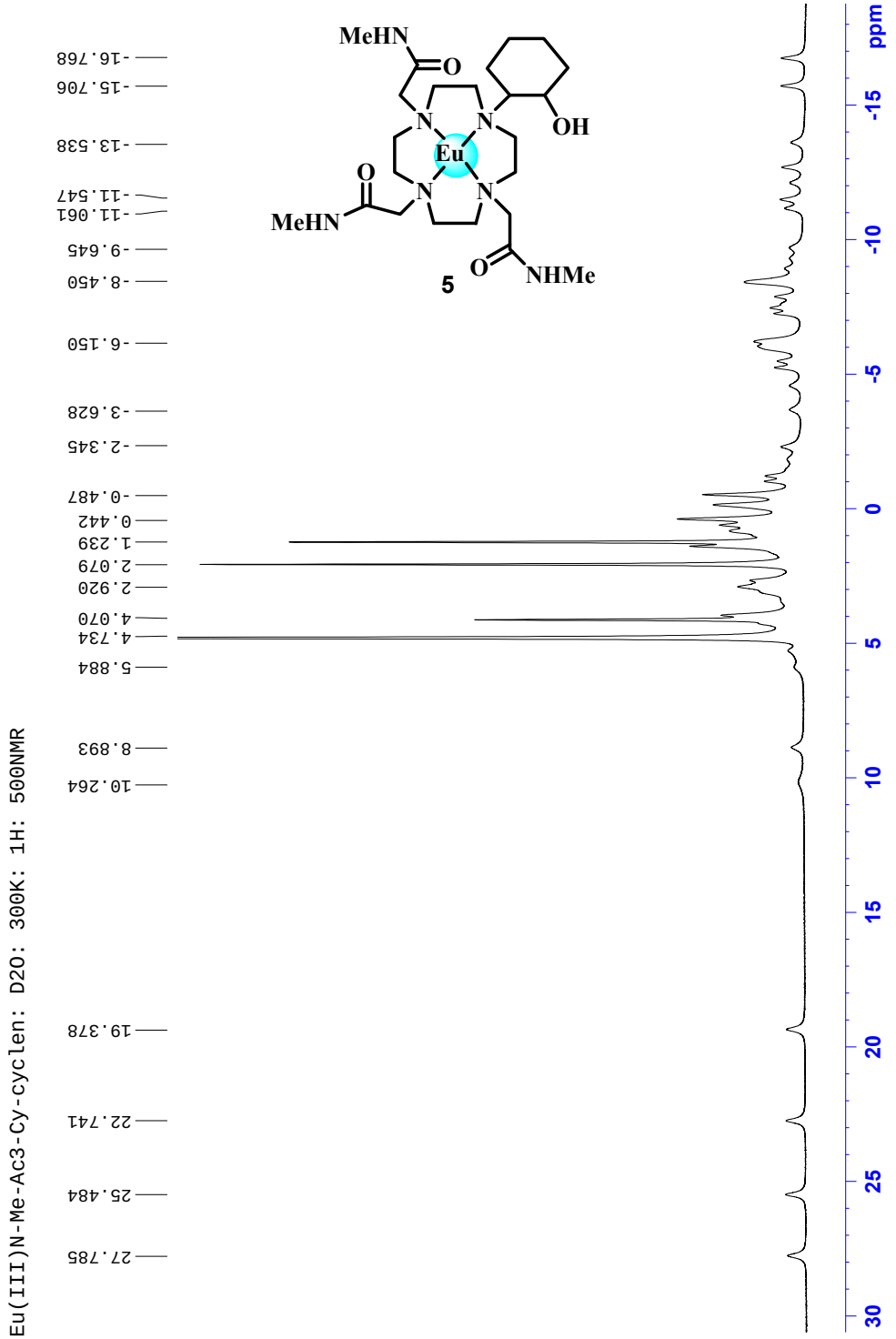
A16: 1,4,7,10-Tetrakis(methylcarbamylmethyl)-1,4,7,10-tetraazacyclodecane (4) – ^{1}H



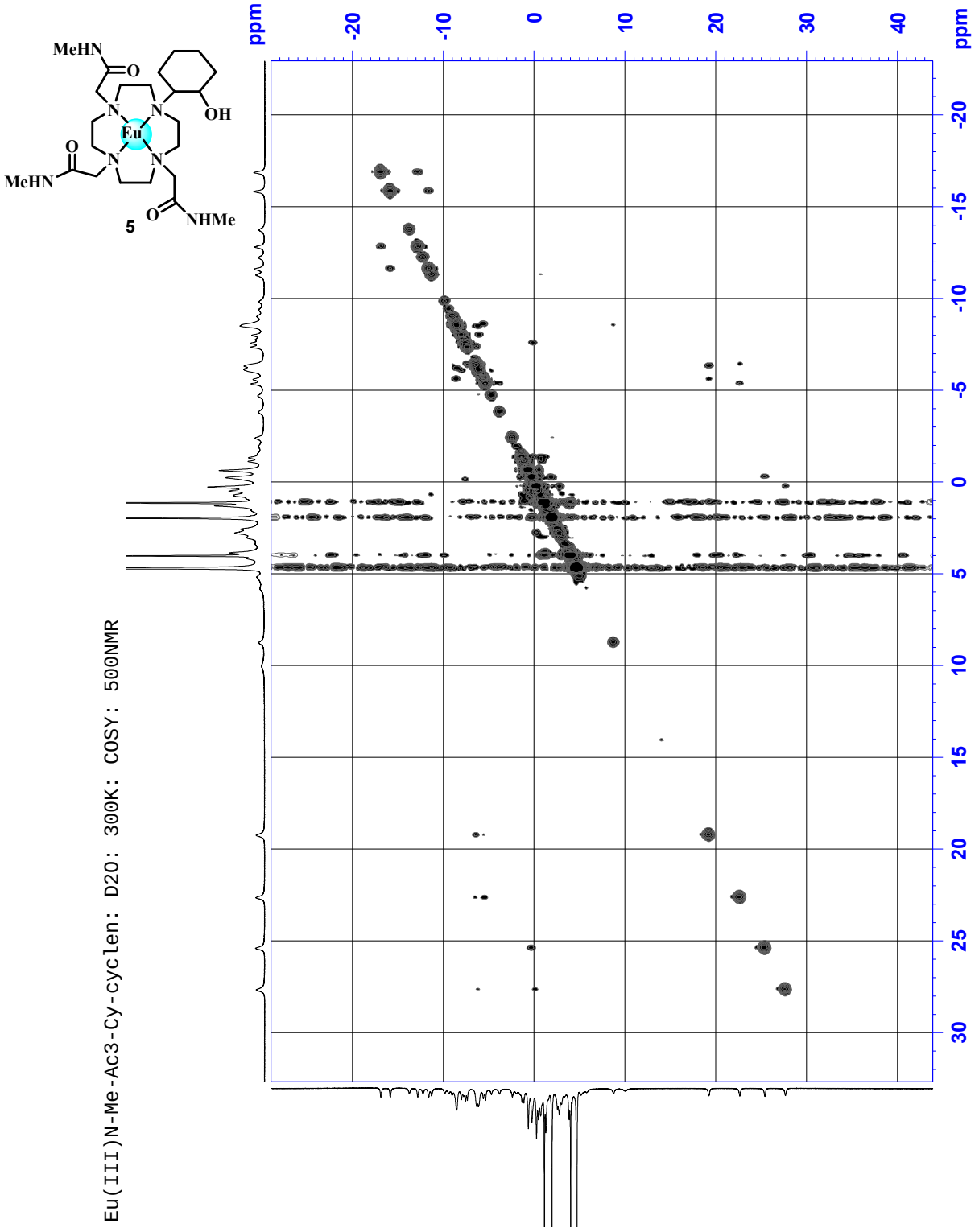
A17: 1,4,7,10-Tetrakis(methylcarbamylmethyl)-1,4,7,10-tetraazacyclodecane (4) – ^{13}C



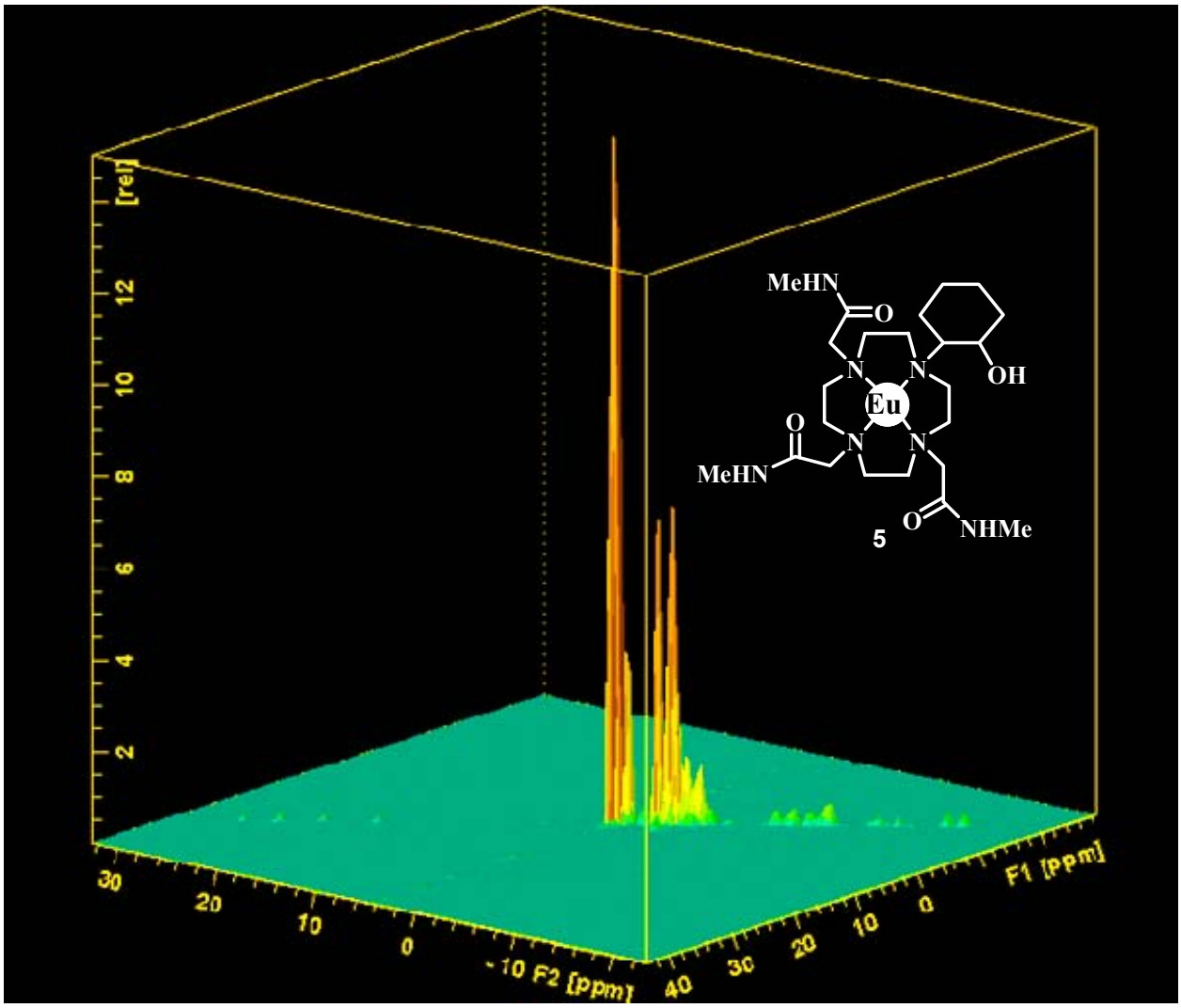
A17: Eu-1,4,7-tris[N-methylcarbamylmethyl]-10-(2-hydroxycyclohexyl)-1,4,7,10-tetraazacyclododecane (5) – ^{1}H



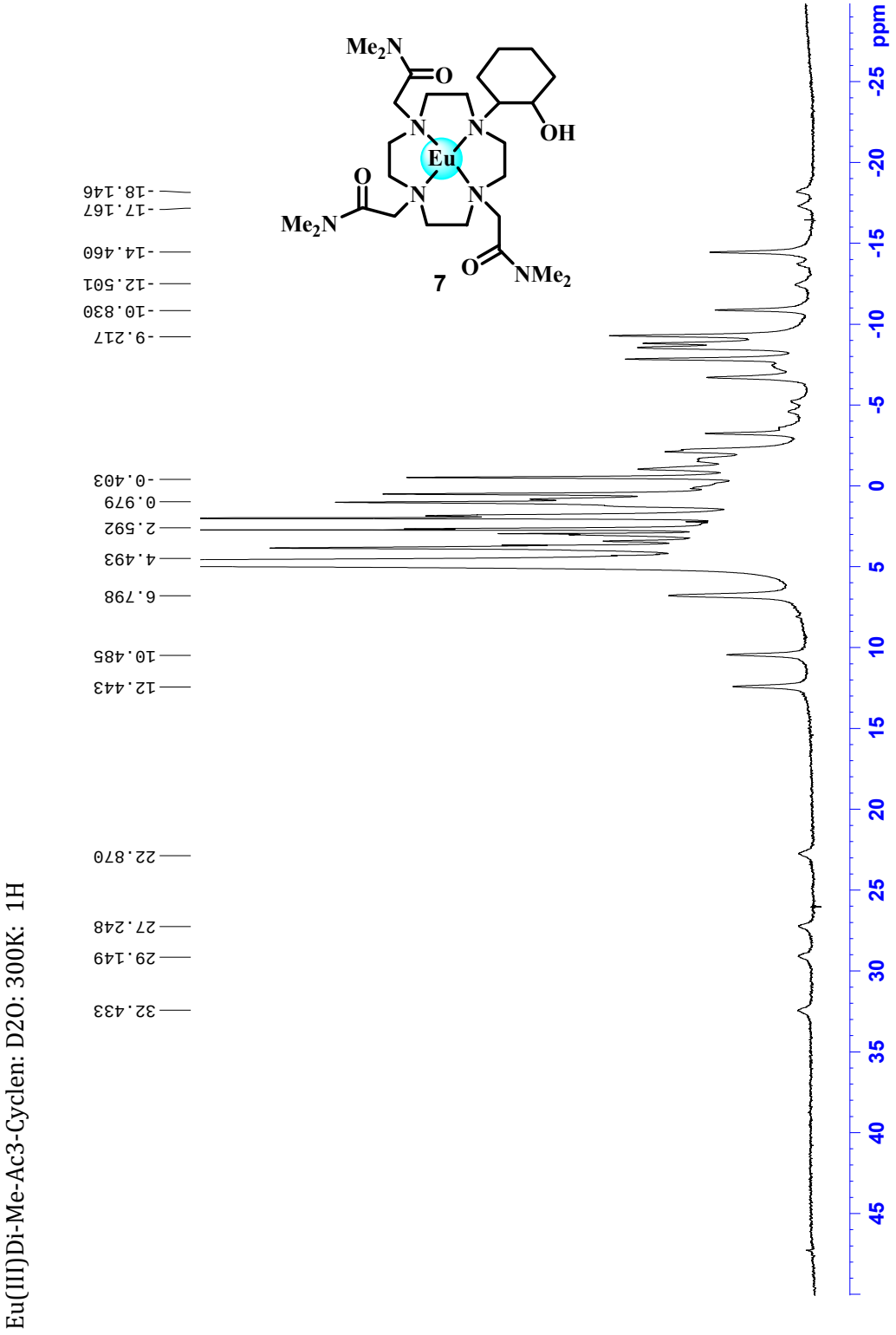
A18: Eu-1,4,7-tris[N-methylcarbamylmethyl]-10-(2-hydroxycyclohexyl)-1,4,7,10-tetraazacyclododecane (5) – COSY



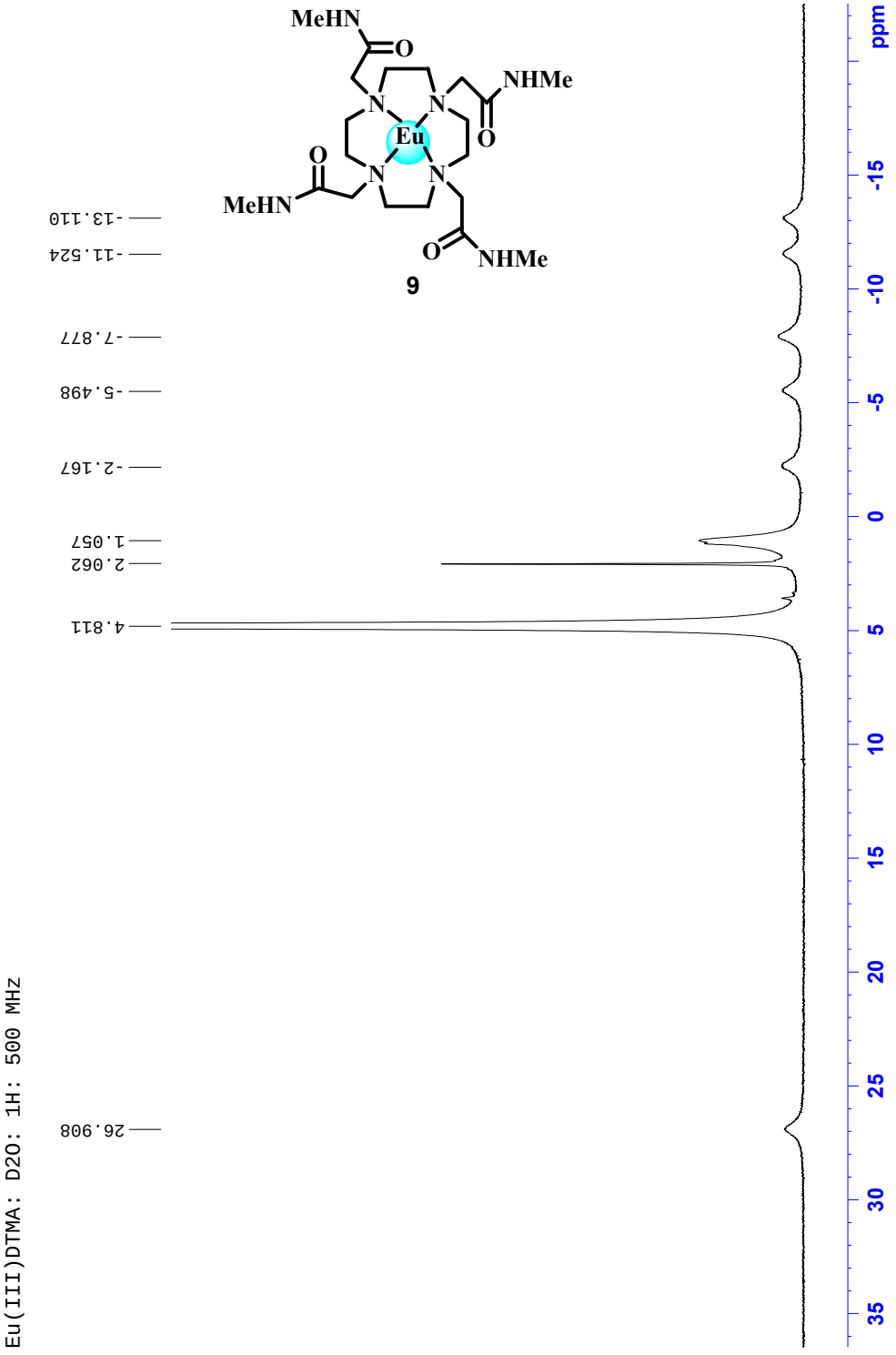
A19: Eu-1-1,4,7-tris[*N*-methylcarbamylmethyl]-10-(2-hydroxycyclohexyl)-1,4,7,10-tetraazacyclododecane (5) – 3D COSY



A20: Eu-1,4,7-tris[*N*,*N*-dimethylcarbamylmethyl]-10-(2-hydroxycyclohexyl)-1,4,7,10-tetraazacyclododecane (7) – 1H

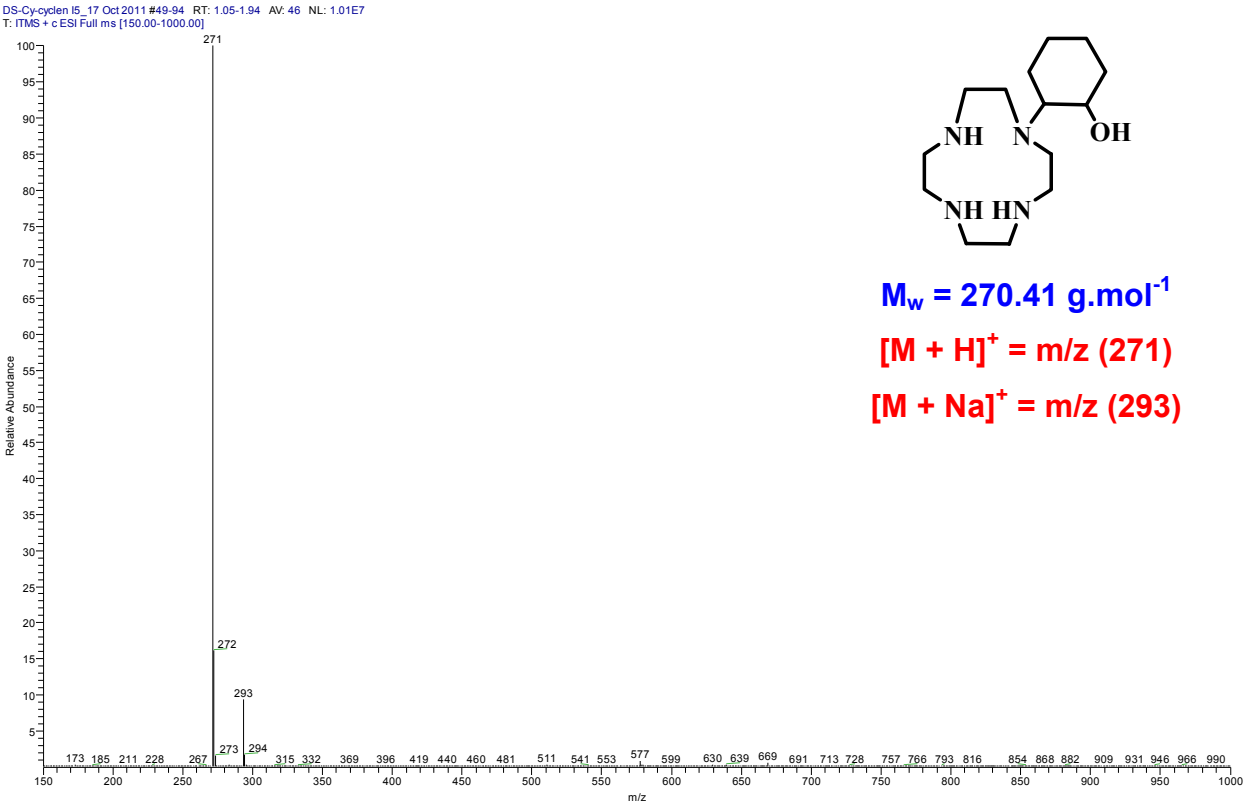


A21: Eu-1,4,7,10-Tetrakis(methylcarbamylmethyl)-1,4,7,10-tetraazacyclodecane (9) – 1H

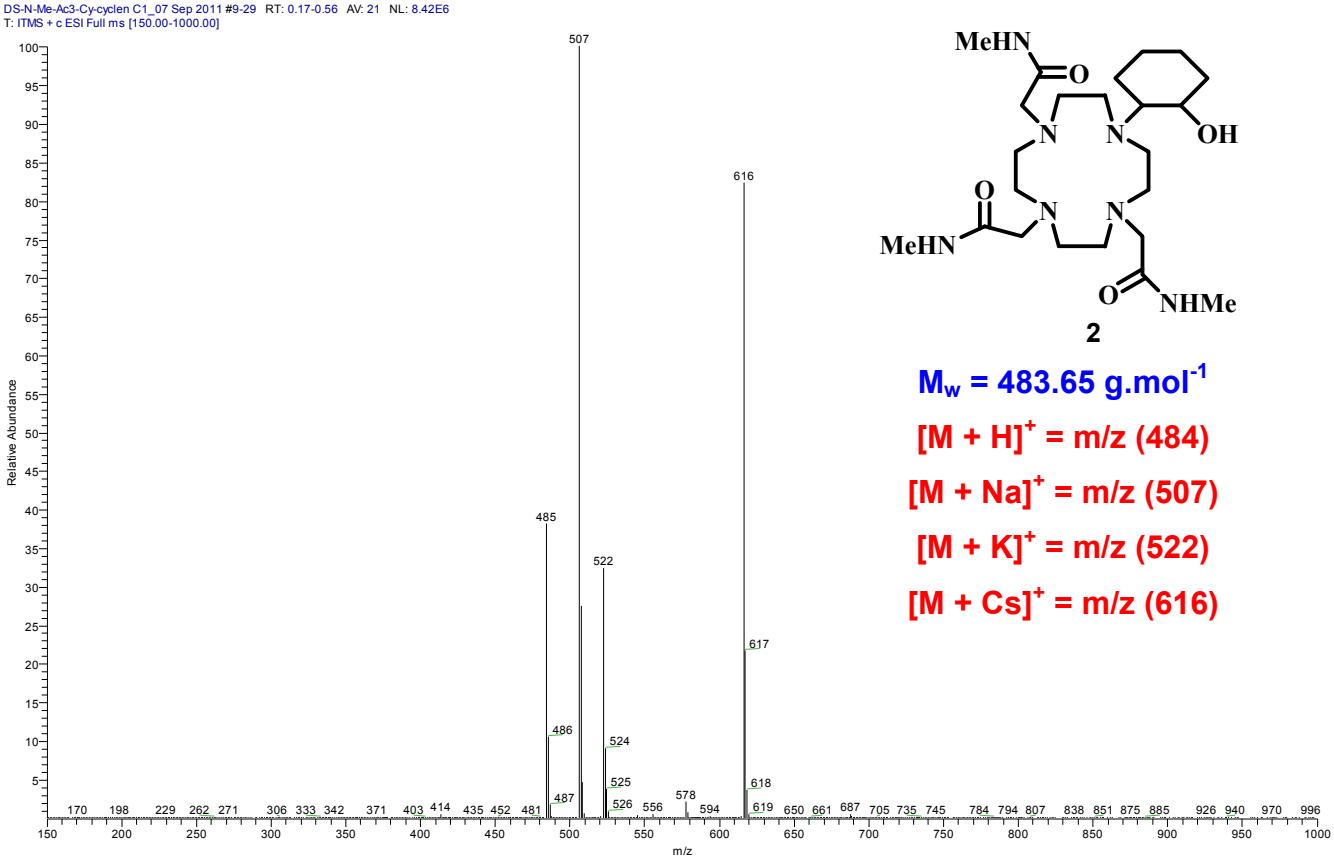


B – ESI-MS

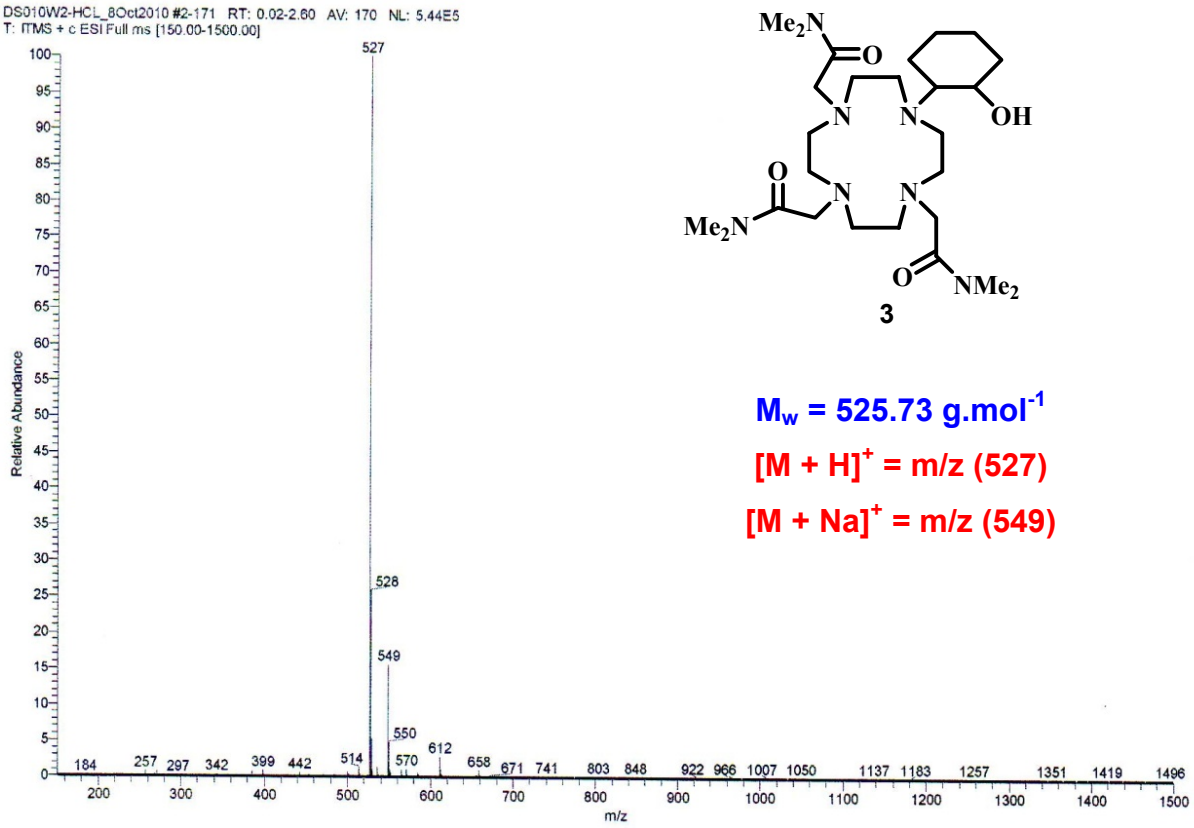
B1: 1-(2-Hydoxycyclohexyl)-1,4,7,10-tetraazacyclodecane (1)



B2: 1,4,7-tris[*N*-methylcarbamylmethyl]-10-(2-hydroxycyclohexyl)-1,4,7,10-tetraazacyclododecane (2)



B3: 1,4,7-tris[*N,N*-dimethylcarbamylmethyl]-10-(2-hydroxycyclohexyl)-1,4,7,10-tetraazacyclododecane (3)



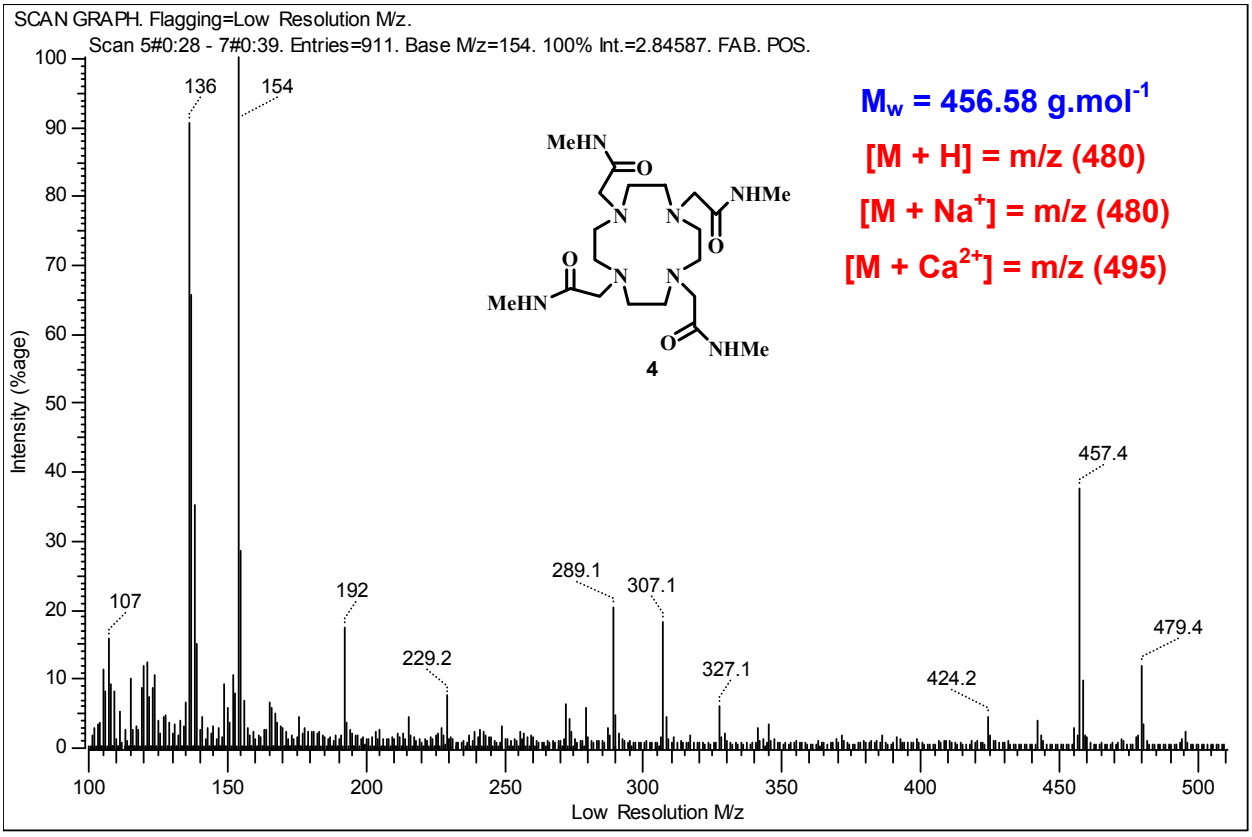
3

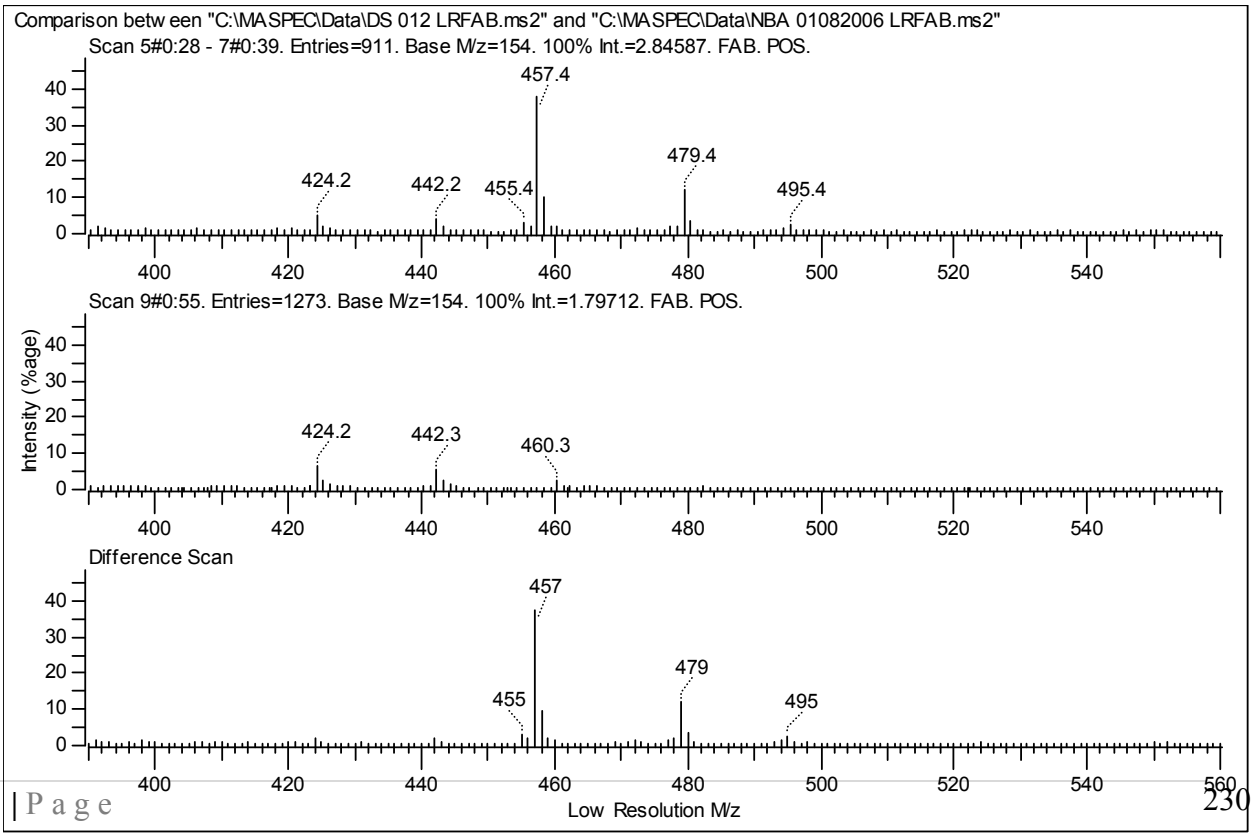
M_w = 525.73 g.mol^{-1}

$[M + H]^+$ = m/z (527)

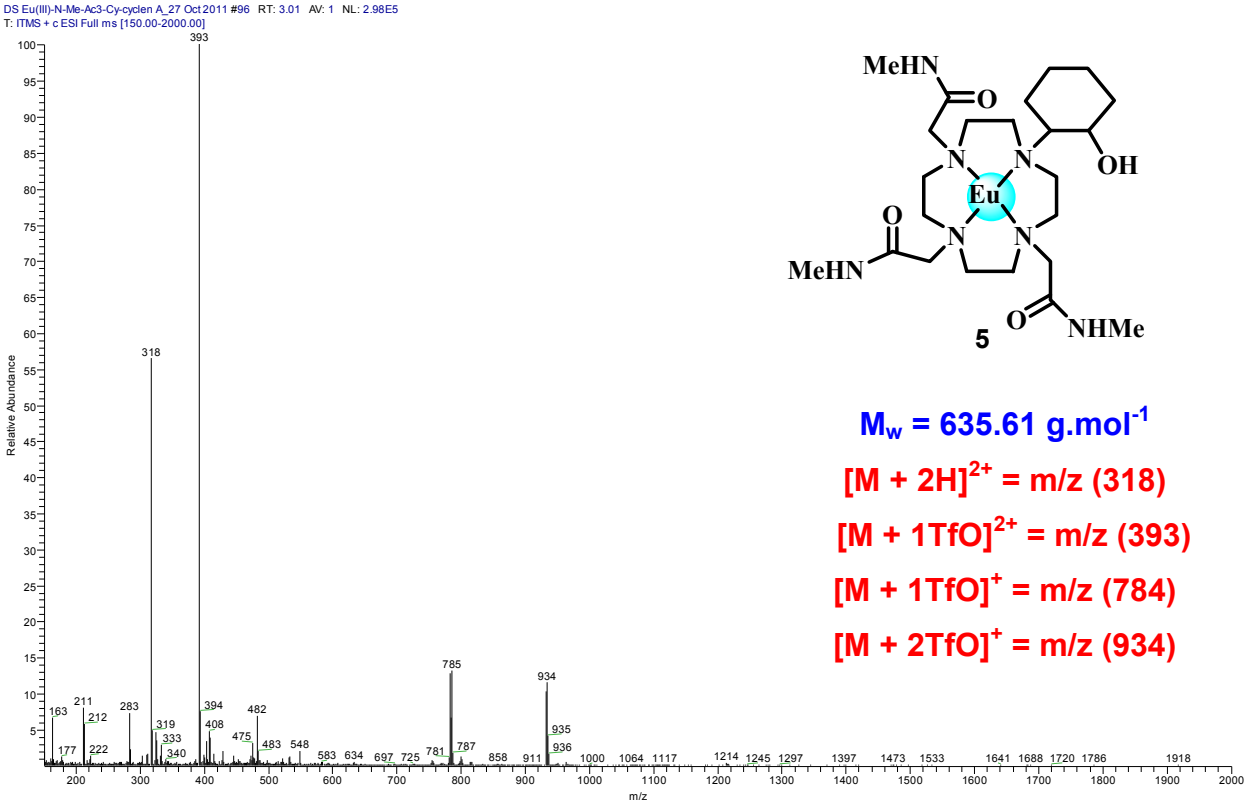
$[M + Na]^+$ = m/z (549)

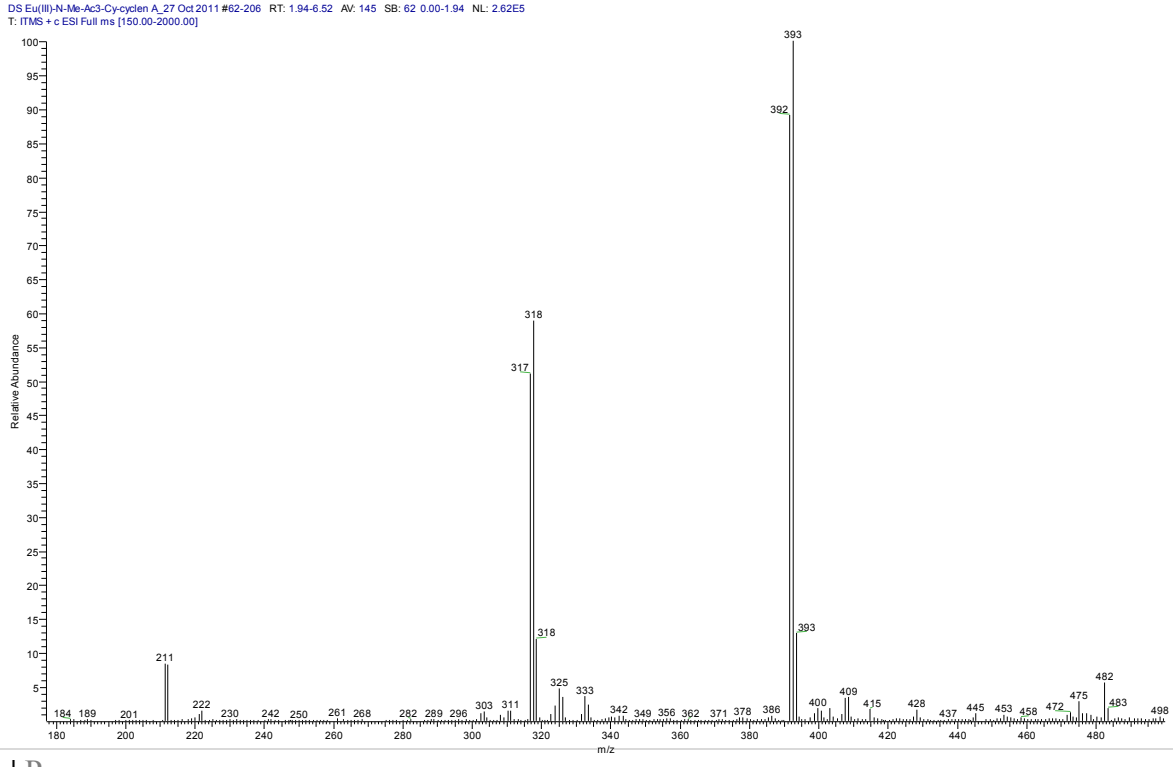
B4: 1,4,7,10-Tetrakis(methylcarbamylmethyl)-1,4,7,10-tetraazacyclodecane (4)



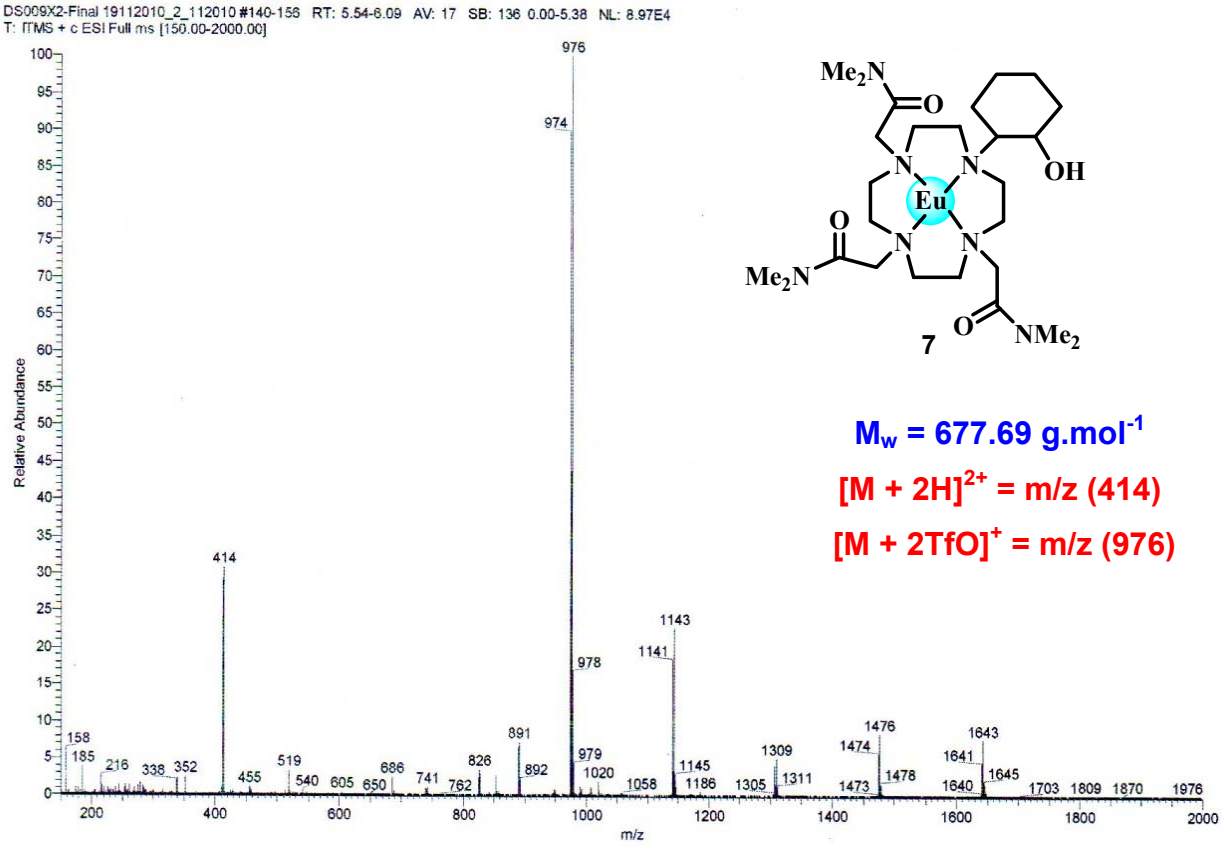


B5: Eu-1,4,7-tris[*N*-methylcarbamylmethyl]-10-(2-hydroxycyclohexyl)-1,4,7,10-tetraazacyclododecane (5)

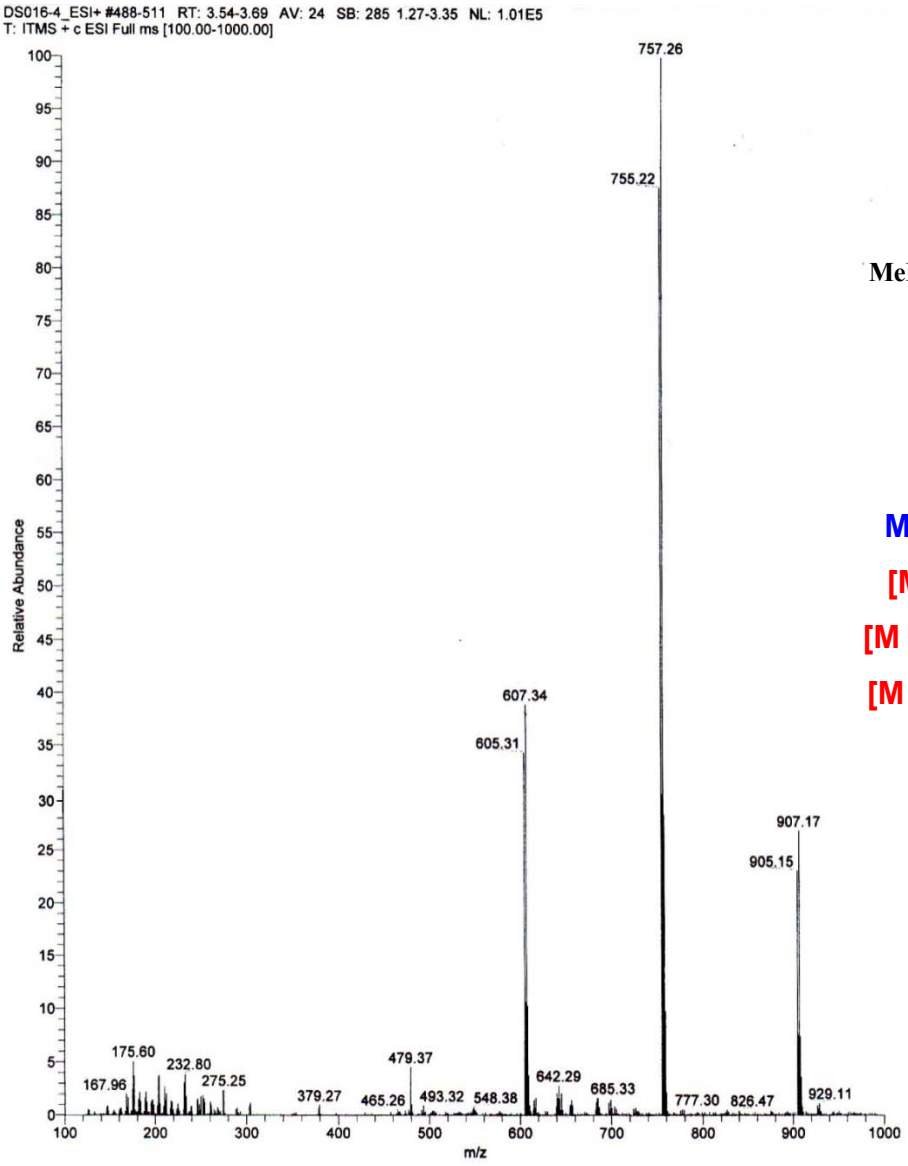


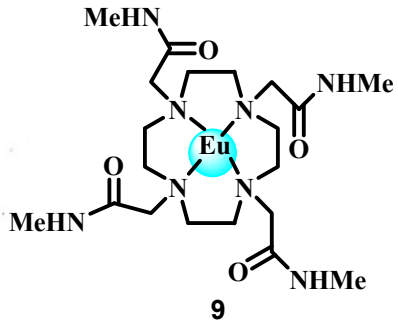


B6: Eu-1,4,7-tris[*N*,*N*-dimethylcarbamylmethyl]-10-(2-hydroxycyclohexyl)-1,4,7,10-tetraazacyclododecane (7)



B7: Eu-1,4,7,10-Tetrakis(methylcarbamylmethyl)-1,4,7,10-tetraazacyclodecane (9)





9

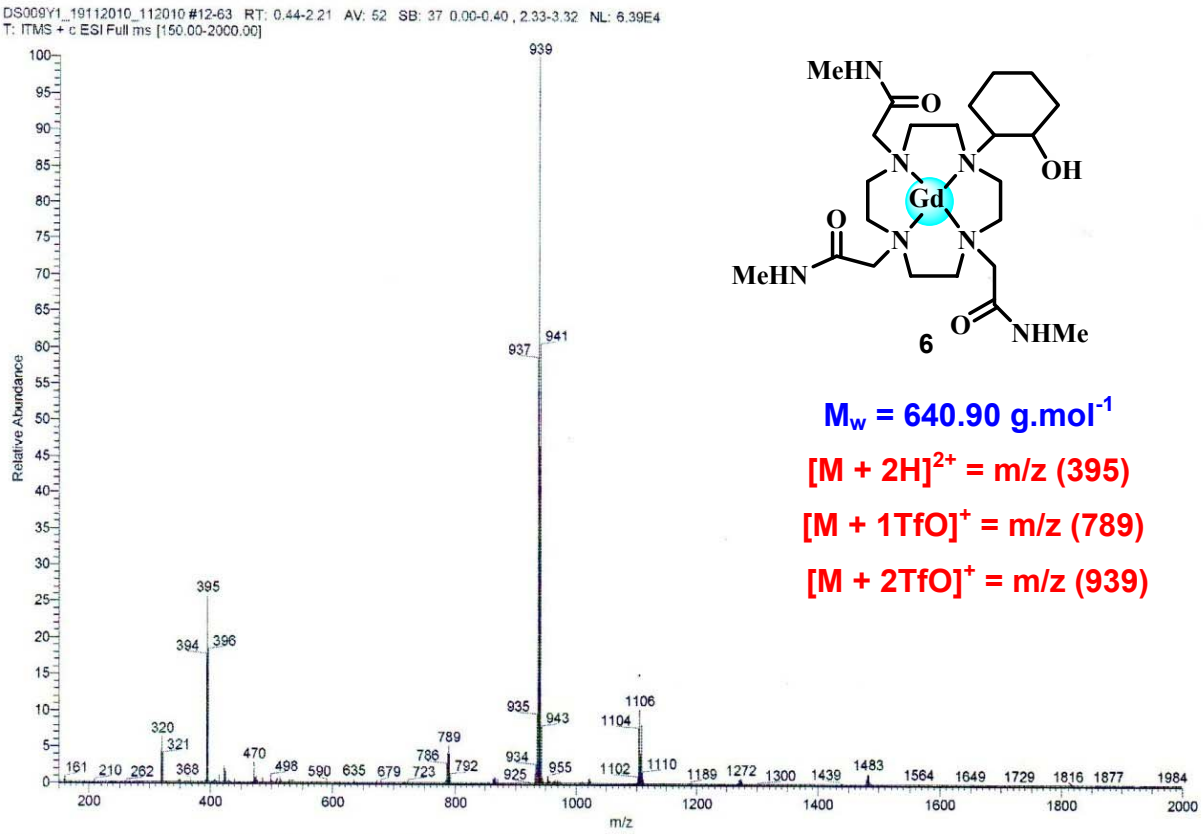
M_w = 608.55 g.mol^{-1}

$[M - H]^+$ = m/z (607)

$[M + 1TfO]^+$ = m/z (757)

$[M + 2TfO]^+$ = m/z (907)

B8: Gd-1,4,7-tris[*N*-methylcarbamylmethyl]-10-(2-hydroxycyclohexyl)-1,4,7,10-tetraazacyclododecane (6)



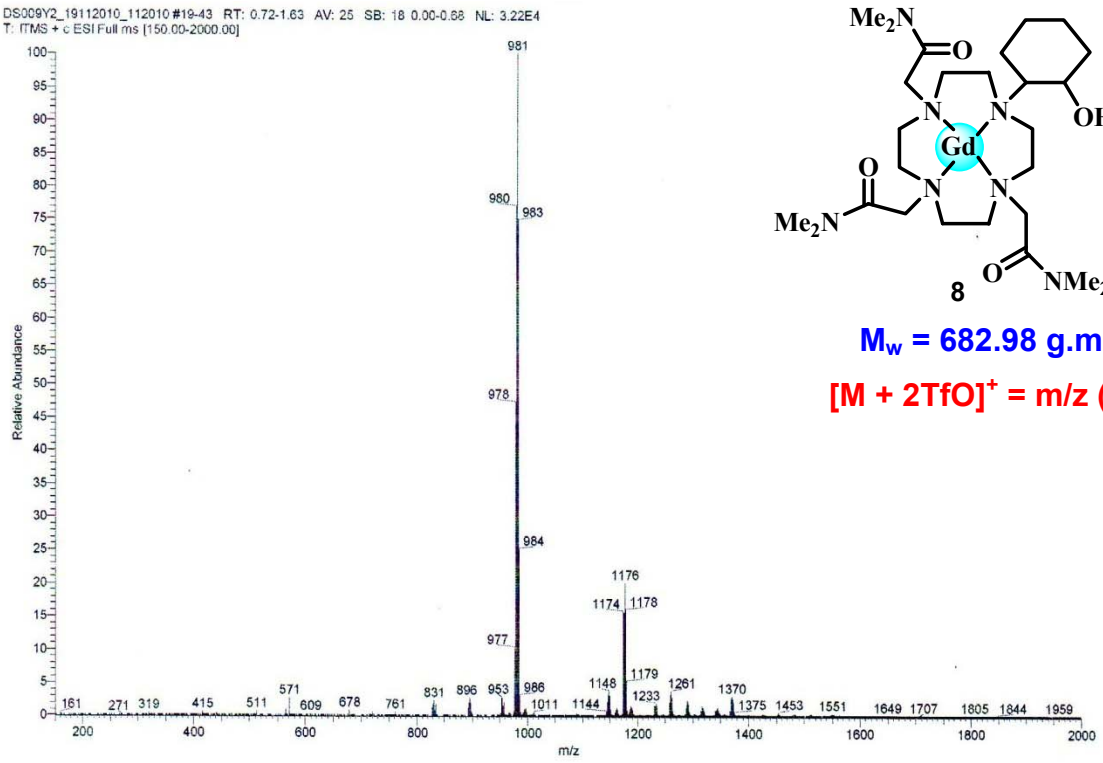
M_w = 640.90 g.mol^{-1}

$[M + 2H]^{2+}$ = m/z (395)

$[M + 1TfO]^{+}$ = m/z (789)

$[M + 2TfO]^{+}$ = m/z (939)

B9: Gd-1,4,7-tris[*N*,*N*-dimethylcarbamylmethyl]-10-(2-hydroxycyclohexyl)-1,4,7,10-tetraazacyclododecane (8)



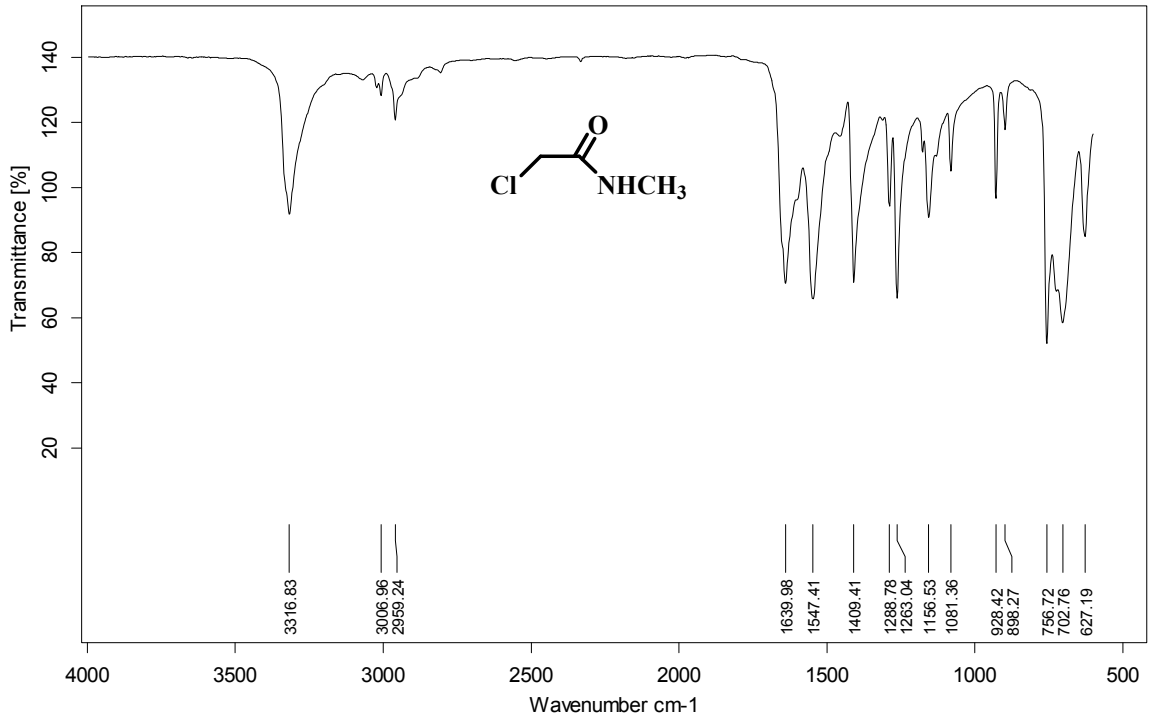
8

M_w = 682.98 g.mol^{-1}

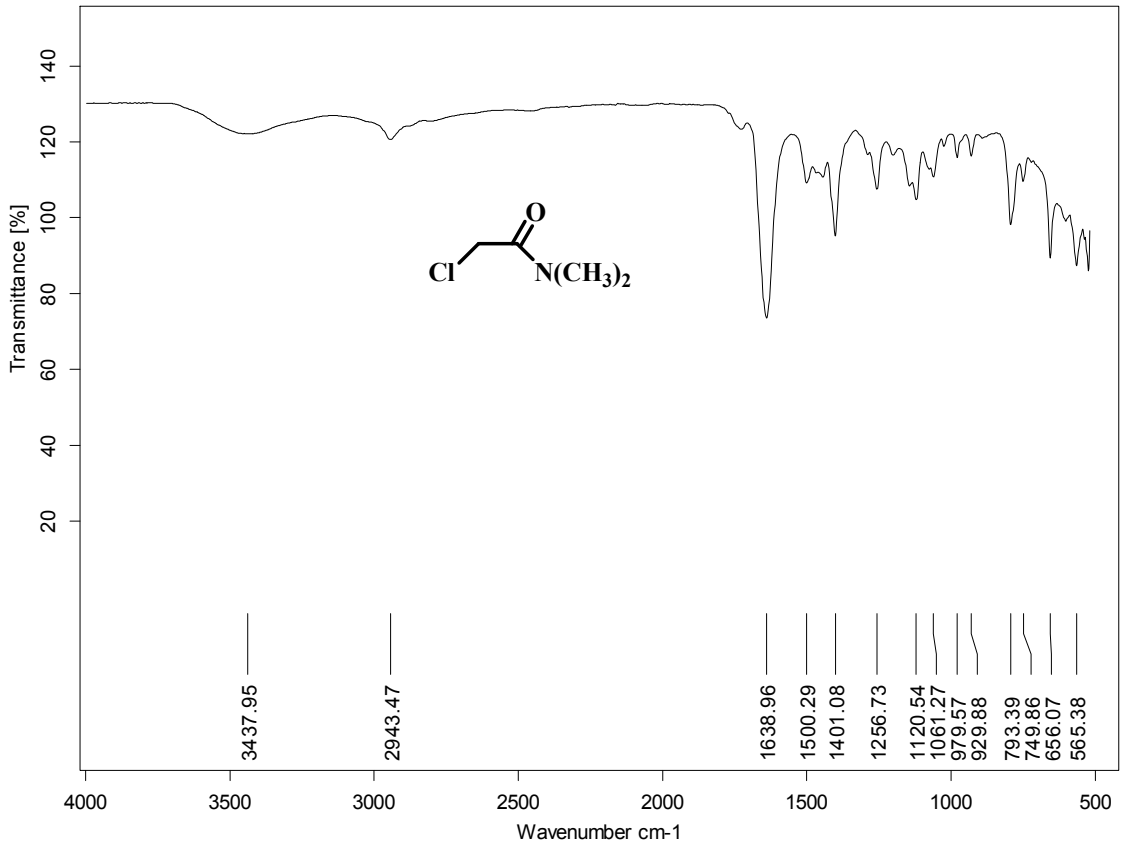
$[M + 2TfO]^+$ = m/z (982).

C- FTIR

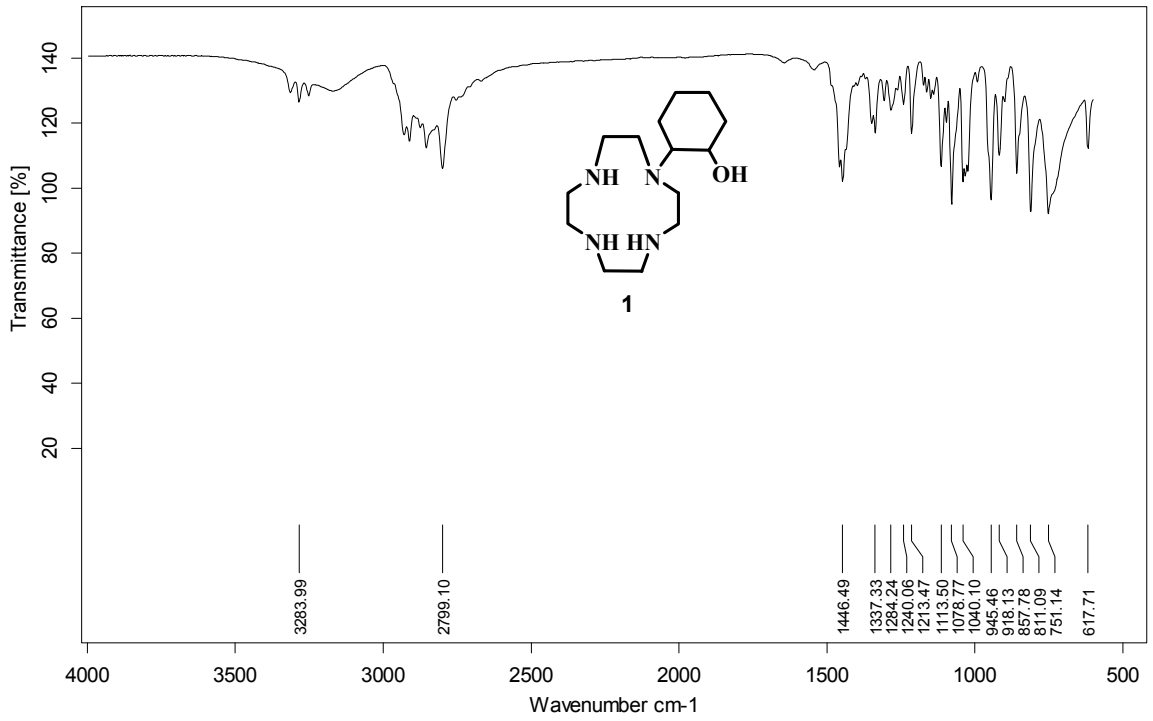
C1: *N*-Me-chloroacetamide



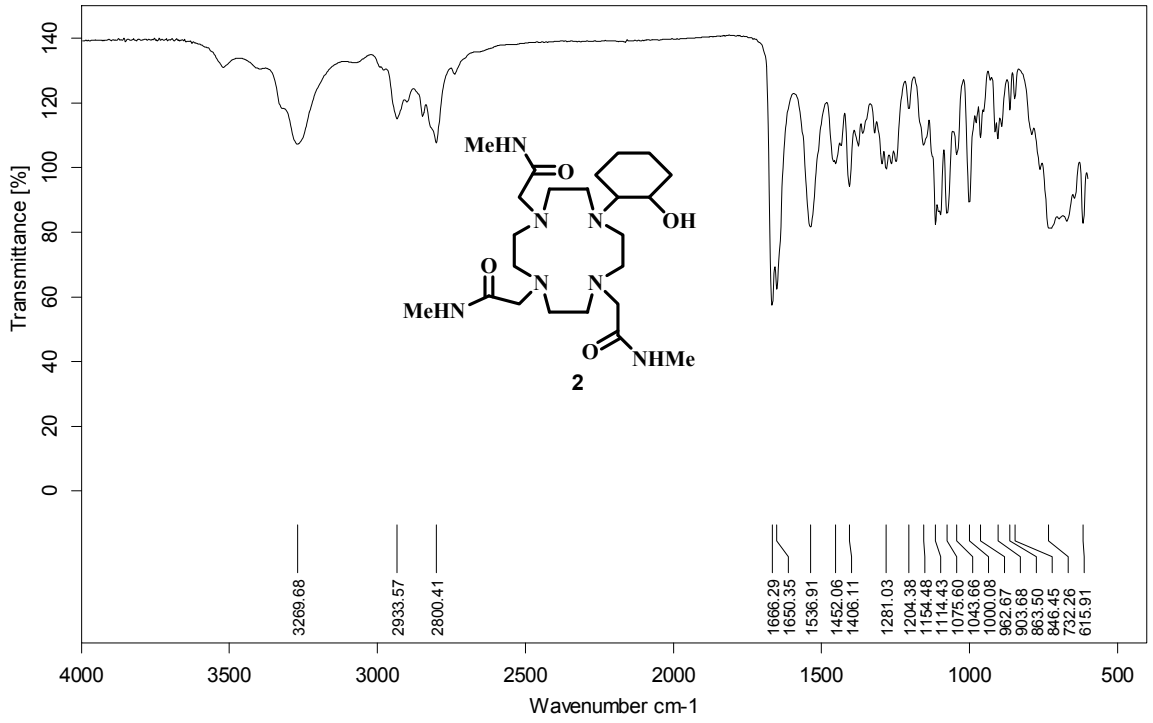
C2: *Di*-Me-chloroacetamide



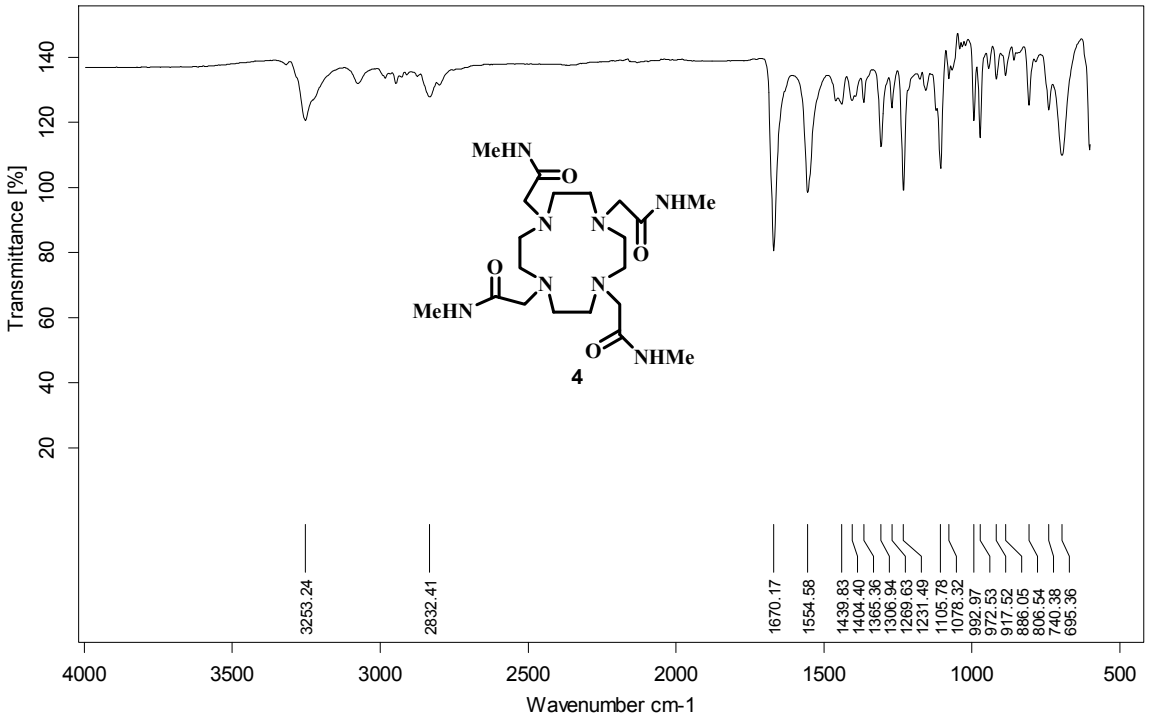
C3: 1-(2-Hydoxycyclohexyl)-1,4,7,10-tetraazacyclodecane (1)



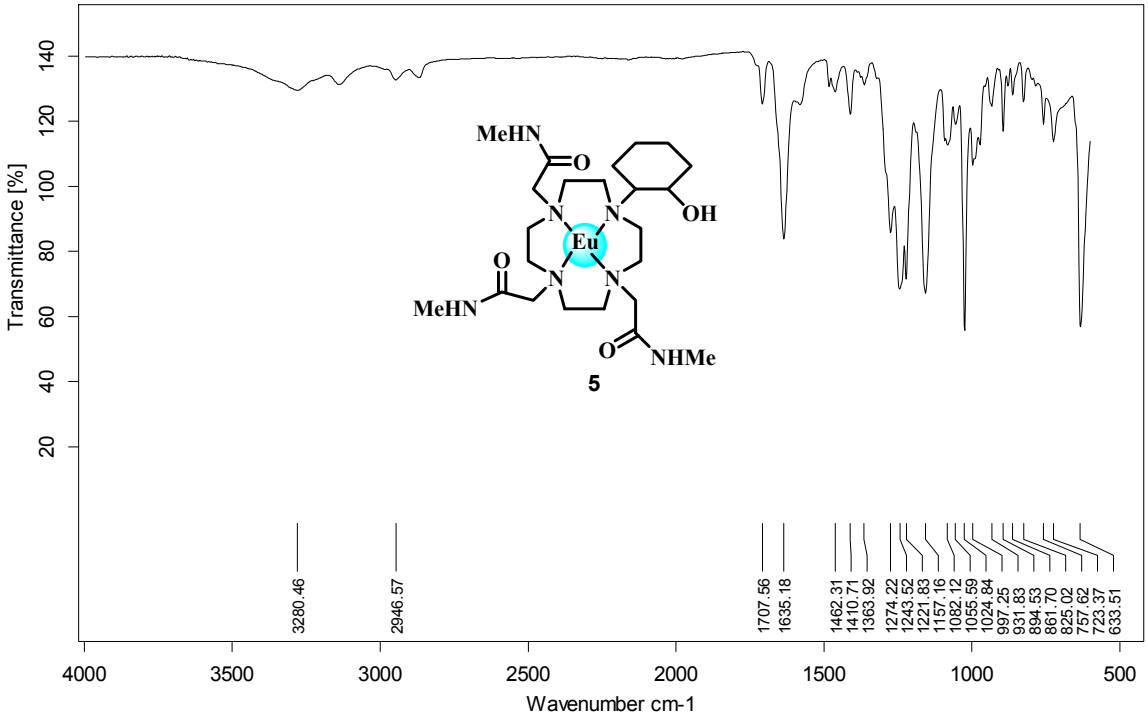
C4: 1,4,7-tris[*N*-methylcarbamylmethyl]-10-(2-hydroxycyclohexyl)-1,4,7,10-tetraazacyclododecane (2)



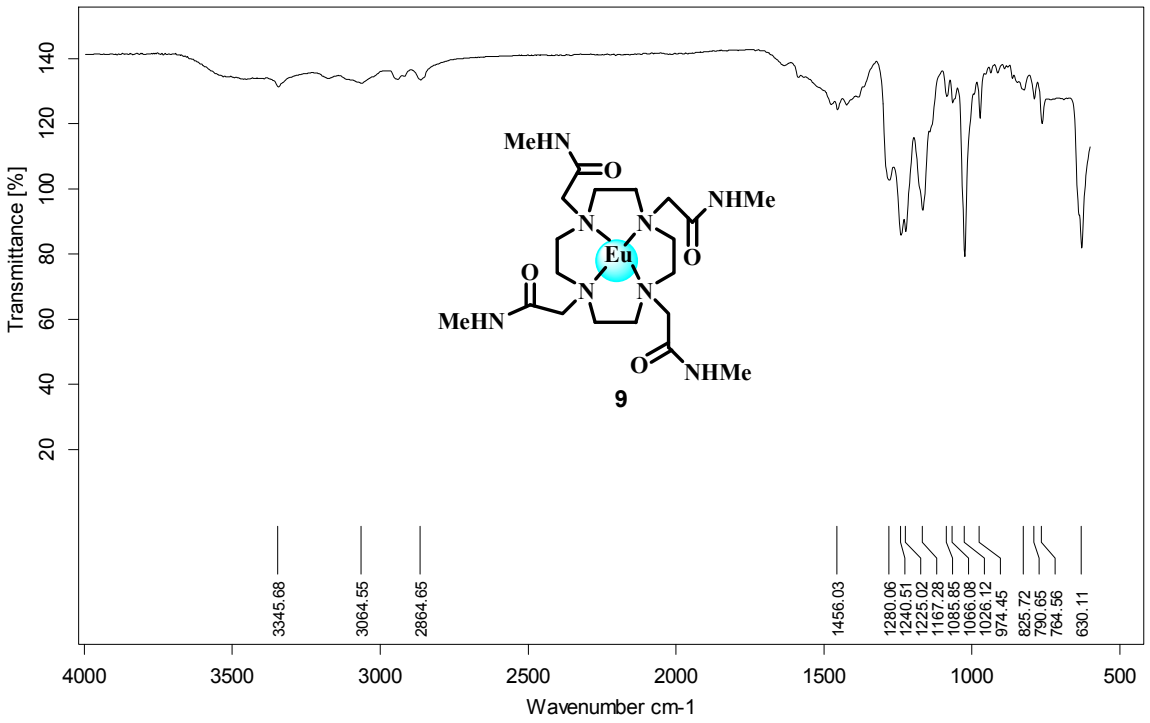
C5: 1,4,7,10-Tetrakis(methylcarbamylmethyl)-1,4,7,10-tetraazacyclodecane (4)



C6: Eu-1,4,7-tris[*N*-methylcarbamylmethyl]-10-(2-hydroxycyclohexyl)-1,4,7,10-tetraazacyclododecane (5)



C7: Eu-1,4,7,10-Tetrakis(methylcarbamylmethyl)-1,4,7,10-tetraazacyclodecane (9)



D: Some Important Calculations and Electrode Standardization

0.05 M KHP standard solution:

m_{KHP} required	=	CVM
	=	0.05 mol/L x 0.250 L x 204.2231 g/mol
	=	2.553 g
m_{KHP} measured	=	2.555 g
C_{KHP}	=	(2.555 g) ÷ (204.2231 g/mol x 0.250 L)
	=	0.050043 mol/L

0.1 M $NaNO_3$ standard solution:

m_{NaNO_3} required	=	CVM
	=	0.1 mol/L x 0.250 L x 84.9949 g/mol
	=	2.1249 g
m_{NaNO_3} measured	=	2.1249 g
C_{NaNO_3}	=	(2.1249 g) ÷ (84.9949 g/mol x 0.250 L)
	=	0.1000013 mol/L

0.05 M NaOH / 0.05 M $NaNO_3$ standard solution:

V_{NaOH} of 0.1 M HNO_3 used	=	0.500 L
m_{NaNO_3} required	=	CVM
	=	0.05 mol/L x 1.0 L x 84.9949 g/mol
	=	4.2497 g
m_{NaNO_3} measured	=	4.2498 g
C_{NaNO_3}	=	(4.2498 g) ÷ (84.9949 g/mol x 1.0 L)
	=	0.0500006 mol/L

Titration with 0.05 M KHP

V_{KHP} used = 5.00 mL

n_{KHP} = 0.050043 mol/L x 0.005 L

= $\underline{2.50215 \times 10^{-4} \text{ mol}}$

Table D1: Titration of 0.05 M KHP with 0.05 M NaOH / 0.05 M $NaNO_3$.

Titration	V_{ini} (mL)	V_{fin} (mL)	V_{Total} (mL)
1	0.08	5.12	5.04
2	0.00	5.06	5.06
3	0.10	5.28	5.18
4	0.00	5.14	5.14

Average volume used titrated = 5.105 mL

Since KHP reacts with NaOH in a 1:1 ratio,

C_{NaOH} = 2.50215×10^{-4} mol ÷ 0.005105 L

= $\underline{0.0490137 \text{ mol/L}}$

Thus, the actual concentration of 0.05 M NaOH / 0.05 M $NaNO_3$ solution is 0.049013 M NaOH / 0.0500006 M $NaNO_3$.

0.05 M HNO_3 / 0.05 M $NaNO_3$ standard solution:

V_{HNO_3} of 0.1 M HNO_3 used = 0.500 L

m_{NaNO_3} required = CVM

= 0.05 mol/L x 1.0 L x 84.9949 g/mol

= 4.2497 g

m_{NaNO_3} measured = 4.2502 g

C_{NaNO_3} = (4.2502 g) ÷ (84.9949 g/mol x 1.0 L)

= $\underline{0.050005 \text{ mol/L}}$

Titration with 0.049013 M NaOH / 0.0500006 M $NaNO_3$

V_{HNO3} used = 5.00 mL

n_{NaOH} = 0.050005 mol/L x 0.005 L

= $\underline{2.50026 \times 10^{-4} \text{ mol}}$

Table D2: Titration of 0.05 M HNO_3 / 0.05 M $NaNO_3$ with 0.05 M NaOH / 0.05 M $NaNO_3$.

Titration	V_{ini} (mL)	V_{fin} (mL)	V_{Total} (mL)
1	0.12	5.14	5.02
2	0.00	5.06	5.06
3	0.00	5.02	5.02
4	0.04	5.08	5.04

Average volume used = 5.035 mL

Since HNO_3 reacts with NaOH in a 1:1 ratio,

C_{HNO3} = 2.50026×10^{-4} mol ÷ 0.005035 L

= $\underline{0.0496576 \text{ mol/L}}$

Thus, the actual concentration of 0.05 M HNO_3 / 0.05 M $NaNO_3$ solution is 0.0496576 M HNO_3 /0.050005 M $NaNO_3$.

Standardization of Electrodes

The titration data obtained for two different electrodes is tabulated below.

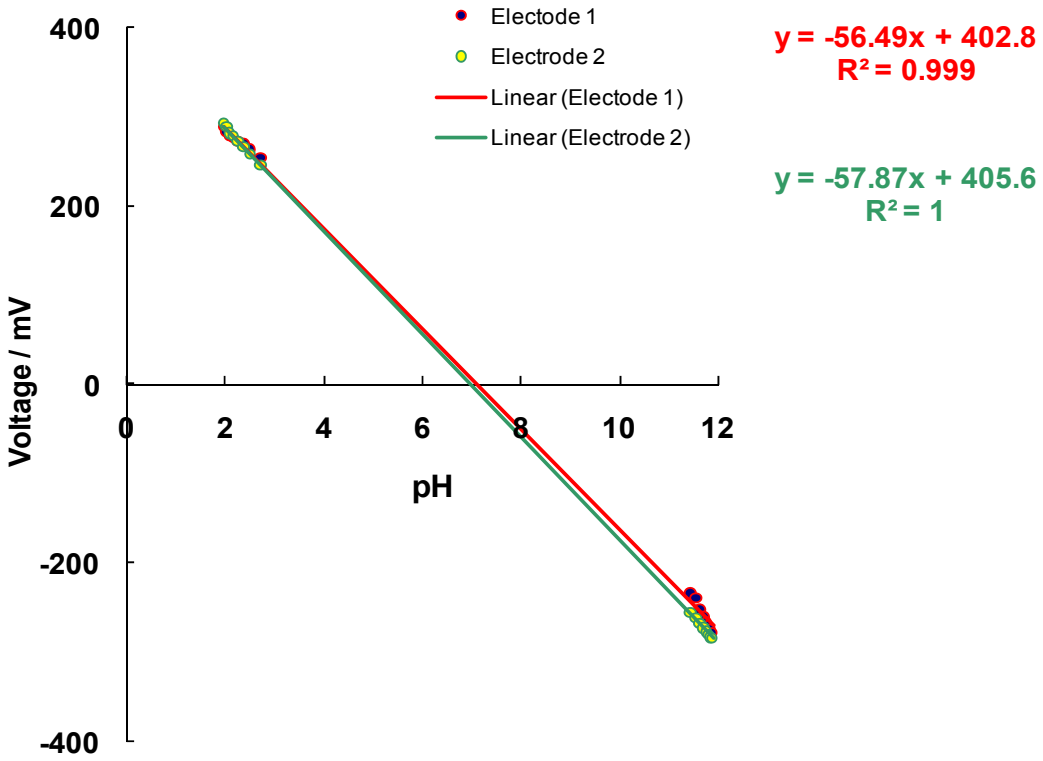
Table D3: Electrode standardization raw data.

V_{NaOH} added (mL)	E (mV) Electrode 1	E (mV) Electrode 2
0.00	297.3	296.2
0.50	289.1	293.3
1.00	283.5	288.5
1.50	278.1	281.9
2.00	276.3	278
2.50	272.3	272
3.00	269.1	265.8
3.50	263	257.7
4.00	254.4	245.6
4.50	239.8	227.3
5.00	213.8	217.8
5.50	-83.7	-222.9
6.00	-162.2	-241.7
6.50	-234.2	-255.8
7.00	-239.7	-262.2
7.50	-252.4	-268.2
8.00	-260.5	-273
8.50	-266.8	-276.9
9.00	-270.5	-279.5
9.50	-274.4	-282.7
10.00	-277.6	-284.5

The electrode standardization was performed on a solution consisting of 5 mL of the 0.0496576 M HNO_3 / 0.050005 M $NaNO_3$ standard solution and 15 mL of the 0.1 M $NaNO_3$ standard solution. This 20 mL solution was titrated with 10 mL of the 0.049013 M NaOH / 0.0500006 M $NaNO_3$ standard solution, which was dispensed in 0.5 mL increments. Voltage readings were measured upon each increment addition via the glass electrode over a 3 minute period, with a 0.1 mV drift constraint allowed for each reading.

$$E_o = pH(slope) + E$$

The value for E_o determined for the particular cell plus glass electrode plus reference electrode used in this study ranged from 402.8 to 405.6 mV, accompanied by a small deviation of the Nernstian slope from the accepted 59.16 mV. Determined values of the Nernstian slope obtained here ranged from 56.49 to 57.87 mV/decade. It is normal for the E_o and Nernstian slope to change for a given glass electrode, which is thought to be caused by changes in the surface structure of the glass with time. This deviation in the Nernstian slope, as well as changes in E^o for the cell, are the reasons that daily determinations of these cell constants were necessary. Nernstian slopes in the range 56-61 mV are considered acceptable.



Shows linear least square fits of electrodes tested.

Note: Electrode 2 was only used in experiments as it showed comparably better fit to the Nernstian Equation than Electrode

E: Spectroscopic Data

Luminescence Data

Table E1: Complex **5** in MCB with KHP

pH	580 nm	593 nm	616 nm	653 nm	686 nm	700 nm
1.98	28.01032	127.3811	104.3255	8.885786	47.70411	84.57339
2.197	28.25131	126.5988	106.4739	8.863433	48.96783	84.38441
2.469	28.19157	127.5536	104.306	9.604146	48.14294	84.36037
2.503	28.83414	132.5533	108.333	9.040313	49.83659	88.45561
2.651	26.2006	132.8248	105.8429	9.328521	47.20216	84.62986
2.796	27.25687	141.8221	112.3092	8.903292	48.43601	91.58847
2.93	33.71307	177.5957	147.1038	11.54678	58.86669	109.2576
3.47	37.21442	198.2178	182.3395	12.26604	65.96891	122.9627
3.885	40.20565	207.7741	207.1436	12.36586	67.12573	126.339
3.95	43.82184	230.1279	251.4288	14.3421	74.88898	140.2473
4.32	47.81548	242.0879	289.2793	15.67754	77.13499	146.6583
4.47	54.7904	282.0136	363.1475	18.16419	95.54459	169.0585
4.71	52.59426	267.2501	361.5172	16.66641	90.25335	163.8173
4.9	66.87595	337.2163	478.7227	21.96202	112.3049	205.471
4.959	67.34241	335.9375	474.9282	21.17924	113.4241	201.5364
5.32	77.36083	391.5547	563.3078	25.14756	131.2099	235.3411
6.101	88.94524	421.7938	618.9667	27.6757	152.0579	263.3185
6.642	89.86274	432.255	636.149	29.19111	152.957	267.0365
6.978	93.78536	442.3407	661.9435	30.3271	158.3971	268.1409
7.171	93.34807	430.2551	615.4591	27.76355	153.5212	263.5741
7.224	94.18813	406.1693	597.4482	28.48067	150.644	262.0091
7.423	92.64413	376.8264	543.4401	27.43141	145.4159	250.0646
8.204	85.42323	287.451	363.8146	23.33539	120.7403	200.3198
8.172	82.62257	271.0667	346.9864	21.90217	115.9694	190.1282
8.381	85.48022	249.6682	310.1425	20.86946	109.225	179.2365
8.47	85.85754	230.5284	298.3781	18.96434	101.5758	169.7413
8.675	86.46285	210.3616	282.8134	19.2936	97.28004	159.3553
8.71	87.02991	164.2497	229.9756	15.39571	79.85363	131.5029
9.382	76.53088	98.19234	147.0627	10.55114	54.58936	87.30116
9.484	81.04065	114.598	170.1228	11.71361	63.02435	99.92001
9.495	75.96996	72.68029	113.7259	8.725314	44.79044	70.72247
9.705	71.84787	73.87054	115.4299	9.125332	46.0648	71.13033
9.889	66.14352	49.75606	86.32747	6.57108	35.5578	53.63659
10.048	63.36357	44.59178	78.5749	6.528862	34.90343	51.61696
10.395	65.049	43.48596	74.03234	6.494727	33.18026	50.02839
10.501	62.77079	38.31433	71.92744	6.088898	31.80132	46.11047
10.91	58.58298	33.42497	62.33338	4.979872	27.73181	40.74892
11.505	58.75228	31.75255	60.6249	5.783909	26.95882	41.18166
12.555	55.31254	33.87047	70.04906	5.677895	25.58411	40.99745

p*K*a Fit Data

Nonlinear Regression **Friday, March 09, 2012, 09:17:25 AM**

Data Source: Data 2 in Eu(III) complex 5 in MCB with KHP 580 nm 2 pKa.JNB
Equation: User-Defined, pK2
H = 10^(-x);
K1 = 10^(-pK1)
K2 = 10^(-pK2)
Den = H^2 + K1*H + K1*K2
f = (H^2*A0 + K1*H*A1 + K1*K2*A2)/Den

R	Rsqr	Adj Rsqr	Standard Error of Estimate
0.99118461	0.98244693	0.98038187	3.17258473

	Coefficient	Std. Error	t	P
A0	29.54823631	1.11777524	26.43486396	<0.00000001
A1	90.37347801	1.04172690	86.75352221	<0.00000001
A2	57.60366058	1.68079443	34.27168694	<0.00000001
pK1	4.71216762	0.04959484	95.01326067	<0.00000001
pK2	9.58354068	0.10150577	94.41375533	<0.00000001

Analysis of Variance:

Analysis of Variance:

	DF	SS	MS
Regression	5	178066.29573585	35613.25914717
Residual	34	342.21999153	10.06529387
Total	39	178408.51572738	4574.57732634

Corrected for the mean of the observations:

	DF	SS	MS	F	P
Regression	4	19154.08634221	4788.52158555	475.74582999	<0.00000001
Residual	34	342.21999153	10.06529387		
Total	38	19496.30633373	513.06069299		

Statistical Tests:

Normality Test (Kolmogorov-Smirnov) Passed (P = 0.89587277)

K-S Statistic = 0.09004608 Significance Level = 0.05000000

Constant Variance Test Passed (P = 0.93681075)

Fit Equation Description:
[Variables]
x = col(1) ' {{prevmin: 0.000000}} {{prevmax: 0.160000}} {{intervals: 100}}
y = col(2)
[Parameters]
A0 = col(2,1) ' {{previous: 29.5482}} {{MinRange: 0}} {{MaxRange: 2}}
A1 = col(2,18) ' {{previous: 90.3735}} {{MinRange: 0}} {{MaxRange: 2}}
A2 = col(2,39) ' {{previous: 57.6037}}
pK1 = 4.5 ' {{previous: 4.71217}}
pK2 = 9 ' {{previous: 9.58354}}
[Equation]
H = 10^(-x);
K1 = 10^(-pK1)
K2 = 10^(-pK2)
Den = H^2 + K1*H + K1*K2
f = (H^2*A0 + K1*H*A1 + K1*K2*A2)/Den
fit f to y
[Constraints]
[Options]
tolerance=1e-018
stepsize=1
iterations=20000

Number of Iterations Performed = 10

Nonlinear Regression Friday, March 09, 2012, 09:53:05 AM

Data Source: Data 1 in Eu(III) complex 5 in MCB with KHP 592 nm 2 pKa.JNB
Equation: User-Defined, pK2
H = 10^(-x);
K1 = 10^(-pK1)
K2 = 10^(-pK2)
Den = H^2 + K1*H + K1*K2
f = (H^2*A0 + K1*H*A1 + K1*K2*A2)/Den

R	Rsqr	Adj Rsqr	Standard Error of Estimate
0.99084592	0.98177563	0.97963159	18.70274773

	Coefficient	Std. Error	t	P
A0	143.22162	7496.78055026	21.12241955	<0.00000001
A1	433.16147	4908.58164966	50.47531559	<0.00000001
A2	42.68138	1476.35195333	6.71941043	0.00000010

pK1 4.586283480.06625694 69.21966596 <0.00000001
pK2 8.438403370.04770984176.86925007 <0.00000001

Analysis of Variance:

Analysis of Variance:

	DF	SS	MS	
Regression	5	2288293.59826116	457658.71965223	
Residual	34	11892.95426487	349.79277250	
Total	39	2300186.5525260	258979.14237246	

Corrected for the mean of the observations:

	DF	SS	MS	F	P
Regression	4	640692.23799796	160173.05949949	457.90843063	<0.00000001
Residual	34	11892.95426487	349.79277250		
Total	38	652585.1922628	317173.29453323		

Statistical Tests:

Normality Test (Kolmogorov-Smirnov) Passed (P = 0.17363925)

K-S Statistic = 0.17316973 Significance Level = 0.05000000

Constant Variance Test Passed (P = 0.92410903)

Fit Equation Description:

```
[Variables]
x = col(1) ' {{prevmin: 0.000000}} {{prevmax: 0.160000}} {{intervals: 100}}
y = col(2)
[Parameters]
A0 = col(2,1) ' {{previous: 143.222}} {{MinRange: 0}} {{MaxRange: 2}}
A1 = col(2,18) ' {{previous: 433.161}} {{MinRange: 0}} {{MaxRange: 2}}
A2 = col(2,39) ' {{previous: 42.6814}}
pK1 = 4.5 ' {{previous: 4.58628}}
pK2 = 9 ' {{previous: 8.4384}}
[Equation]
H = 10^(-x);
K1 = 10^(-pK1)
K2 = 10^(-pK2)
Den = H^2 + K1*H + K1*K2
f = (H^2*A0 + K1*H*A1 + K1*K2*A2)/Den
fit f to y
[Constraints]
[Options]
tolerance=1e-018
stepsize=1
iterations=20000
```

Number of Iterations Performed = 14

Nonlinear Regression **Friday, March 09, 2012, 10:00:44 AM**

Data Source: Data 1 in Eu(III) complex 5 in MCB with KHP 616 nm 2 pKa.JNB
Equation: User-Defined, pK2
H = 10^(-x);
K1 = 10^(-pK1)
K2 = 10^(-pK2)
Den = H^2 + K1*H + K1*K2
f = (H^2*A0 + K1*H*A1 + K1*K2*A2)/Den

R	Rsqr	Adj Rsqr	Standard Error of Estimate
0.99283200	0.98571538	0.98403483	24.71385710

	Coefficient	Std. Error	t	P
A0	115.12593854	8.92294059	12.90224197	<0.00000001
A1	649.17329870	12.14950643	53.43207169	<0.00000001
A2	82.71794362	8.06825219	10.25227542	<0.00000001
pK1	4.60744570	0.04831307	95.36643592	<0.00000001
pK2	8.23854294	0.04504467	182.89718988	<0.00000001

Analysis of Variance:

Analysis of Variance:

	DF	SS	MS
Regression	5	4268661.17792443	853732.23558489
Residual	34	20766.34090667	610.77473255
Total	39	4289427.51883110	109985.32099567

Corrected for the mean of the observations:

	DF	SS	MS	F	P
Regression	4	1432988.46056933	358247.11514233	586.54540873	<0.00000001
Residual	34	20766.34090667	610.77473255		
Total	38	1453754.80147600	38256.70530200		

Statistical Tests:

Normality Test (Kolmogorov-Smirnov) Passed (P = 0.21347919)

K-S Statistic = 0.16566708 Significance Level = 0.05000000

Constant Variance Test Passed (P = 0.35992142)

Fit Equation Description:
[Variables]
x = col(1) ' {{prevmin: 0.000000}} {{prevmax: 0.160000}} {{intervals: 100}}
y = col(2)
[Parameters]
A0 = col(2,1) ' {{previous: 115.126}} {{MinRange: 0}} {{MaxRange: 2}}
A1 = col(2,18) ' {{previous: 649.173}} {{MinRange: 0}} {{MaxRange: 2}}
A2 = col(2,39) ' {{previous: 82.7179}}
pK1 = 4.5 ' {{previous: 4.60745}}
pK2 = 9 ' {{previous: 8.23854}}
[Equation]
H = 10^(-x);
K1 = 10^(-pK1)
K2 = 10^(-pK2)
Den = H^2 + K1*H + K1*K2
f = (H^2*A0 + K1*H*A1 + K1*K2*A2)/Den
fit f to y
[Constraints]
[Options]
tolerance=1e-018
stepsize=1
iterations=20000

Number of Iterations Performed = 12
Nonlinear Regression **Friday, March 09, 2012, 10:10:34 AM**

Data Source: Data 1 in Eu(III) complex in MCB with KHP 653 nm 2 pKa.JNB
Equation: User-Defined, pK2
H = 10^(-x);
K1 = 10^(-pK1)
K2 = 10^(-pK2)
Den = H^2 + K1*H + K1*K2
f = (H^2*A0 + K1*H*A1 + K1*K2*A2)/Den

R	Rsqr	Adj Rsqr	Standard Error of Estimate
0.98999515	0.98009039	0.97774809	1.18261577

	Coefficient	Std. Error	t	P
A0	9.71570043	0.41718093	23.28893694	<0.00000001
A1	29.00206816	0.52358828	55.39098045	<0.00000001
A2	6.04769441	0.42764396	14.14189144	<0.00000001
pK1	4.71305968	0.06171309	76.37050454	<0.00000001
pK2	8.66282965	0.05348310	161.97321247	<0.00000001

Analysis of Variance:

	DF	SS	MS
Regression	5	11473.82961807	2294.76592361
Residual	34	47.55172241	1.39858007
Total	39	11521.38134048	295.42003437

Corrected for the mean of the observations:

	DF	SS	MS	F	P
Regression	4	2340.82921707	585.20730427	418.42960336	<0.00000001
Residual	34	47.55172241	1.39858007		
Total	38	2388.38093947	62.85212999		

Statistical Tests:

Normality Test (Kolmogorov-Smirnov) Passed (P = 0.38087336)

K-S Statistic = 0.14236628 Significance Level = 0.05000000

Constant Variance Test Passed (P = 0.68250855)

Fit Equation Description:

```
[Variables]
x = col(1) ' {{prevmin: 0.000000}} {{prevmax: 0.160000}} {{intervals: 100}}
y = col(2)
[Parameters]
A0 = col(2,1) ' {{previous: 9.7157}} {{MinRange: 0}} {{MaxRange: 2}}
A1 = col(2,18) ' {{previous: 29.0021}} {{MinRange: 0}} {{MaxRange: 2}}
A2 = col(2,39) ' {{previous: 6.04769}}
pK1 = 4.5 ' {{previous: 4.71306}}
pK2 = 9 ' {{previous: 8.66283}}
[Equation]
H = 10^(-x);
K1 = 10^(-pK1)
K2 = 10^(-pK2)
Den = H^2 + K1*H + K1*K2
f = (H^2*A0 + K1*H*A1 + K1*K2*A2)/Den
fit f to y
[Constraints]
[Options]
tolerance=1e-018
stepsize=1
iterations=20000
```

Number of Iterations Performed = 12

Nonlinear Regression **Friday, March 09, 2012, 10:17:02 AM**

Data Source: Data 1 in Eu(III) complex 5 in MCB with KHP 685 nm 2 pKa.JNB
Equation: User-Defined, pK2
H = 10^(-x);
K1 = 10^(-pK1)
K2 = 10^(-pK2)
Den = H^2 + K1*H + K1*K2
f = (H^2*A0 + K1*H*A1 + K1*K2*A2)/Den

R	Rsqr	Adj Rsqr	Standard Error of Estimate
0.99164441	0.98335864	0.98140083	5.77890585

	Coefficient	Std. Error	t	P
A0	51.58945506	2.02181241	25.51643996	<0.00000001
A1	155.29084140	2.59874710	59.75604214	<0.00000001
A2	31.24758988	2.06662051	15.12013926	<0.00000001
pK1	4.75422864	0.05624307	84.53003178	<0.00000001
pK2	8.62860429	0.04803191	179.64315537	<0.00000001

Analysis of Variance:

Analysis of Variance:

	DF	SS	MS
Regression	5	319718.24441725	63943.64888345
Residual	34	1135.45559748	33.39575287
Total	39	320853.70001472	8227.01794910

Corrected for the mean of the observations:

	DF	SS	MS	F	P
Regression	4	67095.48099560	16773.87024890	502.27555329	<0.00000001
Residual	34	1135.45559748	33.39575287		
Total	38	68230.93659308	1795.55096298		

Statistical Tests:

Normality Test (Kolmogorov-Smirnov) Passed (P = 0.21798242)

K-S Statistic = 0.16488904 Significance Level = 0.05000000

Constant Variance Test Passed (P = 0.41167554)

Fit Equation Description:

[Variables]
x = col(1) ' {{prevmin: 0.000000}} {{prevmax: 0.160000}} {{intervals: 100}}
y = col(2)
[Parameters]
A0 = col(2,1) ' {{previous: 51.5895}} {{MinRange: 0}} {{MaxRange: 2}}
A1 = col(2,18) ' {{previous: 155.291}} {{MinRange: 0}} {{MaxRange: 2}}
A2 = col(2,39) ' {{previous: 31.2476}}
pK1 = 4.5 ' {{previous: 4.75423}}
pK2 = 9 ' {{previous: 8.6286}}
[Equation]
H = 10^(-x);
K1 = 10^(-pK1)
K2 = 10^(-pK2)
Den = H^2 + K1*H + K1*K2
f = (H^2*A0 + K1*H*A1 + K1*K2*A2)/Den
fit f to y
[Constraints]
[Options]
tolerance=1e-018
stepsize=1
iterations=20000

Number of Iterations Performed = 13

Nonlinear Regression **Friday, March 09, 2012, 10:21:16 AM**

Data Source: Data 1 in Eu(III) complex 5 in MCB with KHP 700 nm 2 pKa.JNB
Equation: User-Defined, pK2
H = 10^(-x);
K1 = 10^(-pK1)
K2 = 10^(-pK2)
Den = H^2 + K1*H + K1*K2
f = (H^2*A0 + K1*H*A1 + K1*K2*A2)/Den

R	Rsqr	Adj Rsqr	Standard Error of Estimate
0.99111280	0.98230457	0.98022276	10.50033038

	Coefficient	Std. Error	t	P
A0	92.99699818	3.74204722	24.85190396	<0.00000001
A1	267.73768275	4.70772983	56.87193031	<0.00000001
A2	47.69639321	3.70120509	12.88671987	<0.00000001
pK1	4.66455712	0.06083012	76.68170148	<0.00000001
pK2	8.58190209	0.04845446	177.11274706	<0.00000001

Analysis of Variance:

Analysis of Variance:

	DF	SS	MS
Regression	5	954823.27214550	190964.65442910
Residual	34	3748.73589620	110.25693812
Total	39	958572.00804170	24578.76943697

Corrected for the mean of the observations:

	DF	SS	MS	F	P
Regression	4	208098.98697489	52024.74674372	471.85009514	<0.00000001
Residual	34	3748.73589620	110.25693812		
Total	38	211847.72287109	5574.94007556		

Statistical Tests:

Normality Test (Kolmogorov-Smirnov) Passed (P = 0.38013180)

K-S Statistic = 0.14245209 Significance Level = 0.05000000

Constant Variance Test Passed (P = 0.25298603)

Fit Equation Description:

```
[Variables]
x = col(1) ' {{prevmin: 0.000000}} {{prevmax: 0.160000}} {{intervals: 100}}
y = col(2)
[Parameters]
A0 = col(2,1) ' {{previous: 92.997}} {{MinRange: 0}} {{MaxRange: 2}}
A1 = col(2,18) ' {{previous: 267.738}} {{MinRange: 0}} {{MaxRange: 2}}
A2 = col(2,39) ' {{previous: 47.6964}}
pK1 = 4.5 ' {{previous: 4.66456}}
pK2 = 9 ' {{previous: 8.5819}}
[Equation]
H = 10^(-x);
K1 = 10^(-pK1)
K2 = 10^(-pK2)
Den = H^2 + K1*H + K1*K2
f = (H^2*A0 + K1*H*A1 + K1*K2*A2)/Den
fit f to y
[Constraints]
[Options]
tolerance=1e-018
stepsize=1
iterations=20000
```

Number of Iterations Performed = 13

Table E2: Complex **9** in MCB with KHP

pH	580 nm	593 nm	616 nm	689 nm	701 nm
1.961	0.204783	0.631532	0.340893	0.349372	0.741085
2.023	0.295675	0.768908	0.474859	0.376314	0.583287
2.268	0.241227	0.856929	0.573369	0.261365	0.479148
2.49	0.133618	0.803263	0.500406	0.200911	0.475694
2.79	0.231633	1.062729	0.56261	0.249887	0.579279
3.141	0.144799	1.030295	0.680548	0.315253	0.708654
3.372	0.142896	0.94125	0.517955	0.287906	0.706798
3.81	0.336072	1.450299	0.957379	0.359747	0.725373
4.016	0.30553	1.593919	1.322851	0.466916	0.926587
4.4	0.340503	2.023919	1.753657	0.599736	0.88706
4.527	0.404996	1.946747	2.074503	0.520649	1.024189
4.881	0.298564	2.368854	2.743002	0.647384	1.088336
5.1	0.345302	2.730675	3.417781	0.600792	1.311448
5.297	0.495988	3.041573	3.859563	0.839496	1.516452
5.6752	0.611688	3.413275	5.032158	0.876234	1.680039
6.056	0.60071	3.398914	5.16177	0.909239	1.646256
6.258	0.573846	3.647827	5.671446	0.926245	1.819632
6.441	0.546256	3.500638	5.139294	0.93182	1.626458
6.718	0.636532	3.407398	4.982592	1.00575	1.480337
6.95	0.544174	3.260687	4.699016	0.882541	1.500034
7.235	0.589984	2.684019	3.895092	0.872145	1.326272
7.332	0.62496	2.133726	2.927234	0.730765	1.206475
7.706	0.478192	0.955471	1.083364	0.464467	0.847198
7.834	0.320701	0.902709	0.967943	0.484704	0.926159
8.176	0.457485	0.795722	0.769802	0.491164	0.815666
8.38	0.241813	0.942017	0.752844	0.323091	0.787998
8.055	0.341572	0.890042	0.800654	0.403228	0.843556
8.612	0.39422	0.778287	0.756912	0.395388	0.859946
8.8	0.421617	0.870871	0.678344	0.427854	0.821415
8.855	0.304403	0.894666	0.682092	0.412508	0.938606
9.065	0.261968	0.869852	0.866752	0.4788	0.761776
9.221	0.296462	0.862196	0.63652	0.520069	0.836281
9.467	0.378276	0.911486	0.702472	0.397924	0.727511
9.287	0.271439	0.891613	0.729263	0.269471	0.814573
9.687	0.23371	0.83443	0.640605	0.441187	0.817757
9.458	0.287311	1.067662	0.802589	0.392357	0.772455
9.722	0.294482	0.885272	0.763219	0.439985	0.886162
9.785	0.199106	0.819162	0.515089	0.398684	0.846531
11.758	0.277984	0.72905	0.826579	0.242345	0.675763

Eu(III)complex 9 in MCB with KHP
Results for nonlinear 2 pKa fit 580 nm

[Initial paramater estimates]
PK1 = 5.106645
PK2 = 7.71641
A0 = 0.2226436
A1 = 0.6412079
A2 = 0.2806649

[Model]
h=10^(-x)
k1=10^(-pk1)
k2=10^(-pk2)
alpha=h^2+k1*h+k1*k2
y=(a0*h^2+a1*k1*h+a2*k1*k2)/alpha

[Results]
Number of data points : 39
Number of paramaters : 5
Number of parameters varied : 5
Sum of squares of errors : 1.58288917727186E-001
Estimated standard deviation : 6.82316378503460E-002
Mean of residuals : -1.28963763412973E-016
Number of Iterations : 9
R-squared : 0.80073
Adjusted R-squared : 0.77729
F-Statistic : 34.15616

Parameter	Coefficient	Varied	Standard error
PK1	5.106645415224E+000	Yes	0.203066
PK2	7.716409838355E+000	Yes	0.224966
A0	2.226435903625E-001	Yes	0.0237125
A1	6.412078642981E-001	Yes	0.0432441
A2	2.806649458486E-001	Yes	0.0223356

[Correlation matrix]

	1	2	3	4	5
1	1.0000	-0.4153	0.4469	0.6424	0.1127
2	-0.4153	1.0000	-0.0844	-0.6799	-0.5174
3	0.4469	-0.0844	1.0000	0.1369	0.0219
4	0.6424	-0.6799	0.1369	1.0000	0.1922
5	0.1127	-0.5174	0.0219	0.1922	1.0000

Eu(III)complex 9 in MCB with KHP
Results for nonlinear 2 pKa fit 616.02 nm

[Initial paramater estimates]
PK1 = 5.113378
PK2 = 7.159546
A0 = 0.5799183
A1 = 6.465935
A2 = 0.5469474

[Model]
h=10^(-x)
k1=10^(-pk1)
k2=10^(-pk2)
alpha=h^2+k1*h+k1*k2
y=(a0*h^2+a1*k1*h+a2*k1*k2)/alpha

[Results]
Number of data points : 39
Number of paramaters : 5
Number of parameters varied : 5
Sum of squares of errors : 2.85529289881319E+000
Estimated standard deviation : 2.89791654307487E-001
Mean of residuals : -1.15183665000905E-014
Number of Iterations : 9
R-squared : 0.97425
Adjusted R-squared : 0.97122
F-Statistic : 321.63198

Parameter	Coefficient	Varied	Standard error
PK1	5.113377815536E+000	Yes	0.0717764
PK2	7.159545756549E+000	Yes	0.0698058
A0	5.799182973000E-001	Yes	0.10116
A1	6.465934700326E+000	Yes	0.279012
A2	5.469474438731E-001	Yes	0.0820204

[Correlation matrix]

	1	2	3	4	5
1	1.0000	-0.5486	0.4332	0.7443	0.1301
2	-0.5486	1.0000	-0.1114	-0.7830	-0.4338
3	0.4332	-0.1114	1.0000	0.1613	0.0244
4	0.7443	-0.7830	0.1613	1.0000	0.1965
5	0.1301	-0.4338	0.0244	0.1965	1.0000

Eu(III)complex 9 in MCB with KHP
Results for nonlinear 2 pKa fit 592.94 nm

[Initial paramater estimates]
PK1 = 4.847834
PK2 = 7.202269
A0 = 0.9189541
A1 = 4.003031
A2 = 0.754775

[Model]
h=10^(-x)
k1=10^(-pk1)
k2=10^(-pk2)
alpha=h^2+k1*h+k1*k2
y=(a0*h^2+a1*k1*h+a2*k1*k2)/alpha

[Results]
Number of data points : 39
Number of paramaters : 5
Number of parameters varied : 5
Sum of squares of errors : 1.76440150494909E+000
Estimated standard deviation : 2.27802901452697E-001
Mean of residuals : -1.27094445967302E-014
Number of Iterations : 9
R-squared : 0.95467
Adjusted R-squared : 0.94934
F-Statistic : 179.00993

Parameter	Coefficient	Varied	Standard error
PK1	4.847834155072E+000	Yes	0.100116
PK2	7.202269498785E+000	Yes	0.0913513
A0	9.189541165088E-001	Yes	0.0838126
A1	4.003031038145E+000	Yes	0.179371
A2	7.547750198405E-001	Yes	0.0648304

[Correlation matrix]

	1	2	3	4	5
1	1.0000	-0.4988	0.4494	0.7075	0.1185
2	-0.4988	1.0000	-0.1053	-0.7405	-0.4414
3	0.4494	-0.1053	1.0000	0.1565	0.0238
4	0.7075	-0.7405	0.1565	1.0000	0.1835
5	0.1185	-0.4414	0.0238	0.1835	1.0000

Eu(III)complex 9 in MCB with KHP
Results for nonlinear 2 pKa fit 688.98 nm

[Initial paramater estimates]
PK1 = 4.934115
PK2 = 7.371128
A0 = 0.3053049
A1 = 1.029949
A2 = 0.3745963

[Model]
h=10^(-x)
k1=10^(-pk1)
k2=10^(-pk2)
alpha=h^2+k1*h+k1*k2
y=(a0*h^2+a1*k1*h+a2*k1*k2)/alpha

[Results]
Number of data points : 39
Number of paramaters : 5
Number of parameters varied : 5
Sum of squares of errors : 2.03419053252437E-001
Estimated standard deviation : 7.73492943145187E-002
Mean of residuals : 1.08303908765496E-015
Number of Iterations : 9
R-squared : 0.89772
Adjusted R-squared : 0.88568
F-Statistic : 74.60329

Parameter	Coefficient	Varied	Standard error
PK1	4.934115368667E+000	Yes	0.139707
PK2	7.371128343365E+000	Yes	0.148985
A0	3.053048679115E-001	Yes	0.0278965
A1	1.029948655682E+000	Yes	0.056425
A2	3.745962721908E-001	Yes	0.0229343

[Correlation matrix]

	1	2	3	4	5
1	1.0000	-0.4687	0.4481	0.6847	0.1167
2	-0.4687	1.0000	-0.0966	-0.7199	-0.4656
3	0.4481	-0.0966	1.0000	0.1483	0.0229
4	0.6847	-0.7199	0.1483	1.0000	0.1869
5	0.1167	-0.4656	0.0229	0.1869	1.0000

Eu(III)complex 9 in MCB with KHP
Results for nonlinear 2 pKa fit 701 nm

[Initial paramater estimates]
PK1 = 4.96978
PK2 = 7.074696
A0 = 0.622348
A1 = 1.902426
A2 = 0.786448

[Model]
h=10^(-x)
k1=10^(-pk1)
k2=10^(-pk2)
alpha=h^2+k1*h+k1*k2
y=(a0*h^2+a1*k1*h+a2*k1*k2)/alpha

[Results]
Number of data points : 39
Number of paramaters : 5
Number of parameters varied : 5
Sum of squares of errors : 2.43509474426068E-001
Estimated standard deviation : 8.46288565766583E-002
Mean of residuals : 1.67979056590421E-015
Number of Iterations : 9
R-squared : 0.94880
Adjusted R-squared : 0.94278
F-Statistic : 157.52011

Parameter	Coefficient	Varied	Standard error
PK1	4.969780394440E+000	Yes	0.095994
PK2	7.074695735741E+000	Yes	0.107127
A0	6.223480235731E-001	Yes	0.0304147
A1	1.902425633513E+000	Yes	0.0798969
A2	7.864479690511E-001	Yes	0.0234876

[Correlation matrix]

	1	2	3	4	5
1	1.0000	-0.5520	0.4384	0.7477	0.1277
2	-0.5520	1.0000	-0.1152	-0.7794	-0.4235
3	0.4384	-0.1152	1.0000	0.1656	0.0250
4	0.7477	-0.7794	0.1656	1.0000	0.1893
5	0.1277	-0.4235	0.0250	0.1893	1.0000

Table E3: Complex **5** in MCB without KHP

pH	580 nm	593 nm	616 nm	653 nm	686 nm	700 nm
1.778	195.2846	810.663	699.5883	64.13406	325.653	547.6007
2.245	206.6097	845.0241	734.0364	65.40521	336.4706	576.0251
2.333	203.4903	835.7556	728.243	65.16405	333.8904	569.744
2.697	202.9864	853.6873	743.613	65.82397	340.9203	579.3045
2.821	203.5594	838.5414	736.3145	64.75481	337.0712	575.2002
3.145	201.9683	842.98	735.3362	65.40688	338.1154	574.9512
3.358	204.2976	845.9576	738.0281	65.6218	340.7464	569.0624
3.778	202.6357	843.7213	724.5893	63.79672	335.541	568.5742
4.239	202.2702	843.5906	732.3077	65.20831	335.3627	569.0453
4.495	207.3555	840.9897	725.4742	64.35615	341.4245	564.0582
4.9	205.6532	845.7675	728.3318	65.33652	337.0086	565.8182
5.409	202.9387	838.149	724.5651	64.07048	337.6984	564.1691
5.697	202.9371	837.6331	721.7948	65.38525	335.5614	561.1257
5.97	204.9446	841.0306	722.8145	65.35878	339.696	569.0973
6.239	204.3648	840.8464	730.3334	66.22919	337.7013	561.3988
6.33	202.8883	837.8123	726.6285	63.84427	338.7542	565.0295
5.964	205.9308	843.0583	725.1833	62.87744	337.0363	563.5749
6.67	206.1183	841.9871	728.2561	65.20667	341.2728	568.7681
6.15	205.2491	834.825	725.2226	63.95226	336.8221	566.7371
7.298	210.6601	829.8077	723.9879	64.33308	337.0156	566.7156
6.414	210.6279	831.3297	721.8156	64.26594	334.0952	560.9182
6.385	196.2729	772.6138	671.6031	59.13851	314.1742	526.8398
7.096	204.7534	803.772	701.5762	61.27945	325.9899	549.3306
7.498	210.184	775.3029	685.27	60.6262	318.1284	527.0948
7.211	209.8074	771.4942	684.5627	60.62157	316.5522	523.8483
7.993	220.8056	733.2023	663.5981	59.96705	306.6989	513.9951
7.649	234.4881	698.0406	646.1179	56.46826	296.9293	494.1169
8.453	252.9506	619.8992	607.0824	52.35078	272.0445	453.1989
8.785	238.1107	668.6689	639.8068	54.44976	284.4984	474.4576
8.95	274.2381	527.8185	563.2554	48.10026	252.3819	408.7452
8.88	251.0165	622.4475	629.0097	53.29805	277.5058	453.5626
9.089	284.7923	480.8141	553.1343	46.31601	239.1019	383.5215
9.496	309.7236	349.2112	481.7581	38.87819	202.2949	314.4131
10.039	314.8727	341.789	494.6658	39.1232	206.8369	316.2446
10.352	327.0158	245.4566	418.5801	33.73812	175.2239	258.0613
10.467	327.1991	175.9459	326.9938	29.55535	146.103	219.5225
11.501	323.5064	179.4825	334.7118	29.6229	146.7617	220.0659

Eu(III)Complex 5 in MCB without KHP 1pKa Fit
Results for nonlinear fit 580 nm
[Initial paramater estimates]
PK1 = 8.90725
A0 = 204.9185
A1 = 327.8579

[Model]
H=10^(-x)
K1=10^(-pK1)
Alpha=H+K1
Y=(A0*H+A1*K1)/Alpha

[Results]
Number of data points : 37
Number of paramaters : 3
Number of parameters varied : 3
Sum of squares of errors : 1.80425864149277E+003
Estimated standard deviation : 7.28467093506222E+000
Mean of residuals : 5.72377925836756E-011
Number of Iterations : 9
R-squared : 0.97170
Adjusted R-squared : 0.97003
F-Statistic : 583.64012

Parameter	Coefficient	Varied	Standard error
PK1	8.907250008608E+000	Yes	0.0591514
A0	2.049184634586E+002	Yes	1.44553
A1	3.278579018656E+002	Yes	3.91802

[Correlation matrix]

	1	2	3
1	1.0000	0.2759	0.6009
2	0.2759	1.0000	0.0591
3	0.6009	0.0591	1.0000

Eu(III)Complex 5 in MCB without KHP 1pKa Fit
Results for nonlinear fit 592.94 nm
[Initial paramater estimates]
PK1 = 9.036708
A0 = 826.3804
A1 = 204.6111

[Model]
H=10^(-x)
K1=10^(-pK1)
Alpha=H+K1
Y=(A0*H+A1*K1)/Alpha

[Results]
Number of data points : 37
Number of paramaters : 3
Number of parameters varied : 3
Sum of squares of errors : 4.79121469328806E+004
Estimated standard deviation : 3.75390568893725E+001
Mean of residuals : -2.27501052681119E-009
Number of Iterations : 10
R-squared : 0.96857
Adjusted R-squared : 0.96672
F-Statistic : 523.89271

Parameter	Coefficient	Varied	Standard error
PK1	9.036707872803E+000	Yes	0.0609308
A0	8.263803699150E+002	Yes	7.39241
A1	2.046111322649E+002	Yes	21.0156

[Correlation matrix]

	1	2	3
1	1.0000	-0.2818	-0.5956
2	-0.2818	1.0000	0.0594
3	-0.5956	0.0594	1.0000

Eu(III)Complex 5 in MCB without KHP 1pKa Fit
Results for nonlinear fit 616.02 nm

[Initial paramater estimates]
PK1 = 9.174554
A0 = 717.3284
A1 = 368.8554

[Model]
H=10^(-x)
K1=10^(-pK1)
Alpha=H+K1
Y=(A0*H+A1*K1)/Alpha

[Results]
Number of data points : 37
Number of paramaters : 3
Number of parameters varied : 3
Sum of squares of errors : 2.97904355077650E+004
Estimated standard deviation : 2.96004945843840E+001
Mean of residuals : -8.20285611207832E-011
Number of Iterations : 11
R-squared : 0.93515
Adjusted R-squared : 0.93133
F-Statistic : 245.12595

Parameter	Coefficient	Varied	Standard error
PK1	9.174553828425E+000	Yes	0.0891077
A0	7.173284286978E+002	Yes	5.78648
A1	3.688553545145E+002	Yes	17.4237

[Correlation matrix]

	1	2	3
1	1.0000	-0.2908	-0.5974
2	-0.2908	1.0000	0.0656
3	-0.5974	0.0656	1.0000

Eu(III)Complex 5 in MCB without KHP 1pKa Fit
Results for nonlinear fit 653.04 nm
[Initial paramater estimates]
PK1 = 9.021449
A0 = 63.90412
A1 = 31.46271

[Model]
H=10^(-x)
K1=10^(-pK1)
Alpha=H+K1
Y=(A0*H+A1*K1)/Alpha

[Results]
Number of data points : 37
Number of paramaters : 3
Number of parameters varied : 3
Sum of squares of errors : 1.85903563620437E+002
Estimated standard deviation : 2.33832244807882E+000
Mean of residuals : -1.72105362056402E-012
Number of Iterations : 10
R-squared : 0.95615
Adjusted R-squared : 0.95357
F-Statistic : 370.67026

Parameter	Coefficient	Varied	Standard error
PK1	9.021448544378E+000	Yes	0.0725552
A0	6.390412473920E+001	Yes	0.460867
A1	3.146270500199E+001	Yes	1.30252

[Correlation matrix]

	1	2	3
1	1.0000	-0.2809	-0.5960
2	-0.2809	1.0000	0.0591
3	-0.5960	0.0591	1.0000

Eu(III)Complex 5 in MCB without KHP 1pKa Fit
Results for nonlinear fit 685.94 nm

[Initial paramater estimates]
PK1 = 9.046354
A0 = 332.9428
A1 = 159.7469

[Model]
H=10^(-x)
K1=10^(-pK1)
Alpha=H+K1
Y=(A0*H+A1*K1)/Alpha

[Results]
Number of data points : 37
Number of paramaters : 3
Number of parameters varied : 3
Sum of squares of errors : 4.99172365445060E+003
Estimated standard deviation : 1.21167405518765E+001
Mean of residuals : -2.48763851485057E-010
Number of Iterations : 10
R-squared : 0.95804
Adjusted R-squared : 0.95557
F-Statistic : 388.10103

Parameter	Coefficient	Varied	Standard error
PK1	9.046353854199E+000	Yes	0.070732
A0	3.329427891194E+002	Yes	2.38483
A1	1.597469399056E+002	Yes	6.80521

[Correlation matrix]

	1	2	3
1	1.0000	-0.2824	-0.5954
2	-0.2824	1.0000	0.0597
3	-0.5954	0.0597	1.0000

Eu(III)Complex 5 in MCB without KHP 1pKa Fit
Results for nonlinear fit 700 nm

[Initial paramater estimates]
PK1 = 9.047542
A0 = 559.5634
A1 = 236.7965

[Model]
H=10^(-x)
K1=10^(-pK1)
Alpha=H+K1
Y=(A0*H+A1*K1)/Alpha
[Results]
Number of data points : 37
Number of paramaters : 3
Number of parameters varied : 3
Sum of squares of errors : 1.49463407225795E+004
Estimated standard deviation : 2.09665985926773E+001
Mean of residuals : 2.69255053313493E-010
Number of Iterations : 10
R-squared : 0.96359
Adjusted R-squared : 0.96144
F-Statistic : 449.86138

Parameter	Coefficient	Varied	Standard error
PK1	9.047542103745E+000	Yes	0.0656913
A0	5.595633951557E+002	Yes	4.1264
A1	2.367965291627E+002	Yes	11.7803

[Correlation matrix]

	1	2	3
1	1.0000	-0.2825	-0.5954
2	-0.2825	1.0000	0.0597
3	-0.5954	0.0597	1.0000

Table E4: Complex **7** in MCB without KHP

pH	580 nm	593 nm	615 nm	653 nm	686 nm	703 nm
2.036	9.018921	39.50199	37.16164	3.571938	17.04198	22.8214
2.089	9.176717	42.05157	38.17734	3.860089	17.53085	24.24519
2.234	9.109066	41.3186	37.42147	3.934429	17.18196	23.37055
2.48	9.63076	42.5901	38.89782	4.00751	17.38169	24.2912
2.57	8.777876	40.9495	37.70302	3.652858	17.28327	23.293
2.712	9.305861	41.73677	38.28578	3.833423	17.49679	23.85856
3.04	8.883518	40.65905	37.26588	3.672124	16.81368	22.93902
2.795	9.057775	41.05644	37.18943	3.746079	16.72367	23.04039
3.202	9.227151	40.73834	37.93256	3.701778	17.17657	22.98778
3.455	9.310441	41.15077	38.10065	3.921748	17.10158	23.33626
3.9	9.31475	41.5947	38.536	3.514105	17.10585	23.10208
3.83	9.042604	40.82191	37.89815	3.616464	16.93287	22.65738
3.61	9.03078	41.23015	38.23111	3.755315	17.14525	23.35977
3.7	9.093537	42.01402	38.28193	3.833684	17.25118	22.99015
4.4	8.913075	40.06866	37.67798	3.659998	16.72119	22.66446
9.131	18.70716	16.8848	24.76616	2.283224	11.50411	17.74611
7.59	13.27324	29.2193	32.45764	3.063461	14.38656	19.87187
6.1	8.74136	39.11382	36.51947	3.541076	16.34459	21.83517
9.3	19.76696	15.26134	24.95588	2.384143	11.21522	17.35737
4.75	9.832104	43.71656	41.03606	4.151778	18.02407	23.89696
5.686	9.056525	40.33348	38.18675	3.566016	16.91787	22.5694
5.15	9.188657	40.87913	38.29564	3.865413	17.17046	23.05496
5.828	8.917207	40.12515	38.4607	3.703675	17.15668	23.1074
5.3	9.543035	41.59506	39.06663	3.885269	17.32188	23.47002
5.76	9.006239	39.73908	38.06776	3.647251	16.88611	22.42639
5.15	9.125041	40.8679	38.52338	3.710527	16.97848	23.03475
5.86	8.997209	40.34923	38.41415	3.770494	16.95149	23.11111
6.462	8.997209	39.70687	37.51201	3.776748	16.73789	22.72645
6.543	9.113293	39.46829	37.38093	3.707593	16.70143	22.472
6.748	9.010166	39.95811	37.54989	3.783357	16.81192	22.53899
7.11	9.235167	40.06427	37.19304	3.75496	16.75581	22.66415
8.209	9.090235	39.95964	37.12696	3.680652	16.80019	22.30023
7.68	10.24683	35.56054	36.05315	3.532537	15.9577	21.42305
8.13	13.66461	22.93069	29.25729	2.574102	12.49872	17.42059
8.3	14.95468	26.44779	31.26642	2.92833	14.05759	19.45432
8.4	16.9088	22.59986	29.25088	2.753193	13.00028	19.20081
11.102	19.23576	14.5863	25.01279	2.309195	11.0688	16.8913
9.221	18.50754	16.97311	25.65395	2.360528	11.73063	17.29672
9.131	17.7154	20.31077	28.62888	2.718638	12.64252	18.64718
9.92	19.47592	16.00246	25.27393	2.26061	11.51951	17.43029
9.1	18.40962	19.57542	29.89624	2.654403	12.96577	18.07942
9.776	20.09877	14.54212	23.82224	2.190624	10.6909	17.1885
9.66	19.10791	17.11818	27.87422	2.545023	12.25405	17.80682
11.705	19.27056	13.58584	22.70109	2.061752	10.41209	16.87994
11.173	18.70905	13.0161	22.17184	2.104066	9.980494	16.36304
7.93	14.09591	29.92818	32.79905	3.305254	14.94384	20.93826
7.93	14.03125	30.14358	32.73426	3.073264	14.80776	21.0726
8.241	15.85888	23.84538	29.55911	2.998763	13.39	18.96475
8.66	18.73119	18.62437	27.29952	2.488226	12.24844	18.64295
9.159	20.21074	15.37648	24.39324	2.234545	11.57329	17.91834
9.412	20.778	14.59016	23.37108	2.365207	10.93391	17.25284
9.708	20.83962	14.10309	22.89581	2.238063	10.57637	17.43052
10.005	21.06476	13.6221	22.58962	2.32312	10.60525	17.09846
10.296	20.17791	13.32479	21.87313	2.229987	10.15804	16.6144
10.383	19.70017	12.86007	21.30011	2.128994	10.09186	16.45347
10.451	20.33855	13.23603	22.23866	2.035977	10.21455	17.05115
10.541	20.16963	13.46782	21.72208	2.281112	10.31771	16.9247
10.673	19.9552	13.35463	21.60919	2.239969	10.15095	16.70548

Eu(III)complex 7 in MCB without KHP
Results for nonlinear 1pKa Fit 580 nm

[Initial paramater estimates]
PK1 = 8.218037
A0 = 9.093779
A1 = 20.08134

[Model]
H=10^(-x)
K1=10^(-pK1)
Alpha=H+K1
Y=(A0*H+A1*K1)/Alpha

[Results]
Number of data points : 58
Number of paramaters : 3
Number of parameters varied : 3
Sum of squares of errors : 5.86322013723637E+001
Estimated standard deviation : 1.03249214280403E+000
Mean of residuals : 4.90003227768170E-013
Number of Iterations : 9
R-squared : 0.95737
Adjusted R-squared : 0.95582
F-Statistic : 617.60578

Parameter	Coefficient	Varied	Standard error
PK1	8.218037499586E+000	Yes	0.0665992
A0	9.093778922915E+000	Yes	0.197175
A1	2.008133708026E+001	Yes	0.263028

[Correlation matrix]

	1	2	3
1	1.0000	0.3233	0.4926
2	0.3233	1.0000	0.0578
3	0.4926	0.0578	1.0000

Eu(III)complex 7 in MCB without KHP
Results for nonlinear 1pKa Fit 592.94 nm

[Initial paramater estimates]
PK1 = 8.177916
A0 = 40.89266
A1 = 13.99905

[Model]
H=10^(-x)
K1=10^(-pK1)
Alpha=H+K1
Y=(A0*H+A1*K1)/Alpha

[Results]
Number of data points : 58
Number of paramaters : 3
Number of parameters varied : 3
Sum of squares of errors : 3.15595847741551E+002
Estimated standard deviation : 2.39543447469841E+000
Mean of residuals : 6.85971738583547E-013
Number of Iterations : 10
R-squared : 0.96180
Adjusted R-squared : 0.96041
F-Statistic : 692.32658

Parameter	Coefficient	Varied	Standard error
PK1	8.177915597212E+000	Yes	0.0629817
A0	4.089266414889E+001	Yes	0.458594
A1	1.399904543923E+001	Yes	0.604069

[Correlation matrix]

	1	2	3
1	1.0000	-0.3191	-0.4889
2	-0.3191	1.0000	0.0554
3	-0.4889	0.0554	1.0000

Eu(III)complex 7 in MCB without KHP
Results for nonlinear 1pKa Fit 615 nm

[Initial paramater estimates]
PK1 = 8.341026
A0 = 37.99392
A1 = 23.22033

[Model]
H=10^(-x)
K1=10^(-pK1)
Alpha=H+K1
Y=(A0*H+A1*K1)/Alpha

[Results]
Number of data points : 58
Number of paramaters : 3
Number of parameters varied : 3
Sum of squares of errors : 1.46766482931752E+002
Estimated standard deviation : 1.63354874670150E+000
Mean of residuals : -2.46258966882144E-012
Number of Iterations : 10
R-squared : 0.94066
Adjusted R-squared : 0.93850
F-Statistic : 435.89748

Parameter	Coefficient	Varied	Standard error
PK1	8.341026383804E+000	Yes	0.0796541
A0	3.799391925896E+001	Yes	0.309483
A1	2.322033019218E+001	Yes	0.431034

[Correlation matrix]

	1	2	3
1	1.0000	-0.3356	-0.5084
2	-0.3356	1.0000	0.0672
3	-0.5084	0.0672	1.0000

Eu(III)complex 7 in MCB without KHP
Results for nonlinear 1pKa Fit 653.04 nm
[Initial paramater estimates]
PK1 = 8.216227
A0 = 3.756226
A1 = 2.227853

[Model]
H=10^(-x)
K1=10^(-pK1)
Alpha=H+K1
Y=(A0*H+A1*K1)/Alpha

[Results]
Number of data points : 58
Number of paramaters : 3
Number of parameters varied : 3
Sum of squares of errors : 1.92125891980468E+000
Estimated standard deviation : 1.86900990794819E-001
Mean of residuals : 1.30846602709877E-014
Number of Iterations : 9
R-squared : 0.92990
Adjusted R-squared : 0.92735
F-Statistic : 364.80392

Parameter	Coefficient	Varied	Standard error
PK1	8.216227048839E+000	Yes	0.0866573
A0	3.756226052081E+000	Yes	0.0356965
A1	2.227852758514E+000	Yes	0.0475907

[Correlation matrix]

	1	2	3
1	1.0000	-0.3232	-0.4924
2	-0.3232	1.0000	0.0577
3	-0.4924	0.0577	1.0000

Eu(III)complex 7 in MCB without KHP
Results for nonlinear 1pKa Fit 685.94 nm

[Initial paramater estimates]
PK1 = 8.28279
A0 = 17.0485
A1 = 10.68018

[Model]
H=10^(-x)
K1=10^(-pK1)
Alpha=H+K1
Y=(A0*H+A1*K1)/Alpha

[Results]
Number of data points : 58
Number of paramaters : 3
Number of parameters varied : 3
Sum of squares of errors : 2.50971628401996E+001
Estimated standard deviation : 6.75508735428338E-001
Mean of residuals : -3.12893269722955E-016
Number of Iterations : 9
R-squared : 0.94570
Adjusted R-squared : 0.94373
F-Statistic : 478.97111

Parameter	Coefficient	Varied	Standard error
PK1	8.282790321796E+000	Yes	0.0757072
A0	1.704850483657E+001	Yes	0.128473
A1	1.068018474765E+001	Yes	0.17516

[Correlation matrix]

	1	2	3
1	1.0000	-0.3300	-0.5001
2	-0.3300	1.0000	0.0624
3	-0.5001	0.0624	1.0000

Eu(III)complex 7 in MCB without KHP
Results for nonlinear 1pKa Fit 703 nm

[Initial paramater estimates]
PK1 = 8.084887
A0 = 23.08789
A1 = 17.06947

[Model]
H=10^(-x)
K1=10^(-pK1)
Alpha=H+K1
Y=(A0*H+A1*K1)/Alpha

[Results]
Number of data points : 58
Number of paramaters : 3
Number of parameters varied : 3
Sum of squares of errors : 2.80069576871179E+001
Estimated standard deviation : 7.13594711648743E-001
Mean of residuals : 1.01240002372817E-012
Number of Iterations : 9
R-squared : 0.93522
Adjusted R-squared : 0.93286
F-Statistic : 396.99656

Parameter	Coefficient	Varied	Standard error
PK1	8.084887029383E+000	Yes	0.0839442
A0	2.308788761702E+001	Yes	0.137395
A1	1.706947434879E+001	Yes	0.176121

[Correlation matrix]

	1	2	3
1	1.0000	-0.3094	-0.4826
2	-0.3094	1.0000	0.0511
3	-0.4826	0.0511	1.0000

Table E5: Complex **5** in Water

pH	580 nm	593 nm	616 nm	653 nm	686 nm	700 nm
1.89	184.3495	757.5199	658.6595	59.21292	305.3577	517.6694
2.569	191.8092	788.2394	676.0637	60.68227	310.0902	533.5911
2.969	192.0077	795.1722	689.8506	61.78461	317.8637	536.5387
3.13	196.0352	803.4358	699.526	63.00753	321.2828	542.2555
3.35	195.1807	801.14	702.4911	62.16301	323.7544	544.2304
3.689	197.6151	809.7134	699.2607	63.22436	323.1023	547.5717
3.698	194.8846	805.7063	703.4588	61.56657	321.7393	545.3578
3.825	198.4539	809.0768	701.4655	62.46199	323.7696	548.577
4.042	196.8673	799.4653	699.565	62.71805	320.5756	546.6083
4.375	197.3572	808.257	696.9099	62.26994	325.5774	547.2878
4.795	196.3206	811.0889	699.9565	61.66362	321.9992	547.7372
5.21	198.1039	800.1104	698.5717	61.97143	320.1256	546.4984
5.398	203.9506	825.6872	716.6693	63.69745	331.5274	552.1426
5.789	201.6318	812.8804	706.5741	63.48131	326.1329	554.2812
5.902	198.9117	818.1832	713.2211	63.09072	330.7667	553.9396
6.014	205.8602	811.6509	714.1716	63.52386	332.3515	556.4669
6.33	199.5831	781.6427	694.3349	60.35399	322.9432	538.8073
6.8	206.3995	830.1756	721.696	64.78285	335.9355	561.4416
6.485	203.4051	811.2666	708.7524	64.25299	333.2972	552.414
7.179	203.3354	807.4875	708.4608	63.39521	330.6143	556.6631
6.963	200.633	764.6931	675.8947	60.67384	317.117	523.2955
7.064	204.0868	763.8388	677.2546	61.15548	315.7415	527.0772
7.245	214.2067	703.8189	642.9781	56.33001	295.5341	494.7468
7.749	221.0903	673.6494	628.8132	56.33971	287.5481	481.263
8.275	248.3836	573.6673	577.1117	51.99474	259.1734	433.4363
8.645	264.8663	517.3972	550.042	47.77931	246.6835	408.6101
8.205	217.9028	698.5002	643.6962	56.68527	292.9313	491.8618
8.989	287.7796	403.7613	478.033	41.48519	212.7179	346.8142
7.8	257.4459	555.3839	580.881	50.02658	256.7005	422.6779
8.21	222.6935	666.2631	632.6204	55.20226	285.081	480.6864
9.445	311.0316	320.1701	470.3271	38.43673	194.3806	298.1468
9.848	317.5209	191.4067	342.4972	29.99405	151.7482	226.8269
10.498	318.372	184.017	342.3402	29.30731	149.9083	223.1408
10.33	318.2306	175.1089	321.4289	27.82008	144.0217	218.3494
10.803	315.8904	205.5085	378.5991	30.70507	158.3967	231.3869
11.08	320.1266	173.6463	328.418	29.09633	144.2694	215.0247
11.335	318.0231	175.1918	333.8505	28.33884	144.8318	220.7039

Eu(III)Complex 5 in Water
Results for nonlinear fit 580 nm
[Initial paramater estimates]
PK1 = 8.529524
A0 = 198.8802
A1 = 319.717

[Model]
H=10^(-x)
K1=10^(-pK1)
Alpha=H+K1
Y=(A0*H+A1*K1)/Alpha

[Results]
Number of data points : 37
Number of paramaters : 3
Number of parameters varied : 3
Sum of squares of errors : 2.87782939219027E+003
Estimated standard deviation : 9.20011092035160E+000
Mean of residuals : 1.41569380467748E-010
Number of Iterations : 10
R-squared : 0.96475
Adjusted R-squared : 0.96268
F-Statistic : 465.32641

Parameter	Coefficient	Varied	Standard error
PK1	8.529523623592E+000	Yes	0.0735237
A0	1.988801880704E+002	Yes	1.95573
A1	3.197169573776E+002	Yes	3.70821

[Correlation matrix]

	1	2	3
1	1.0000	0.3535	0.4567
2	0.3535	1.0000	0.0608
3	0.4567	0.0608	1.0000

Eu(III)Complex 5 in Water
Results for nonlinear fit 592.94 nm

[Initial paramater estimates]
PK1 = 8.66228
A0 = 794.7341
A1 = 182.6688

[Model]
H=10^(-x)
K1=10^(-pK1)
Alpha=H+K1
Y=(A0*H+A1*K1)/Alpha

[Results]
Number of data points : 37
Number of paramaters : 3
Number of parameters varied : 3
Sum of squares of errors : 5.62037095894085E+004
Estimated standard deviation : 4.06577210630580E+001
Mean of residuals : -1.72982485992947E-009
Number of Iterations : 10
R-squared : 0.97214
Adjusted R-squared : 0.97050
F-Statistic : 593.10806

Parameter	Coefficient	Varied	Standard error
PK1	8.662280032790E+000	Yes	0.0671875
A0	7.947341105825E+002	Yes	8.53284
A1	1.826687656596E+002	Yes	16.8561

[Correlation matrix]

	1	2	3
1	1.0000	-0.3520	-0.4592
2	-0.3520	1.0000	0.0650
3	-0.4592	0.0650	1.0000

Eu(III)Complex 5 in Water
Results for nonlinear fit 616.02 nm

[Initial paramater estimates]
PK1 = 8.773084
A0 = 694.0275
A1 = 341.6401

[Model]
H=10^(-x)
K1=10^(-pK1)
Alpha=H+K1
Y=(A0*H+A1*K1)/Alpha

[Results]
Number of data points : 37
Number of paramaters : 3
Number of parameters varied : 3
Sum of squares of errors : 2.40969345003827E+004
Estimated standard deviation : 2.66220466466858E+001
Mean of residuals : -8.00788523329714E-010
Number of Iterations : 11
R-squared : 0.96335
Adjusted R-squared : 0.96119
F-Statistic : 446.79866

Parameter	Coefficient	Varied	Standard error
PK1	8.773084251968E+000	Yes	0.0797235
A0	6.940274535499E+002	Yes	5.52633
A1	3.416400663926E+002	Yes	11.3289

[Correlation matrix]

	1	2	3
1	1.0000	-0.3485	-0.4660
2	-0.3485	1.0000	0.0693
3	-0.4660	0.0693	1.0000

Eu(III)Complex 5 in Water
Results for nonlinear fit 653.04 nm

[Initial paramater estimates]
PK1 = 8.729027
A0 = 61.92849
A1 = 29.10421

[Model]
H=10^(-x)
K1=10^(-pK1)
Alpha=H+K1
Y=(A0*H+A1*K1)/Alpha

[Results]
Number of data points : 37
Number of paramaters : 3
Number of parameters varied : 3
Sum of squares of errors : 1.80618254030522E+002
Estimated standard deviation : 2.30484307256113E+000
Mean of residuals : -1.69887950835546E-011
Number of Iterations : 9
R-squared : 0.96850
Adjusted R-squared : 0.96664
F-Statistic : 522.62748

Parameter	Coefficient	Varied	Standard error
PK1	8.729026898468E+000	Yes	0.0728451
A0	6.192849135425E+001	Yes	0.480556
A1	2.910420632132E+001	Yes	0.970398

[Correlation matrix]

	1	2	3
1	1.0000	-0.3501	-0.4628
2	-0.3501	1.0000	0.0675
3	-0.4628	0.0675	1.0000

Eu(III)Complex 5 in Water
Results for nonlinear fit 685.94 nm

[Initial paramater estimates]
PK1 = 8.691616
A0 = 321.2804
A1 = 148.7264

[Model]
H=10^(-x)
K1=10^(-pK1)
Alpha=H+K1
Y=(A0*H+A1*K1)/Alpha

[Results]
Number of data points : 37
Number of paramaters : 3
Number of parameters varied : 3
Sum of squares of errors : 5.31293873809889E+003
Estimated standard deviation : 1.25005161518128E+001
Mean of residuals : 2.24442571510090E-010
Number of Iterations : 11
R-squared : 0.96682
Adjusted R-squared : 0.96486
F-Statistic : 495.30459

Parameter	Coefficient	Varied	Standard error
PK1	8.691616359178E+000	Yes	0.0740867
A0	3.212803978737E+002	Yes	2.61597
A1	1.487263658358E+002	Yes	5.21719

[Correlation matrix]

	1	2	3
1	1.0000	-0.3513	-0.4606
2	-0.3513	1.0000	0.0660
3	-0.4606	0.0660	1.0000

Eu(III)Complex 5 in Water
Results for nonlinear fit 700 nm

Results for nonlinear fit

[Initial paramater estimates]
PK1 = 8.726345
A0 = 540.9201
A1 = 220.5824

[Model]
H=10^(-x)
K1=10^(-pK1)
Alpha=H+K1
Y=(A0*H+A1*K1)/Alpha

[Results]
Number of data points : 37
Number of paramaters : 3
Number of parameters varied : 3
Sum of squares of errors : 1.53948169964044E+004
Estimated standard deviation : 2.12788330316388E+001
Mean of residuals : -9.73308559124406E-010
Number of Iterations : 11
R-squared : 0.97173
Adjusted R-squared : 0.97007
F-Statistic : 584.35699

Parameter	Coefficient	Varied	Standard error
PK1	8.726344738705E+000	Yes	0.0688407
A0	5.409200552467E+002	Yes	4.43778
A1	2.205824160931E+002	Yes	8.95323

[Correlation matrix]

	1	2	3
1	1.0000	-0.3502	-0.4626
2	-0.3502	1.0000	0.0674
3	-0.4626	0.0674	1.0000

UV-vis Spectroscopy

Table E6: Complex **5** in MCB with KHP

pH	270 nm
1.98	1.305625
2.197	1.320841
2.469	1.347536
2.503	1.365916
2.651	1.394075
2.796	1.418099
2.93	1.446764
3.47	1.44661
3.885	1.448236
3.95	1.388812
4.32	1.328537
4.47	1.234064
4.71	1.139309
4.9	1.054316
4.959	0.875898
5.32	0.711834
6.101	0.700737
6.642	0.692219
6.978	0.679651
7.171	0.675923
7.224	0.68923
7.423	0.682015
8.204	0.67018
8.172	0.67453
8.381	0.678296
8.47	0.683334
8.675	0.681853
8.71	0.675737
9.382	0.678191
9.484	0.685397
9.495	0.686253
9.705	0.692435
9.889	0.6963
10.048	1.079838
10.395	0.697999
10.501	0.699021
10.91	0.717802
11.505	0.714721
12.555	0.726859

Eu(III)Complex 5 in MCB (UV-vis data)
Results for nonlinear 3pKa fit 270nm
[Initial paramater estimates]
PK1 = 2.836829
PK2 = 5.107513
PK3 = 11.12444
A1 = 1.260615
A2 = 1.119702
A3 = 0.8905569
A4 = 0.9298276

[Model]
h=10^(-x)
k1=10^(-pK1)
k2=10^(-pK2)
k3=10^(-pK3)
den=k1*k2*k3+h*k1*k2+h^2*k1+h^3
y=(a1*h^3+a2*h^2*k1+a3*h*k1*k2+a4*k1*k2*k3)/den

[Results]
Number of data points : 39
Number of paramaters : 7
Number of parameters varied : 7
Sum of squares of errors : 7.45425820948338E-003
Estimated standard deviation : 1.52625544731659E-002
Mean of residuals : -6.25884894125747E-016
Number of Iterations : 9
R-squared : 0.98838
Adjusted R-squared : 0.98621
F-Statistic : 453.81952

Parameter	Coefficient	Varied	Standard error
PK1	2.836829195770E+000	Yes	0.244515
PK2	5.107512524344E+000	Yes	0.103099
PK3	1.112444172140E+001	Yes	0.625016
A1	1.260614674132E+000	Yes	0.0201748
A2	1.119701705581E+000	Yes	0.0149151
A3	8.905569487869E-001	Yes	0.00390635
A4	9.298276224933E-001	Yes	0.0159935

[Correlation matrix]

	1	2	3	4	5	6	7
1	1.0000	0.5186	-0.0208	-0.8690	-0.7051	-0.0550	-0.0066
2	0.5186	1.0000	-0.0903	-0.2892	-0.8194	-0.2381	-0.0288
3	-0.0208	-0.0903	1.0000	0.0106	0.0368	0.3796	0.6539
4	-0.8690	-0.2892	0.0106	1.0000	0.4256	0.0280	0.0034
5	-0.7051	-0.8194	0.0368	0.4256	1.0000	0.0971	0.0117
6	-0.0550	-0.2381	0.3796	0.0280	0.0971	1.0000	0.1212
7	-0.0066	-0.0288	0.6539	0.0034	0.0117	0.1212	1.0000

Table E7: Complex **9** in MCB with KHP

pH	280 nm
1.961	0.9422
2.023	0.947905
2.268	0.956222
2.49	0.970745
2.79	0.989895
3.141	1.018736
3.372	1.015012
3.81	1.006344
4.016	0.979469
4.4	0.933777
4.527	0.894786
4.881	0.812545
5.1	0.744871
5.297	0.681434
5.6752	0.61693
6.056	0.557943
6.258	0.547851
6.441	0.540642
6.718	0.518937
6.95	0.528551
7.235	0.526409
7.332	0.512557
7.706	0.520525
7.834	0.518232
8.176	0.518073
8.38	0.517918
8.612	0.538678
8.8	0.517412
8.855	0.534553
9.065	0.520146
9.221	0.519238
9.467	0.515455
9.287	0.537765
9.288	0.517573
9.687	0.510972
9.458	0.512126
9.722	0.518102
9.785	0.517064
11.758	0.517733

Eu(III)complex 9 in MCB UV-vis 280 nm
Results for nonlinear 2pKa Fit
[Initial paramater estimates]
PK1 = 2.550131
PK2 = 4.972754
A0 = 0.9164963
A1 = 1.040775
A2 = 0.5202184

[Model]
h=10^(-x)
k1=10^(-pk1)
k2=10^(-pk2)
alpha=h^2+k1*h+k1*k2
y=(a0*h^2+a1*k1*h+a2*k1*k2)/alpha

[Results]
Number of data points : 39
Number of paramaters : 5
Number of parameters varied : 5
Sum of squares of errors : 1.77142460479367E-003
Estimated standard deviation : 7.21808310220949E-003
Mean of residuals : 4.00090061686144E-016
Number of Iterations : 9
R-squared : 0.99885
Adjusted R-squared : 0.99871
F-Statistic : 7367.03517

Parameter	Coefficient	Varied	Standard error
PK1	2.550131396450E+000	Yes	0.161552
PK2	4.972753964626E+000	Yes	0.0187795
A0	9.164963493518E-001	Yes	0.0133008
A1	1.040775403424E+000	Yes	0.00607356
A2	5.202184093968E-001	Yes	0.001511

[Correlation matrix]

	1	2	3	4	5
1	1.0000	-0.4893	0.9024	0.6522	0.0673
2	-0.4893	1.0000	-0.3190	-0.7636	-0.2776
3	0.9024	-0.3190	1.0000	0.4230	0.0433
4	0.6522	-0.7636	0.4230	1.0000	0.1098
5	0.0673	-0.2776	0.0433	0.1098	1.0000

Table E8: Complex **5** in MCB without KHP

pH	308 nm
1.778	0.03559
2.245	0.039326
2.333	0.045816
2.697	0.044506
2.821	0.035366
3.145	0.03277
3.358	0.041104
3.778	0.041157
4.239	0.047476
4.495	0.031677
4.9	0.050038
5.409	0.043017
5.697	0.040264
5.964	0.045388
5.97	0.046874
6.15	0.044815
6.239	0.040149
6.33	0.039593
6.385	0.054566
6.385	0.053091
6.67	0.04096
7.096	0.041237
7.211	0.056847
7.298	0.043575
7.498	0.042582
7.649	0.064904
7.993	0.050136
8.453	0.0782
8.785	0.067091
8.88	0.073117
8.95	0.07764
9.089	0.081186
9.496	0.105292
10.039	0.102942
10.352	0.114364
10.467	0.131605
11.501	0.123583

Eu(III)Complex 5 in MCB without KHP (UV-vis)
Results for nonlinear fit 308 nm
[Initial paramater estimates]
PK1 = 9.021969
A0 = 0.04373711
A1 = 0.1217163

[Model]
H=10^(-x)
K1=10^(-pK1)
Alpha=H+K1
Y=(A0*H+A1*K1)/Alpha

[Results]
Number of data points : 37
Number of paramaters : 3
Number of parameters varied : 3
Sum of squares of errors : 1.96453463798658E-003
Estimated standard deviation : 7.60134399491413E-003
Mean of residuals : 1.64419625741944E-017
Number of Iterations : 9
R-squared : 0.92259
Adjusted R-squared : 0.91804
F-Statistic : 202.60771

Parameter	Coefficient	Varied	Standard error
PK1	9.021969354471E+000	Yes	0.0981306
A0	4.373710630057E-002	Yes	0.00149809
A1	1.217163226822E-001	Yes	0.00423492

[Correlation matrix]

	1	2	3
1	1.0000	0.2809	0.5960
2	0.2809	1.0000	0.0591
3	0.5960	0.0591	1.0000

Table E9: Complex **7** in MCB without KHP

pH	263 nm
2.036	0.21903
2.89	0.339009
2.48	0.328977
2.57	0.40531
2.795	0.28414
3.203	0.29896
3.61	0.342286
3.455	0.18832
11.1173	0.25599
8.3	0.26474
8.4	0.15205
6.543	0.15642
10.27	0.11595
11.1	0.305644
9.92	0.317564
9.1	0.25929
3.04	0.371807
11.705	0.11154
5.25	0.357616
9.3	0.18639
8.5	0.2867
3.534	0.308422
3.9	0.333055
5.76	0.491057
5.76	0.491546
5.828	0.315592
5.3	0.339477
6.1	0.397148
6.748	0.19368
3.534	0.308422
3.9	0.333055
5.76	0.491057
5.76	0.491546
5.828	0.315592
5.3	0.339477

Table E10: Complex **5** in Water

pH	313 nm
1.89	0.033986
2.569	0.031918
2.969	0.026391
3.13	0.031801
3.35	0.035397
3.689	0.038327
3.698	0.041915
3.825	0.02916
4.042	0.044423
4.375	0.034841
4.795	0.033683
5.21	0.030099
5.398	0.040167
5.789	0.035012
5.902	0.042825
6.014	0.03708
6.33	0.043045
6.8	0.042745
6.485	0.040072
7.179	0.040905
6.963	0.045435
7.064	0.048394
7.245	0.048875
7.749	0.051128
8.275	0.06805
8.645	0.070917
8.205	0.056578
8.989	0.090072
7.8	0.065264
8.21	0.048044
9.445	0.096376
9.848	0.115295
10.498	0.116143
10.33	0.12162
10.803	0.116196
11.08	0.12438
11.335	0.115513

Eu(III)Complex 5 in Water UV-vis
Results for nonlinear fit 313 nm
[Initial paramater estimates]
PK1 = 8.700094
A0 = 0.03822352
A1 = 0.1183201

[Model]
H=10^(-x)
K1=10^(-pK1)
Alpha=H+K1
Y=(A0*H+A1*K1)/Alpha

[Results]
Number of data points : 37
Number of paramaters : 3
Number of parameters varied : 3
Sum of squares of errors : 1.42838630518005E-003
Estimated standard deviation : 6.48161723006382E-003
Mean of residuals : -3.43918269367604E-017
Number of Iterations : 9
R-squared : 0.95885
Adjusted R-squared : 0.95643
F-Statistic : 396.17175

Parameter	Coefficient	Varied	Standard error
PK1	8.700093530930E+000	Yes	0.0830246
A0	3.822351864155E-002	Yes	0.00135527
A1	1.183201085184E-001	Yes	0.00271045

[Correlation matrix]

	1	2	3
1	1.0000	0.3510	0.4610
2	0.3510	1.0000	0.0664
3	0.4610	0.0664	1.0000

F: Lifetime Measurements

Complex 5 (with MCB + KHP) in Water (pH 4.710)
Lifetimes Report

Report Time : Mon 30 Jan 11:36:36 AM 2012
Software version: 1.1(132)
Operator:

Data name	Number of cycles	Ex. Wavelength	Em. Wavelength	Ex. Slit	Em. Slit
580 nm	50	240.00	580.00	20	10

Lifetimes Report

Report Time : Mon 30 Jan 11:36:36 AM 2012
Software version: 1.1(132)
Operator:

Data name	Number of cycles	Ex. Wavelength	Em. Wavelength	Ex. Slit	Em. Slit
580 nm	50	240.00	580.00	20	10

Single Exponential Result Table
Sample Name: 580 nm
Equation: A1 exp(-k1*time) + C

Start (ms): 0.00
Stop (ms): 100.00

k1 (ms-1)	A1	C	S.D.
3.149±0.1	13.8404±0.9	0.0245±0.0	0.0244

Complex 5 (with MCB +KHP) in D_2O (pH 4.695)
Lifetimes Report

Report Time : Tue 31 Jan 12:01:25 PM 2012
Software version: 1.1(132)
Operator:

Data name	Number of cycles	Ex. Wavelength	Em. Wavelength	Ex. Slit	Em. Slit
580 nm	50	240.00	580.00	20	10

Lifetimes Report
Report Time : Tue 31 Jan 12:01:25 PM 2012
Software version: 1.1(132)
Operator:

Data name Number of cycles Ex. Wavelength Em. Wavelength Ex. Slit Em. Slit

580 nm 50 240.00 580.00 20 10

Single Exponential Result Table
Sample Name: 580 nm
Equation: A1 exp(-k1*time) + C

Start (ms): 0.00
Stop (ms): 100.00

k1 (ms-1)	A1	C	S.D.
0.569±0.0	4.6882±0.1	0.0237±0.0	0.0264

Complex 5 (with MCB + KHP) in Water (pH 5.320)
Lifetimes Report
Report Time : Mon 30 Jan 12:03:35 PM 2012
Software version: 1.1(132)
Operator:

Data name	Number of cycles	Ex. Wavelength	Em. Wavelength	Ex. Slit	Em. Slit
580 nm	50	240.00	580.00	20	10

Lifetimes Report

Report Time : Mon 30 Jan 12:03:35 PM 2012
Software version: 1.1(132)
Operator:

Data name	Number of cycles	Ex. Wavelength	Em. Wavelength	Ex. Slit	Em. Slit
580 nm	50	240.00	580.00	20	10

Single Exponential Result Table
Sample Name: 580 nm
Equation: A1 exp(-k1*time) + C

Start (ms): 0.00
Stop (ms): 100.00

k1 (ms-1)	A1	C	S.D.
3.120±0.1	18.7102±0.8	0.0004±0.0	0.0224

Complex 5 (with MCB +KHP) in D_2O (pH 5.321)
Lifetimes Report
Report Time : Tue 31 Jan 12:16:31 PM 2012
Software version: 1.1(132)
Operator:

Data name	Number of cycles	Ex. Wavelength	Em. Wavelength	Ex. Slit	Em. Slit
580 nm	50	240.00	580.00	20	10

Lifetimes Report

Report Time : Tue 31 Jan 12:16:31 PM 2012
Software version: 1.1(132)
Operator:

Data name	Number of cycles	Ex. Wavelength	Em. Wavelength	Ex. Slit	Em. Slit
580 nm	50	240.00	580.00	20	10

Single Exponential Result Table
Sample Name: 580 nm
Equation: A1 exp(-k1*time) + C

Start (ms): 0.00
Stop (ms): 100.00

k1 (ms-1)	A1	C	S.D.
0.568±0.0	7.9435±0.1	0.0192±0.0	0.0248

Complex 5 (with MCB + KHP) in Water (pH 7.423)
Lifetimes Report

Report Time : Mon 30 Jan 12:22:29 PM 2012
Software version: 1.1(132)
Operator:

Data name	Number of cycles	Ex. Wavelength	Em. Wavelength	Ex. Slit	Em. Slit
580 nm	50	240.00	580.00	20	10

Lifetimes Report
Report Time : Mon 30 Jan 12:22:29 PM 2012
Software version: 1.1(132)
Operator:

Data name	Number of cycles	Ex. Wavelength	Em. Wavelength	Ex. Slit	Em. Slit
580 nm	50	240.00	580.00	20	10

Single Exponential Result Table
Sample Name: 580 nm
Equation: A1 exp(-k1*time) + C

Start (ms): 0.00
Stop (ms): 100.00

k1 (ms-1)	A1	C	S.D.
2.849±0.1	16.5018±0.6	0.0360±0.0	0.0239

Complex 5 (with MCB +KHP) in D_2O (pH 7.424)
Lifetimes Report

Report Time : Tue 31 Jan 12:49:15 PM 2012
Software version: 1.1(132)
Operator:

Data name	Number of cycles	Ex. Wavelength	Em. Wavelength	Ex. Slit	Em. Slit
580 nm	50	240.00	580.00	20	10

Lifetimes Report

Report Time : Tue 31 Jan 12:49:15 PM 2012
Software version: 1.1(132)
Operator:

Data name	Number of cycles	Ex. Wavelength	Em. Wavelength	Ex. Slit	Em. Slit
580 nm	50	240.00	580.00	20	10

Single Exponential Result Table
Sample Name: 580 nm
Equation: A1 exp(-k1*time) + C

Start (ms): 0.00
Stop (ms): 100.00

k1 (ms-1)	A1	C	S.D.
0.601±0.0	17.5452±0.1	0.0342±0.0	0.0253

Complex 5 (with MCB + KHP) in Water (pH 8.172)
Lifetimes Report
Report Time : Mon 30 Jan 12:35:52 PM 2012
Software version: 1.1(132)
Operator:

Data name	Number of cycles	Ex. Wavelength	Em. Wavelength	Ex. Slit	Em. Slit
580 nm	50	240.00	580.00	20	10

Lifetimes Report
Report Time : Mon 30 Jan 12:35:52 PM 2012
Software version: 1.1(132)
Operator:

Data name	Number of cycles	Ex. Wavelength	Em. Wavelength	Ex. Slit	Em. Slit
580 nm	50	240.00	580.00	20	10

Single Exponential Result Table
Sample Name: 580 nm
Equation: A1 exp(-k1*time) + C

Start (ms): 0.00
Stop (ms): 100.00

k1 (ms-1)	A1	C	S.D.
2.592±0.1	13.3319±0.5	0.0385±0.0	0.0231

Complex 5 (with MCB +KHP) in D_2O (pH 8.174)
Lifetimes Report

Report Time : Tue 31 Jan 01:12:28 PM 2012
Software version: 1.1(132)
Operator:

Data name	Number of cycles	Ex. Wavelength	Em. Wavelength	Ex. Slit	Em. Slit
580 nm	50	240.00	580.00	20	10

Lifetimes Report

Report Time : Tue 31 Jan 01:12:28 PM 2012
Software version: 1.1(132)
Operator:

Data name	Number of cycles	Ex. Wavelength	Em. Wavelength	Ex. Slit	Em. Slit
580 nm	50	240.00	580.00	20	10

Single Exponential Result Table
Sample Name: 580 nm
Equation: A1 exp(-k1*time) + C

Start (ms): 0.00
Stop (ms): 100.00

k1 (ms-1)	A1	C	S.D.
0.637±0.0	18.1833±0.1	0.0365±0.0	0.0258

Complex 5 (with MCB + KHP) in Water (pH 8.710)
Lifetimes Report

Report Time : Mon 30 Jan 01:36:29 PM 2012
Software version: 1.1(132)
Operator:

Data name	Number of cycles	Ex. Wavelength	Em. Wavelength	Ex. Slit	Em. Slit
580 nm	50	240.00	580.00	20	10

Lifetimes Report
Report Time : Mon 30 Jan 01:36:29 PM 2012
Software version: 1.1(132)
Operator:

Data name	Number of cycles	Ex. Wavelength	Em. Wavelength	Ex. Slit	Em. Slit
580 nm	50	240.00	580.00	20	10

Single Exponential Result Table
Sample Name: 580 nm
Equation: A1 exp(-k1*time) + C

Start (ms): 0.00
Stop (ms): 100.00

k1 (ms-1)	A1	C	S.D.
2.799±0.1	14.8444±0.6	0.0593±0.0	0.0237

Complex 5 (with MCB +KHP) in D_2O (pH 8.714)
Lifetimes Report

Report Time : Tue 31 Jan 01:47:47 PM 2012
Software version: 1.1(132)
Operator:

Data name	Number of cycles	Ex. Wavelength	Em. Wavelength	Ex. Slit	Em. Slit
580 nm	50	240.00	580.00	20	10

Lifetimes Report
Report Time : Tue 31 Jan 01:47:47 PM 2012
Software version: 1.1(132)
Operator:

Data name	Number of cycles	Ex. Wavelength	Em. Wavelength	Ex. Slit	Em. Slit
580 nm	50	240.00	580.00	20	10

Single Exponential Result Table
Sample Name: 580 nm
Equation: A1 exp(-k1*time) + C

Start (ms): 0.00
Stop (ms): 100.00

k1 (ms-1)	A1	C	S.D.
0.808±0.0	23.2327±0.1	0.0147±0.0	0.0280

Complex 5 (with MCB + KHP) in Water (pH 9.382)
Lifetimes Report

Report Time : Mon 30 Jan 01:53:06 PM 2012
Software version: 1.1(132)
Operator:

Data name	Number of cycles	Ex. Wavelength	Em. Wavelength	Ex. Slit	Em. Slit
580 nm	50	240.00	580.00	20	10

Lifetimes Report

Report Time : Mon 30 Jan 01:53:06 PM 2012
Software version: 1.1(132)
Operator:

Data name	Number of cycles	Ex. Wavelength	Em. Wavelength	Ex. Slit	Em. Slit
580 nm	50	240.00	580.00	20	10

Single Exponential Result Table
Sample Name: 580 nm
Equation: A1 exp(-k1*time) + C

Start (ms): 0.00
Stop (ms): 100.00

k1 (ms-1)	A1	C	S.D.
2.953±0.1	15.7803±0.7	0.0292±0.0	0.0234

Complex 5 (with MCB +KHP) in D_2O (pH 9.382)
Lifetimes Report
Report Time : Tue 31 Jan 02:06:23 PM 2012
Software version: 1.1(132)
Operator:

Data name	Number of cycles	Ex. Wavelength	Em. Wavelength	Ex. Slit	Em. Slit
580 nm	50	240.00	580.00	20	10

Lifetimes Report

Report Time : Tue 31 Jan 02:06:23 PM 2012
Software version: 1.1(132)
Operator:

Data name	Number of cycles	Ex. Wavelength	Em. Wavelength	Ex. Slit	Em. Slit
580 nm	50	240.00	580.00	20	10

Single Exponential Result Table
Sample Name: 580 nm
Equation: A1 exp(-k1*time) + C

Start (ms): 0.00
Stop (ms): 100.00

k1 (ms-1)	A1	C	S.D.
0.971±0.0	15.4437±0.1	0.0479±0.0	0.0250

Complex 5 (with MCB + KHP) in Water (pH 9.484)
Lifetimes Report

Report Time : Mon 30 Jan 02:11:29 PM 2012
Software version: 1.1(132)
Operator:

Data name	Number of cycles	Ex. Wavelength	Em. Wavelength	Ex. Slit	Em. Slit
580 nm	50	240.00	580.00	20	10

Lifetimes Report

Report Time : Mon 30 Jan 02:11:29 PM 2012
Software version: 1.1(132)
Operator:

Data name	Number of cycles	Ex. Wavelength	Em. Wavelength	Ex. Slit	Em. Slit
580 nm	50	240.00	580.00	20	10

Single Exponential Result Table
Sample Name: 580 nm
Equation: A1 exp(-k1*time) + C

Start (ms): 0.00
Stop (ms): 100.00

k1 (ms-1)	A1	C	S.D.
2.727±0.1	13.3816±0.5	0.0190±0.0	0.0216

Complex 5 (with MCB +KHP) in D_2O (pH 9.485)
Lifetimes Report

Report Time : Tue 31 Jan 02:21:59 PM 2012
Software version: 1.1(132)
Operator:

Data name	Number of cycles	Ex. Wavelength	Em. Wavelength	Ex. Slit	Em. Slit
580 nm	50	240.00	580.00	20	10

Lifetimes Report
Report Time : Tue 31 Jan 02:21:59 PM 2012
Software version: 1.1(132)
Operator:

Data name	Number of cycles	Ex. Wavelength	Em. Wavelength	Ex. Slit	Em. Slit
580 nm	50	240.00	580.00	20	10

Single Exponential Result Table
Sample Name: 580 nm
Equation: A1 exp(-k1*time) + C

Start (ms): 0.00
Stop (ms): 100.00

k1 (ms-1)	A1	C	S.D.
1.115±0.0	15.8620±0.1	0.0196±0.0	0.0242

Complex 5 in Water (pH 4.375)
Lifetimes Report
Report Time : Mon 30 Jan 09:51:46 AM 2012
Software version: 1.1(132)
Operator:

Data name	Number of cycles	Ex. Wavelength	Em. Wavelength	Ex. Slit	Em. Slit
580 nm	50	240.00	580.00	20	10

Lifetimes Report

Report Time : Mon 30 Jan 09:51:46 AM 2012
Software version: 1.1(132)
Operator:

Data name	Number of cycles	Ex. Wavelength	Em. Wavelength	Ex. Slit	Em. Slit
580 nm	50	240.00	580.00	20	10

Single Exponential Result Table
Sample Name: 580 nm
Equation: A1 exp(-k1*time) + C

Start (ms): 0.00
Stop (ms): 100.00

k1 (ms-1)	A1	C	S.D.
2.374±0.0	30.3587±0.4	0.0038±0.0	0.0210

Complex 5 in D_2O (pH 4.375)
Lifetimes Report

Report Time : Tue 31 Jan 09:16:39 AM 2012
Software version: 1.1(132)
Operator:

Data name	Number of cycles	Ex. Wavelength	Em. Wavelength	Ex. Slit	Em. Slit
580 nm	50	240.00	580.00	20	10

Lifetimes Report

Report Time : Tue 31 Jan 09:16:39 AM 2012
Software version: 1.1(132)
Operator:

Data name	Number of cycles	Ex. Wavelength	Em. Wavelength	Ex. Slit	Em. Slit
580 nm	50	240.00	580.00	20	10

Single Exponential Result Table
Sample Name: 580 nm
Equation: A1 exp(-k1*time) + C

Start (ms): 0.00
Stop (ms): 100.00

k1 (ms-1)	A1	C	S.D.
0.556±0.0	28.4077±0.1	0.0145±0.0	0.0351

Complex 5 in Water (4.795)

Lifetimes Report

Report Time : Mon 30 Jan 10:12:20 AM 2012
Software version: 1.1(132)
Operator:

Data name	Number of cycles	Ex. Wavelength	Em. Wavelength	Ex. Slit	Em. Slit
580 nm	50	240.00	580.00	20	10

Lifetimes Report
Report Time : Mon 30 Jan 10:12:20 AM 2012
Software version: 1.1(132)
Operator:

Data name	Number of cycles	Ex. Wavelength	Em. Wavelength	Ex. Slit	Em. Slit
580 nm	50	240.00	580.00	20	10

Single Exponential Result Table
Sample Name: 580 nm
Equation: A1 exp(-k1*time) + C

Start (ms): 0.00
Stop (ms): 100.00

k1 (ms-1)	A1	C	S.D.
2.331±0.0	30.1144±0.4	0.0437±0.0	0.0212

Complex 5 in D_2O (pH 4.799)

Lifetimes Report

Report Time : Tue 31 Jan 10:00:46 AM 2012
Software version: 1.1(132)
Operator:

Data name	Number of cycles	Ex. Wavelength	Em. Wavelength	Ex. Slit	Em. Slit
580 nm	50	240.00	580.00	20	10

Lifetimes Report

Report Time : Tue 31 Jan 10:00:46 AM 2012
Software version: 1.1(132)
Operator:

Data name	Number of cycles	Ex. Wavelength	Em. Wavelength	Ex. Slit	Em. Slit
580 nm	50	240.00	580.00	20	10

Single Exponential Result Table
Sample Name: 580 nm
Equation: A1 exp(-k1*time) + C

Start (ms): 0.00
Stop (ms): 100.00

k1 (ms-1)	A1	C	S.D.
0.559±0.0	28.4178±0.1	0.0600±0.0	0.0323

Complex 5 in Water (pH 8.275)

Lifetimes Report

Report Time : Mon 30 Jan 10:38:49 AM 2012
Software version: 1.1(132)
Operator:

Data name	Number of cycles	Ex. Wavelength	Em. Wavelength	Ex. Slit	Em. Slit
580 nm	50	240.00	580.00	20	10

Lifetimes Report

Report Time : Mon 30 Jan 10:38:49 AM 2012
Software version: 1.1(132)
Operator:

Data name	Number of cycles	Ex. Wavelength	Em. Wavelength	Ex. Slit	Em. Slit
580 nm	50	240.00	580.00	20	10

Single Exponential Result Table
Sample Name: 580 nm
Equation: A1 exp(-k1*time) + C

Start (ms): 0.00
Stop (ms): 100.00

k1 (ms-1)	A1	C	S.D.
2.453±0.0	32.2414±0.5	0.0326±0.0	0.0254

Complex 5 in D_2O (pH 8.298)

Lifetimes Report

Report Time : Tue 31 Jan 10:28:45 AM 2012
Software version: 1.1(132)
Operator:

Data name	Number of cycles	Ex. Wavelength	Em. Wavelength	Ex. Slit	Em. Slit
580 nm	50	240.00	580.00	20	10

Lifetimes Report

Report Time : Tue 31 Jan 10:28:45 AM 2012
Software version: 1.1(132)
Operator:

Data name	Number of cycles	Ex. Wavelength	Em. Wavelength	Ex. Slit	Em. Slit
580 nm	50	240.00	580.00	20	10

Single Exponential Result Table
Sample Name: 580 nm
Equation: A1 exp(-k1*time) + C

Start (ms): 0.00
Stop (ms): 100.00

k1 (ms-1)	A1	C	S.D.
0.987±0.0	74.7819±0.2	0.0432±0.0	0.0461

Complex 5 in Water (pH 8.645)

Lifetimes Report

Report Time : Mon 30 Jan 10:55:28 AM 2012
Software version: 1.1(132)
Operator:

Data name	Number of cycles	Ex. Wavelength	Em. Wavelength	Ex. Slit	Em. Slit
580 nm	50	240.00	580.00	20	10

Lifetimes Report

Report Time : Mon 30 Jan 10:55:28 AM 2012
Software version: 1.1(132)
Operator:

Data name	Number of cycles	Ex. Wavelength	Em. Wavelength	Ex. Slit	Em. Slit
580 nm	50	240.00	580.00	20	10

Single Exponential Result Table
Sample Name: 580 nm
Equation: A1 exp(-k1*time) + C

Start (ms): 0.00
Stop (ms): 100.00

k1 (ms-1)	A1	C	S.D.
2.392±0.0	33.3749±0.4	0.0385±0.0	0.0253

Complex 5 in D_2O (pH 8.646)

Lifetimes Report

Report Time : Tue 31 Jan 10:55:46 AM 2012
Software version: 1.1(132)
Operator:

Data name	Number of cycles	Ex. Wavelength	Em. Wavelength	Ex. Slit	Em. Slit
580 nm	50	240.00	580.00	20	10

Lifetimes Report

Report Time : Tue 31 Jan 10:55:46 AM 2012
Software version: 1.1(132)
Operator:

Data name	Number of cycles	Ex. Wavelength	Em. Wavelength	Ex. Slit	Em. Slit
580 nm	50	240.00	580.00	20	10

Single Exponential Result Table
Sample Name: 580 nm
Equation: A1 exp(-k1*time) + C

Start (ms): 0.00
Stop (ms): 100.00

k1 (ms-1)	A1	C	S.D.
0.924±0.0	66.8742±0.2	0.0060±0.0	0.0480